Doctoral theses at NTNU, 2022:14

Håkon Myklebust

Fume Formation and Measurements in the Metal Production Industry

Doctoral thesis

NTNU
Norwegian University of Science and Technology
Thesis for the Degree of
Philosophiae Doctor
Faculty of Natural Sciences
Department of Materials Science and Engineering

NTNU
Norwegian University of
Science and Technology

Håkon Myklebust

Fume Formation and Measurements in the Metal Production Industry

Thesis for the Degree of Philosophiae Doctor

Trondheim, January 2022

Norwegian University of Science and Technology
Faculty of Natural Sciences
Department of Materials Science and Engineering

NTNU
Norwegian University of
Science and Technology

NTNU
Norwegian University of Science and Technology

Thesis for the Degree of Philosophiae Doctor

Faculty of Natural Sciences
Department of Materials Science and Engineering

ISBN 978-82-326-5959-3 (printed ver.)
ISBN 978-82-326-5234-1 (electronic ver.)
ISSN 1503-8181 (printed ver.)
ISSN 2703-8084 (online ver.)

Doctoral theses at NTNU, 2022:14

Printed by NTNU Grafisk senter

Contents

Preface

The thesis was submitted in partial fulfillment of the degree of Doctor of Philosophy. The work was carried out at the Department of Materials Science and Engineering at the Norwegian University of Science and Technology (NTNU), from August 2016 to June 2021. This research was funded by the Centre for Research-Based Innovation, SFI Metal Production, NFR Project number 237738.

Acknowledgements

There are many people I would like to express my heartfelt gratitude to. First of all I would like to thank my Wife, Anne Marte Ellertsen, who helped push me through those dark times when I was certain I would never finish. I had never thought of having two kids while finishing a doctoral thesis was a realistic prospect, but together we made it 'till the end, and there's nobody else I'd rather go through such an intense journey with.

This would never have been close to possible without the endless patience and support from my supervisor Gabriella Tranell. She has pushed me to be my best, helped me use my strengths and get past my shortcomings, and given leeway when times have been too tough. I cannot thank you enough for believing in me and helping me over these (almost) five years.

I would also like to give my thanks to my Co-supervisor, Stefan Andersson. His help with modelling has been invaluable, and the discussions back and forth trying to understand old articles and sanity-check my results were integral to completing this work. Similarly I want to thank Thor Anders Aarhaug, who joined the team later and was promoted to Co-supervisor at the end. He provided the starting point for the entire sensor part of my PhD-work, and has been an incredible resource when going forward with that part.

To every current and former member of the SiManTi-group: you have my thanks for all the great feedback, discussions, and learning opportunities over these years. I am also grateful for all the good times baking gingerbread, playing games, and travelling together. You've certainly added flavor to this experience! Special

thanks here goes to my friends in E-331 whom I've shared an extra bond and many tips and tricks with. Plastering the wall with funny motivational posters and engineering comics was just one of the many things that brightened long working days.

When choosing to specialize in process metallurgy, only a single other student joined me and we've been working together with almost everything since then. Erlend Bjørnstad has been my better half at the university for almost 7 years, and without him I'd never have learned everything I've needed to get to this point. You're truly a great friend and co-worker, and I hope I've helped you even a third of how much you've helped me!

I would like to give special thanks to the engineering staff at the department who helped me perform my laboratory work. In particular I would like to thank my good friend Dmirty Slizovski, whom the department could never run without, and his office-partner in arms Ivar Ødegård. I would also like to specifically thank Ingeborg Solheim and Steinar Prytz at SINTEF, both whose help has been essential.

I have performed several measurement campaigns, and I want to sincerely thank Eramet, Elkem, and Hydro for supporting my endeavors and helping me perform my research at their plants, as well as Norce for their support and equipment. I would also like to thank some specific people who helped me set up and run the campaigns, as well as proving advice and discussions: Heiko Gaartner, Hege Indresand, and Morten Isaksen.

The authors would like to thank the Centre for Research-Based Innovation (SFI Metal Production, NFR Project number 237738) for funding the project. UNINETT Sigma2 – the National Infrastructure for High Performance Computing and Data Storage in Norway is acknowledged for a generous grant of computer time (project NN9353K).

Abstract

Airborne Particulate Matter (PM) is considered to be a major concern for both occupational health and the environment, and in the metal production industry, the level of such particles in the air can be considerable. A better understanding of the mechanisms of fume formation and the operational parameters affecting the fume formation rate, may help in reducing and managing fuming. Additionally, good measurement techniques and equipment can give insight to when and where fuming rates are at the highest, and how well implemented measures are working. Current measuring equipment for in-situ measurements of PM emissions is generally large and expensive or lacks the required time and spatial resolution to provide accurate information on the intensity and variations over time of the emissions.

The first part of this work aimed to investigate the evaporation rates of pure liquid manganese in an inert atmosphere given variations in the temperature and the flow conditions above the surface. The evaporation rates were attained through laboratory experiments measuring the flux with respect to temperature and gas velocity above the metal melt. The evaporation fluxes were found to increase linearly with increasing flow rates of the gas, and exponentially with increasing temperature. The flow and mass transfer was simulated with Comsol Multiphysics, and the modelled fluxes based on the simulated concentration gradient across the surface was found to closely match the experimental fluxes at 1400 and 1550°C, with some deviation at 1700°C.

The second part of this work aimed to investigate the effects of oxygen content and gas flow rate on the fuming rate and fume particulate properties for liquid high carbon ferromanganese. The fuming rates were attained through laboratory

experiments measuring the fume flux with respect to oxygen content and gas velocity above a metal melt. The generated fumes were also characterized in terms of particle size and element distribution between fume and melt. The fuming rates were found to increase with increasing oxygen content and flow rate of the gas up to a point, following theoretical predictions. However, the highest flux values measured were above the theoretical limitations of the evaporation flux in vacuo given the alloy bulk composition. It is hypothesized that the high rate of fuming is caused by an increased manganese activity at the alloy surface due to local decarburization of the alloy in contact with the oxidizing gas. A model based on existing theories on oxidation-enhanced evaporation, given the assumption of decarburization, were able to predict flux values across varying oxygen concentrations given a single calibration point.

The third part of this work aimed at testing and evaluating distributed micro sensors for in-situ spatial monitoring of dust intensity in the metal-production industry. Small, low cost sensors for measuring PM have generated interest in recent years, providing widespread monitoring of PM-levels in the environment. However, such sensors have not yet been sufficiently tested under conditions relevant for the indoor environment of the metallurgical industry. This study aims to bridge this gap by benchmarking the commercial, low-cost Nova PM SDS011 particle sensor in two different ferroalloy plants towards the Fidas 200S which has been suitability-tested and certified according to the latest EU requirements (EN 15267, EN 16450) (1). 12 Nova sensors were tested over three months at a silicomanganese alloy (SiMn) plant, and 35 sensors were tested during one month at a silicon (Si) plant. In addition, 12 Nova sensors were tested in an aluminium (Al) plant without reference equipment. The results showed that the low-cost Nova sensors exhibited all the same trends and peaks in terms of PM concentration, but consistently measured lower dust concentrations than the Fidas 200S. The difference was larger at the silicon plant, which is in line with expectations due to the size- and mass fractions of particles in Si-dust compared to SiMn dust and the larger measurement range of the Fidas, particularly in regards to particles larger than 1.7μm of which the Nova can only estimate based on the amount of smaller dust. The results from the Al plant showed that separations of only a few meters had large impacts on the fume levels, and that individual peaks could be correlated directly to the process events in the electrolysis hall, both in regards to fume levels and the properties of the fumes.

Variation between sensors in each closely placed group was found to be mostly within a spread of +/- 20% at the SiMn and Al plant, with more variations at the Si

plant. Sensor reliability was good at the SiMn and Al plant, with no lasting sensor failure, but at the Si plant more than half of the sensors stopped working over the course of the measurement campaign. Both high variation and low reliability at the Si plant is believed to be partially due to the SiO_2 fumes causing damage to the electronics. Despite the difference in absolute values between the Nova and the Fidas, the Nova sensors were found to provide valuable data for comparing dust levels over time for different processes, at different locations, and under different operational conditions. It is estimated that with proper calibration for each type of dust, the data gathered by the Nova can be useful for spatial monitoring over time as tool for assessing e.g effects of dust mitigation measures.

List of Papers

Paper I: *Evaporation and Diffusion of Mn in Inert Systems*,
Myklebust HAHO, Andersson S, Tranell G (2018)
The Minerals, Metals & Materials Series 2018, CFD Modeling and Simulation in Materials Processing; p. 97-110
DOI: https://doi.org/10.1007/978-3-319-72059-3_10
Contributions:

- Myklebust HAHO: Lead author, experimental work, flux modelling
- Andersson S: Dicussions, collaboration on flux modelling, modelling of diffusion coefficients
- Tranell G: Discussions, paper feedback and correction

Paper II: *Measurement system for diffuse emissions in primary aluminum production*,
Myklebust HAHO, Aarhaug TA, Tranell G (2020)
The Minerals, Metals & Materials Series 2020, Light Metals; p. 735-743
Contributions:

- Myklebust HAHO: Lead author, assembling and coding of equipment,
- Aarhaug TA: Discussions, paper feedback and correction
- Tranell G: Discussions, paper feedback and correction

Paper III: *Oxidation-Enhanced Evaporation in High-Carbon Ferromanganese*,
Myklebust HAHO, Andersson S, Tranell G (2021)

Oxidation of Metals 2021; Volume 95. p. 269-290
DOI: https://doi.org/10.1007/s11085-021-10023-0
Contributions:

- Myklebust HAHO: Lead author, experimental work, flux modelling
- Andersson S: Dicussions, collaboration on flux modelling, modelling of diffusion coefficients
- Tranell G: Discussions, paper feedback and correction

Paper IV: *Distributed Sensor System for Diffuse Emissions*,
Myklebust HAHO, Aarhaug TA, Tranell G (2021)
Sent to Atmosphere: https://www.mdpi.com/journal/atmosphere.
Contributions:

- Myklebust HAHO: Lead author, assembling and coding of equipment,
- Aarhaug TA: Discussions, paper feedback and correction, setting up equipment
- Tranell G: Discussions, paper feedback and correction

List of Tables

List of Figures

Chapter 1

Introduction

Airborne Particulate Matter (PM) is considered a concern for both occupational health and the environment. Exposure to high levels of particles has been linked to asthma, lung cancer, pneumonia, chronic obstructive pulmonary disease (COPD) and other respiratory and cardiovascular syndromes, the level of which relate to the size, composition and properties of the particles (2, 3, 4, 5, 6, 7, 8, 9, 10). Inhalation of certain manganese (Mn) compounds has also been linked to inflammation and neuropsychological disturbances (11, 12, 13). The dust produced in aluminium electrolysis often contain high levels of fluorine which may generate hydrofluoric acid if it comes into contact with water (14). Silica fumes at concentrations above $0.028\mu g/cm^2$ have been found to induce cytotoxicity in a human astrocytoma cell line, with significant reduction in viability of the cells being found at lower levels as well when the silica is crystalline in nature (15). However, these fumes are not only a concern in terms of workers health, but also contribute to the so-called fugitive emissions which may be harmful to the local, urban communities as well as the environment at large .

It is well known that ultrafine particles have a much greater surface area and different physico-chemical characteristics (16, 17) compared to their larger counterparts. They may therefore be more reactive, behave differently in the respiratory system, and give rise to increased biological responses (18). The smaller the particles, the further into the human system they can penetrate, including the bronchi for PM up to 10 μm(PM10), the lungs for PM up to 2.5 μm(PM2.5), and even through the lungs and into the circulatory system for ultrafine particles below 0.1 μm(PM0.1) (19, 20, 21). Because of this, the measurement of different PM fractions in workplace environments is very important for the safety of the workers, and knowing

how and where the fumes are produced and how to limit fuming is equally important to be able to improve working conditions and reduce emissions. With that in mind, this project has largely been divided in two parts; one focused on studying the fundamentals of fume formation from manganese and ferromanganese alloys through experimental work and modelling, and the other focused on investigating the usability of a low-cost sensor system for measuring PM concentrations in the metal production industry.

1.1 Fume formation

As the chemical composition and morphology (particle shape) of particles originating from different ferroalloy industries and processes vary greatly, it is important to understand the mechanisms by which dusts are generated and how the characteristic properties of the particles depend on process parameters. With such knowledge, primary dust generation may be partially controlled. This knowledge may also aid in the design of more effective dust capturing systems.

In the current project, specific focus has been made in understanding the formation mechanisms, rate, and properties of fume from manganese alloys. Manganese is extensively used as an alloying element for the iron- and steelmaking industry in the form of ferromanganese (FeMn) and silicomanganese (SiMn) (22), and ferromanganese alloys can be further classified into high-carbon ([C]-7.0wt%), medium-carbon ([C]<2.5wt%), and low-carbon ([C]<0.5wt%) grades (23), of which this work used high-carbon ferromanganese (HCFeMn) in FeMn experiments. The production of both FeMn and SiMn commonly takes place in an electric submerged arc furnace through carbothermic reduction of Mn ores as well as quartz in the case of SiMn. An important and not yet thoroughly studied part of the dust formation from liquid Mn alloys such as FeMn and SiMn is the evaporation and gas-phase diffusion of Mn. In contrast to silicon (Si), which has a very low vapor pressure and will mostly react with oxygen to form dust via a two-step oxidation process, Mn evaporates noticeably at temperatures above the melting point. For SiMn-alloys, this leads to possible reactions between Si oxides and Mn fumes, but can also cause a competition for oxygen close to the surface of the liquid alloy where if little oxygen reaches the surface, a limited amount of Si-containing fume will be formed (24). Because of these reasons, the experimental study and subsequent modelling of evaporation rates of Mn is important and coupled to prevailing theory on oxidation-enhanced evaporation (25, 26).

The principle aims of this part of the PhD work were to investigate the evapora-

tion rates of manganese given varying diffusion conditions as well as quantifying the effects of the oxidation-enhanced evaporation by performing experiments with liquid pure Mn and HCFeMn exposed to varying oxygen concentrations and gas flow velocities. Qualitative and quantitative investigations were conducted on the fumes generated from the HCFeMn experiments, including element and size distributions, while only quantitative investigations were conducted for the Mn evaporation experiments.

This part of the work resulted in 2 papers, which are included as Paper I and Paper III in this thesis. The relevant literature for the work is presented in section 2.1 and 2.4, and the methods for experimental and modelling work is presented and discussed in section 3.1-3.2. The results on this topic are summed up, presented, and discussed in section 4.1. The overall conclusions and suggestions for future work is presented in section 5.1-5.2.

1.2 Dust measurements

According to current EU-regulations, exposure to PM10 in ambient air should be limited to a maximum of 50 μg/m^3 averaged over a 24-hour period with a maximum of 35 permitted exceedences per year. The yearly average is limited to 40 μg/m^3 for PM10 and 25 μg/m^3 for PM2.5 (27). Workplace PM exposure is often monitored by personal portable devices while monitoring of ambient plant PM levels are often measured using one or more fixed measurement stations that measure for long periods at a time. These stations are expensive to set up, which limits the number of spatial measurement points that can be realistically achieved. The use of less expensive, portable setups would circumvent this issue and allow for a much higher spatial resolution, which can be of particular use in the extremely varied environment that is the case for metal production plants. A better spatial resolution allows for tracking the flow of particles in the plant and can work as a tool for evaluating measures taken to reduce and capture PM emissions. Low-cost microsensors are not widely in use neither for air-pollution monitoring in general nor industry in particular. It is however being considered by the European Commission for air pollution monitoring and personal exposure, and with the technological improvements could become a "game changer" (28).

The principal aims of this part of the PhD work were to investigate the usability of a single type of low-cost PM sensor, the Nova PM SDS011 ("Nova"). Measurement campaigns in Al, Si and SiMn alloy plants were performed, and for parts of the campaigns the Nova was benchmarked towards the state of the art PM sensor;

Fidas 200S ("Fidas"). Along with the accuracy investigations, both the sensor lifetime, internal variation in groups of sensors, and drift over time were studied. In addition, the value of spatial resolution was evaluated, and the varying size distributions were correlated with process events where data was accessible. How the Nova handled the different types of fumes compared to the Fidas was also investigated.

This part of the work has resulted in 2 papers, which are included in this thesis as Paper II and IV. The relevant literature for the work regarding fume sources is presented in section 2.1-2.4, regarding sensor technology in section 2.5 and the methods for testing the sensors is presented and discussed in section 3.3. The results on this topic are summed up, presented, and discussed in section 4.2. The overall conclusions and suggestions for future work is presented in section 6.3.

Chapter 2

Literature Review

This literature review is organized with first a general background on metallurgical plants, the fumes therein, and why emission of particulate matter (PM) from these processes is an important subject. Second and third are two sections on the aluminium and silicon production processes and emission sources respectively, to serve as a background for the fume measurement campaigns. Fourth is an in-depth description of the ferromanganese production process and emission sources, including mechanisms such as oxidation-enhanced vaporisation as a basis for PM generation, as a background for both the fume measurement campaigns and the experimental and modelling work on evaporation and oxidation of manganese and ferromanganese. The last section gives an overview of different PM measurement techniques and equipment for fumes, with a focus on the measurement techniques and specific sensors used in this work.

2.1 General Background

Dust, or particulate matter, formation in metal production is a problem which occurs when thermally generated gases from a process condense and/or oxidise into particles or when mechanical processes, such as transportation, crushing and sieving of raw materials, generate small particles which are then suspended in the air. Fumes are as such categorized as either thermally or mechanically generated, but although they originate from different sources and through different mechanisms, the methods to measure them are typically the same. Such methods include, for example, fume sampling where filters catch fumes which can then be measured and analyzed, optical sensors which use light scattering, light absorption or light extinction to continuously measure the size and amount of particles in the air, and the microbalance method in which particles collect on a filter and cause the oscillation frequency of a quartz tube to vary (29).

Thermally generated fumes originate from any part of the metal production process in which liquid metal is in contact with air, or from the reduction processes in the furnace itself. Five different fume formation mechanisms are illustrated in Figure 2.1 (30), showing a variety of reactions that form particles from a liquid metal. The emission points where fumes formed in any of these ways are introduced into the ambient air includes the furnaces where and when they are open, as well as tapping, refining, and casting areas (31), where the liquid or evaporated metal or oxide reacts with the oxygen in the air to create oxide particles. Mechanically generated fumes originate from where materials are treated in a way that allows for parts of the material to be broken off. This could be during transport and handling of the more easily broken down raw materials, or during processing of the product such as crushing and sieving. Mechanically generated fumes can also come in the form of particles not originating from the raw materials themselves, but instead from sources such as sand brought in by vehicles, metal shavings from moving parts, rust and flaking paint.

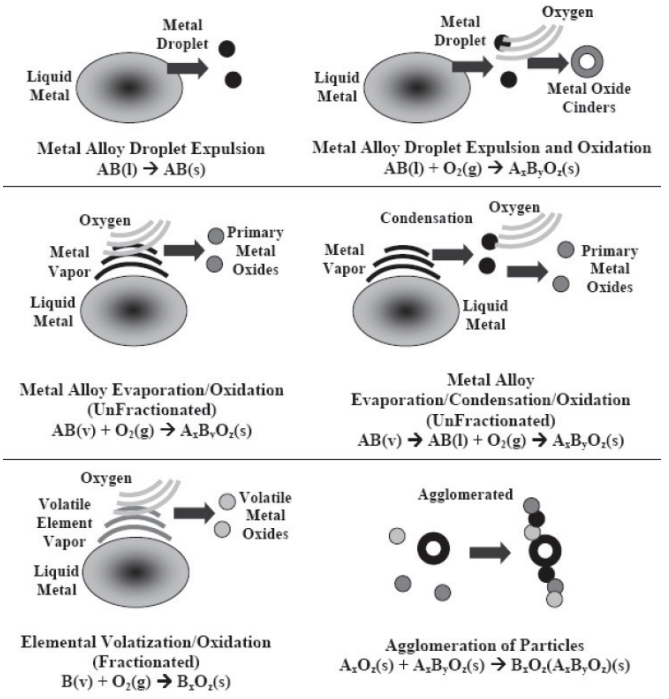

Figure 2.1: Fume formation mechanisms from a liquid metal (30).

Based on the chemical content of the dust, as well as how it was formed, PM vary greatly both in morphology and size and hence, how harmful to health it is. The European Commission distinguishes between PM10, the slightly larger particles still categorized as dangerously small, and PM2.5, the smaller and thus more dangerous particles. Both categories have regulated limits for average concentrations workers are exposed to, at 40 and 25 $\mu g/m^3$ for PM10 and PM2.5 respectively. Particularly dangerous substances such as Polycyclic Aromatic Hydrocarbons, Lead, and Nickel that may condense as dust also have specific limits (27). H. L. Johnsen (5) concluded after a five-year study among employees in Norwegian smelters, that line operators had an increased decline in lung functions compared to employees not exposed to PM, showing that current levels are harmful to the workers and that improvements towards the working environment in regards to PM is needed. Such improvements can only be made by understanding from where, how much, and what fumes are generated and spread throughout the smelting plants.

The spreading of the fumes is important, especially towards designing measures such as fume hoods or other ventilation. Fume spreading models can, along with measurement campaigns, be used to estimate exposure in different working areas (32). Dust spreading is strongly affected by temperature, as there are large fluctuations in the smelting plant environment and both pressure and thermal buoyancy has an impact on the flow of particles, and as such models need access to temperature data to give good approximations. As dust capturing efficiency depends on many factors , including fume hood shape, particle size, particle density, hall-wind, and suction rate (33), it is important to gain as much information as possible to get the most effective systems in place for improving working conditions and reducing diffusive emissions.

2.2 Production of Primary Aluminium

Primary aluminium is produced through electrolytic reduction of alumina (Al_2O_3) using the Hall–Héroult process where the alumina is reduced to aluminium in a cryolite bath in a cell which consists of a steel shell lined with carbon. The metal acts as the cathode while carbon electrodes extending into the solution acts as the anode. The electrolytic reduction of Al_2O_3 by the carbon electrode occurs following the reaction shown in reaction R1:

$$2\,Al_2O_3 + 3\,C \rightleftharpoons {}_4Al + 3\,CO_2 \qquad [R1]$$

Liquid aluminum deposits below the cryolite bath from where it is tapped usu-

ally every 24 to 48 hours. Two different categories of the Hall–Héroult process are identified by the carbon anodes used in the process. They can either be baked in the process, so called Söderberg electrodes, or be pre-baked, the former which while requiring less energy and labor to produce do release more fumes during the production and also results in a less efficient electrolysis process. Due to this, the pre-baked anode is currently preferred over the Söderberg electrode (34). As the carbon anodes are depleted in the process, the Söderberg electrode is continuously replenished by adding carbon "paste" to the top of the anode casing which is then baked by the heat of the cell as it moves downwards. For the pre-baked anodes this requires opening of the electrolysis cell to replace the entire anode at which point fumes inside the cell are released into the electrolysis hall (34). A schematic of the electrolysis process is displayed in Figure 2.2:

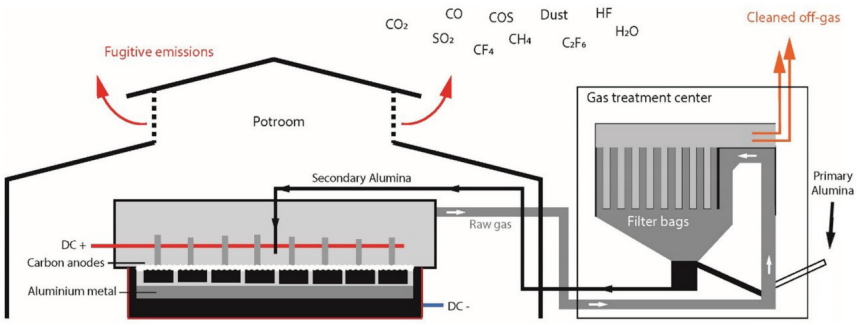

Figure 2.2: Schematic of the material flow among the smelting process, gas treatment centre and emissions (35).

The fumes inside the electrolysis cells mainly consists of condensed bath fumes as cryolite, chiolite, sodium tertrafluoroaluminate, aluminium fluoride, and sodium fluoride, and contain varying amounts of impurities. The content of contaminants increases significantly in particles larger than 1 μm in diameter, with submicron not having detectable amounts of neither V, Ti, Fe, Ni, or Mo. The $NaAlF_4$-pattern is dominant in the submicron particle size classes, which originate from condensation and hydrolysis of the vapor phases and are a characteristic background cell emission assumed to be mainly dependant on bath evaporation conditions (36). While most of these fumes are contained within the cells where the off-gas is filtered before its release, it is necessary to open the cells for several operations over the course of the production cycle. Examples of such operations are the anode change and cell tapping. To effectively gauge the particulate emissions from each different operation, a constant measurement system in necessary. Several previous studies provide an incomplete picture as the time-resolution is limited (14).

The air-suspended particulate matter in the potrooms of aluminum smelters is commonly referred to as "potroom dust", and is typically process-related material that has escaped confinement as mentioned (37). Potroom dust typically form a significant component of the total PM emitted from a smelting site, with studies measuring as much as 85% of PM2.5 emissions are emitted through the roof vents above the potroom (38).

In both the Söderberg and the Prebake processes, mixtures of aluminium oxides and cryolite are the dominant particle groups, but particulates not specifically related to the smelting process, such as rust, silicates, and sea salts, can also be found in potroom dust in small quantities. Flouride-containing coating has been observed on aluminum oxide and cryolite particles, which exhibits a nanostructure that most likely enhances the solubility in the lung, and the coated particles and agglomorates may be excellent vehicles for transporting these reactive gases into the thoracic region of the lung. This nano-layer of flourine-containing deposits on most particles may also form HF after deposition in the lung or exposure to the respiratory humidified air (39). This health hazard is a significant driving force towards reducing potroom dust, both in the form of fugitive emissions, and for the working environment in the plants.

2.3 Production of Metallurgical Grade Silicon

Metallurgical Grade Si (MG-Si) is mainly produced in a Submerged Arc Furnace (SAF), and a schematic of the process for Si production along with the location of the primary emission sources are shown in Figure 2.3 (31).

Typically for Si production, the SAF is semi-sealed or open. In an open configuration, the canopy hood is located 2-2.7m above the furnace rim which allows for stoking during operation, but also lets fumes escape unless sufficient draft is provided. A semi-sealed furnace has a tightly fitted, water-cooled, hood that fits tightly around the top of the furnace which disallows stoking from the outside. While it is not airtight around each electrode and fumes may escape unless sufficient draft is provided, there is less fuming from a semi-sealed furnace compared to an open configuration (40).

As shown in Figure 2.3, there are many sources of fugitive emissions in the metal production process surrounding the SAF. In his PhD-work, Kamfjord (41) gathered estimated data on the fume sources and relative amounts in the Si-prduction pro-

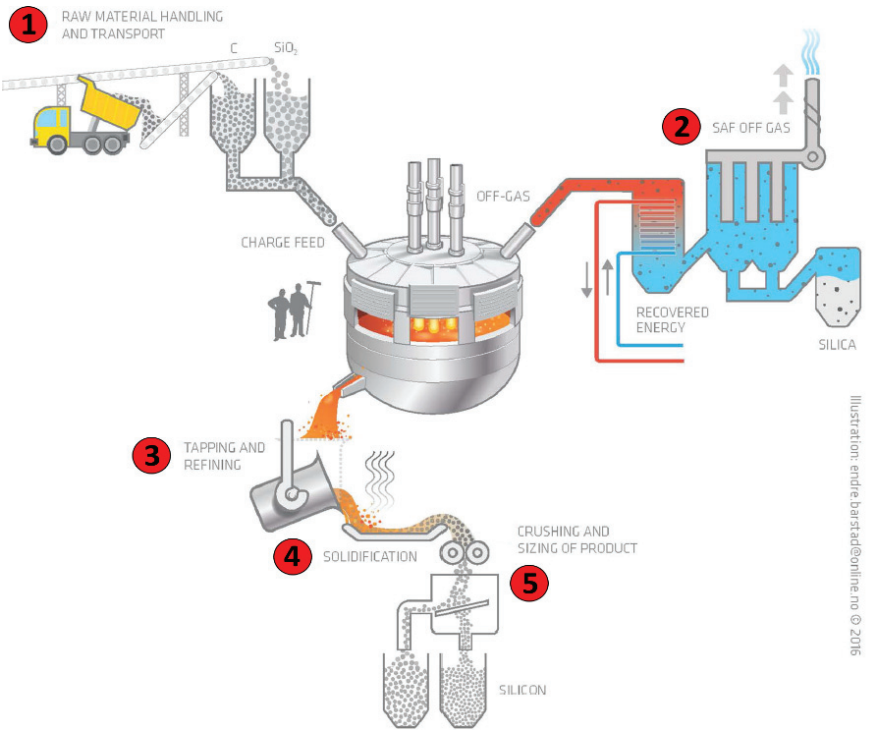

Figure 2.3: High silicon alloy production and its primary emission sources, with permission from Kero et. al (2016) (31). 1) Raw material handling and transport 2) SAF off-gas 3) Tapping and refining 4) Casting 5) Crushing and sizing of product.

cess from Tveit, Myrhaug et al. (2008) summarized in Table 2.1:

Exposure of liquid silicon to air results in large amounts of condensed silica (SiO_2) fumes, which consists of spherical, amorphous silica particles with an average diameter of around 60nm (42). These particles also agglomerate after formation, leading to the size fractions measured through laser diffraction being much higher. Figure 2.4 a) and b) show SEM imagery of the fume particles from SiMn and Si production respectively (24) (42).

The flux of silica from the high-silicon alloy refining ladle was found by Næss to be approximately 1 kg of silica per ton of Si produced (43). Næss also established the major mechanism behind the fume formation; active oxidation of the liquid silicon surface, which means that the extent of the oxidation is coupled with the surface area exposed to air. The oxidation happens in two steps, with liquid silicon reacting with oxygen at the surface to form SiO gas as shown in reaction R2 first,

Table 2.1: Overview of estimated process emissions in Si-production. From Kamfjord (41).

Work process	Share of diffuse emissions	Share of internal pollution	Description of emission
Raw material handling from key to storage	0-5%	0%	Fumes generated by transportation, conveyor belts, etc.
Raw material transport from storage to furnace	0-5%	5-10%	Fume generated by raw material mixing and internal transportation to furnace
Furnace processes	10-20%	5-20%	Smoke and fume escaping the off-gas system and spreading inside the plant
Tapping	20-40%	30-50%	Smoke and fume from tapping processes
Casting	20-40%	15-25%	Smoke and fume from metal handling
Crushing, screening, and packing	5-15%	5-15%	Metal fume from operations
Off-gas system	5-10%	0-5%	Fume and smoke escaping channels, fans etc.
Product packing of collected fume from off-gas	0-5%	5-10%	Fume into work environment from operations

before being subsequently oxidised in a combustion reaction in the air to become SiO_2 fumes as shown in reaction R3. These fumes consists of small, amorphous, spheres of glassy silica (44).

$$\mathrm{Si(l)} + \frac{1}{2}\,\mathrm{O_2(g)} \rightleftharpoons \mathrm{SiO(g)} \qquad \text{[R2]}$$

$$\mathrm{SiO(g)} + \frac{1}{2}\,\mathrm{O_2(g)} \rightleftharpoons \mathrm{SiO_2(l/s)} \qquad \text{[R3]}$$

If the resulting partial pressure of SiO(g) from reaction R2 at the surface is higher than the equilibrium partial pressure for the reaction between Si and SiO_2 shown

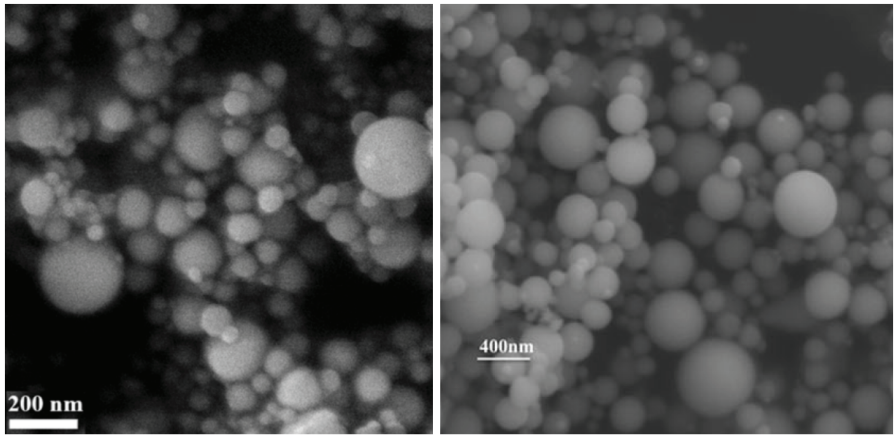

Figure 2.4: SEM (secondary electron detection) images showing fume particles from a) Si filter fume generated experimentally at 1550 °C (42) and b) typical SiMn filter fume generated experimentally at 1500–1700 °C (24). Note the difference in scale.

in reaction R4 however, a protective layer of SiO_2 may be formed at the surface (45).

$$\frac{1}{2}\,Si(l) + \frac{1}{2}\,SiO_2(s) \rightleftharpoons SiO(g) \qquad [R4]$$

This happens when the oxygen partial pressure above a stagnant silicon surface is increased above a certain maximum pressure (6.1 x 10^{-3} atm at 1410°C according to Wagner (45)), and the formation of SiO_2 following reaction R5 causes a passivisation of the surface which inhibits further oxidation (42).

$$Si(l) + O_2(g) \rightleftharpoons SiO_2(l/s) \qquad [R5]$$

In industrial locations, a stagnant surface is not the standard condition however, and neither is stable laminar flows above it. Turbulent, moving surfaces with turbulent natural convection due to the high temperature gradients are the observed conditions during industrial measurements (42), making precise calculations challenging.

Surface oxidation is not the only process in which fumes are formed outside the furnace however, with the most notable example being during ladle refining. Fig-

ure 2.5 shows a sketch of the possible macroscopic fume formation mechanisms in the Si refining ladle (44), where oxidation from the refining bubbles and fuming from splashing of liquid silicon represent such other mechanisms.

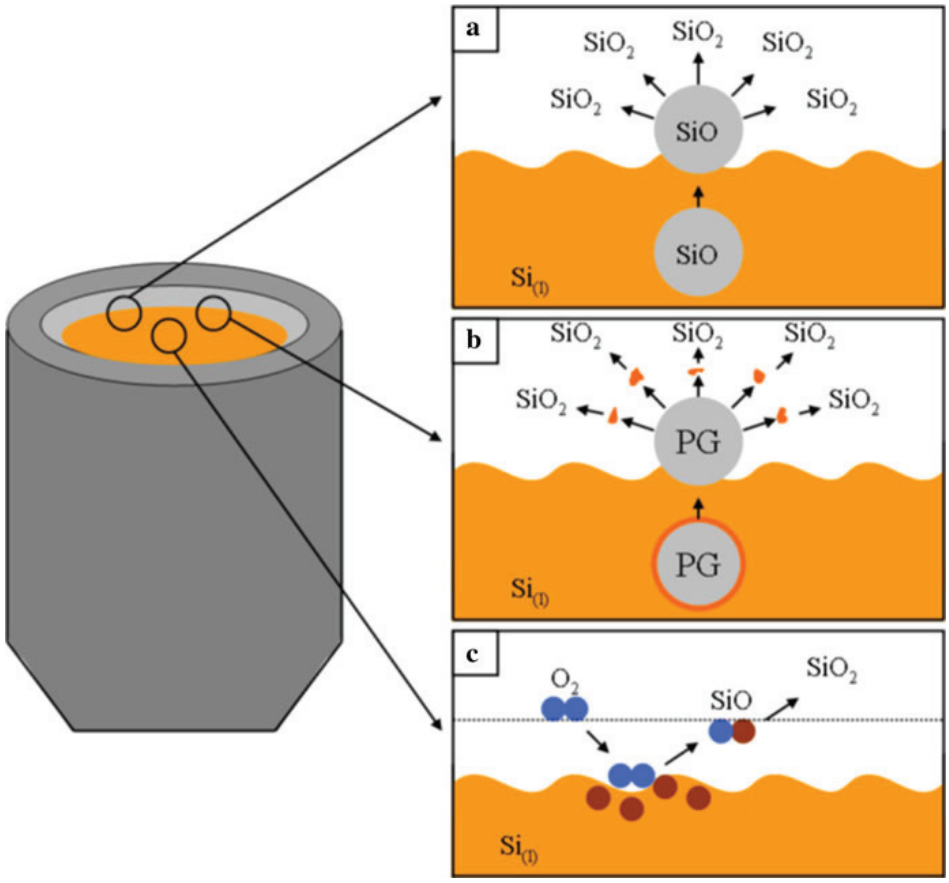

Figure 2.5: Simple sketch of the possible macroscopic mechanisms in the ladle: a) oxidation of SiO from the refining bubbles, b) fuming from splashing of liquid silicon due to the drag of the purge gas (PG) in the bubbles, and c) surface oxidation when in contact with oxygen in air. From Næss et. al (2012) (44).

2.4 Production of Manganese Ferroalloys

Manganese ferroalloys, such as high-carbon ferromanganese (HCFeMn), low-carbon ferromanganese (LCFeMn), and silicomanagese (SiMn) are all, like MG-Si, mainly produced in the SAF. A schematic of the process for FeMn production along with the location of the primary emission sources are shown in Figure 2.6 (46), and this

is similar for SiMn-production.

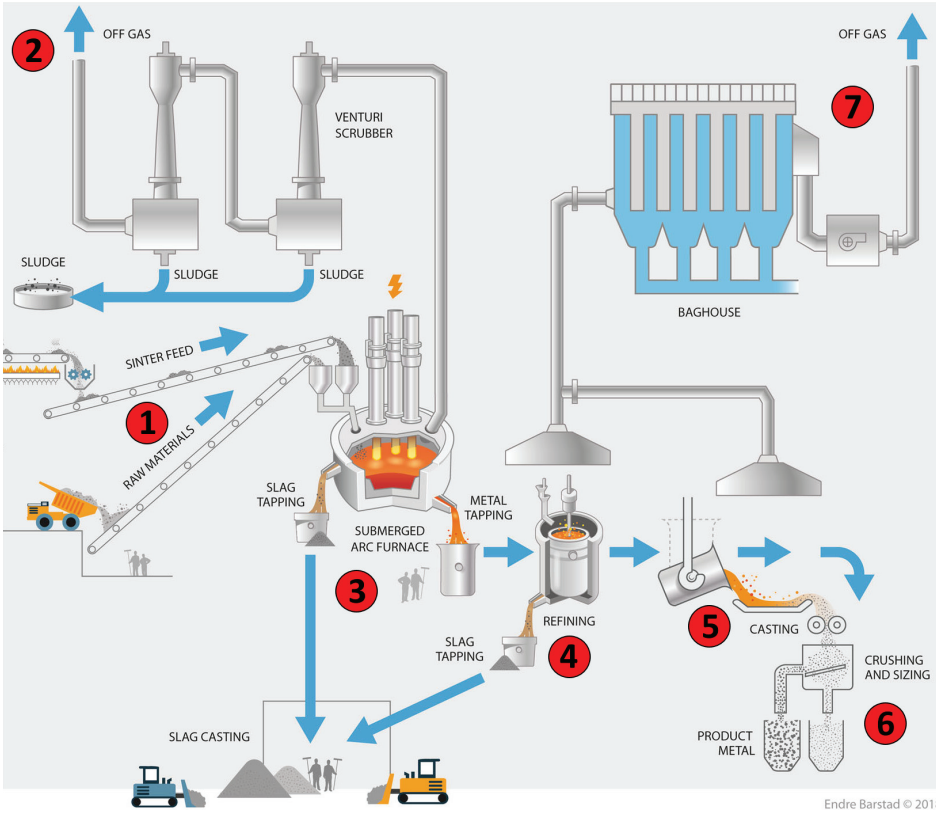

Figure 2.6: Schematic overview of a typical Mn-ferroalloy production plant and its primary emission sources, from Kero et. al (2019) (46). 1) Raw materials transport and handling 2) SAF off-gas 3) Tapping 4) Refining 5) Casting 6) Crushing and sizing 7) Internal ventilation off-gas.

Typically for SiMn and FeMn production, unlike for Si, the SAF is sealed. A sealed furnace has separate sealed chutes for raw materials, allowing a complete seal on the furnace (40). The production of the desired metal is achieved through carbothermic reduction of the ores inside the SAF. Mn is added through manganese ores most commonly containing MnO_2 like Pyrolusite, although different oxide types as well as carbonates, silicates, and sulfides also exist in significant abundance and economic importance. Several types of manganese ore also have varying content of Si and Fe in addition to other major elements such as aluminium(Al), magnesium(Mg) and many trace elements (47). Si, when desired, is added through SiO_2, quartz, or through (Fe)Si off-grade qualities or Si refining skulls. Fe is sim-

ilarly added through Mn ores high in iron oxides where a higher Fe content is needed. Fluxes such as limestone ($CaCO_3$) are added where the slag basicity must be controlled, and the prerequisite carbon is usually added in the form of coke mixed with the other carbon raw materials such as petroleum coke, charcoal, or anthracite (22).

2.4.1 Mechanisms of thermal fume generation

Liquid FeMn and SiMn metal is cast at temperatures above 1500 °C in air, where the vapor pressure of manganese is high, typically > 0.01 atm for FeMn, but lower for SiMn. Reactions between the Mn vapor and oxygen in the atmosphere leads to the formation of oxide fumes. Figure 2.7,(48) shows the stability diagram for manganese and its oxides for different oxygen partial pressures and temperatures. It can be seen from the diagram that at 1500°C, oxygen pressures above 10^{-15} atm will lead to the formation of manganese monoxide (solid), and as the temperature decreases, higher oxides become stable. The oxide formation follows the reactions shown in reaction R6 through R12, with their corresponding Gibbs free energy valid from 0 to 2000°C as calculated by Factsage 7.0 (48),(49) using FactPS and FToxide databases.

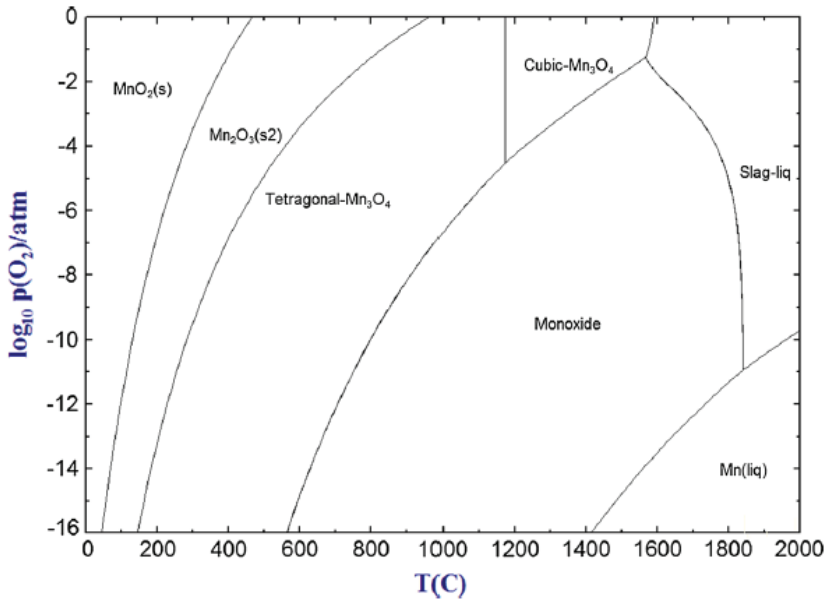

Figure 2.7: Calculated equilibrium relations in the Mn–O system using Factsage (48, 49).

$$\mathrm{Mn(l)} \leftrightharpoons \mathrm{Mn(g)} \quad \Delta \mathrm{G}^{\circ}(\mathrm{kJ}) = 225.61 - 0.1124\,\mathrm{T}\,(^{\circ}\mathrm{C}) \qquad \text{[R6]}$$

$$\mathrm{Mn(g)} + \frac{1}{2}\,\mathrm{O_2(g)} \leftrightharpoons \mathrm{MnO(l)} \quad \Delta \mathrm{G}_l{}^{\circ}(\mathrm{kJ}) = -556.27 + 0.1715\,\mathrm{T}\,(^{\circ}\mathrm{C}) \qquad \text{[R7]}$$

$$\mathrm{Mn(g)} + \frac{1}{2}\,\mathrm{O_2(g)} \leftrightharpoons \mathrm{MnO(s)} \quad \Delta \mathrm{G}_s{}^{\circ}(\mathrm{kJ}) = -603.64 + 0.1972\,\mathrm{T}\,(^{\circ}\mathrm{C}) \qquad \text{[R8]}$$

$$3\,\mathrm{MnO(s)} + \frac{1}{2}\,\mathrm{O_2(g)} \leftrightharpoons \mathrm{Mn_3O_4(s_1)} \quad \Delta \mathrm{G}^{\circ}(\mathrm{kJ}) = -194.32 + 0.1222\,\mathrm{T}\,(^{\circ}\mathrm{C}) \qquad \text{[R9]}$$

$$2\,\mathrm{Mn(g)} + \frac{3}{2}\,\mathrm{O_2(g)} \leftrightharpoons \mathrm{Mn_2O_3(s_2)} \quad \Delta \mathrm{G}^{\circ}(\mathrm{kJ}) = -1358.3 + 0.4907\,\mathrm{T}\,(^{\circ}\mathrm{C}) \qquad \text{[R10]}$$

$$\frac{2}{3}\,\mathrm{Mn_3O_4(s_1)} + \frac{1}{6}\,\mathrm{O_2(g)} \leftrightharpoons \mathrm{Mn_2O_3(s_2)} \quad \Delta \mathrm{G}^{\circ}(\mathrm{kJ}) = -21.459 + 0.0148\,\mathrm{T}\,(^{\circ}\mathrm{C}) \qquad \text{[R11]}$$

$$\frac{1}{2}\,\mathrm{Mn_2O_3(s_2)} + \frac{1}{4}\,\mathrm{O_2(g)} \leftrightharpoons \mathrm{MnO_2(s)} \quad \Delta \mathrm{G}^{\circ}(\mathrm{kJ}) = -24.599 + 0.0522\,\mathrm{T}\,(^{\circ}\mathrm{C}) \qquad \text{[R12]}$$

where $\mathrm{Mn_3O_4(s_2)}$ and $\mathrm{Mn_2O_3(s_2)}$ represents tetragonal (low-temperature) $\mathrm{Mn_3O_4}$ and cubic (high-temperature) $\mathrm{Mn_2O_3}$, respectively (48).

For thermally generated fumes from FeMn, MnO_x-particles as formed through these reaction make up most of the dust, alongside trace elements and some iron oxides. At 1500°C, $\mathrm{Mn_3O_4}$ is the most stable oxide at high oxygen concentrations, while MnO is the most stable oxide at lower oxygen concentrations (50). Particles from laboratory experiments on fume formation from FeMn performed by Kero et. al (50) were found to have varying composition based which of 3 deposition locations the dust was collected from. Major elements were Mn and O, with Fe

included at the closest deposition point. Minor elements were Ca and Mg, with Fe included when it was not a major element, and Si included at the middle deposition location. Trace elements were Al, K, and Na, with Si included where it was not a minor element, and Zn included at the middle deposition location. Average particle size from these experiments were calculated by Brunauer-Emmet-Teller surface adsorbtion method (BET) and found to be 0.77 μm, which was significantly larger than the protoparticle size found by SEM at around 0.2 μm. Figure 2.4 a) and b) in the previous section show SEM imagery of the fume particles from SiMn and Si production respectively (24) (42).

Thermally generated SiMn fumes formed by oxidation of liquid (Si) and evaporated (Mn) metals consists mainly of Si, Mn, and O, forming various complex oxides. Secondary elements include Mg, Ca, Al and K, and trace elements include Na, Fe, Zn, Cu and Cl (51). Due to the higher vapor pressure of Mn over the melt, Mn can evaporate and react with oxygen some distance above the surface while Si requires direct oxidation at the surface. In the case of SiMn, with high enough evaporation rates compared to the oxygen gradient above the surface, it is possible that very little oxygen reaches the surface to react with the Si, although this is not the case in regular industrial situations.

The industrial average aerodynamic diameter of these fume particles, as recorded by an Electrical Low Pressure Impactor (ELPI), is around 100nm (51), while SEM analysis of fumes generated experimentally in laboratory scale by Ma et al. (24) show that the majority of protoparticles (the singular particles, in this case mostly spheres, defined before agglomeration and clustering) have a diameter between 50 and 200nm, although fume particles generated at higher temperatures are notably smaller. For agglomerate size fractions measured through laser diffraction (LD) on the same dust however, the majority of particulates have a diameter in the range of 500-2000nm, and are also less influenced by temperature. Particle size distribution (PSD) analysis from SEM of HCFeMn fumes with and without water sprays around the casting beds by Gates et al. (52) showed that 25% and 79% of the protoparticles collected at roof level were below 200nm in diameter respectively. This effect was believed to be from a combination of the reduced temperature and that water droplets capture fumes by impactation.

Manganese evaporation mechanisms and kinetics

In the production process for ferroalloys such as ferromanganese and silicomanganese, the produced melt is in contact with air during several steps of the process. Most notably during tapping, refining and casting, the melt is exposed to air

without a protective slag layer over an extended duration. During this time, there are two possible reactions for each metal in the alloy, Evaporation and oxidation, which may be summed as shown in reaction R13 for evaporation, and in reaction R14 and R15 for oxidation in one or two steps. It must be noted that some metals, such as Mn or Fe, have other oxidation steps after the first, i.e. Mn_2O_3 and Fe_3O_4.

$$\mathrm{Me(l)} \leftrightharpoons \mathrm{Me(g)} \qquad \text{[R13]}$$

$$\mathrm{Me(l,g)} + 1/2\mathrm{O_2(g)} \leftrightharpoons \mathrm{MeO(s,l)} \qquad \text{[R14]}$$

$$\mathrm{MeO(s)} + 1/2\mathrm{O_2(g)} \leftrightharpoons \mathrm{MeO_2(s)} \qquad \text{[R15]}$$

If the equilibrium vapor pressure of the metal is high enough, as it is for Mn at temperatures above the melting temperature, reaction R13 will happen regardless of the presence of oxygen at the surface. When the metal, either as liquid on the surface or as gas above it, comes into contact with oxygen it will oxidize following equation R14. For some metals such as Si, the oxidation takes place in two steps already in the diffusion layer, and reaction R15 will take place once the oxide particles comes into contact with more oxygen. For reaction R13, the equilibrium partial pressure of Mn vapor over a pure Mn liquid is derived from the formula for Gibbs free energy and may be written as:

$$\mathrm{p_{Mn(g)}} = p_0 \cdot \exp\left(\frac{-\Delta \mathrm{G}^\circ}{\mathrm{R} \cdot \mathrm{T}}\right) \qquad (2.1)$$

Where:
$\mathrm{Flux}_{evaporation}$ = flux of evaporation [g/m^{2}s] $\mathrm{p}_{Mn(g)}$ = partial pressure of Mn(g) just above the surface [Pa]
p_0 = standard pressure defined as 1 atm = 101325 Pa
R = Universal gas constant = 8.3144626 J/Kmol
T = temperature [K]
ΔG° = standard change in Gibbs energy for the reaction [J/mol].

The flux from evaporation at the surface can then be defined as shown in equation 2.2, which is a form of the Hertz-Knudsen equation (53) multiplied by M_{Mn} to get

the mass flux rather than the molar flux:

$$\text{Flux}_{\text{evaporation}} = (\text{p}_{\text{Mn(g),eq}} - \text{p}_{\text{Mn(g)}}) \cdot \sqrt{\frac{\text{M}_{\text{Mn}}}{\text{N}_{\text{A}} \cdot 2 \cdot \pi \cdot \text{k}_{\text{B}} \cdot \text{T}}} \tag{2.2}$$

Where:
$p_{Mn(g)}$ = partial pressure of Mn(g) just above the surface [Pa]
$p_{Mn(g),eq}$ = equilibrium partial pressure of Mn(g) from equation 2.1
N_A = Avogadro's number = $6.02214076 \cdot 10^{23}$ [/mol]
k_B = Boltzmann's constant = $1.38065 \cdot 10^{-23}$ J/K
M_{Mn} = molar mass of Mn = 54.938 g/mol
T = temperature [K]

For diffusion, the flux can be defined by equation 2.3,

$$\text{Flux}_{\text{diffusion}} = \text{D} \cdot \frac{\text{p} - \text{p}_{\text{Mn(g),bulk}}}{\text{DiffZ}} \cdot \frac{\text{N}_{\text{A}}}{\text{RT}} \cdot \frac{\text{M}_{\text{Mn}}}{\text{N}_{\text{A}}} \tag{2.3}$$

Where:
D = diffusion coefficient [m^2/s]
$p_{Mn(g),bulk}$ = partial pressure of Mn(g) in the bulk gas [Pa]
DiffZ = diffusion layer thickness [m] defined by equation 2.4 for a cylindrical container with a central gas flow directed vertically down onto a molten metal surface (54) as shown in Figure 2.8.

$$\text{DiffZ} = \frac{\text{L} \cdot 4.52}{\text{Re}^{1/2} \cdot \text{Sc}^{1/3}} \tag{2.4}$$

Where:
Re = Reynold's number defined by equation 2.5 [unitless]
Sc = Schmidt's number defined by equation 2.6 [unitless]

$$\text{Re} = \frac{\text{uL}}{\nu} \tag{2.5}$$

$$\mathrm{Sc} = \frac{\nu}{\mathrm{D}} \tag{2.6}$$

And:
L = radius of the cylindrical container [m]
ν = dynamic viscosity [Pa · s]
u = bulk flow velocity [m/s]
D = diffusion coefficient [m^2/s]

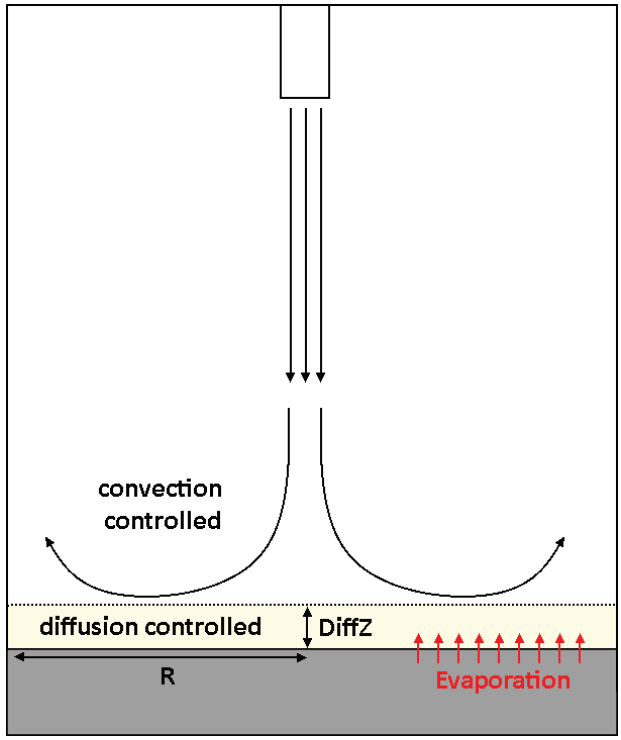

Figure 2.8: Schematic of a cylindrical container with liquid metal and a vertical gas flow from the top. Mass transfer of metal is divided in three parts: Evaporation, diffusion, and convection.

Figure 2.8 shows the three steps of mass transfer of metal: Evaporation, diffusion, and convection. Convection flux is far higher than diffusion flux, thus the evaporation and diffusion fluxes are the focus of this study. Equation 2.2 and 2.3 describes the flux of Mn(g) to and from the surface gas layer. As manganese evaporates, it is transferred from the metal surface and into the air above it, from which it diffuses through the diffusion layer over a distance defined by equation 2.4. Assuming

steady state where there is no buildup of Mn(g), the two fluxes must be equal and the two equations can be solved together as most of the factors are known, with the temperature and flow being the two variables assuming the radius of the container is constant. Assuming constant flow, temperature, and geometry, most of equation 2.2 and 2.3 are constant and you can write the mass balance as shown in equation 2.7:

$$(p_{Mn(g)} - p_{Mn(g),bulk}) \cdot C_{diff} = (p_{Mn(g),eq} - p_{Mn(g)}) \cdot C_{evap} \tag{2.7}$$

Which when solved for $p_{Mn(g)}$ gives equation 2.8:

$$p_{Mn(g)} = \frac{p_{Mn(g),eq} \cdot C_{evap} + p_{Mn(g),bulk} \cdot C_{diff}}{C_{diff} + C_{evap}} \tag{2.8}$$

Where C_{diff} and C_{evap} are defined as:

$$C_{diff} = \frac{D}{DiffZ} \cdot \frac{M_{Mn}}{RT} \tag{2.9}$$

$$C_{evap} = \sqrt{\frac{M_{Mn}}{N_A \cdot 2 \cdot \pi \cdot k_B \cdot T \cdot}} \tag{2.10}$$

And:
$p_{Mn(g)}$ = partial pressure of Mn(g) just above the surface [Pa]
$p_{Mn(g),eq}$ = equilibrium partial pressure of Mn(g) from equation 2.1
$p_{Mn(g),bulk}$ = partial pressure of Mn(g) in the bulk gas [Pa]
N_A = Avogadro's number = $6.02214076 \cdot 10^{23}$ [/mol]
k_B = Boltzmann's constant = $1.38065 \cdot 10^{-23}$ J/K
D = diffusion coefficient [m^2/s]
DiffZ = diffusion layer thickness [m] defined by equation 2.4 M_{Mn} = molar mass of Mn = 54.938 g/mol
R = Universal gas constant = 8.3144626 J/Kmol
T = temperature [K]
N_A = Avogadro's number = $6.02214076 \cdot 10^{23}$ [/mol]
k_B = Boltzmann's constant = $1.38065 \cdot 10^{-23}$ J/K

Oxidation-enhanced evaporation

Early studies focusing on modelling of the generic metal-oxidizer system by Wagner (45), Turkdogan et al. (25) and Rosner (26) have laid the theoretical found-

ation for modelling evaporation and oxidation rates. However, development and validation of kinetic models for more specific applications such as high-carbon ferromanganese (HCFeMn), have not previously been performed.

Theory states that the metal evaporation rate is rate-limiting at ambient oxygen levels above a certain "critical" value, and that below this value, for a given gas flow-rate and temperature, the flux is directly proportional to the ambient oxygen partial pressure following equation 2.11. This is due to the diffusion being rate-limiting and that the ambient oxygen partial pressure determines the concentration gradient of oxygen through the diffusion layer as shown in Figure 2.9, of which the diffusion rate is directly proportional to.

$$J_i = \frac{M_{Mn} \cdot \alpha \cdot h}{R \cdot T} p_{O_2} \tag{2.11}$$

Where:
J_i = fume flux as limited by diffusion through the boundary layer [g/m^{2}s]
M_{Mn} = molar mass of Mn = 54.938 g/mol
R = Universal gas constant = 8.3144626 J/Kmol
T = temperature [K]
p_{O_2} = ambient partial pressure of oxygen [Pa]
h = average film mass-transfer coefficient for the transport of oxygen through the aerodynamic diffusion boundary layer which is calculable for known flow conditions [m/s]
α = number of moles of metal vapor required to combine with one mole of oxygen, valid for any metal [unitless]

Rosner's work on this "oxidation-enhanced" evaporation (26) confirmed the results of Turkdogan et al. in highly dilute isothermal systems, and also found additional effects based on the condensation process as a limit for fuming in oxidizer-rich ambient gasses. Rosner described the system graphically as shown in Figure 2.9.

Rosner derived a formula for the critical transition pressure of oxidizing agents valid even when approaching pure gaseous oxidizers, shown in Equation 2.12:

$$Y^*_{O,e} = 1 - \left(\frac{1}{1 - Y_{M,w}}\right)^{-(r/D_{ox-met})(F^*_{RXN}-1)} \tag{2.12}$$

Where:
$Y^*_{O,e}$ = critical mass fraction of oxygen in the ambient gas [unitless]

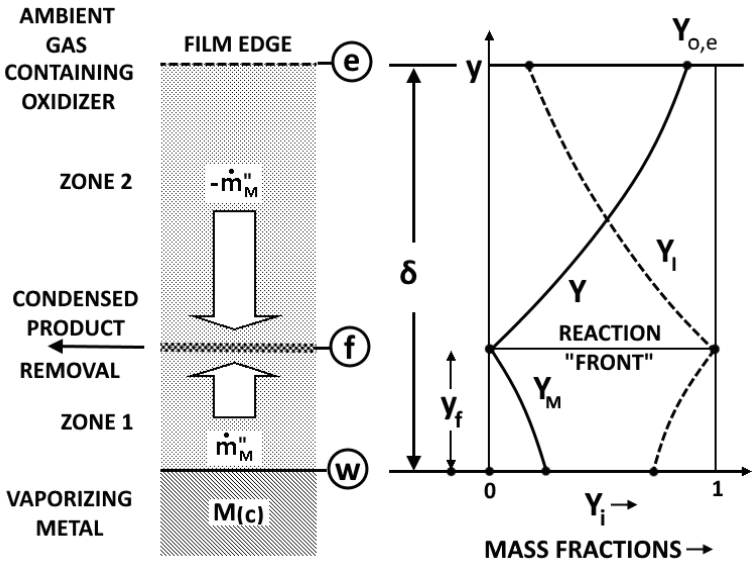

Figure 2.9: Reaction and condensation-enhanced metal vaporization; two-film model and notation. Redrawn from Rosner (26). With e we denote the film edge, f the reaction front, w the liquid surface, $\dot{m}''_M$ the metal flux, y the concentration, I the inert gas, M the metal, and O oxygen. δ the film thickness, often referred to as the diffusion layer thickness.

$Y_{M,w}$ = mass fraction of metal vapour at the gas-metal interface [unitless]
r = mass of oxidizer that reacts with a unit mass of metal vapor [unitless]
F^*_{RXN} = critical reaction factor defined in equation 2.13 [unitless]
D_{ox-met} = oxidiser-to-metal diffusion density ratio defined by equation 2.16 [unitless].

$$F^*_{RXN} = \dot{m}''_{vac}/\dot{m}''^0 \tag{2.13}$$

Where:
$\dot{m}''^0$ = flux given no homogeneous chemical reaction [g/m^{2}s] which in our case relates to an ambient oxygen partial pressure at effectively zero
$\dot{m}''_{vac}$ = maximum evaporation flux [g/m^{2}s] which can be given by the Hertz-Langmuir expression shown in equation 2.14 according to kinetic theory:

$$\dot{m}''_{vac} = \frac{\alpha_s}{4} \cdot \frac{p_{Mn(g)}}{k_B T_w} \cdot \left(\frac{8 k_B T_w}{\pi M_{Mn}}\right)^{1/2} \cdot M_{Mn} \tag{2.14}$$

Where:

α_s = sticking factor [unitless], which describes the ratio between the number of molecules that desorb and adsorb from the same surface during a time interval, and is considered to be 1 in the case of a liquid metal
$p_{Mn(g)}$ = equilibrium partial pressure of manganese vapor at the metal surface [Pa]
k_B = Boltzmann's constant = $1.38065 \cdot 10^{-23}$ J/K
T_w = temperature at the metal surface [K]
M_{Mn} = molar mass of Mn = 54.938 g/mol

Assuming oxygen contents below $Y^*_{O,e}$, Rosner introduced the formula shown in equation 2.15, which defines the flux ratio between a system with no oxygen in the ambient gas and one with a given oxygen partial pressure

$$F_{RXN} = 1 + \frac{(\overline{D_{O-I}\rho})_2}{(\overline{D_{M-I}\rho})_1} \cdot \frac{1}{r} \cdot \frac{ln[1/(1-Y_{O,e})]}{ln[1/(1-Y_{M,w})]} \tag{2.15}$$

$$D_{ox-met} = (\overline{D_{O-I}\rho})_2 / (\overline{D_{M-I}\rho})_1 \tag{2.16}$$

Where:
F_{RXN} = reaction factor [unitless]
$(\overline{D_{i-j}\rho})x$ = mean Fickian binary diffusion coefficient [m^2/s] for species i and j multiplied by the total mass density of the gas mixture in zone x relating to the zones in Figure 2.9, O relates to the oxidizer, I the inert gas, and M the metal vapor.
$Y_{i,j}$ = mass fraction of species i at surface j relating to Figure 2.9 [unitless].

With this, the critical oxygen fraction where evaporation becomes the rate limiting factor can be calculated if the flux with no oxidizer present can be calculated or found through experiments. The theoretical fluxes given an ambient oxygen partial pressure below this critical fraction can also be calculated.

2.4.2 Earlier industrial studies of Mn-alloy fuming

You et al. (23) studied evaporation of manganese during the industrial oxygen refining process experimentally, and confirmed that due to the high vapor pressure of manganese in ferromanganese melts there is a significant loss due to evaporation. An empirical equation for the evaporation loss was derived based on a sampling system, and is shown in equation 2.17:

$$\frac{(W_{Mn})_{evap}}{W_{metal}} = \beta \cdot \sum_{i=1}^{n} \left(\frac{(p_{Mn(g)})_i}{\sqrt{T_i}} \cdot (t_{i+1} - t_i) \right) \tag{2.17}$$

Where: $(W_{Mn})_{evap}$ = evaporation loss of manganese [g] W_{metal} = amount of hot metal charged(iron) [g]
$beta$ = The apparent vaporization coefficient [unitless], a function of process variables such as oxygen and inert gas flow rates
$p_{Mn(g)}$ = partial pressure of Mn(g) just above the surface [Pa]
i = order of sampling [unitless]
T = temperature [K]
t_{i+1}-t_i = time interval between sampling [min].

The apparent vaporization coefficient, β, was found to be significantly affected by the fraction of top blown oxygen, which concurs with the previously discussed theories.

Lee and Kolbeinsen (55) studied the kinetics of the oxygen refining process for high-carbon ferromanganese, where they found that when the vapor pressure of manganese vapor becomes high, the rate of manganese loss is controlled by the mass transfer of manganese vapor through the diffusion boundary layer adjacent to the interface of melt and gas, and that the formation of MnO mist increases with melt temperature. As the temperature is an important factor in the evaporation rate of manganese, this will also have an impact on the fuming rates.

Gates et al.(56, 52) also studied fuming rates in ferromanganese, with a focus on the effect of water vapor in the bulk gas. The rate of fuming was found to decrease with increased water content in the atmosphere and that fume particles were found in larger clusters rather that fine dust with moist atmospheres. While this effect was not fully explained, a decrease in temperature with the addition of water to the atmosphere may partly explain the results. They also found notable amounts of ZnO in the dust from their experiments with higher water vapor content.

Table 2.2: Different dust measurement techniques and the most important differences between them.

Type	Examples	Description	Main Application	Limitations	Advantages	Ref
Nephel-ometer	Nova SDS011, Plantower PMS5003, Sharp GP2Y	Measures scattered light at an angle (typically 90°) for all particles in a chamber	Continuous point PM measurements	Limited detection range, Must be calibrated to the spesific dust for each PM fraction	Can be very low cost, Gives trustworthy values when calibrated well	(57, 58, 59)
Optical particle counters	Fidas 200S, GRIMM, Alphasense	Measures scattered light by each individual particle in a flow	Continuous point PM measurements, Size fraction analysis	Advanced and comparatively expensive, Must be calibrated for optical properties and density	Gives an accurate complete size distribution when calibrated well, Measures individual particles	(60, 61, 62)
Optical transmission device	LaserDust, DustHunter	Measures forward light scattering or opacity from a light source passing over a longer distance	Continous line PM measurements	Must be calibrated to the specific dust	Gives a line average	(63)
Cascade impactors	ELPI, MOUDI-II	Seperates particles based on their inertia	Size fraction analysis, Can be made for continous PM measurements with additional technology	Must be calibrated for aerodynamical properties, Advanced and comparatively expensive and large	Wide size range, Collects dust for analysis, Only dependant on aerodynamic properties	(64, 65, 66)
Filter sampling	Leckel SEQ47/50, Merck millipore filters	Gathers dust of a certain size range in a filter with a controlled flow rate	Gravimetric fume measurements, calibration of other sensors	Gives the average over the measurement period, Filter must be manually collected and weighed	Not dependant on aerodynamic or optical properties of the dust, Very accurate, Collects dust for analysis	(67, 68)

2.5 Measuring dust concentrations in indoor plant environments

There are several different techniques that can be used to measure PM, and many existing systems utilizing each technique. Table 2.2 shows a selection of systems for PM measurements along with some key factors to consider when choosing what is most suitable:

The most common low-cost instrument type for measuring PM concentration in ambient air is Optical Particle Sensors (OPS's), although they can be found in more expensive and higher quality versions as well. OPC's can be split into two distinct types: Nephelometers and Optical Particle Counters (OPC's). In both cases the particles scatter light according to Mie-theory (58), which describes how small particles scatter light of varying wavelengths given their size and optical properties, and this scattered light is measured and correlated to a PM concentration. In the case of Nephelometers, particles are measured as an **ensemble** and the scattered light is measured across a wide range of angles. Typically this range is from 7° to 173° to avoid pure forward and backwards scattering, but some Nephelometers, sometimes referred to as photometers, only measures at a single angle. Near forward and backward scattered light that is not measured by the detector is identified as a truncation error, and is more prevalent for larger particles (>1 μm) (69). In either case the total scattering amplitude is correlated to a mass measurement from a calibration equipment, such as a filter sampler (61).

OPC's work very similarly to Nephelometers, but instead of measuring a number of particles in an ensemble, they measure the light scattered by **individual** particles and assign each pulse to a size bin based on its intensity. This results in a histogram that can be presented as a particle size distribution (61). The optical properties, such as refraction index and particle shape, of the measured particles are of significant importance to the scattering of light, and as such it is equally important with OPC's to calibrate with the correct dust to achieve a high accuracy. This is due to how different particles have different response curves, as calculated with Mie-theory, across varying particle diameters. This curve must be assumed correctly to get accurate diameter values for the particles measured (70).

Across limited straight distances, it is also possible to detect particles in a line by measuring the forward scattered light. Incident laser light that is scattered by the dust particles along the line can be collected onto a solid-state sensor for dust quantification. At high dust concentrations where forward scattering is not applicable, it is possible to measure the dust level by the opacity across the same line (63). These too must be calibrated against other equipment, such as a filter sampler, as

the base principle is the same as for a nephelometer.

Optical light scattering, while commonly used, is not the only optical technique for continuous PM measurements. Light absorption or light extinction can, similarly to light scattering, be used to achieve continuous measurements of the size and amount of particles in the air (29).

Besides light scattering techniques, gravimetric methods are commonly used as they are the most accurate (29). Filter sampling exists as a reliable method to measure average PM levels over a period of time, with the added benefit of having dust samples ready for analysis as soon as the measurement period is over (67). It is a traditional system for monitoring fugitive emissions in the aluminum production process, where a simple setup can consist of tubes and pumps that allow the air from the potroom to be iso-kinetically lead through a filter which collects the dust. After a set period the dust is measured and can be chemically analysed, which can provide accurate monitoring of its content. Advanced sampling inlets (68) can limit the size of particles allowed into the system by precisely controlling the pump strength to where larger particles have too high inertia to be sucked into the system, which in combination with the filter allows for only specific size fractions to be measured. It does however give a low time- and spatial resolution. Another gravimetric technique is the microbalance method where particles collect on a filter and cause the oscillation frequency of a quartz tube to vary (29).

Another type of measurement methods are cascade impactors, which are capable of distinguishing between a large spread of size fractions without consideration for the optical properties of the particles. In an cascade impactor, the particles are sorted depending on their aerodynamic size through a series of stages where the difference in particle inertia in a laminar field flow separate them (66). While not affected by optical parameters, the aerodynamic diameter is influenced by both morphology and density, which must be taken into consideration. An example capable of continuous measurements is the Electrical Low Pressure Impactor (ELPI), where the particles are charged to a known level before they are classified in a cascade impactor into 14 size fraction. As each particle is sorted in its bin, an electrometer detects the charge and as the measured current signal is directly related to the number of particles, this can be used to identify the number of particles continuously sorted into each bin (64).

Technology for measuring dust levels through visual telemetry is also under development, with plans for constant measurement of hydrogen fluoride which is

present in the dust particles from the aluminum production process, but it is still not widely used (71).

Besides using only measurements, it is also possible to model PM concentrations in areas between sensors given that enough information is available. Any model is limited by coverage, reliability and distribution of monitoring stations however, but can help fill the information gap between measurement points. Mechanistic models are based on three-dimensional physical calculations using mathematical equations, but such models are complex and time-consuming to implement and often prove inaccurate. For this reason, statistical methods which aim to discover relationships between PM values and other explanatory variables based on a number of assumptions are more prevalent. Together with machine learning methods where an artificial intelligence without any assumptions learns to find patterns and relationships that are not necessarily obvious in the data, they cover the vast majority of models used in recent times (29).

If the most important knowledge is the degree of exposure for each individual worker, it is possible to combine fume measurements in notable working zones with workstation logbook data to estimate the exposure. Jørgensen et. al (2020) (72) did a study where measurements at the four major working zones at a Ferrosilicon (FeSi) plant (tapping area, casting area, ladle transport corridor, and control room) were combined with the attendance time at each zone for each worker and compared to continuous measurements with filter sampling carried by each worker. The ratio between the logbook method and the individual measurements was on average 1.02, which indicated that the logbook results could be used as a substitute for personal sampling when such sampling is not possible, at least in the FeSi industry. As a supplement, the notebook method is also useful towards identifying the most polluted areas of the workplace, enabling companies to take action to reduce exposure (72). To use such a method to estimate individual exposure it is important to have good data on the fume concentration in each area, and as spatial variations at metallurgical plants can be very high (73), a distribution of low-cost sensors can give a more accurate estimate of a large zone than a single more advanced sensor. Regular calibration with personal samplers is a possibility to counteract errors that can accumulate over time from factors such as reduced light source intensity or changes in particle properties at the location.

2.5.1 Sensor advantages and limitations

In the current study, the aim was to investigate and benchmark the performance in terms of precision and reliability of a specific low-cost nephelometer - the Nova PM SDS11 ("Nova") - in different metallurgical plant environments. In addition to the Nova, there are many variations of low-cost micro-sensors available. The following assortment of sensors, similarly to the Nova, are all OPS's that determine particle size through application of Mie-theory on light pulses scattered by individual or groups of particles:

- Sharp GP2Y1010 (74)
- Shinyei PPD42NS (75)
- Plantower PMS1003 (59, 76)
- AirBeam (77)
- Alphasense Optical Particle Counter (OPC-N2) (62)
- Wuhan Cubic PM3007 (78)

Similar to the Nova, these sensors are all compact, light, have low power consumption, high sampling frequency, and cost in the range of around ten to a couple hundred USD. These sensors, like the Nova, also have a lower particle size measurement range of near 0.3μm at which the sensors only has a 50% detection efficiency. This limit is also present for OPC's, and it is present due to the limitation of Mie-scattering where instrumental efficiency decreases rapidly as the spectrum of scattered particles becomes a broad Poissonian distribution when the particle size is small enough. At around 0.3μm, depending on the particle's index of refraction, the average photoelectric count per particle is only about 5. The particle scattering response falls off at a rate of r^6 in this size region, making increased light intensity and scattering chamber evacuation have very limited effect in lowering the lower size limit (70).

Additionally, low-cost Nephelometers have varying ranges in which they measure effectively, and then estimate the desirable values such as PM2.5 and PM10 by extrapolation. This can lead to grossly inaccurate measurements in many cases, particularly if the size distribution of the measured dust vary from the one used in calibration (79). OPC's do not have this limitation, as they measure a wider range of size bins from the individual scattered light pulses. Low-cost Nephelometers

also usually have a limited lifetime on their light source, as provided by their individual manufacturers, and over the course of their lifetimes the light intensity can weaken which would affect the measured PM values.

The advantages of low-cost sensors are large however, as they allow for cost-efficient monitoring with a much higher spatial resolution. In areas with varying dust sources, such as metallurgical plants, using a spread of sensors require calibration for each type of particle due to the potential variation in optical properties as previously mentioned. This would be the case for both Nephelometers and OPC's, which limits the benefit of using OPC's over the more simple Nephelometers. As the size fractions most widely screened for are PM2.5 and PM10, it would only require calibration for those two to achieve good results.

2.5.2 The Nova sensor

The Nova PM SDS011 is a low-cost Nephelometer sensor that consists of an integrated fan which sucks air in through a short tube and past a laser diode and the paired optical receptors. Measurement of the scattered light results in a signal that can be read from the output connections of the sensor and interpreted by appropriate software into values for PM2.5 and PM10 in a 0-999.9 and 0-1999.9 $\mu g/m^3$ range respectively, measuring particles with a diameter down to around 0.3 μm (57). As previously mentioned the Nova does not measure these size distributions directly, with the two bins, 0.3-2.5μm and 2.5-10μm, correspond approximately to <0.8μm and 0.7-1.7μm respectively, from which PM2.5 and PM10 values are extrapolated based on the calibrations done by the manufacturer. Kuula et. al (2020) (79) concluded that the Nova measurements for PM10 can be grossly inaccurate, but that it has the potential to accurately measure PM2.5 which is supported by other studies (80, 21).

The sensor runs off a 5V current which can be supplied through any regular microchip, and it has an output frequency of 1/s. Its maximum working current is 100mA and the sleeping current is 2mA, allowing it to run on a battery for a long time especially if a lower output frequency is sufficient allowing the sensor to run on resting current a portion of the time. Its reported operating temperature range is -20 to 50 °C and with a relative error of 10%. A sketch of the Nova is shown in Figure 2.10.

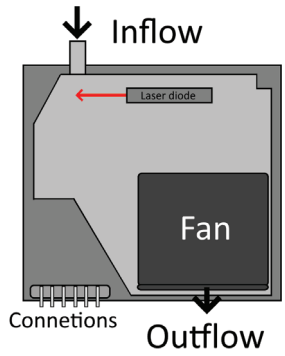

Figure 2.10: Sketch of the Nova PM SDS011 sensor.

2.5.3 The Fidas sensor

The Fidas 200S is a state of the art OPC specifically designed for regulatory air pollution control and measures continuously in a 0.18-180 μm range. It calculates and records PM1, PM2.5, PM4 and PM10, in addition to PM_{tot}, the particle number concentration C_n and the particle size distribution. It is approved for simultaneous monitoring of PM10 and PM2.5 according to standards VDI 4202-1, VDI 4203-3, EN 12341, EN 14907, EN 16450, and the EU Equivalence Guide GDE and certified in compliance with standards EN 15267-1 and -2. (81) which specify maximum permissible measurement uncertainties and testing requirements (82).

Figure 2.11 shows a sketch of the Fidas sensor system, redrawn from images provided by the manufacturer (60). It is equipped with a stable high intensity LED light source with a long lifetime which is used for the single particle light scattering size analysis. The scattered light impulse generated by each particle is detected at an angle of 85° to 95°, and the particle number and diameters are measured based on the number and level of the scattered light impulses respectively. It is able to detect particles down to 180nm diameter through the use of precise optics, high light output from the polychromatic LED used, and powerful signal processing electronics using logarithmic A/D conversion. This can be vital in regards to correct approximation of PM2.5 in particular, especially when there is a large fraction of particles smaller than 300nm such as in areas near roads (81). To take the optical properties of the measured particles into account, calibration with the dust to be measured must be performed to achieve accurate results, typically measuring alongside a gravimetric method. Post-processing can only take into account variations in particle density (81). This is due to how different particles have different response curves, as calculated with Mie-theory, across varying particle

diameters. This curve must be assumed correctly to get accurate diameter values for the particles measured (70).

The Fidas operates with a volume flow of around 0.3m^3/h and utilizes a sampling head which allows for representative sampling even under strong wind conditions, as well as a drying line which prevents condensation from causing measurement errors. It also comes with a weather station that provides data on the ambient air temperature, pressure, and relative humidity, which is both used to regulate the drying line, and is stored to be used along with the PM data for further analysis (81).

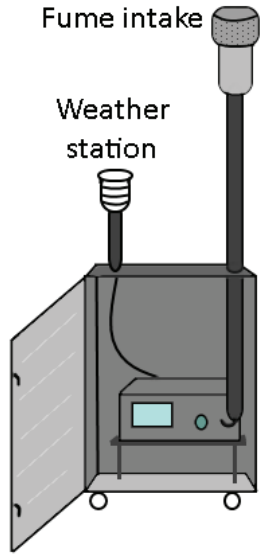

Figure 2.11: Sketch of the Fidas200S sensor measurement system, redrawn from images provided by Palas (60).

2.5.4 Sensor comparison

The Nova measures particulate matter in the ranges of 0.3-2.5 μm(PM2.5) and 0.3-10 μm(PM10), while the Fidas 200S measures from 0.18 μm to 100 μm, separated into four values capped at maximum 1, 2.5, 4 and 10 μm (PM1, PM2.5, PM4, and PM10). Both sensors use optical light scattering to register particles in the air, where coherent pulses of infrared light is aimed through the flow of particles where the particles scatters the light according to laser diffraction theory (83).

The most important differences in the equipment is that the Nova, as a Nephelometer, measures the average for a group of particles, whereas the Fidas, as an OPC, measures each individual particle which allows for a more detailed size fraction analysis to be provided. Another important difference is the range of particle sizes measured, as for the Fidas the more advanced equipment used allows for detection of particles down to 180nm and up to 18μm, where the Nova is limited to a lower boundary of 300nm at which point the detection rate is only at 70% (60) (57), and with an effective upper limit of 1.7μm (79). While both sensors must be calibrated with the correct particles to get accurate results due to varying optical properties as previously mentioned, the Nova is also very dependant on the size distribution of the fumes to correctly estimate particularly PM10 values. As the Fidas has an advanced sampling head and dries the sample fumes before it reaches the sensor it is better suited for measurements in high flow and relative humidity, whereas the Nova has no such feature. The quality of the components used in general is also a potentially important factor in regards to stability of measurements and lifetime for the sensor. The central technical parameters of the two sensors as provided by the manufacturers are described in table 2.3.

Table 2.3: Technical parameters for the Nova SDS011 and Fidas 200S as given by the manufacturers (57) (60).

Parameter	Nova	Fidas
Measuring output(PM)	PM2.5,PM10	PM1,PM2.5,PM4,PM10
Concentration range	0-999.9 μg/m^3	0-10000 μg/m^3
Measuring range	0.3-10 μm	0.18-180 μm
Response time	1s	<2s
Sample treatment	none	Drying and heating
Dimensions	71 · 70 · 23 mm	450 · 320 · 180.5 mm
Power consumption	max. 0.5W	approx. 200W

2.5.5 PM measuring studies using the Nova SDS011 sensor

The Nova sensor has been the subject of several studies in varied settings. Genikomsakis et al. performed mobile field testing comparing the Nova with a AP-370 by HORIBA suitable for constant air pollution measurements on an electric bike in the city of Mons, Belgium. PM values ranged from 0 to 5 μg/m^3 with the resulting R^2 values ranging from 0.93-0.95 after taking temperature and relative humidity into account (83). Badura et al. compared a group of three copies of the Nova sensor together with groups of three other similarly low-cost systems in a common box under the same measurement conditions over half a year near a park and a

residential area in Wroclaw, Poland. The Nova was found to be one of the most precise in terms of reproducability between units, and also when compared to the control unit with an R^2 value of 0.82 using 15 minute averages, but it was found to be sensitive to high relative humidities (RH > 80%) (80). Liu et al. tested the Nova sensors by co-locating three of the sensors at an official, air quality monitoring station equipped with reference-equivalent instrumentation in Oslo, Norway over a four month period and found inter-sensor correlations R values higher than 0.97, and confirmed the sensor's susceptibility to high relative humidity. They concluded that when used correctly, the sensor could have significant potential for implementing dense monitor networks in areas with relative humidities below 80% (21). When compared to similar low-cost sensors, the Nova sensor has been shown to be amongst the best in several studies (84) (85), but as mentioned it struggles at higher humidities, which was further investigated by Jayaratne et.al along with other sensors where several showed an increase in PM-level above a relative Humidity of 75% (86). It was also found to have a low sensitivity to larger particles within the range it is supposed to be measuring however, with a study by Kuula et. al (79) where several reference aerosols were used to test individual sensor's detection efficiency of varying size fractions found that the Nova effectively only measured particles up to a diameter of 1.7μm. In industrial settings there has been less work done to test these sensors however, which is a key driving force for this work.

Chapter 3

Methods

This work is as previously mentioned split into three distinct parts:

- Laboratory experiments of fuming from pure Mn and HCFeMn
- Kinetic modelling of fuming from the laboratory experiments
- In-situ plant measurements of dust concentration using the low-cost PM-sensor NOVA PM SDS011

The experimental work on fuming from pure Mn includes 13 experiments with varying temperatures and argon flow rates, where the mass loss for each experiments was measured. These experiments were performed to develop a more fundamental understanding on the evaporation rates of Mn and how it is influenced by the diffusion layer thickness and the temperature.

The experimental work on HCFeMn includes 46 experiments with varying gas flow rates and oxygen contents in air blown onto the metal surface, where the flux from the experiments were measured and the dust produced analyzed. These experiments were performed to develop a more fundamental understanding of the influence oxygen content and diffusion layer thickness has on the fume formation and PM characteristics over liquid HCFeMn, and to quantify the effect of oxidation-enhanced evaporation.

The on-site dust measurements include three measurement campaigns at three different metal production plants. The first was performed at the Eramet plant in Kvinesdal, which produces silicomanganese, the second at the Hydro plant in Husnes,

which produces Aluminum, and the third was performed at the Elkem plant in Thamshavn, which produces Metallurgical Grade Silicon. These measurements were performed using the Nova PM SDS011 sensor, and was accompanied by the Fidas 200S PM sensor for comparison during the campaign at Elkem Thamshavn and for a calibration period at Eramet Kvinesdal. The tests were designed to provide insight into the usefulness of distributed PM sensors in the metallurgical industry.

Table 3.1: Summary of experiments and measurement campaigns in this work.

Laboratory experiments				
Material	Furnace	Crucible	Gas	No. of experiments
Mn	Tube Furnace	Alumina	Ar	13
HCFeMn	Induction	Graphite	N_2 + O_2	37+9

Measurement Campaigns		
Location	Duration	Sensors
Eramet Kvinesdal	3 months	12 Nova, 1 Fidas for a day
Hydro Husnes	2 months	12 Nova
Elkem Thamshavn	1 month	35 Nova, 1 Fidas

3.1 Experimental work

Fuming experiments were split in two parts, the first in which pure manganese was heated with a controlled inert (Ar) gas flow at the surface and the second where industrial HCFeMn was similarly heated with an oxygen-containing flow.

3.1.1 Experimental work on Mn-evaporation

Figure 3.1 shows a sketch of the experimental setup together with a picture of the crucible used after an experiment and the mesh which was used in the COMSOL-model calculating the flow patterns inside the crucible. The experiments were performed inside a graphite tube furnace which was purged with 6N Argon and kept in an Argon atmosphere of around 1.3 bar to avoid oxidation. Inside the graphite tube, an alumina crucible with height 40mm and diameter 27mm was used as the container for the experiments. The crucible was fitted with a lid to further limit contamination from the surrounding atmosphere, and an alumina paste was used to seal the lid. An alumina tube with inner diameter of 3mm was inserted into a hole in the center of the lid, through which argon was blown into the crucible. Another hole in the lid with diameter 3mm was the only outlet in the system.

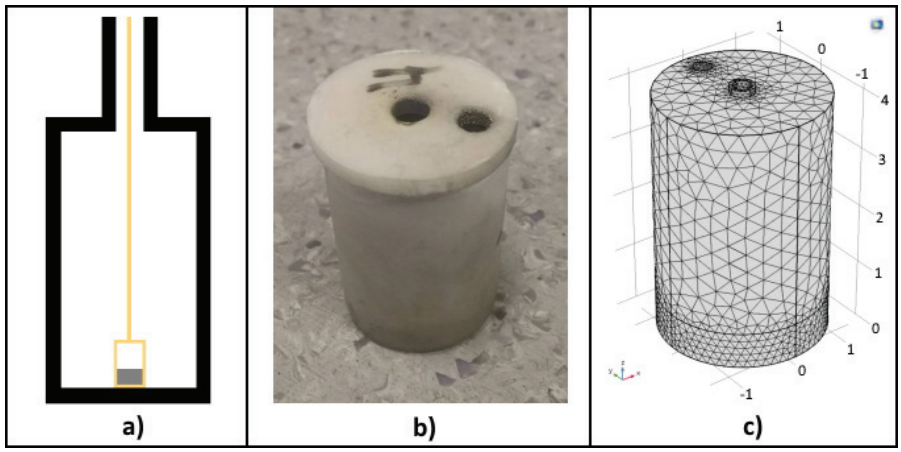

Figure 3.1: a) Sketch of the experimental setup. An outer tube of graphite with an inner alumina crucible and tube connected to an argon source. The atmosphere inside the tube was purged with argon before and during the experiments, and argon was blown at different rates through the tube in each experiment. b) Alumina crucible after finished experiment. The middle hole was used for the alumina tube, while the smaller hole was used as the outlet for the gas and vapor. c) The mesh used in the COMSOL model. It has a total of 36587 domain elements, 4286 boundary elements, and 395 edge elements.

The crucible was filled with 15 (+/- 0.5) grams of 99.9% Mn chips. The chips had a slightly tarnished and oxidized surface, and while the surface was sanded down to minimize this, there was a small amount of oxide present in the experiments. As a first approach however, this was assumed not to affect the evaporation rate. Each sample was pre-treated at 150 °C for 30 minutes to remove any humidity from the sample and the sealing paste, and the crucible set-up was weighed before and after pre-treatment. Longer pre-treatment time or higher temperatures were found not to produce any further weight loss in the sample.

The sample was inserted into the furnace, which was then vacuumed to between 80 and 200 mTorr before it was purged with argon and kept at around 1.3 bar. After purging, the chamber was heated to the desired temperature over 30 minutes and held at that temperature for further 60 minutes before being cooled. During the entire heating, holding and cooling period, argon was inserted through the alumina tube at a constant flowrate. The different temperatures and flowrates for each experiment are shown in Table 3.2. After cooling, the crucible weight was again measured and the mass loss calculated. As the only reaction happening was evaporation of Mn, the flux of Mn out of the system could be calculated for each

experiment.

Table 3.2: Argon Flow rates, temperatures, holding times, and Sample contents for the experiments.

Exp nr.	Flow rate (l/min)	Temp (°C)	Holding Time (min)	Sample content
10	0.0	1400	60	100% Mn
5	0.5	1400	60	100% Mn
7	1.0	1400	60	100% Mn
2	0.0	1550	60	100% Mn
12	0.25	1550	60	100% Mn
3	0.5	1550	60	100% Mn
6	0.5	1550	60	100% Mn
1	1.0	1550	60	100% Mn
4	1.0	1550	60	100% Mn
8	0.0	1700	60	100% Mn
11	0.5	1700	60	100% Mn
9	1.0	1700	60	100% Mn
13	1.0	1700	60	100% Mn

3.1.2 Experimental work on fume formation in HCFeMn

The experimental setup for fume formation in HCFeMn is shown in Figure 3.2, and has been used in previous studies by Kero et al. (50), Næss et al. (42), Gates et al. (56), and Ma et al. (48). A standard grade HCFeMn was used with a composition as shown in Table 3.3, which was heated to 1550 +/- 10 °C in a graphite crucible covered by a specially designed lid placed inside a 75kW Inductotherm induction furnace. The lid had four holes; one for a graphite thermowell where an S-type thermocouple was placed, one for the graphite and alumina gas lance, one for the exhaust port leading through the cooling system to the filter box, and one which was covered by a graphite plug which served as a safety valve in case of pressure buildup due to clogging in the exhaust system.

The gas lance was made from alumina to avoid reactions between the gas and the lance, which was placed inside a graphite tube to protect against thermal shock. The gas flow rate through the lance varied from 1 to 5 l/min, controlled with a mass flow meter, which corresponds to a gas velocity of approximately 5.28 to 26.39 m/s at the lance tip. Each experiment was subjected to a gas flow for at most 20 minutes at 1550°C, and temperature measurements were conducted at several points between the crucible and filter before and after the gas flow was initiated.

Experiments exhibiting a high rate of fume formation had their gas flow duration cut short to avoid clogging of the exhaust and filter system, which would lead to fumes leaving the system through the safety valve and as such leading to erroneous flux calculations.

After each experiment, the dust from the fume was collected at three sites: the tube connecting the cooler to the lid, named the "transition tube", the cooler, and the filter. An average of more than 60% of the dust was collected in the filter, 25% in the cooler and the rest in the transition tube. The complete dataset with calculated averages and standard deviation is shown in Appendix A. Figure 3.2 shows the average deposition temperatures, with the first number showing the temperature just before the gas flow was turned on, and the second showing the temperature in the middle of the experiment.

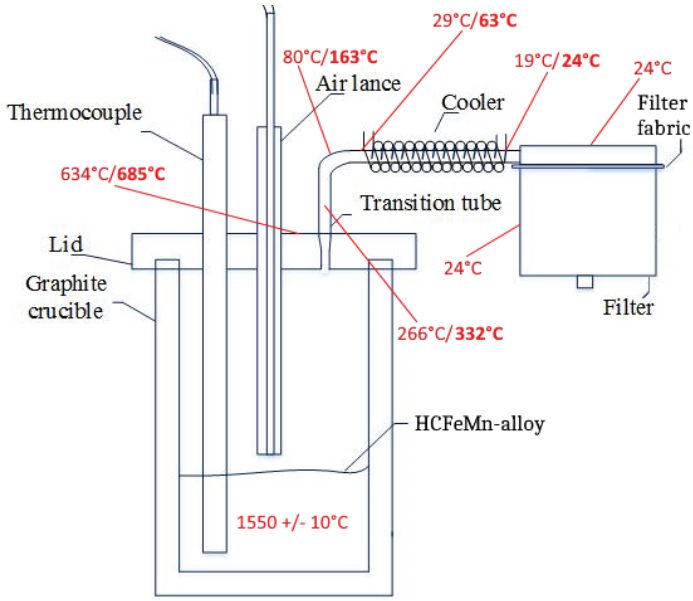

Figure 3.2: The experimental setup with average temperatures as measured during the 16 first experiments. Where there was a difference, the temperature while the gas was flowing is in **bold** beside the temperature measured just before the gas flow was started. The experiments were carried out with a goal temperature of 1550°C in the alloy, and with a distance of 2cm between the lance tip and the metal surface.

Table 3.3 shows the chemical composition of the metal used in the experiments as measured by ICP-MS. The range in the carbon content is specified by the supplier,

but since the experiment occurs in a graphite crucible, the bulk carbon concentration is expected to approach saturation during the experiment.

Table 3.3: Chemical composition of the HCFeMn used in the experiments as measured by ICP and given in WT%. The range in the carbon content is specified by the supplier, but the actual value is of lesser importance due to the usage of a graphite crucible, leading to carbon saturation during experiments

Mn	Fe	C	P	Na	Si
72.1%	12.3%	6.5-7.5%	0.137%	0.06%	0.02%
S	Mg	K	Pb	Al	Zn
0.009%	0.004%	0.003%	0.003%	0.001%	0.001%

After each experiment, the amount of dust in each part of the outflow system was measured by comparing the weight of each individual component before and after the experiment. The components were thoroughly cleaned and dried in between each experiment. As soon as the measurements were completed, the dust from each site was gathered for further studies. The resulting mass flux (J_m) from each experiment was calculated from the total mass increase in the outlet system, following equation 3.1:

$$J_m = m/At \tag{3.1}$$

Where:
J_m = mass flux [g/m^{2}s]
m = measured dust mass generated in the experiment [g]
A = alloy-to-air surface area which equals the crucible cross-section [m^2]
t = holding time [s]

Notably, there was no observable slag formation during the experiments.

To investigate the importance of oxygen access to the reactions, experiments were conducted with different gas mixtures between oxygen and air. Table 3.4 shows the list of all experiments performed for this study. Synthetic air, with a composition of 21% O_2 and 79% N_2, was used together with pure N_2 and O_2 to reach the required concentrations. All gasses were at 5.0 quality, with maximum amount of H_2O equal to 5ppma.

Table 3.4: Experimental matrix, all experiments performed at 1550°C, with a holding time of 20minutes. *5 l/min flow rate experiments were not viable for flux analysis as the high flow lead to substantial fume leakage, but the dust was still analyzed for size distribution and composition.

O_2-content	Gas flow rate	No of parallels
0 %	1 l/min	3
10.5 %	1 l/min	4
21 %	1 l/min	3
35 %	1 l/min	2
50 %	1 l/min	2
0 %	3 l/min	3
5 %	3 l/min	5
10.5 %	3 l/min	3
21 %	3 l/min	3
35 %	3 l/min	6
50 %	3 l/min	3
10.5 %	5 l/min	2*
21 %	5 l/min	3*
35 %	5 l/min	4*

Dust generated during fuming was analyzed using inductively coupled plasma mass spectrometry, laser diffraction, and imaged by scanning electron microscopy, to see how both elemental and particle size distributions are affected by the varying flow rates and oxygen concentrations.

3.1.3 Experimental control and accuracy

The control of gas flow and area is very good with only negligible variation in such induction furnace experiments as performed here, and the temperature variations are in the order of 0.3% (43). When measuring the fume weights, the scales used had an accuracy of 0.01 to 0.1g depending on the weight of the item on the scales yielding a maximum uncertainty of around 15%, which is considered common and acceptable for this type of research (87).

A minimum of two parallels were performed for each set of parameters, with most having 3 or more parallels. The 95% confidence interval for the calculated flux given each set of parameters varied from 0.021 to 0.402 g/m^{2}s, which when divided by the mean for the parallels yielded 95% confidence interval variations from 3.7% to 58.1% of the mean value. These values are quite high, and may be due to local temperature differences or small changes in the height of the lance tip. Another

explanation could be surface oxidation, which was not possible to ascertain or rule out in these experiments. Better temperature control near the surface and a more robust system for fastening the lance at the required height could both potentially improve the accuracy of the experiments by avoiding small variations from erosion and oxidation of the graphite lid where the top of the lance rested.

3.2 Modelling

In addition to the experiments performed, modelling was done to complement the results and provide grounds for making conclusions based on the results. A model of flux rates as a function of oxygen partial pressure in the bulk gas based on the work of Rosner and Turkdogan (26, 25) was used, as well as kinetic modelling of diffusion coefficients which were needed for the flux calculations.

3.2.1 Modelling of diffusion coefficients

Diffusion coefficients of Mn-Ar and Mn-N_2 gas mixtures were calculated by Stefan Andersson (SINTEF Industry) using Chapman-Enskog kinetic theory (88, 89). In short, the Chapman-Enskog theory relates the interaction potentials and collision dynamics of atoms to the transport properties of monatomic gases, i.e., self-diffusivity, viscosity and thermal conductivity. Although the theory was developed for atoms, it is often applied to small molecules as well.

The intermolecular interaction potentials were calculated by high-level quantum chemical calculations and subsequently fitted to Morse potentials. To calculate the energy data points, the CCSD(T) (coupled cluster with single and double excitations and a perturbative treatment of triple excitations) method was used with the aug-cc-pVQZ basis set (90, 91). The Mn-Ar interaction potential was calculated at a range of interatomic distances of 3-7 Å. For the Mn-N_2 interactions, the interaction potential was evaluated at a range of distances (2-7 Å) along the vector Mn and the center of mass of N_2, and at angles between that vector and the N_2 bond vector evenly spaced in steps of 5° from 5° to 85°. The CFOUR code (92, 93) was used for all CCSD(T) calculations.

Diffusion coefficients of the gas mixtures of species A and B were calculated as shown in equation 3.2 (89):

$$D_{\mathrm{AB}} = \frac{3}{16}\sqrt{\frac{2(RT)^3}{\pi}\left(\frac{1}{M_{\mathrm{A}}}+\frac{1}{M_{\mathrm{B}}}\right)}\frac{1}{N_A p_{tot}\sigma_{\mathrm{AB}}^2\Omega_{D,\mathrm{AB}}} \tag{3.2}$$

Where:
D_{AB} = diffusion coefficient of the gas mixtures of species A and B [m^2/s]
R = Universal gas constant = 8.3144626 J/Kmol
T = temperature [K]
M_x is the molar mass of specie x [g/mol]
N_A = Avogadro's number = $6.02214076 \cdot 10^{23}$ [/mol]
p_{tot} = total pressure in the gas mixture [Pa]
$\Omega_{D,\mathrm{AB}}$ = temperature-dependent collision integral, which describes the deviation of a real gas from the ideal hard-sphere gas behaviour [unitless]
σ_{AB} = average of the individual hard-sphere radii, σ_{A} and σ_{B} as defined in equation 3.3 [Å]:

$$\sigma_{\mathrm{AB}} = \frac{1}{2}(\sigma_{\mathrm{A}} + \sigma_{\mathrm{B}}) \tag{3.3}$$

The Mn-Ar potential was fitted to a standard Morse potential expression according to equation 3.4:

$$V(R) = D_e \left(e^{-2a(R-R_e)} - 2e^{-a(R-R_e)} \right). \tag{3.4}$$

In the case of Mn and N_2 the interaction potential was fitted to a Morse potential for several angles of approach, θ, of the Mn atom towards the N_2 molecule:

$$V(R,\theta) = D_{e,\theta} \left(e^{-2a(R-R_{e,\theta})} - 2e^{-a(R-R_{e,\theta})} \right) \tag{3.5}$$

Where:
V = morse potential [J]
D_e = Morse potential well depth [K]
R = center-of-mass distance between Mn and N_2 [Å]
R_e = equilibrium center-of-mass distance between Mn and N_2 [Å]
θ = the angle of approach [rad]
a = width parameter [1/Å]

By placing the N_2 bond vector along the $z-$axis and the N_2 center of mass at the origin, one can express the system in spherical coordinates R, θ, ϕ. R then lies along the vector between the Mn atom and the N_2 center of mass and the θ angle is the angle between this vector and the N_2 bond vector. The ϕ angle describes rotation of Mn around the N_2 bond. Subsequently, the effective interaction potential was calculated by averaging the angle-dependent potential over all Mn-N_2 angles:

$$V_{eff}(R) = \frac{\int_0^{\pi}\int_0^{2\pi} V(R,\theta)\sin\theta d\theta d\phi}{\int_0^{\pi}\int_0^{2\pi}\sin\theta d\theta d\phi} = \int_0^{\frac{\pi}{2}} V(R,\theta)\sin\theta d\theta \tag{3.6}$$

with the second equality being due to the potential being cylindrically symmetric around the N_2 bond and also symmetric with respect to approach of Mn towards either end of N_2. $V_{eff}(R)$ was thereafter fitted to a new set of Morse parameters:

$$V_{eff,fit}(R) = D_{e,eff}\left(e^{-2a_{eff}(R-R_{e,eff})} - 2e^{-a_{eff}(R-R_{e,eff})}\right) \tag{3.7}$$

Where:
$D_{e,eff}$ = 88.2 K
$R_{e,eff}$ = 4.93 Å
a_{eff} = 1.04 $Å^{-1}$

Using these parameters, values of $\Omega_{D,\mathrm{AB}}$ were interpolated from tabulated values for Morse potentials for relevant temperatures (94).

Diffusion coefficients of the N_2-O_2 gas mixture were also calculated using Eq. (3.2) but with literature Lennard-Jones parameters (89) and the corresponding expressions for the collision integral. This resulted in diffusion coefficients of 3.43 cm^2/s for Mn-Ar, 3.66 cm^2/s for Mn-N_2 and 4.37 cm^2/s for O_2-N_2 at 1550°C and a pressure of 1 atm.

3.2.2 Modelling of Mn evaporation in vacuo

The original model for evaporation of Mn in vacuo, as presented in Paper I, was based on equation 2.2 and 2.3 as shown in section 2.2.2. In steady-state where there is no buildup of Mn above the surface, the diffusion and evaporation flux defined in these two equations are equal, and this is an assumption for the model. Table 3.5 shows the temperature-dependant values used in the model for each of 1400, 1550, and 1700 °C respectively. The thermodynamical values were taken from NIST-JANAF Thermochemical Tables (95), where values for gases below boiling temperature were extrapolated from the data given in the tables. The extrapolated data was found to deviate from values found experimentally by at most 1.97 kJ/mol for ΔH and 1.2 J/mol for ΔS which is well within the experimental uncertainty. Additionally, the radius of the cylindrical container was 0.0135m.

In the model, the flux was calculated by finding the partial pressure of Mn(g) at the surface where the evaporation flux was equal to the diffusion flux given the

Table 3.5: Values used in the evaporation modelling.

Value	at 1400°C	at 1550°C	at 1700°C
Diffusion coefficient for Mn-Ar (m^2/s)	2.93 E-4	3.43 E-4	3.97 E-4
Viscosity of Ar (kg*m/s)	7.87 E-5	8.01 E-5	8.42 E-5
Density of Ar (kg/m^3)	0.29	0.27	0.25
Average flow into the crucible (m/s)	13.5	14.7	15.9
ΔH (kJ/mol)	313.8	315.9	318.4
ΔS (J/mol)	210.7	211.9	213.2

other parameters. The diffusion flux, following equation 2.3, 2.4, and 2.5 shown in section 2.4.1, is proportional to the square root of the bulk flow velocity in the model, and due to the high vapor pressure of Mn(g) above 1400°C the total flux is almost entirely limited by the diffusion flux.

3.2.3 Flux modelling for HCFeMn in oxygen-containing atmospheres

Rosner's reaction factor F_{RXN} (26) was explained in section 2.4.1 and the formula shown in equation 2.15, and a model based on this factor was used alongside the experimental data to predict the experimental yield. In the model, the experimental value for 0% O_2 is multiplied with the calculated reaction factor F_{RXN} for the different O_2 bulk concentrations. The values for diffusion coefficients and mass fractions at the different boundaries was calculated for each 1% O_2 starting at 0%, and used to generate the F_{RXN} for each point using equation 2.15. The flux was then estimated at each point according to equation 3.8.

$$J_i = J_{0\%} \cdot F_{RXN,i} \tag{3.8}$$

Where:
J_i = mass flux [g/m^2s]
F_RXN, i = reaction factor [unitless] as defined by equation 2.15
i = O_2 percentage in bulk

When utilizing this model it is important to note that if any assumptions concerning either the diffusion density ratio, mass fraction of the metal in the vapor, or oxygen in the bulk gas are compromised, then the model values from equation 2.15 must be recalculated. This is due to the flux calculation being very sensitive with respect to these parameters.

The theoretical value for the manganese evaporation flux in vacuo was also calculated using the Hertz-Langmuir expression as shown in equation 2.14. In theory this value should constitute an "upper bound" which the flux values would converge towards as the oxygen content is increased (26). The partial pressure of manganese can be calculated from the formula for Gibbs free energy as shown in equation 3.9, but as the liquid Mn is not pure, the activity must be taken into consideration. Rearranged for partial pressure this becomes as shown in equation 3.9 (96):

$$p_{Mn(g),eq} = 101325 \cdot a_{Mn} \cdot exp\left(\frac{241780 - 104.46 \cdot T}{-8.314 \cdot T}\right)(Pa) \tag{3.9}$$

Where:
$p_{Mn(g),eq}$ = equilibrium partial pressure of Mn(g) above the melt [Pa]
a_{Mn} = activity of manganese in the melt [unitless]
T = temperature = 1823.15°K in the experiments performed in this work on HCFeMn.

The values for standard enthalpy and entropy given by Joo et. al were cross-checked against tabulated values by Landolt-Börnstein (97) and found to give standard Gibbs energy values within 1% of each other. The activity of manganese was calculated using Factsage 7.3 (49) with chemical compositions given in Table 3.3, and an initial carbon content of 7wt%, which represents the carbon saturation of the alloy at 1550°C. The software performs Gibbs energy minimization to calculate the distribution of elements in the different phases, using among others the Gibbs-Duhem equation. This equation does not take surface effects such as decarburization or other factors that makes the surface concentrations vary from the bulk concentrations into consideration.

3.3 Distributed sensor system

Due to the nature of the industrial locations for which this work has its focus, the particle measurement technique based on the light scattering principle was considered the most fitting. Light scattering is the most widely used method for continuous measurements, and having measurements with a high time resolution is very useful in industrial situations where there are many different processes that generate PM and where implementation of and changes in local measures such as ventilation and changes in routines such as opening of hall doors can produce measurable changes in PM. The Nova PM SDS011 ("Nova") was chosen as the best fit for a low-cost sensor utilizing that principle due to its established good

performance in environments with relative humidities below 75%, as well as its ease of use both as an individual sensor and to be set up in clusters and widespread sensor networks.

The complete setup for the Nova sensor system included the Nova PM SDS011 sensor connected to a microchip together with a temperature and humidity sensor placed in a closed box as shown in Figure 3.3. The system consisted of two sensors and a microchip which collected and forwarded the data to a central server, all contained in a 3D-printed PVC box which measured around 13*10*4cm. The Nova PM SDS011 sensor reports the concentration of PM10 and PM2.5 in $\mu g/Nm^3$ (micrograms per normal cubic meter), while the HTU21D reports temperature in $^\circ$ C along with the relative humidity. Both sensors conveyed the measurements to the ESP32S (the ESP8266 was used early, but was later changed to the newer model) microchip via sets of dupont cables which also powered the sensors with electricity from the microchip. The microchip was powered with 5V 1A of electricity provided from an external power source, and while the system protected the components to a degree, the model was not airtight. Air from outside the box was sucked into the dust sensor through a short 2mm diameter tube by the flow created with an integrated fan, while the temperature and humidity sensor was placed on the outside of the box where it measured the ambient air.

The Nova sensor measured the concentration of fine particles (98), while the humidity sensor measures the relative humidity (RH) through change of capacitance and temperature (T) though changing resistance. The system measured continuously and provided a snapshot of these values approximately every five seconds. The data was transferred through local WiFi using the chip's integrated WiFi receptor, and the sensors could as such be spread across as large an area as a single network could cover. To receive the data, a Raspberry Pi v3 (RPi) was connected to the same local network at a static ip-address which the sensors could send the packages of data to. The RPi stored the data locally in .csv format, one file per sensor per day, using an external hard drive with at least 500GB capacity allowing for more than a decade of measurements with 200 sensors to be stored before running out of space. In addition the RPi could in the final iterations of the system send the data to a database on an online server from where the data could be easily graphically accessed for live monitoring.

The Fidas sensor utilizes the same principles for measurements of PM, RH and T, and stores the data locally in 10-second intervals on its internal computer from where they can be gathered using an USB-drive. It is also able to send data to a

server from where it can be viewed and gathered. Before the measurement period started, the Fidas calibration was verified using a monodisperse test aerosol made with SiO_2, where the particle diameter measured was compared to the known diameter of the particles in the test aerosol. The temperature and humidity is measured through a weather station attached to the system container near the fume intake, as shown in the sketch of the system on figure 2.11.

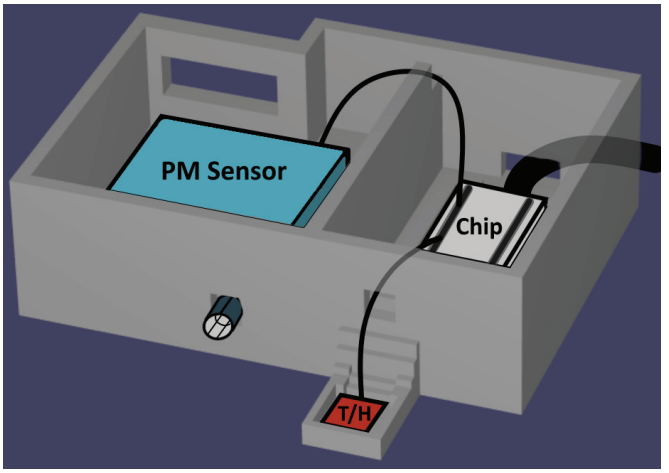

Figure 3.3: Schematic of the sensor system with the Nova PM SDS011 sensor, used alongside the HTU21D temperature and humidity sensor, and a microchip that collects and forwards the data. Each box was closed with a matching lid to limit exposure.

The data from the Nova sensors was stored as .txt files with each line containing a single data point with values for the time of measurement, PM2.5, PM10, relative humidity, and temperature. Each file held the data for one sensor over one day, and were imported into and processed using Matlab R2019b (99) (earlier versions were used in the beginning of the project). The data from the Fidas was retrieved in their own custom format which was sent to the manufacturer and returned as Excel-files with the data stored in 2-minute averages on each line. To reduce noise, the Nova measurements were gathered in 1-minute averages before further processing. All data was smoothed using a sliding average across 15 data points to reduce the noise further, but when generating graphs that spanned across several weeks, the data was gathered in 15-minute averages and smoothed across 6 hours with the same algorithm due to the large variations from hour to hour in the environments where the measurements were done. 95 percent confidence intervals (95% CI) were also calculated for groups of Nova sensors using the values for each sensor at each point in time to generate the range of which there is a 95 %

probability that the true value lies, given no systematic measurement error. It was calculated as shown in equation 3.10:

$$95\%CI = \overline{x} \pm \tau \cdot \frac{\sigma}{\sqrt{n}} \tag{3.10}$$

Where:
$\overline{x}$ = mean fume measurement value [g/Nm^3]
n = sample size (number of sensors in the group) [unitless]
τ = T-distribution value [unitless], defined by n and the desired confidence interval percentage, can be looked up in known tables
σ = standard deviation [g/Nm^3] calculated as shown in equation 3.11:

$$\sigma = \sqrt{\frac{\sum(x - \overline{x})^2}{n - 1}} \tag{3.11}$$

3.3.1 Aluminum plant

The Aluminum plant, owned by Hydro, is located only a few hundred meters from a large fjord in the southwestern part of Norway. The measurements were performed during the months of August and September.

At the aluminum plant, directly above the electrolysis cells, 12 Nova sensors were placed in groups of four at three different positions inside a Robertson roof monitor (A natural draft roof ventilator which funnels the air out while stopping rain, marked in Figure 3.4), one in the center, and one halfway to each side along the same axis as the production cells are placed. This roof monitor room is 9.75 meters long and is located 12 meters above the hall floor. Fumes from the processes of several cells pass through here as shown in Figure 3.4. Sensor 1-4 are placed in the middle, sensor 5-8 to the left and sensor 9-12 to the right, relative to a person standing in the middle and looking towards the sensors, with a distance of 2.4 meters between each group as well as the end walls as shown in figure 3.5. Local weather data were acquired from a weather station on the aluminium plant and used as background data for the measurements. In addition, a record of process events on the aluminum production cells just below the sensors relating to anode exchanges, measurements, and tapping were acquired from Hydro.

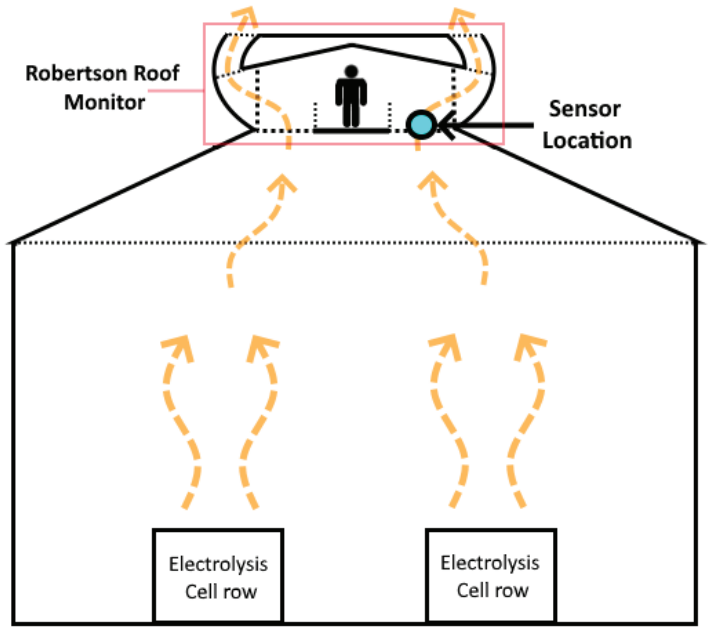

Figure 3.4: Locations of the sensors marked with an arrow above the electrolysis cell rows, inside the Robertson roof monitor.

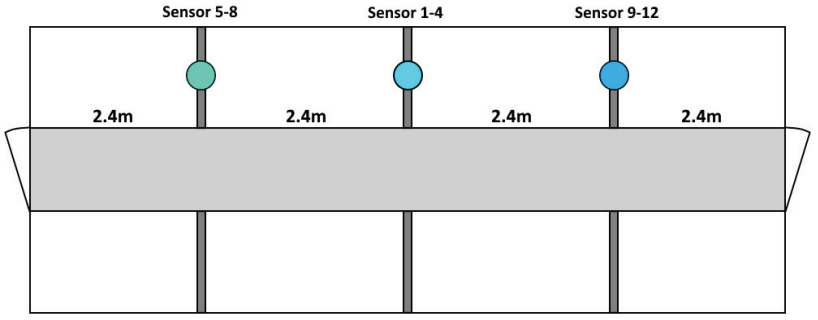

Figure 3.5: Locations of the three sensor groups inside the Robertson roof monitor.

3.3.2 Silicomanganese plant

The Silicomanganese plant, owned by Eramet, is located near the end of a small fjord in the southern part of Norway. The measurements were performed during the months of June through September, with the calibration being performed at the end of the period. A power outage shut down the data storage system for the Nova sensors which did not have an automatic restart function at the time, limiting the

available data. The extended period lasted for more than two months with only the Nova sensors, while the calibration period lasted for most of a day and a night where the Nova sensors were placed close to the Fidas. For both periods, twelve Nova sensors were divided into three groups of four sensors stacked on top of each other. In both periods, the sensors were placed in a hallway adjacent to the tapping hall, with one wall-section being an opening towards the tapping hall, and another being the outer walls of the furnace itself. Figure 3.6 shows the approximate sensor locations for the measurement periods.

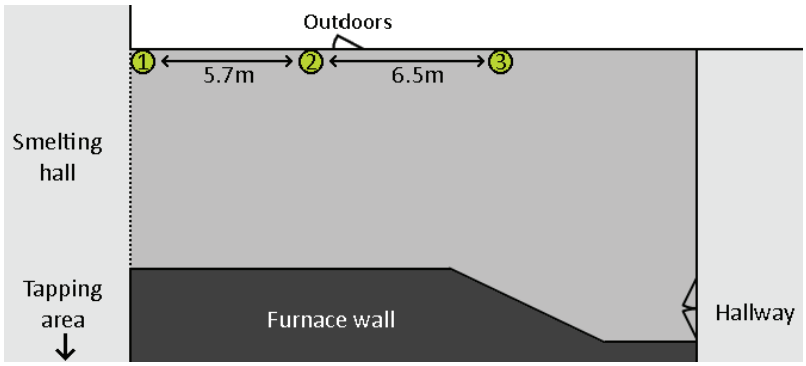

Figure 3.6: Approximate sensor locations during the middle and last measurement period for the measurement campaign at the SiMn plant. The ceiling height is 6.45m, and the entire section leading out to the smelting hall is open allowing for free flow of fumes into the measurement area. During the middle period, four Nova sensors were each placed at point 1, 2 and 3, roughly 1.5m above the floor along the wall section. During the last period, all 12 Nova sensors were placed together at point 3, with the Fidas sensor placed with the fume intake approximately 30cm away from the Nova sensors.

3.3.3 Silicon plant

The Silicon plant, owned by Elkem, is located along a large fjord near the middle of Norway. The measurements were performed during the months of May and June, with the measurement period lasting for about one month. 35 Nova sensors placed in vertical groups of 5 near the inlet for a Fidas sensor for the full duration of the campaign. The sensors were placed on a mezzanine floor above the furnace body where the electrode feeding takes place, inside the hall in which tapping is performed. Figure 3.7 shows the approximate location of the sensor group along with the relevant process locations.

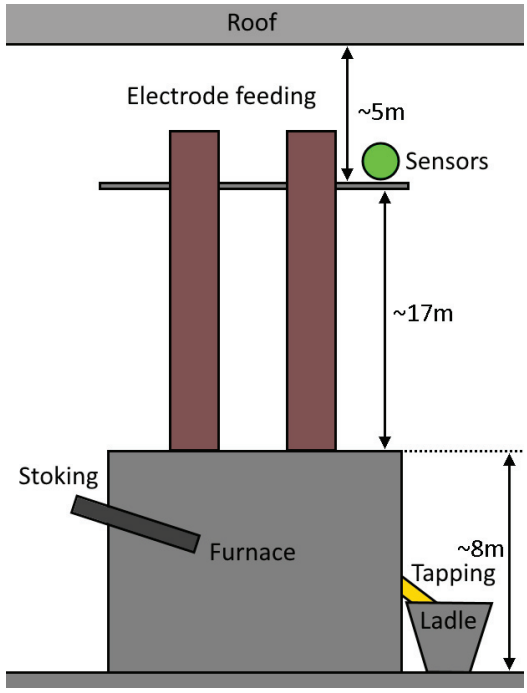

Figure 3.7: Approximate sensor location (Green circle near the top) during the measurement campaign at the Si plant. All 35 Nova sensors were placed with their fume inlets within 20cm of the Fidas' fume inlet. There is a fuming hood designed to capture most of the tapping fumes, and there is also several layers of partial flooring between both the tapping and stoking areas, and the sensors. Fumes and smoke not captured by the fuming hood will eventually flow up along the sides of the furnace and reach the sensors however, and fumes that gathers below the roof will also be picked up by the sensors which are only a couple meters below. Redrawn from sketch provided by the smelting plant.

Chapter 4

Results and discussions

This section covers the results from the experimental work and modelling of manganese alloy fuming and dust formation, as well as the dust measurement campaigns at the aluminium, silicomanganese, and silicon production plants. The chapter also contains the discussion of these results.

4.1 Evaporation and fuming experiments

In this subsection, the results and discussions from the evaporation and fuming experiments are presented together with the modelling done alongside the experiments. Evaporation of pure Mn is presented first, followed by the HCFeMn fuming results and diffusion-, oxidation-, and flux discussions based on the results. The models used are presented along with the results they are modelling. Finally, the size distribution and elemental distribution of the dust from the HCFeMn fuming experiments are presented and discussed. This section is based on Papers I and III.

4.1.1 Evaporation of Mn

The measured flux values from the experiments performed on evaporation of pure Mn are shown in Table 4.1 and in Figure 4.1:

According to the original model presented in Paper I and explained in section 3.2.2, the fluxes were expected to be proportional to the square root of the flow rate following equation 2.3, 2.4, 2.5 and 2.6, but as can be seen from Figure 4.1, the experimental fluxes instead show a near linear correlation between the flow

Table 4.1: Flux values from the experiments performed on evaporation of pure Mn in an Ar atmosphere with an impinging jet flow of Ar. The negative flux value from exp #10 is assumed to be from a small amount of oxygen, supplied either from the ppm concentration in the Ar, the alumina crucible, or from the tarnished starting Mn-chip surface, reacting with the metal to form heavier oxides.

Exp nr.	Flow rate (l/min)	Temp (°C)	Flux (g/m^{2}s)
10	0.0	1400	-0.05
5	0.5	1400	0.19
7	1.0	1400	0.49
2	0.0	1550	0.03
12	0.25	1550	0.38
3	0.5	1550	0.81
6	0.5	1550	0.79
1	1.0	1550	1.54
4	1.0	1550	1.78
8	0.0	1700	0.14
11	0.5	1700	3.76
9	1.0	1700	5.45
13	1.0	1700	5.00

rate and the evaporation flux. This model also showed an unexplained difference of factor 4 between the modelled and experimental flux values. Due to this, additional investigations were later made into the modelled values. A couple of errors in the original calculations were found, including a misformatting in temperature and a slightly incorrect radius. The corrected values made with the original model are shown in Figure 4.2, compared to the old model and the experimental data.

The corrected modelled values are much closer to the experimental values, but as the flow model as previously mentioned gives fluxes proportional to (flow rate)$^{0.5}$ the modelled values fall off at higher flow rates compared to the more linear experimental results. Due to this, investigations into a better model continued.

One notable exception to the linear trend was evaluated first however; a reduced flux in the experiments with the highest flow rate at 1700°C. This reduced rate is believed to be due to there being too little metal in the crucible, as the expected value given linearity would be around 15.5g, while only 15g of Mn was used in the experiments. As the metal evaporates, the distance from the gas lance to the surface increases, and when the remaining metal volume is low enough, the surface area will be reduced at the molten metal no longer covers the entire cross-section of

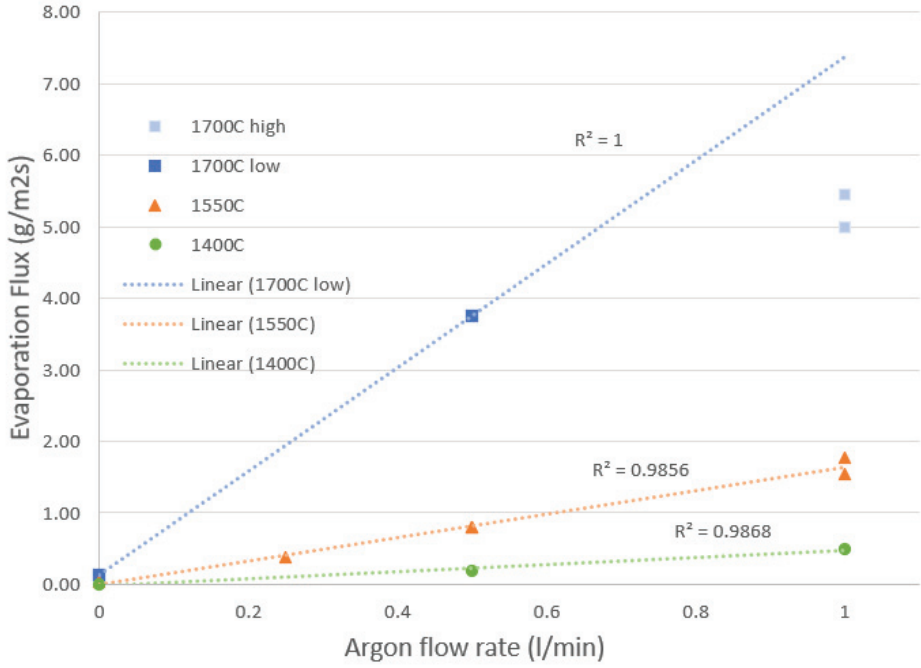

Figure 4.1: Flux values with trend lines from the experiments performed on evaporation of pure Mn in an Ar atmosphere with an impinging jet flow of Ar. Trend lines for the 1700° results are limited to the 0 and 0.5 l/min flow rate experiments due to a reduced flux from the 1 l/min experiments caused by other factors.

the crucible. The maximum change in flux due to increasing distance from the gas lance to the metal surface was estimated to only be around 1%, but the reduction in evaporation due to reduced surface area is proportional to the degree of surface loss which was significant at the end of the previously mentioned experiment as shown in Figure 4.3.

During the investigations when calculating the partial pressure of Mn(g) above the surface that lead to equal flux from evaporation and diffusion using equation 2.8 was above 99.9% of the equilibrium value (0.00823-0.11356 atm at 1400-1700°C) given the variables used in this work. As such the partial pressure of Mn(g) was assumed to be equal to the equilibrium value for the continuing diffusion calculations. The diffusion layer thickness and the cross-surface velocity were the two largest uncertainties in the first diffusion model, and further work was as such done to approximate those values more accurately. An updated axisymmetric Comsol (100) model with a finer mesh was used look at the velocity boundary layer, which

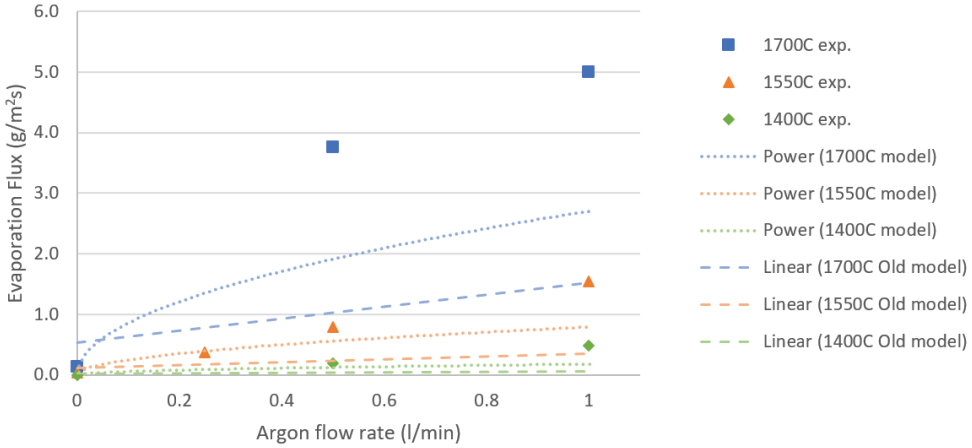

Figure 4.2: Modelled vs Experimental flux values. The experimental values show the mean for each set of parameters, the modelled values show the ones calculated by the original model for the Mn evaporation experiments after correcting mathematical errors, and the old modelled values show the values calculated with the original version of the model for comparison.

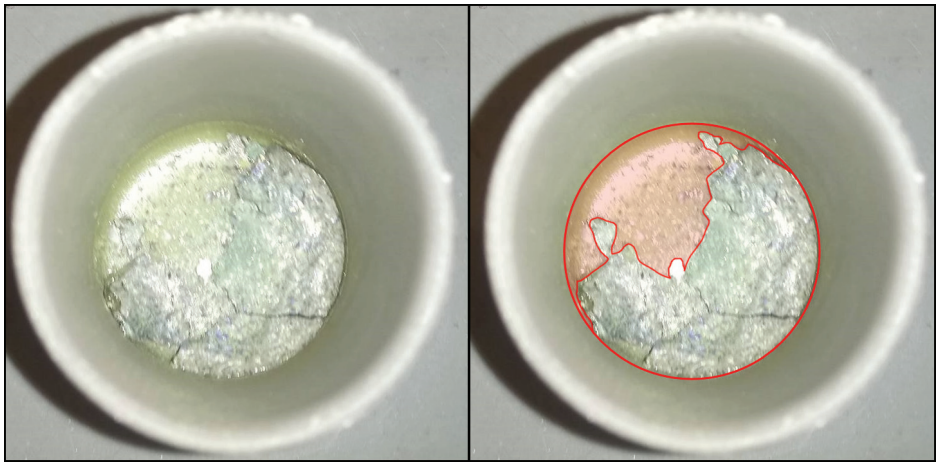

Figure 4.3: Inside the crucible after the experiment with the highest amount of evaporation. The surface area has been reduced by about one third at the end of the experiment.

was found to be almost ten times shorter than the previously calculated diffusion layer thickness. At 1400°C and 1 l/min flow, the cross-surface top velocity was simulated to be around 5m/s around 0.6mm above the surface, compared to the 5.4mm diffusion layer thickness previously estimated, with the value reducing and

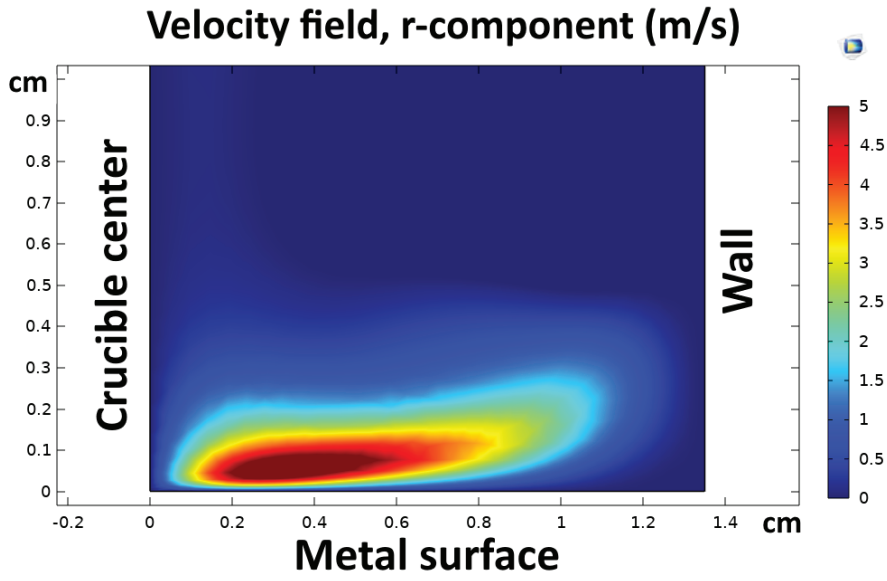

Figure 4.4: Radial component of the flow velocity inside the crucible at 1400°C and 1 l/min flow. Steady-state simulation using Comsol (100).

the distance increasing towards the edges of the crucible as shown in Figure 4.4. Although the limited mass transport makes the effective diffusion layer thickness larger than the velocity boundary layer thickness, the diffusion gradient is still larger in the new model.

In order to take the variations across the surface as well as the limitations from mass convection away from the diffusion layer into account, an expanded steady-state Comsol model with transport of dilute species in addition to flow equations was used. Values for diffusion coefficients, viscosity, density, and inflow were calculated given the temperature and gas flow for each simulation, and the surface concentration of evaporated manganese was set equal to the equilibrium value. The resulting concentration gradient for the example at 1400°C with 1 l/min flow averaged 23.96 mol/m^4, and the vapor concentration across that simulation is shown in Figure 4.5.

Figure 4.6 show the experimental flux values and the modelled flux values using the new model. For the modelled values, simulations were done for flow rates of 0.01, 0.1, 0.25, 0.5, 1, 1.5 and 2 l/min at each temperature, and a linear interpolation forced through origo of these are shown in the figure with R^2-values exceeding 0.998 for all three lines.

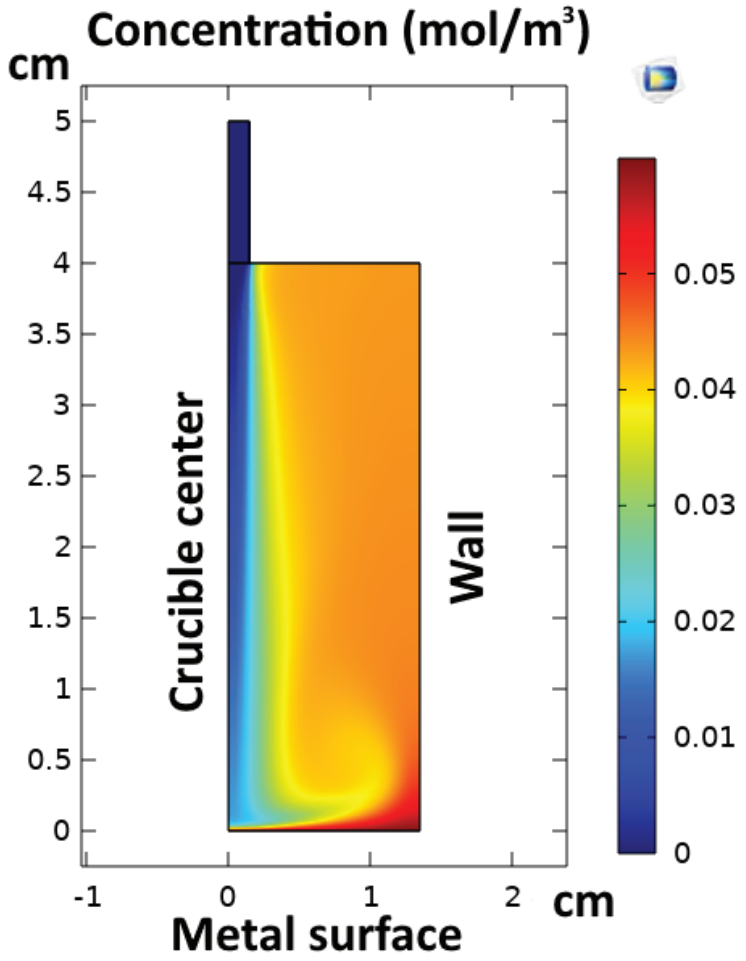

Figure 4.5: Fume concentration inside the crucible at 1400°C and 1 l/min flow. Steady-state simulation using Comsol (100).

The new modelled values are approximately linear, except for a small dip at and around 0.2 l/min flow rate and correlate very well with the experimental values. Particularly for 1400 and 1550°C the values match well, with some deviation for the results at 1700°C.

A contribution to the remaining difference at 1700°C may be due to evaporation happening before and after the furnace has reached its goal temperature, as the heating of the crucible from room temperature lasted 30 minutes and cooling las-

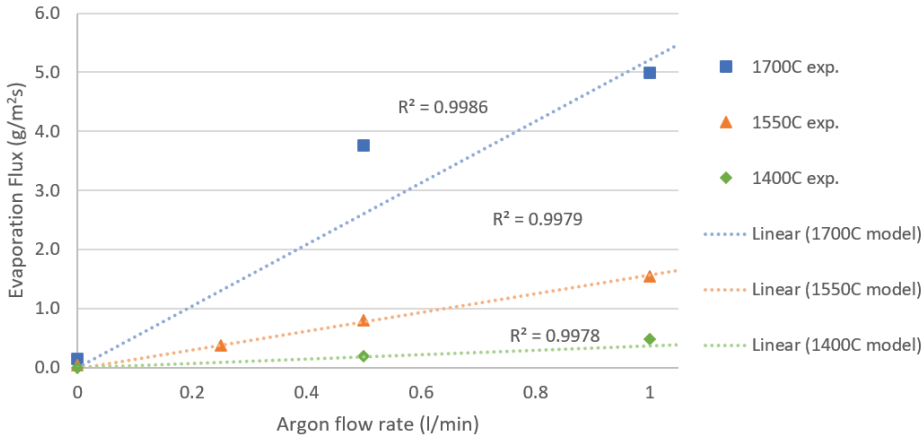

Figure 4.6: Experimental values, averaged for each set of parameters, and modelled flux values using the new model with average surface concentration gradients calculated using Comsol (100). R^2-values are for the modelled interpolation lines compared with the modelled values generated for 0.01, 0.1, 0.25, 0.5, 1, 1.5 and 2 l/min at each temperature.

ted approximately 10-15 minutes. Using an approximation of the flux at each temperature for the 0.5 l/min flow rate experiments using the modelled values, the total mass loss during heating was estimated to be 0.174g which is equivalent to an increase in flux of 0.169 g/m^{2}s. Together with a flux increase from the cooling period estimated to be around a third of this, it is assumed to account for around a fourth of the difference between the experimental and modelled values at 1700°C. For the experiments at 1550°C, this additional flux from heating and cooling is calculated to be around a third of the value estimated for 1700°C, and far less for the 1400°C experiments.

Small amounts of oxygen from the inert gas could also increase the flux to some degree, but with the gas in use being argon 6.0 N, the worst case scenario of 0.0001% O_2 at 1 l/min would only introduce 0.00134mmol of oxygen over the course of the holding time. Assuming that every oxygen molecule contributes to the formation of additional 2 MnO-molecules, it still only amounts to 0.000147g of Mn removed from the crucible, which is not significant.

Considering these new modelled values, it is deemed possible that the experimental flux for 0.5 l/min at 1700°C is an outlier and the fluxes for 1 l/min at 1700°C were not significantly reduced due to surface area reduction at the end of the experiments. In such a case the experimental flux for 0.5 l/min at 1700°C would be

around 4.997+0.2=5.197 g/m^{2}s which is still below the modelled value of 5.402 g/m^{2}s. Further experiments with several parallels are needed to verify or refute these theories.

4.1.2 Diffusion, oxidation and flux of HCFeMn alloy

With the diffusion rate of Mn(g) from the surface to the reaction surface being the limiting factor for the mass transfer from metal to air, its calculation is the most important one. The diffusion coefficient was approximated as shown in chapter 3.2.1 using equation 3.2, and the diffusion rate is calculated by multiplying the coefficient with the concentration gradient as shown in equation 2.3. This equation must be altered when a reaction is taking place inside the diffusion boundary layer as the distance over which the vapor must diffuse is shortened as shown in Figure 2.9 when the reaction plane replaces the surface as the end point for diffusion of oxygen from the bulk gas. Once the system is in balance and the diffusion rate is lower than the evaporation rate, the surface concentration of Mn(g) does not change and is decided by the equilibrium partial pressure of Mn(g) given the activity of Mn and the temperature in the metal. If the diffusion rate exceeds the evaporation rate however, then the surface concentration of Mn(g) will be reduced which in turn will lower the concentration gradient and slow down the diffusion rate. At that point, the evaporation rate will be the rate limiting factor. The minimum concentration of O_2 in the bulk gas required for this transition is defined as shown in equation 2.12 (26).

A simplification of the system that is used because the reaction rate between Mn(g) and O_2 is high, is that the reaction happens along a plane, the reaction "front". If the reaction rate is not faster than the rate of Mn(g) transport to the front however, the reaction front becomes a reaction "band", a volume in which the reaction takes place. Figure 4.7 shows how the concentration changes inside the diffusion boundary layer when there is a reaction, both in the case of very fast reaction rates where all the reactants are expended upon contact, and if the reaction rate is slower and a reaction "band" forms in which the reaction happens.

If there was no reaction, the diffusion distance would be equal to the boundary layer thickness, δ, and the driving force would be the difference in concentration at the surface and in the bulk gas, but with the reaction the diffusion distance is shortened to y_f or y_b for a reaction front or a reaction band respectively, and the Mn(g) concentration at that point is defined as 0 for this system. Given the system studied here, the reaction happening at the reaction front or band is the oxidation

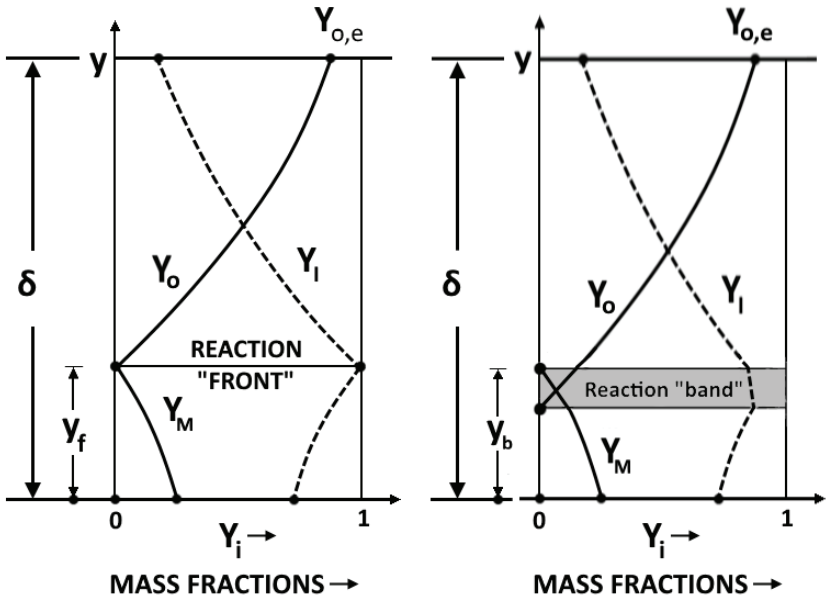

Figure 4.7: Diffusion boundary layer concentrations of oxygen, metal, and inert gas given the assumption of instantaneous reaction along the "front" or non-instantaneous reaction inside a "band". Based off original drawing by Rosner et al. (26).

of Mn(g) to MnO, as can be determined from the phase diagram shown in Figure 2.7, which is shown in reaction 16.

$$\mathrm{Mn\,(g)} + \frac{1}{2}\,\mathrm{O_2(g)} \leftrightarrow \mathrm{MnO(s)}, \Delta \mathrm{G^{\circ}(kJ)} = -603.64 + 0.1972\,\mathrm{T} \qquad \text{[R16]}$$

Given the temperature in the experiments are approximately 1823.15°K, the Gibbs free energy of reaction is approximately -244 kJ. The following reaction rate r_{ox} can be written as shown in equation 4.1 (101):

$$r_{ox} = k(T)[\mathrm{Mn}(g)]^s[\mathrm{O_2}(g)]^t \qquad (4.1)$$

Where:
[Mn(g)] and [O_2(g)] = concentrations of Mn and O_2 respectively [mol/m^3]
s and t = partial reaction orders for Mn and O_2 respectively [unitless]
k(T) = temperature-dependent rate constant [reaction order dependant]

Figure 4.8 shows the fluxes from the HCFeMn experiments along with fluxes from some related works (48, 56) and lines showing the maximum theoretical flux given different assumptions regarding the activity of manganese in the metal.

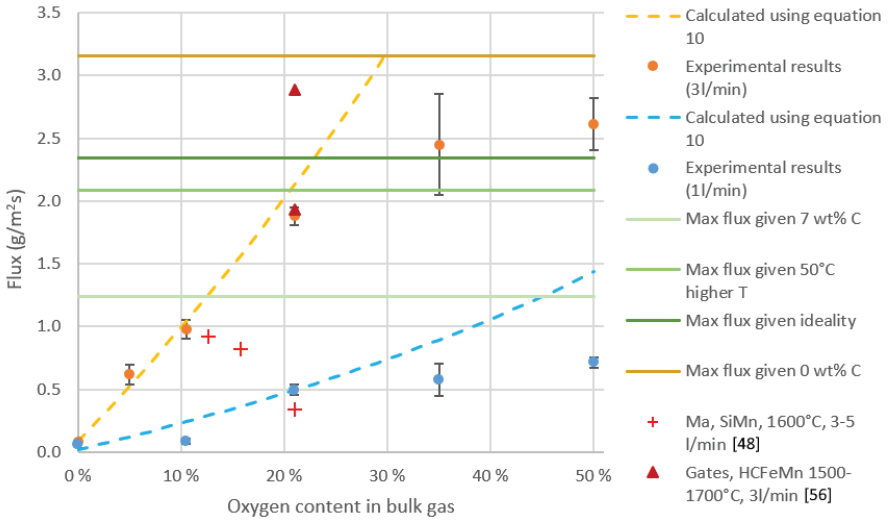

Figure 4.8: Relation between the measured experimental flux values and the ones calculated with the formula from Rosner (26). Includes the maximum evaporation flux, calculated using equation 3.9 and 4.2 given four different assumptions affecting the Mn(g) partial pressure: Baseline assumption of 1550°C and the equilibrium concentration of 7 wt% carbon in the melt with a negative deviation from ideality from the Mn-C interactions, temperature increased to 1600°C, ideality instead of negative deviation between Mn and C, and a surface carbon concentration of 0 wt%. The calculated line for 1 l/min uses 21% oxygen as the baseline due to instability in the fume generation at the lowest levels of oxygen and flow. Data from Ma et al. (48) and Gates et al. (56) are shown for comparison, but the difference in temperature (1600°C and 1500-1700°C for Ma and Gates' experiments respectively), flow rate(3-5 l/min and 3 l/min for Ma and Gates' experiments respectively), and/or metal composition (SiMn and HCFeMn for Ma and Gates' experiments respectively) must be considered. The higher fluxes correspond to the higher flow rate and temperature for Ma and Gates respectively.

The theoretically calculated flux lines shown in Figure 4.8 are estimated based on four different sets of assumptions, with the baseline assumptions being a temperature of 1550°C and the equilibrium concentration of 7 wt% carbon in the melt with a negative deviation from ideality from the Mn-C interactions which strongly

reduced the activity of manganese with increasing carbon content:

- Baseline assumption with activity coefficients calculated with Factsage version 7.3 (49).
- Baseline assumptions, but with the temperature of the molten alloy assumed to be 50° higher.
- Baseline assumptions except that ideality is assumed for the activity of manganese giving no reduction in the manganese activity from the carbon content.
- Assumed no carbon at the melt surface, giving no reduction in manganese activity from Mn-C interactions, and increasing the concentration of Mn slightly.

The manganese activities given these assumptions are calculated with a formula presented by Lee (102) for the activity coefficient of manganese based on the assumption that manganese and iron behave as an ideal solution, which is shown in equation 4.2:

$$ln(\gamma_{Mn}(Fe-Mn-C)) = (-0.4822+576.7/T)x_C + (5.1498-10842/T)x_C^2 + (-25.821+8289.7/T)x_C^3 - 4943.8x_C^4x_{Fe}^5 \quad (4.2)$$

Where:
γ_{Mn} = activity coefficient of Mn [unitless]
x_i = atom fraction of species i [unitless]
T = temperature [K]

The manganese activity was also calculated with Factsage for the baseline assumption, giving a 10% lower value. This difference, while not insignificant, is incomparable to the differences between the different assumptions.

Given that the melt in our system is in contact with solid carbon, the graphite crucible, we can assume carbon saturation in the bulk melt. Using the approximation for carbon saturation levels done by Lee (102), we get a C atom fraction of 0.271 in our system using T = 1550°C, which when entered into equation 4.2 together with the Fe and Mn concentration from table 3.3 gives a Mn activity coefficient of

0.59 which when multiplied with the Mn concentration of 72.1% gives a total Mn activity of 0.375. The value calculated with the Factsage software as previously mentioned was slightly lower at 0.345. To study the effect of the Mn-C interactions, we can assume ideality for the activity of Mn in the Mn-Fe-C-system, at which point the activity becomes equal to the concentration at 0.72. Lastly, if we assume that the air blown on the alloy to a significant extent reaches the melt surface and decarburizes the melt surface, the result is a higher Mn concentration at the surface than in the bulk, which coupled with a higher activity coefficient results in an associated higher Mn activity and Mn vapor pressure. Figure 4.9 shows a sketch of concentration profiles in such a system where the reaction band for manganese oxidation reaches the surface allowing for carbon to react with oxygen as well. As the Fe-Mn system behaves close to ideally (103) with no carbon present, the activity coefficient is close to 1, and the activity in our system approaches 0.856.

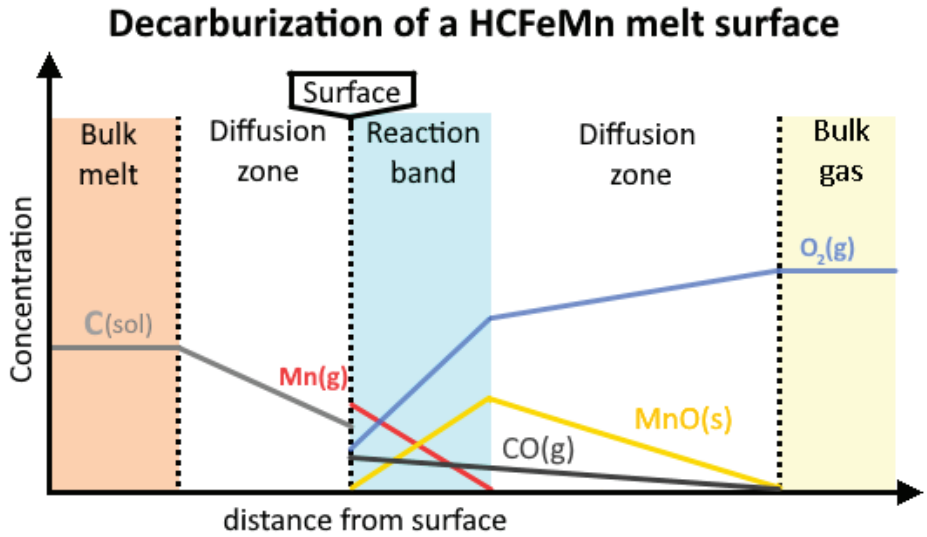

Figure 4.9: Sketch of concentration profiles for solved carbon, manganese vapor, manganese oxide fumes, oxygen gas, and carbon monoxide gas, in a system where oxygen reaches the surface to react with carbon.

The maximum evaporation fluxes in vacuo shown as lines in Figure 4.8 given the different Mn activities and temperatures were calculated directly using equation 2.14 and 3.9, and this value should constitute a limit which the flux values would converge towards as the oxygen content is increased (26). Of the resulting lines, only the one from the assumption of no carbon at the surface is higher than the ex-

perimental results at high oxygen concentrations. The experimental values seem to flatten out towards a value of around 2.75 g/m^{2}s, which would match well with an assumption of almost no carbon at the surface. As all the other assumptions in isolation do not sufficiently increase the maximum evaporation flux above the experimental results, at least some decarburization is deemed very likely to have occurred. ΔG° for carbon reacting with oxygen to form carbon monoxide at 1550°C is -248.4 kJ/mol (104) which is more negative than the ΔG° for manganese reacting with oxygen at -244.1 kJ/mol following reaction 16. Following the formula for Gibbs free energy shown in equation 4.3 and assuming equal activities of MnO and CO, which both will be quickly removed from the reaction front, the activity of carbon must be around 75% of the activity of manganese vapor for the Gibbs energy of the two reactions to be equal.

$$\Delta G = \Delta G^\circ + RTln(K) \tag{4.3}$$

Where:
ΔG = Gibbs free energy [J/mol]
ΔG° = standard Gibbs free energy [J/mol]
K is the reaction quotient [unitless] defined as:

$$K = \frac{a_{prod}}{a_{reac} \cdot a_{O_2}^{0.5}} \tag{4.4}$$

Where:
a_{prod} and a_{reac} = activities of the product (MnO(s) or CO(g)) and the non-oxygen reactant (Mn(g) or C(s)) respectively [unitless] at the reaction plane
a_{O_2} = activity of oxygen [unitless] at the reaction plane.

Given that the activity of manganese vapor is at most 0.0290 for the assumption of no carbon as calculated using equation 3.9, this leads to a maximum equilibrium activity of carbon of around 0.022, which is much lower than the bulk carbon molar concentration of 0.271. Assuming a similar negative deviation from ideality due to Mn-C interactions for C as for Mn, the bulk carbon activity is still around 0.16, more than 7 times smaller than the calculated equilibrium carbon activity with oxygen present, which supports the theory of decarburization when oxygen reaches the surface. Factors that contribute to convection in the melt must be considered however, as they would reduce the time carbon particles need to diffuse to the surface and reduce decarburization. Inductive stirring is such a factor which

is very relevant given the experimental setup used in this work, and future studies should be made to quantify the effect and compare the effective rate at which carbon moves to the surface compared to the rate at which it reacts with oxygen given various parameters.

The Mn-evaporation experiments and modelling showed a linear trend between the flux and the flow rate which starts around origo with almost no flux if there is no flow of gas above the metal surface. Diffusion, and as such the forced convection which increases the concentration gradient powering the diffusion by reducing the diffusion layer thickness following equation 2.4, is the limiting factor here, although experimental results found the diffusion layer thickness to be a function of the flow rate to the power of 1 rather than 0.5. This agrees with the results of the HCFeMn oxidation experiments, where the flux from the 3l/min experiments where 3.8 times larger than from the 1l/min experiments using synthetic air. Figure 4.10 shows the experimental flux values as a function of the flow rate for each oxygen concentration, with linear interpolation lines forced through origo symbolising the linearity found in the evaporation experiments and how those results suggest that the relationship between the 1l/min and 3l/min fluxes would align.

A trend can be seen here in which the flux values given each temperature increase at a rate faster than linearity. For an impinging gas jet as the one used in the experiments, the mass transfer coefficient should be a function of the flow velocity to the power of 3/4 according to the work of Scholtz and Trass (105) on mass transfer in impinging gas jets, while classical flat-plate theory for gas reacting at an interface gives the mass transfer coefficient as a function of the square root of the flow velocity (43) but neither of these fit with the experimental results. The new modeled values for evaporation give curves that best match a quadratic formula with low coefficients for the flowrate^2, which are more in line with the results from the HCFeMn results as well. This may be because of the narrow crucibles used, where a larger part of the surface has a high velocity field compared to on a theoretical flat plane and a change in inflow velocity thus contributes to a larger change in mass transfer from the surface.

4.1.3 Size fractions

Manual particle counting (PC) was performed on SEM-images of the dust from the filters. This size distribution is shown in Figure 4.11(a), with the mean(median) values being 113(98)nm, 116(111)nm and 1008(719)nm for 5l/min 35% O_2, 5l/min 10% O_2, and 1l/min 35% O_2 respectively. LD was also performed on the filter

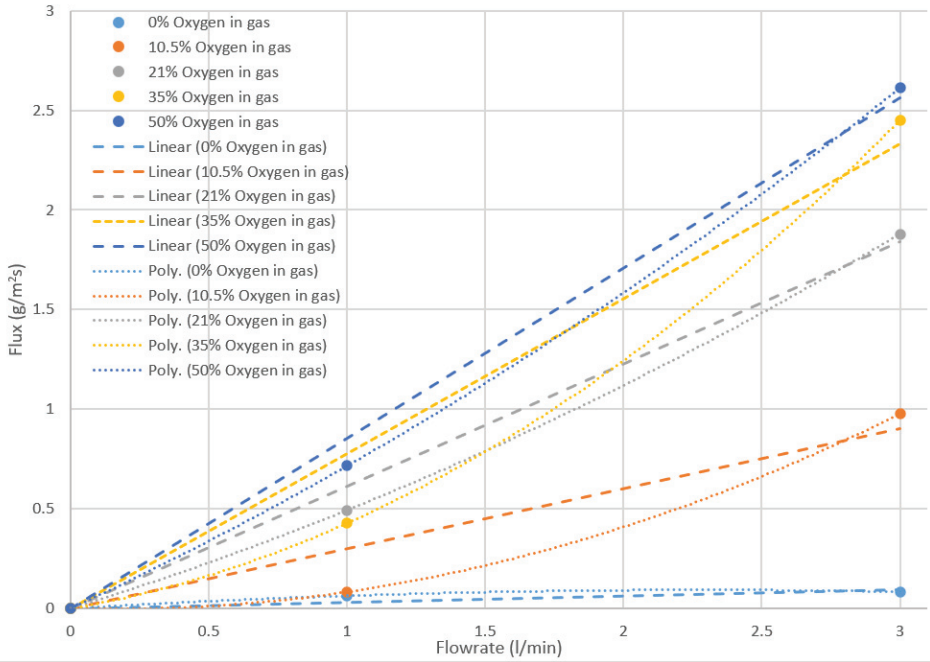

Figure 4.10: Experimental flux over the flow rate for each oxygen concentration. Linear interpolation forced through origo shows how the trend found in the Mn evaporation experiments predicted that the 1l/min and 3l/min experiments would align compared to each other. Second degree polynomial interpolation is shown as a comparison and is believed to be a better fit.

samples from each category of bulk gas oxygen content and flow rate, and the resulting average particle sizes for each flow rate is shown in Figure 4.11(b) with respect to the oxygen partial pressure, together with the average proto particle size from the PC.

The most notable results here are that the flow rate has a clear negative correlation with particle size, and that the oxygen concentration only has a clear effect on particle size at the lowest flow. The results show a clear correlation between the mean cluster size measured with LD and the mean proto particle size measured through PC, with the mean cluster size being around six times larger than the mean primary particle size.

The effect of oxygen concentration in the bulk gas at the lowest flow rate is theorized to be due to the increased fuming rate at higher oxygen concentrations, as the

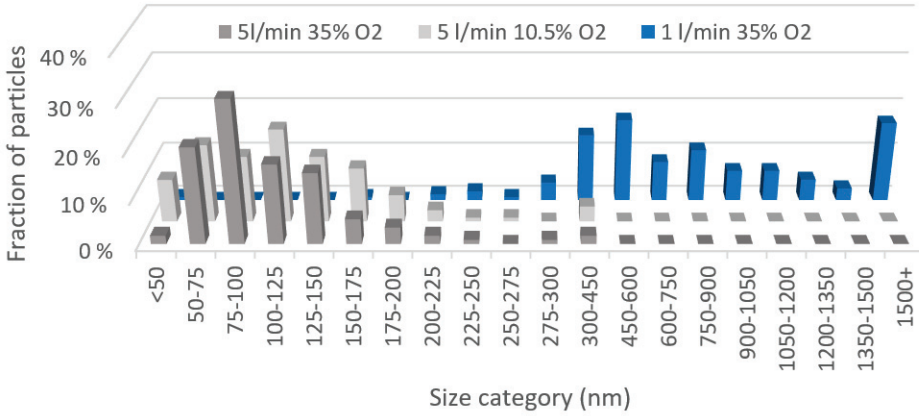

(a) Size distribution of particles from the filter dust of three experiments, measured manually from SEM-images. Note the change in box width from 300nm.

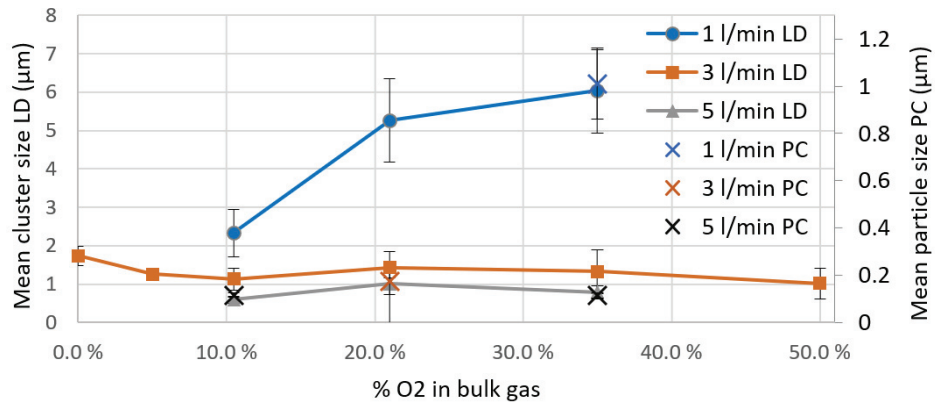

(b) LD and PC results, showing average cluster and particle sizes for each flow rate with respect to the oxygen partial pressure. Error bars show the 95% confidence interval given the data.

Figure 4.11: Size distribution measured with laser diffraction and particle counting.

concentration of particles is an important factor to the particle growth (42). The increase in particle size with increasing oxygen concentration in the experiments performed with 1 l/min gas flow is very similar to the increase in flux shown in Figure 4.8 in section 4.1.2 for the same experiments, which supports this theory.

The large increase in particle size with decreasing flow rate does not match with the theory of increasing fuming rates at higher flux just proposed, as the flux decreases with decreasing flow rates. This increase is instead believed to be due to

the increased residence time for growing particles in zones with higher temperatures, and generally the time the particles are suspended in air as an aerosol before reaching the filter. The rate constant for the growth of SiO_2 particles calculated from hard-sphere collision theory between monomers and clusters was found to be proportional to $T^{1/2}$ by Næss et. al (42), and this is assumed to be similar for MnO particles. This approximation assumes that both individual molecules and particle clusters behave like spherical particles, that growth is mainly the result of individual molecules attaching themselves to existing clusters, and that evaporation from and attractive interaction between the particles are ignored.

Variations from the assumptions of attractive interactions and evaporation would change the rate constant proportionality, but regardless of the exact degree of temperature dependency, the length of the growth period will largely affect the end size of the particles. Due to this, the flow rate becomes equally critical as residence time in both the higher temperature zones and otherwise before reaching the filter is proportional to the inverse of the flow velocity. Particles formed in the 1 l/min flow rate experiments would have a three times higher residence period in warmer zones compared to the particles formed in the 3 l/min experiment, and the factor difference between the two range from around 2 at 10% oxygen in the bulk gas to around 4 at 35%. Figure 4.12 shows the mean cluster size as measured by LD over the inverse of the inflow velocity.

The average of the values for the three different oxygen concentrations used in the bulk gas show an almost perfectly linear correlation with the residence time for the particles as represented by the inverse of the inflow velocity, with a slope of almost 4.5. The spread at particularly the highest residence time from the 1 l/min flow rate experiments show that there are other factors than just residence time, and that the effect of oxygen concentration is far from negligible.

4.1.4 Elemental distribution

The distribution of major elements in the dust for varying bulk oxygen concentrations as well as for the HCFeMn alloy used is shown in Figure 4.13 together with SiMn pilot scale results from Ma et al. (106).

The results show clear relations between the concentration of most of the elements and the oxygen content in the bulk gas, i.e. for all the trace elements except phosphorous, the concentration is higher in the dust than in the metal. The elements Zn, Mg, Pb, Na, S, and Al show a general trend of lowered concentration with increasing oxygen in the bulk gas, with Zn having an especially high concentration

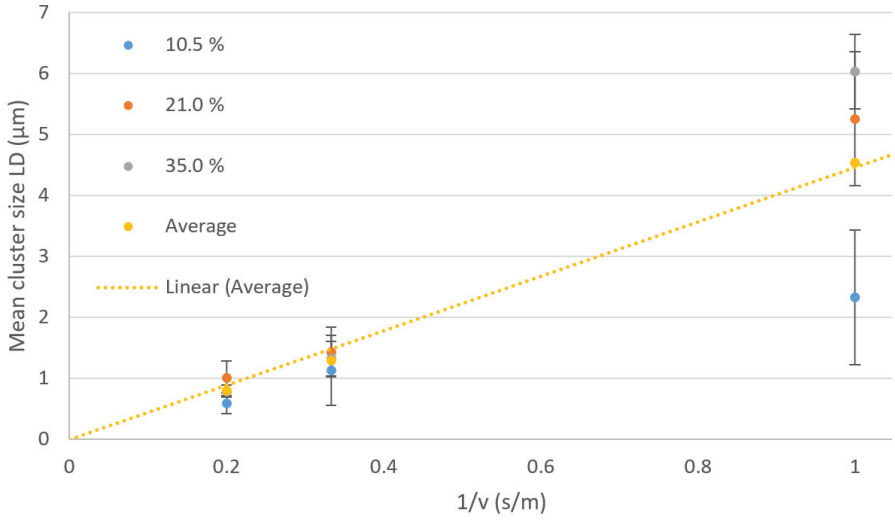

Figure 4.12: Mean cluster size as meaured by LD over the inverse of the inflow velocity in the experiments with three different oxygen concentrations in the bulk gas, as well as the average of the three and a linear interpolation forced through origo with an R^2 value of 0.9977.

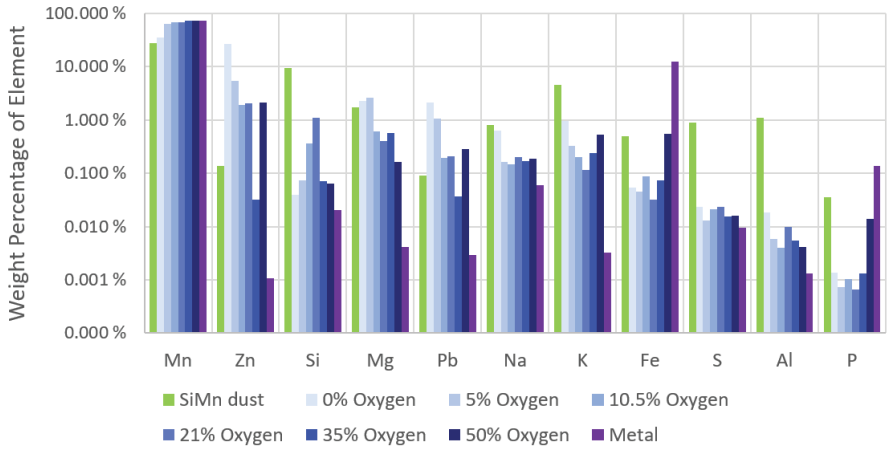

Figure 4.13: Element distribution for the most relevant elements (except oxygen) as measured by ICP-MS. The purple bars refer to samples taken from the metal chips used in the experiments, while the remaining blue bars are from dust samples taken from the filter in each experiment. The green bars show SiMn pilot scale results from Ma et al. (106). Note the logarithmic scale on the Y-axis.

at low O_2 levels. Si has a distinct peak at and around the regular oxygen level of 21%, whereas the K concentration is at its lowest in the dust at the same oxygen level. P and Fe both increase significantly at the 35 and 50% level, while staying relatively flat at lower O_2 concentrations.

Ma et al. (106) studied the elemental distribution in the silicomanganese production, where they found that base and transition metal elemental distribution mostly behave in good accordance with Gibbs energy of oxidation, while alkali metals fuming is controlled by their low boiling point. The most prevalent elements in the dust from pilot scale experiments were in order: Mn, Si, K, Ca, Mg, Al, S, Na, Fe, Ba, B, Zn, Pb, Sr, P. This agrees with the distribution found in this study, given that Mn, Fe and Si concentrations in the metal are different, and that Ca, Ba, B, and Sr were not screened for in this study. The most notable differences are the high amount of Zn and the low amount of Al, S and P in the FeMn dust, compared to the SiMn dust.

The trend of decreasing element concentration with increasing oxygen concentration in the gas for the majority of the trace elements is theorized to potentially be due to several factors. One is their low concentration in the metal. When the amount of oxygen is increased, the flux also increases, which would deplete the metal surface of the trace elements more quickly than at lower oxygen concentrations and fluxes. Another is that decarburization of the surface affects the activities, where an increased Mn activity coefficient is matched with a similar reduction for most trace elements. For P and Fe the opposite is the case however, and the sharp increase at particularly 50% O_2 indicates that they are more likely to transfer to the dust from the metal when oxygen reaches the surface. It is notable that the trend in either case is towards the concentration in the metal however, which could indicate that the higher oxygen content reduces the bias in fume concentrations compared to the metal concentration that is present particularly in the experiments with the lower oxygen concentrations in the gas.

Figure 4.14 shows a SEM image of typical dust particles from an experiment with 3l/min flow rate of synthetic air, showing the structure of the particles. These are primarily cF8 MnO-crystals, given that more than 90wt% of the dust, excluding oxygen, is manganese. The green color of the dust from the filters matches the characteristic green color of MnO-crystals.

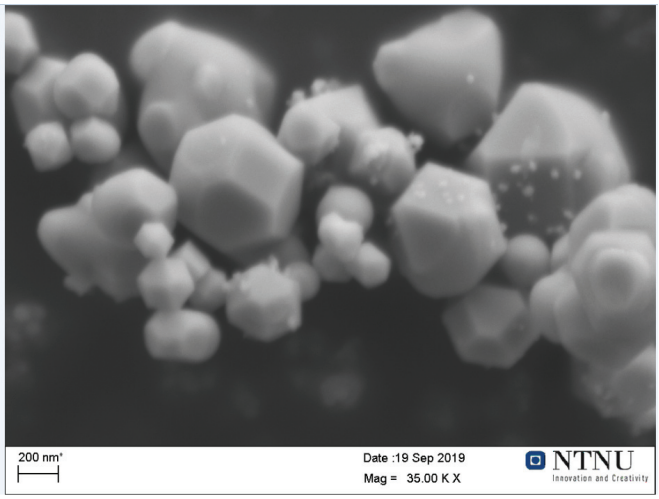

Figure 4.14: SEM picture of filter dust particles from an experiment with 3l/min flow rate of synthetic air.

4.2 Distributed dust sensors field tests

In this section, results from the three dust measurement campaigns performed at an SiMn, Al, and MG-Si production plant are presented along with discussions of the results. The results from all three campaigns are discussed in each subsection, with the measurements themselves being presented first, followed by a focus on spatial variations, comparisons with the reference equipment, deviation between sensors, and finally statistical reliability and the reliability of the sensors themselves.

4.2.1 Dust load variation, size fractions, and process events

Of the three measurement campaigns, precise data for the process events nearby was only obtained for the Al-campaign, and a 24-hour period with 9 marked process events are shown in Figure 4.15. The process events marked here are listed in table 4.2.

Every single noted process event matches a peak in the dust measurements, although some of the peaks are rather small compared to the largest ones. There are many peaks that does not match any of the noted events, but as only the events related to the two cells directly below the sensor were provided, there are many events happening close enough for the sensors to pick up on the increased fuming from those as well. Outside the notable peaks, the baseline PM levels are near 0 with a spread of peaks smaller than 100 μg/Nm^3 that likely are related to events happening on either side of cell 148 and 149.

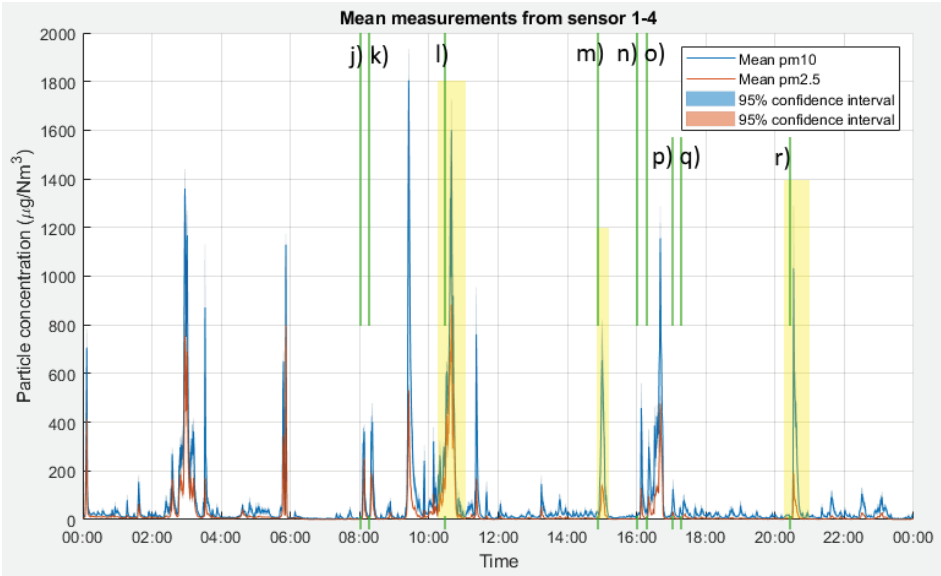

Figure 4.15: Mean values of PM10 and PM2.5 for sensors 1-4 over the course of the second day. 95% confidence intervals are shown as a shaded area above and below the mean values. Three peaks are highlighted, with Figure 4.16 showing the difference in size fractions between these highlighted peaks. The lines labeled j)-r) refer to the actions listed in Table 4.2.

Table 4.2: The recorded processes performed on the two cells (148 and 149) below the sensors. The labels match the lines marked in Figure 4.15.

Time	Event	Cell	label	peak (μg/Nm^3)
08:02	Covering after anode exchange	149	j)	380
08:14	Cutting for anode exchange	148	k)	400
10:39	Anode exchange	148	l)	1600
14:54	Covering after anode exchange	148	m)	650
16:02	Drilling of tapping hole	149	n)	460
16:14	Drilling of measurement hole	148	o)	300
17:04	Measuring	148	p)	130
17:17	Tapping	149	q)	90
20:29	Covering of measurement hole	148	r)	1030

Three of the periods in figure 4.15 are highlighted, and Figure 4.16 shows the difference in size fractions over each of these highlighted peaks.

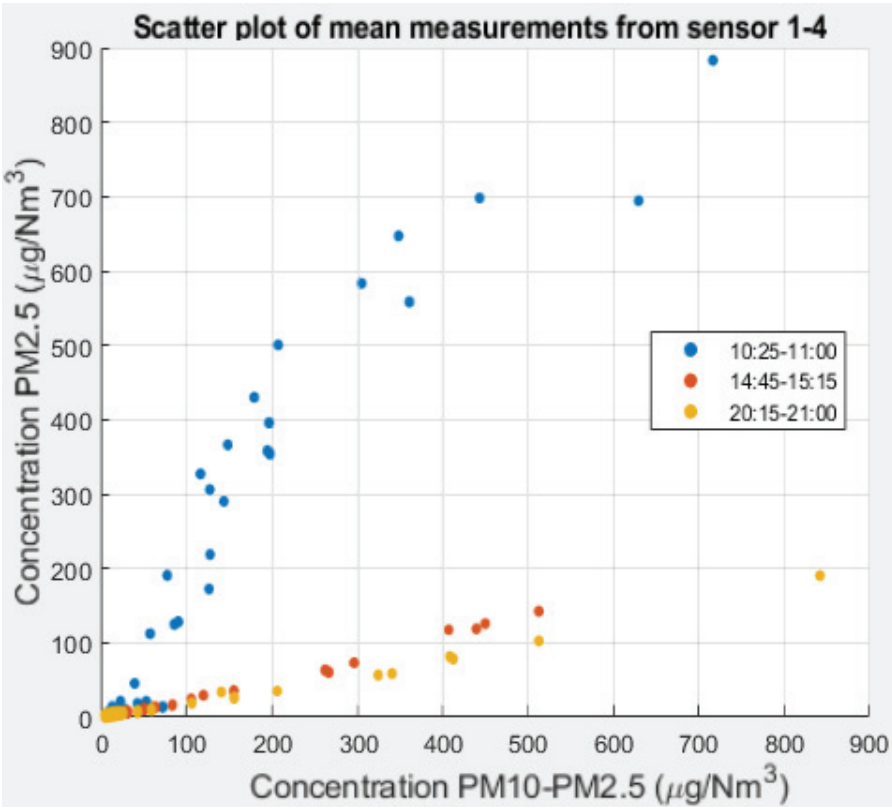

Figure 4.16: Mean values of PM10 and PM2.5 for sensors 1-4 for three limited time periods. The values for PM10 minus the value for PM2.5 is shown on the x-axis and the values for PM2.5 are shown on the y-axis. Each color corresponds to measurements from a specific time period, which relates to a specific process as shown in Table 4.2

.

The difference in particle size fractions are clearly visible, with the first peak relating to an anode exchange has a much larger fraction of PM2.5 than the other two peaks relating to the covering after anode exchange and of a measurement hole.

This clearly shows that the sensors pick up on the rapid changes in PM levels when different events are happening below, which speaks to the usefulness of such a setup for areas where varied fume-producing processes are carried out regularly. It's possible to monitor which event types produce the most PM in general, and which produce the finer fumes. Such knowledge and a constant monitoring can be vital tools when assessing measures and routine changes in regards to their ef-

ficiency in reducing PM, or when deciding when and where it is most efficient or necessary to implement changes.

Where it is not possible to relate dust intensity directly to process events, a different tool that can be useful to look at is the diurnal patters that emerges after measuring for an extended period. Figure 4.17 shows the diurnal pattern from the campaign at the SiMn-plant, along with the 95 % confidence interval, calculated using data that was smoothed both lightly and heavily.

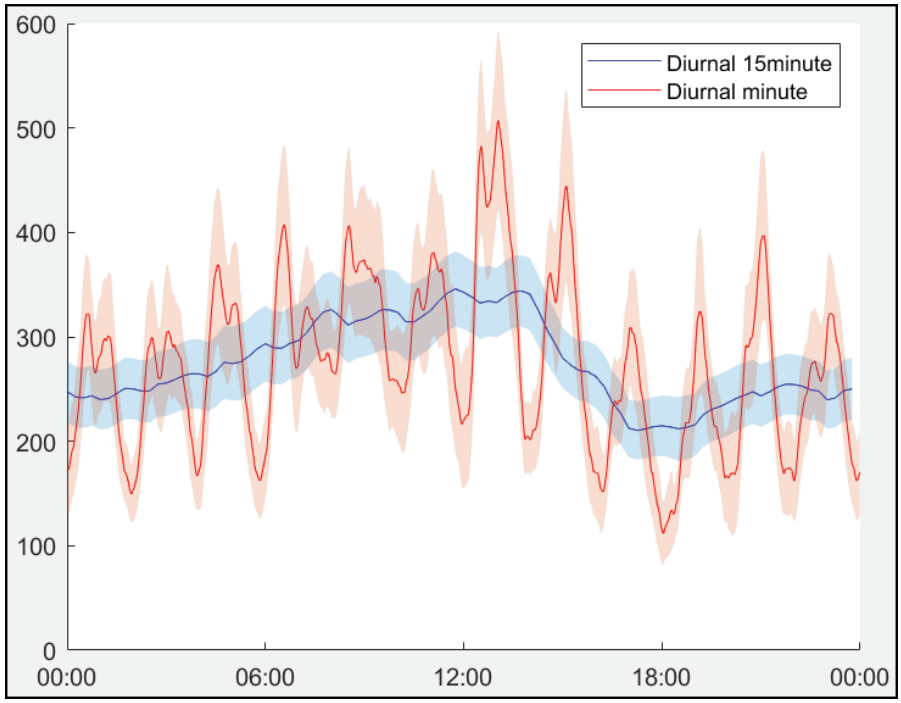

Figure 4.17: Diurnal pattern of the PM10 as measured by 4 Nova sensors over a period of around one month in the SiMn-plant. The data was gathered in 15- and 1-minute averages which were in turn smoothed with a sliding average spanning 6 hours and 30 minutes total respectively. The shaded area show the 95% confidence interval for the **70** days of averaged data.

A pattern emerges where one can note how the PM levels are highest around noon and lowest in the evenings. There is also a pattern of peaks every 2 hours over the course of the day, and this could possibly be related to process routines such as tapping, casting, product transportation, stoking, etc. that are relatively stable on a day-to-day basis. It is similarly possible to create a pattern comparing PM2.5 and

PM10 to look at the times of day where there is the most fine particles in an area of the plant. With such a pattern available, it could be possible to have an automatic system which aimed to curb these regular peaks for instance by controlling hall wind.

While it was not performed during these test campaigns, it is possible to have groups of sensors placed around a plant to monitor spreading from known emission points, for instance following the marked sources in the high silicon alloy production shown in Figure 2.3. With a system for reporting what events are performed at which times, and scattered sensors around the emission sources, one could get an accurate picture of which processes produce what levels of PM and to what degree and how fast the fumes spread from the emission point. This could allow for improved efficiency in dealing with the problem of PM emissions and exposure.

4.2.2 Deviation from sensor location

Both at the SiMn- and the Al-plant, sensor groups were placed a certain distance apart as seen in Chapter 3. In both cases the measurements were performed in the same room with only a few meters separating the groups. Figure 4.18 and 4.19 show the mean and 95% confidence interval for each of the 3 groups of 4 sensors over a shorter period where individual dust peaks can be studied:

For both cases it can be seen that the location has a large impact on the PM concentrations measured over each peak despite the sensor groups being in the same room with only a few meters between each group. By looking at the 95% confidence interval for each group which are not large enough to encompass the values from the other groups, it can be concluded that the differences in measurements are statistically significant. It must also be noted that it varies which group measures the most dust over each peak, which means it's not possible to generate a simple formula for extrapolating the PM concentrations in the rooms just from a single sensor. The importance of multiple sensor locations can as such not be ignored if an accurate representation of the PM levels in an area is desired.

4.2.3 Fidas comparisons

To verify the quality of the measurements done by the Nova sensors, the state of the art PM measuring equipment Fidas200s was used as a reference equipment for two of the campaigns. Figure 4.20(a) to 4.21(b) shows the Nova and Fidas measurements for PM10-PM2.5 and PM2.5 over a day and night at the Si- and SiMn-plant, while Figure 4.22 a-d shows scatter plots comparing the Nova to the

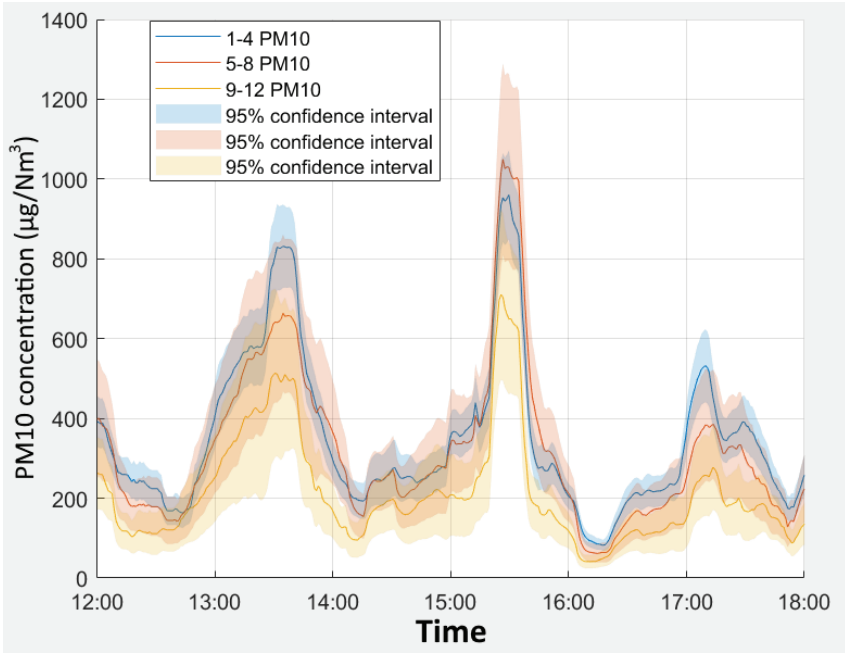

Figure 4.18: Mean values and 95% confidence interval for each sensor group for six hours during the SiMn measurement campaign.

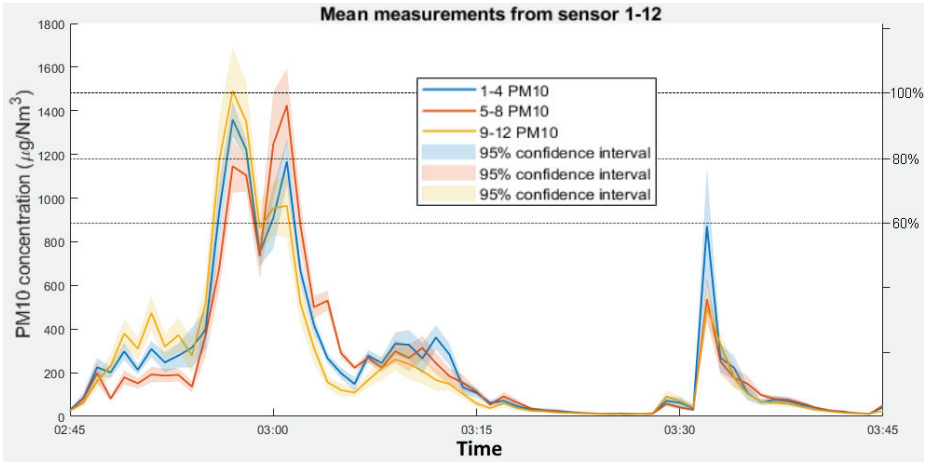

Figure 4.19: Mean values and 95% confidence interval for each sensor group for one hour during the Aluminium measurement campaign. The right hand y-axis is normalized with respect to the highest value measured in this period for easier comparison.

Fidas measurements for the same periods.

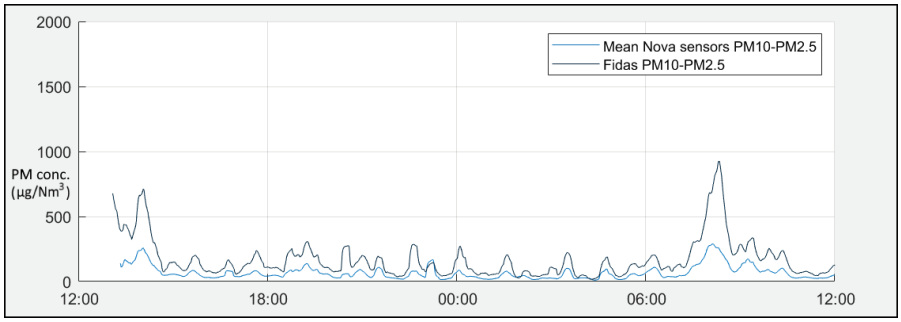

(a)

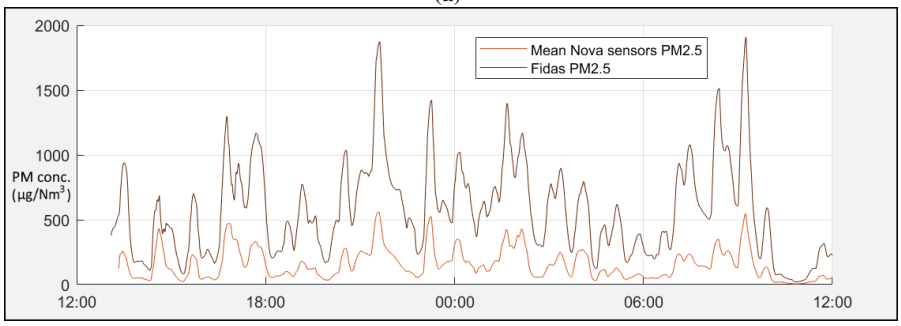

(b)

Figure 4.20: PM10-PM2.5 (a) and PM2.5 (b) as measured by 35 Nova sensors and the Fidas sensor over a period of 24 hours in the Si-plant. The data was gathered in 1-minute averages which were in turn smoothed with a sliding average spanning 15 minutes total. Mean values for the Nova sensors are shown together with the 95% confidence interval and the Fidas values.

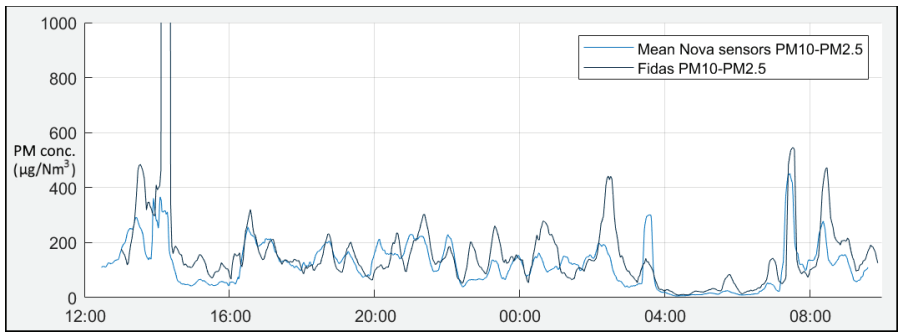

(a)

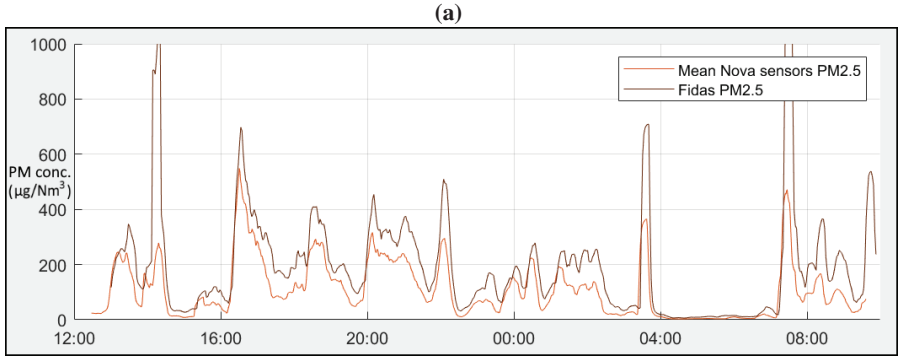

(b)

Figure 4.21: PM10-PM2.5 (a) and PM2.5 (b) as measured by 12 Nova sensors and the Fidas 200S over a period of 21 hours during the final calibration period at the SiMn-plant. The data was gathered in 1-minute averages which were in turn smoothed with a sliding average spanning 15 minutes total. Mean values for the Nova sensors are shown together with the 95% confidence interval and the Fidas values.

From these plots, several things are worth noting:

- The Nova and the Fidas measures mostly all the same changes in PM levels, but the exact value can vary significantly between them.
- The deviations in measured PM concentration between the Fidas and the Nova is much larger at the Si-plant compared to the SiMn-plant.
- The deviation between the Fidas and the Nova in PM2.5 is mostly linear for both plots, but with some more scatter at the Si-plant.
- The PM10-PM2.5/PM2.5 particle ratio is mostly linear at the SiMn-plant, but curves and scatters somewhat at the Si-plant, where also the largest fraction of data points are below 0.

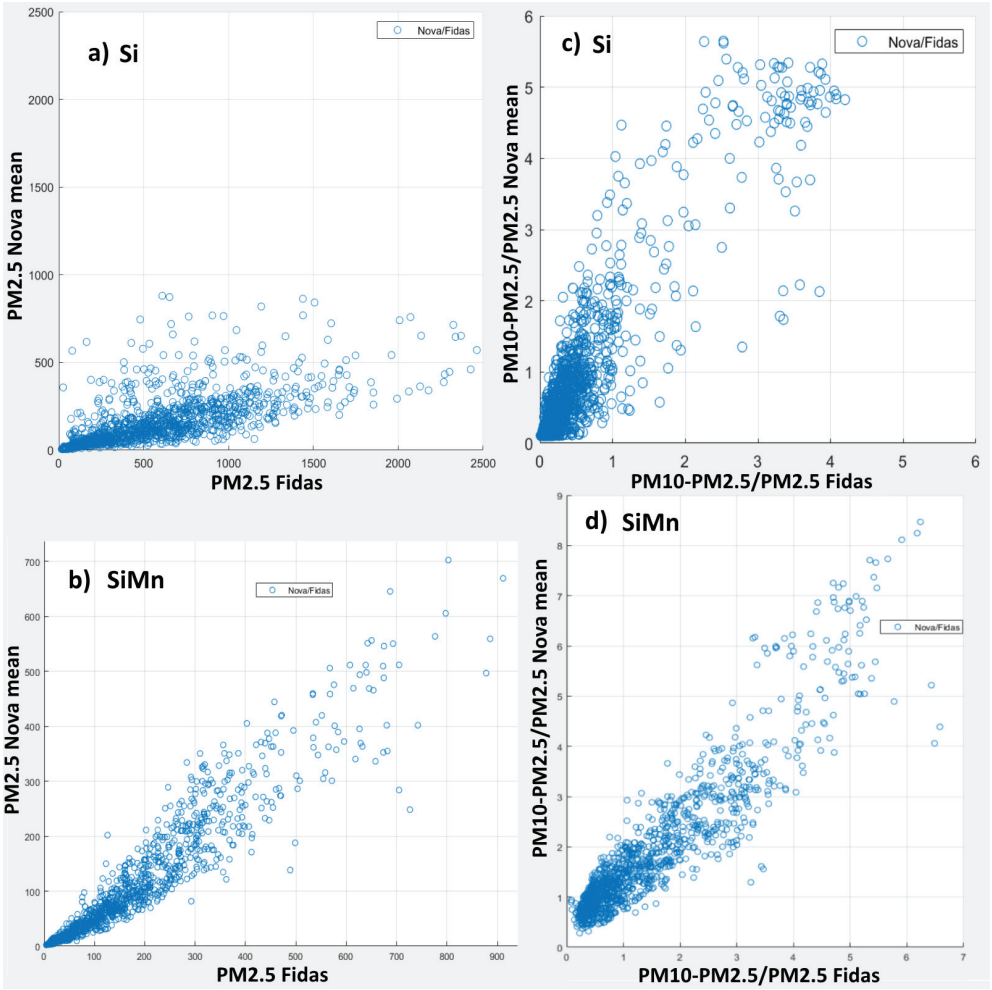

Figure 4.22: Nova measurements compared to Fidas measurements over a 24 and 21 hour period at the Si- and SiMn-plant respectively. Plot a) and b) shows the PM2.5 comparisons, while plot c) and d) show the comparison of the ratio of larger particles (PM10-PM2.5) to the smaller particles (PM2.5).

The larger difference in especially PM2.5 measurements at the Si-plant are believed to be due to better calibration for the Fidas, which was calibrated towards SiO_2 and should as such have quite accurate assumptions for particle density and to some degree the optical properties. This difference is likely due to the lower average particle size of the fumes at the Si-plant as can be seen in Figure 4.20(b). Due to the Nova not being able to effectively "see" particles above 1.7μm in diameter, and instead estimating PM10 values based on its calibration settings as mentioned

in section 2.3.2, the much larger fraction of PM10 reported by the Nova can be a result of it overestimating the larger particles when in reality the fraction of large particles is much smaller than it was calibrated for.

4.2.4 Internal deviation between sensors in a group

Figure 4.23 shows the relative deviation to mean for the four sensors in group 1 over the course of 2 months at the SiMn measurement campaign, while Figure 4.24 shows the same data adjusted by multiplying with a factor corresponding to its average deviation from the mean value. Figure 4.25 shows the measurements of four groups of five sensors during calibration performed at NTNU using a particle generator, with additional graphs showing the values adjusted in the same way.

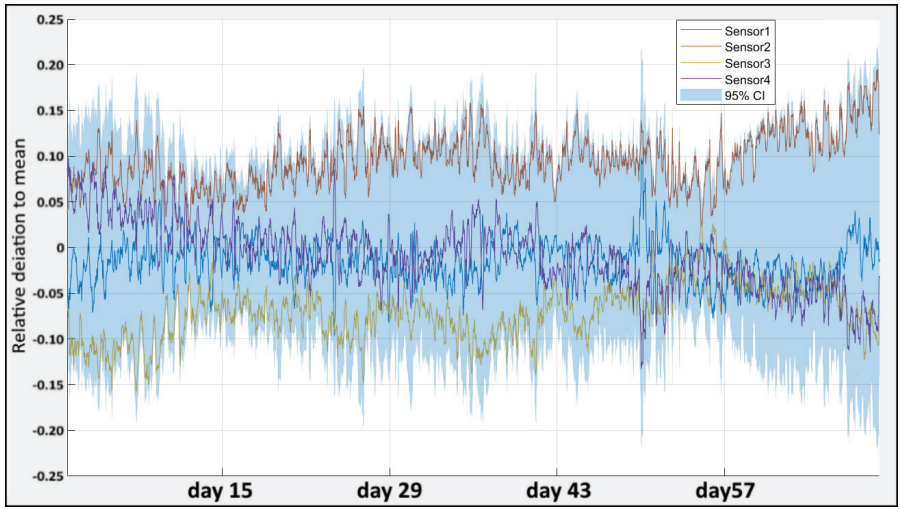

Figure 4.23: Relative deviation to the mean PM10 values for the first group of Nova sensors over a 2-month period of the measurement campaign at the SiMn-plant together with the 95% confidence interval for the dataset.

Both data sets show how the variation between sensors in a group are overall stable enough that doing a simple factor adjustment reduces the spread significantly. It is important to take note of any trends over time however, such as Sensor 4 in Figure 4.24 which seems to trend overall negatively over the course of the 2 months. Such drift over time could signs of sensor deterioration in some form, for instance that an inlet is getting partially clogged over time. Such adjustment has shown to be of great value when the sensor calibration is off, despite potential methodology deficiencies.

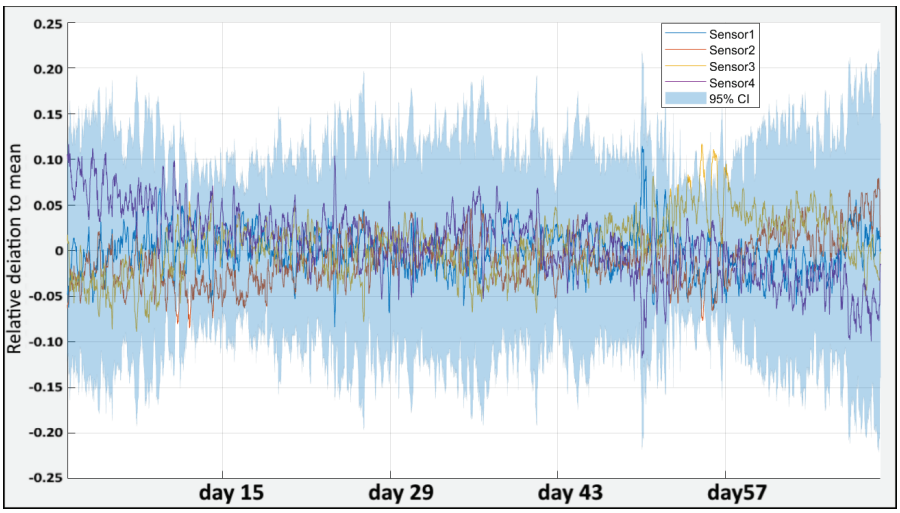

Figure 4.24: Relative deviation to the mean PM10 values for the first group of Nova sensors over a 2-month period of the measurement campaign at the SiMn-plant, adjusted by multiplying the values from each sensor by its average deviation from the mean, together with the 95% confidence interval for the original dataset.

When not considering the time aspect of the internal deviation, the data can be shown in an X/Y-plot for better comparison. Figure 4.26 to 4.28 show the PM10 values measured by individual sensors compared to the mean value measured by all sensors at the same location for the entire measurement campaigns at the SiMn and Si plants, limiting the selection from the Si plant to 8 sensors that well represent the various results seen from that measurement campaign:

The plots made with data from the SiMn-plant show a very small deviation between the sensors, with the slight deviation to each side being most notable near the range of 800-1600 μg/Nm^3. The discrepancy near the highest and lowest PM values measured were all very closely packed, showing that the deviation is most notable in the middle region, which could be due to fast changes in PM levels being picked up at slightly different times by each sensor, leading to deviation at times when the fume concentration is changing between the high and the low extremes.

For the plots made with data from the Si-plant, the results are more varied, with some sensors showing mostly very tightly packed comparisons near the 1:1-line, while for others there are large spreads or even clear "splits" where the sensor over-measures for some duration and under-measures at other periods. It is also possible to see in Figure 4.28 that Sensor 19 started measuring much lowers for the

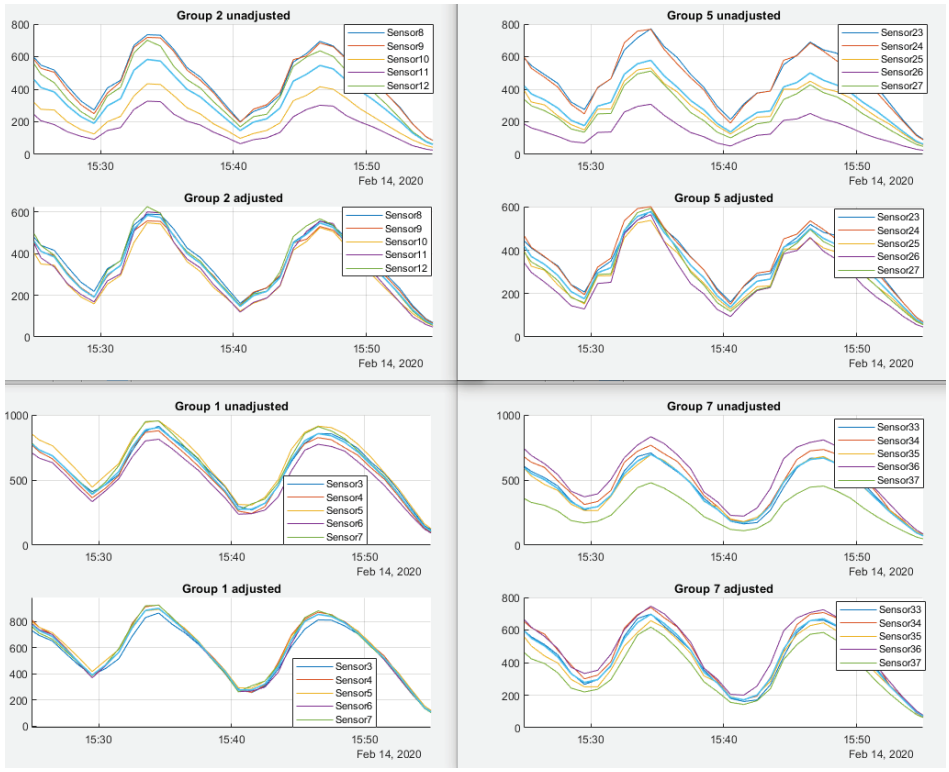

Figure 4.25: Relative deviation to the mean PM10 values for four group of Nova sensors over half an hour during calibration performed at NTNU with a particle generator, together with the same data sets adjusted by multiplying the values from each sensor by its average deviation from the mean.

final few minutes before shutting down, as noted by the three singular dots away from the main line.

The larger spread between the Nova sensors at the Si-plant is likely also due to the factory calibration being ill-suited for Silica fumes, although details from the manufacturer on how the calibration was performed were not acquired despite several attempts at contact. The calibration was likely particularly bad for PM10, which allowed for smaller errors to propagate when the sensors tried to calculate the values from the amount of smaller particles that were detected. There was also many sensors that stopped working during the measurement campaign, and several sensors could have been giving more erroneous data as time passed before they shut down completely, which is discussed further in the following subsection.

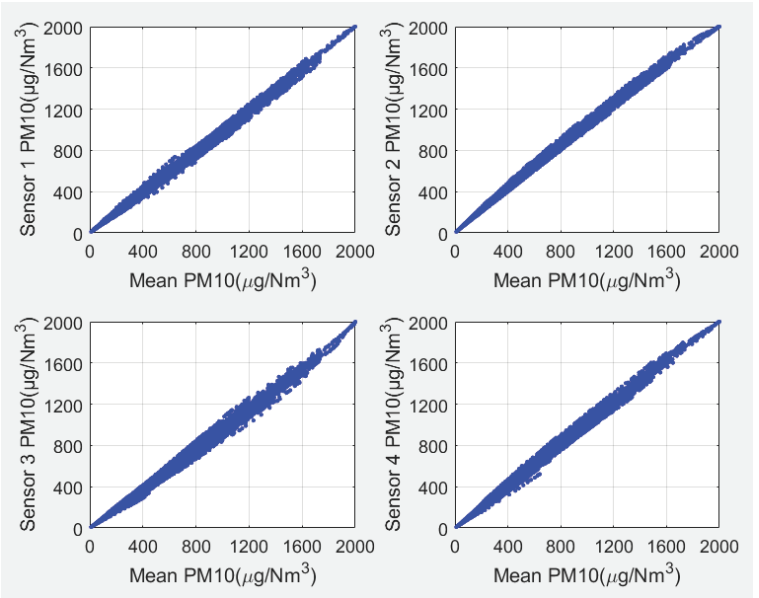

Figure 4.26: PM10 values for individual sensors compared to the average for all sensors at the same location for the measurement campaign at the SiMn-plant.

When looking at the sensors where there were no particular problem showing in the plots, the spread was mostly quite low, and it is believed that with good calibration and protection that increases reliability as will be discussed in the next section, the Nova sensors will have results much more similar to those from the SiMn-plant.

4.2.5 Sensor reliability

During the three measurement campaigns, the reliability of the sensors were very different. At the SiMn plant, 12 sensors were used and the mean up-time of the sensors was almost 100% with all sensors working as they should at the end of the 3-month campaign. 3 of the sensors started measuring significantly lower after some time however, the believed cause being a partial clogging of the extended inlet tube used in that campaign, which was supported by the fact that blowing through the tubes at the end of the campaign caused the sensors to measure about the same again afterwards. At the Al plant, 12 sensors were also used and the up-time was similarly almost 100% with all sensors working at the end of the 2.5-month campaign. In both campaigns however, power shutdown caused the entire setup to be down for some longer periods as the restart system didn't yet function as intended and a manual restart was required. As the measurements continued

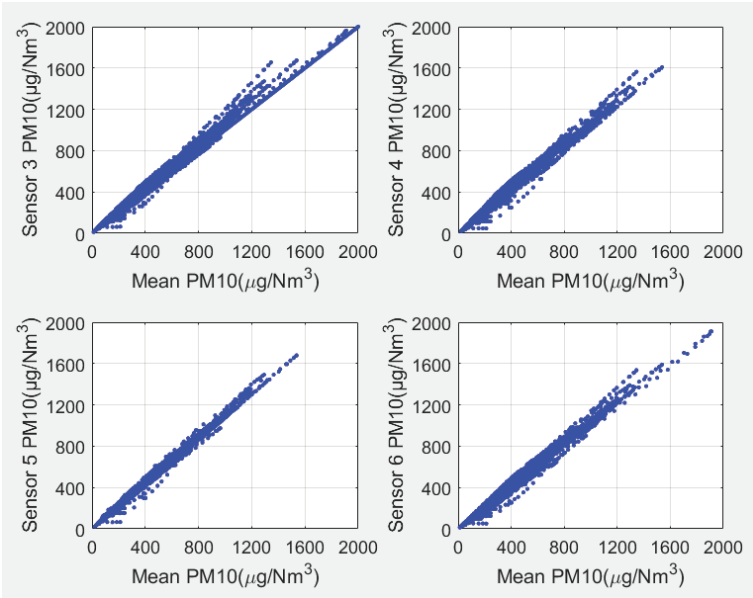

Figure 4.27: PM10 values for individual sensors compared to the average for all sensors at the same location for the measurement campaign at the Si-plant.

immediately after the minicomputer and the router was restarted, it is safe to assume that the sensors were working as intended also during this down-time. At the Si-plant however, where 35 sensors were used, the up-time was only 21.7% on average during the 1-month campaign, after removing 6 sensors that gave erroneous data instead of no data when failing. At the lowest, for a time only 2 sensors were sending correct data, but restarting and cleaning the dust inlet with pressurized air had a beneficial effect and allowed up to 15 of the non-responsive sensors to start providing data again. The number of active sensors would begin to fall again after a while however going down to 3 again by the end of the campaign, and continuous cleaning and restarting was not possible. A system to force regular restarts of the sensors has been added after the last campaign, which could alleviate some of the problem at least.

The results from the Al and SiMn campaigns clearly shows that dust in itself, even when the sensors and the electronics is poorly protected, is not enough to shut the system down. The case was very different at the Si-plant. As has been shown in the previous sections, the Si-based fumes have a much larger percentage of smaller particles compared to SiMn and Al-based fumes, which may be the reason for the large degree of electronics failure here. Another possibility is that the Si-based

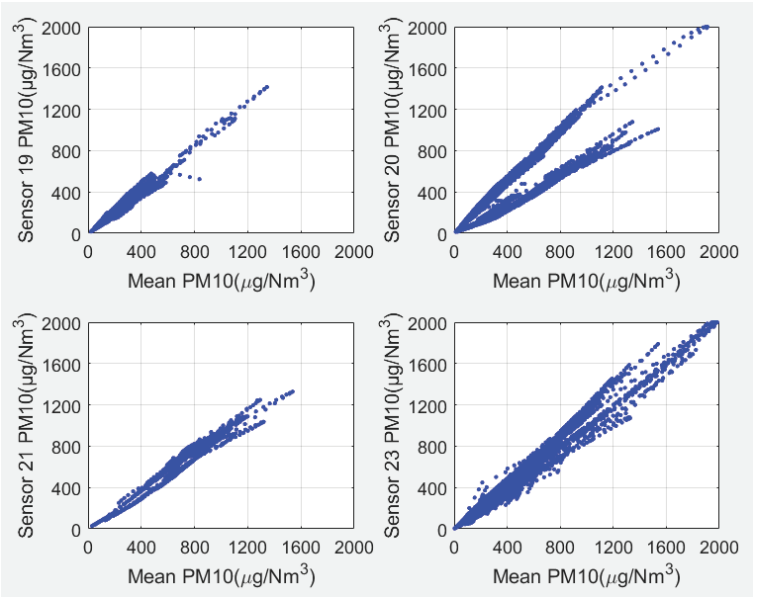

Figure 4.28: PM10 values for individual sensors compared to the average for all sensors at the same location for the measurement campaign at the Si-plant.

fumes have electrical properties that causes errors in the currents between the pins or other components on the microchip, which is supported by the fact that sensors were found to provide erroneous data and not just shutting down. In either case, protecting the components completely from the dust should remove the problem.

The highest measured relative humidities were below 40% at the SiMn-plant, below 45% at the Si-plant, and below 25% at the Al-plant, which are all significantly lower than the boundary of around 80% RH where condensation causes inflation in the PM readings for the Nova and is as such not considered to have influenced the PM readings in this work.

4.2.6 Statistical reliability

Despite the low average sensor up-time at the Si-plant, the amount of data available was still sufficient to perform statistical analysis. Particularly for the periods at the Si-plant with the lowest amount of sensors running however, the data must be considered with that in mind.

All data points from each sensor were first gathered into 1-minute averages that were smoothed with a sliding average over 30 minutes. For the longer periods the data was gathered in 15-minute averages that were smoothed over 6 hours. The statistical analysis was performed by calculating standard deviation and the following 95% confidence interval using the data for all sensors at the approximately same location. The 95% confidence interval generally was in the range of +/- 10-20%, but as mentioned in the previous section, this was in large parts due to calibration differences between the sensors which can be adjusted for. The remaining deviation within groups is to be expected as the sensors will never measure exactly the same air, and the local variations can only be truly removed from the data by sufficiently smoothing the data.

When comparing the Nova to the reference equipment there were large differences, but these too were relatively stable over time and presumably in large parts due to calibration differences. The differences in the lower particle diameter range must be considered in all cases however, and more importantly, so must the low maximum particle size detected by the Nova. Doing size analysis on the fumes could allow for extrapolation of data and estimation of fume levels below and above the measured range, but a more reliable and simple method would be to perform proper calibration of the sensors using the same fumes as are to be measured. This would have to include simultaneous measurements using gravimetric methods measuring both PM10 and PM2.5 beside the Nova sensors for a set period near each major fume source.

When calibration has been thoroughly performed, deviation between sensors after smoothing must come from extremely local, yet stable, differences in PM concentrations, or from a difference in sensitivity between sensors. By swapping sensor locations during calibration the former can be confirmed or rejected, and differences in sensor sensitivities can be considered for post-processing adjustments once all other factors have been evaluated.

Chapter 5

Conclusions

5.1 Experimental work and modelling of Mn evaporation

In order to better understand the kinetics of fume/dust formation in the Mn-ferroalloys production industries, experiments investigating the evaporation rate and diffusion of pure Mn in an argon atmosphere at temperatures from 1400 to 1700°C and flow rates from 0 to 1 l/min, have been carried out.

Experimental work was performed to better understand the kinetics of fume/dust formation in the Mn-ferroalloys production industries. Both the evaporation rate and diffusion of pure Mn, under an argon atmosphere, were investigated between 1400 to 1700°C, and at gas flow rates up to 1 l/min. The experimental results were further compared with predictions from a proposed mathematical model of the system. From this work, the following conclusions may be drawn:

- In a small scale experimental system, simple flow models are not sufficient to calculate evaporative mass transfer from the metal surface, as long as the gas is delivered in the form of an impinging jet into a small crucible.

- Using Comsol to model the flow and mass transfer, while assuming equilibrium Mn vapor pressure at the surface, gave evaporation results very much in line with the experimental results.

- Linear interpolation over the measured values for flow rates of 0.01, 0.1, 0.25, 0.5, 1, 1.5, and 2 l/min gave R^2-values above 0.997. Models fits proportional to (flow rate)$^{0.5}$ or (flow rate)$^{0.75}$ did adequately reflect the experimental results.

- Pure Mn(l) exhibits fast evaporation rates at temperatures above 1400C. It was calculated that for the evaporation rate to be equal the diffusion rate, the partial pressure of Mn(g) at the surface must be above 99.9% of the equilibrium partial pressure

- The proposed model predicts that a temperature increase in the metal from 1400 to 1550C, and from 1550 to 1700C, both increased the flux by a factor 3 to 4. This was somewhat higher than the measured values between 1550 and 1700C.

5.2 Experimental work and modelling of fume formation from HCFeMn

A model for oxidation-enhanced evaporation based on the work of Rosner (26), was compared to experimental results for the fuming rates of high carbon ferro-manganese at 1550°C, blown with air at oxygen concentrations from 0 to 50 vol% and flow rates from 0 to 5 l/min. Dusts captured in these experiments was also analysed with ICP-MS, LD, and SEM, to locate and quantify the species present in said dust, and to determine the size distribution of the dust particles. From this work, the following conclusions may be drawn:

- The measured fuming flux follows the theoretical predictions by Rosner, up to a critical O_2 concentration before tapering off. This flux ceiling occurred at approximately twice the theoretical evaporation rate-limit, given a carbon-saturated bulk-alloy composition at the metal surface.

- Several theories for the high flux measured were presented, with the most notable being an increased Mn activity at the surface compared to the bulk phase. This was concluded to occur due to a weakening of the carbon-manganese interactions at the surface due to a decrease in surface carbon content. The reduction in surface carbon content is likely due to surface oxidation/decarburization.

- The concentration of most trace elements (Zn, Mg, Pb, Na, S, and Al) in the PM decreased with increasing oxygen concentration in the bulk gas. This is believed to be due to the surface concentration being lowered when high oxygen content in the bulk gas causes an increased fuming flux. Another possible contribution is that decarburization of the surface increases the Mn activity which causes a correlating decrease in activity for the trace elements.

- Iron and phosphorous content in the dust both rose sharply at the highest oxygen concentrations. In the metal, a strong affinity between iron and phosphorous leads to iron affecting the phosphorous vapor pressure (106).
- The average size for both particle clusters (0.59-6.01μm) and individual oxide particles (0.11-1.01μm) correlate closely across varying gas flow rates and oxygen concentrations, with the average radii of the clusters being around six times greater than that of the individual particles for each set of parameters where measurements were done.
- Higher flow rate was found to have a strong effect towards reducing both individual and cluster particle size, with the mean cluster size had a near linear correlation with the inverse of the inflow velocity at a slope of almost 4.5 μm per s/m.
- Higher oxygen concentration in bulk gas was found to have a strong effect towards increasing particle size at low flow rates, but had a very small effect at higher flow rates.

The industrial implications of these findings are:

- The validation of the proposed models' makes it possible to better estimate the amount of fumes generated, which allows more efficient refining and ventilation systems to be designed.
- Carbon has a strong negative effect on the activity coefficient of manganese, and as such affects the fuming rate of Mn-alloys. With low carbon content at the surface, either due to low carbon content in the alloy, or through decarburization of the surface, the activity of manganese is strongly increased, which increases fuming rates.

5.3 Distributed sensor system

A low-cost PM sensor for PM2.5 and PM10, Nova PM SDS011, was tested and benchmarked towards the state-of-the-art PM sensor Fidas 200S during two measurements campaigns at a silicomanganese and a silicon metal production plant where 12 and 35 Nova sensors in groups of 4 and 5 were used respectively. A separate measurement campaign at an aluminium plant with 12 Nova sensors in groups of 4 and no reference equipment was also performed. The long term data (1 month and longer) for the Nova sensors were studied in regards to deviations within each group and to investigate the differences between the plants. Short

term data (around 24h) with both sensor types was studied to compare the deviation between the sensor types both for PM10-PM2.5 and PM2.5. More detailed size fraction comparisons were compiled from the Fidas data, highlighting the difference in size fraction between SiMn and Si fumes. Systematic variation in measurements from small spatial differences and between PM concentration peaks originating from different process events were studied from the campaign at the aluminium plant.

Following are the main conclusions inferred within each category previously discussed:

- Fumes from different processes and events vary widely in the measured properties, which indicates either size fraction differences or major differences in optical properties.
- Over time, clear diurnal patterns emerge which show when the greatest amount of fuming occurs during each day.
- For measurements in both SiMn and Si production plants, the Nova sensors picked up on almost all the same peaks as the Fidas sensor, and the increases and decreases in fume levels are similarly captured by both sensor systems.
- The PM2.5 measurement comparison between the Nova and the Fidas at the SiMn plant showed a small spread and an linearity close to 1:1, with a small deviation towards the Nova measuring less than the Fidas. The same comparison at the Si plant showed some more spread, and a linearity around 1:5 with the Fidas measuring around five times as high values for PM2.5 overall. This is believed to be in part due to the Fidas being well calibrated for SiO_2 and also able to detect particles in the size range on 180-300nm, which the Nova cannot. In addition, the Nova factory calibration is possibly not adequate to accurately measure the SiO_2 fumes, although repeated attempts at getting these details from the manufacturer was unsuccessful.
- The relation between Nova and Fidas for larger particles (PM10 - PM2.5) divided by smaller particles (PM2.5) is strongly clustered and show linearity close to 1:1 for the measurements at the SiMn plant. For the measurements at the Si plant, this relation is more spread and with the Nova sensors measuring an on average much higher fraction of larger particles. This is believed to be due to the Nova overestimating the fraction of the larger particles (>1.7μm) it cannot measure directly, which becomes prevalent with the overall low concentration of larger particles in the Si fumes.

- Deviations within each group of Nova sensors and between groups for both the SiMn and Si-campaign showed a relatively stable deviation from the mean value. Given a stable deviation over time, it would be possible to compensate for the internal deviation of the Nova sensors through a calibration period to get a much lower measurement spread. For most groups the spread was within +/- 20% relative deviation, close to the 15% relative deviation level provided by the manufacturer.

- The Nova sensors were able to measure clear differences in optical properties (Particle sizes or otherwise) of fumes originating from different process events at the Aluminium plant. They also measured systematical differences across each concentration peak based on spatial variation.

- For future industrial measurements campaigns, an improved and preferably airtight casing for the Nova system is considered important to improve length of life, and it is believed that using 4-5 sensors in each group to have room for 1-2 failures before service and potential replacements are needed would provide sufficient lifetime for the system as a whole to not cause unnecessary expenses in this regard.

The industrial implications of these findings are:

- The fumes from different metallurgical processes and other fume sources vary widely and as such, sensors must be calibrated accordingly.

- Given good individual calibrations, the Nova sensors are believed to be well suited as a low-cost option for measuring the PM concentrations in various parts of both SiMn-, Si-, and Al-plants. The PM2.5 measurements were found to be particularly solid, with PM10 being more reliant on good calibration and unchanging size fractions within the fumes.

- A system of two filter samplers for gravimetric measurements of PM10 and PM2.5 placed alongside groups of Nova sensors near each fume source is believed to provide a strong foundation for reliable measurements. Regular checks with calibration equipment to look for drift and other changes that can occur over time is recommended.

- Small spatial variation can give large variation in fume concentration, which must be taken into account when estimating exposure and emissions.

Chapter 6

Future work

It is recommended that experimental studies and modelling of the fuming from SiMn alloys is carried out in accordance with the current study. In addition, expanding the range of flow rates to where modelling on the effect of flow conditions on the current FeMn system can be done more extensively, is recommended. Additionally, doing experiments with no carbon present in neither the alloy nor the crucible would be vital to validate the theory of decarburization, which is of particular interest.

The sensor system needs two things to function properly in varying metallurgical locations: 1) Good calibration for PM10 and PM2.5 with each specific type of dust particles to be measured, and 2) a casing that protects the components from the fumes. For calibration, using filter samplers with a sampling inlet that limits particles above 2.5 and 10μm alongside groups of sensors near each fume source is proposed as a good calibration method. An improved casing to protect the sensor system has been designed, and using epoxy to encase the most vulnerable components is proposed to provide additional protection. Testing the system in various environments after implementation of the improved casing and with gravimetric calibration equipment at hand, alongside a well calibrated reference sensor such as the Fidas 200S, is suggested to validate the system for continued industrial measurements. In addition, future academic work towards setting the system up to be used systematically alongside a dust spreading model is also recommended.

Bibliography

[1] Contrec (2020) *Fine dust measuring instrument model Fidas® 200 S*. Contrec, Technology in Science and Health. https://www.contrec.ch/en/fine-dust-measurement-devices/feinstaubmessgeraet-modell-fidas-200s-3, accessed 24.11.2020

[2] Liu H-Y, Dunea D, Iordache S, Pohoata A (2018) *Review of Airborne Particulate Matter Effects on Young Children's Respiratory Symptoms and Diseases.*. Atmosphere 2018, 9, 150.

[3] Liu H-Y, Bartonova A, Schindler M, Sharma M, Behera SN, Katiyar K, Dikshit O. (2013) *Respiratory Disease in Relation to Outdoor Air Pollution in Kanpur, India.*. Arch. Environ. Occup. Health 2013, 68, 204–217.

[4] Johnsen HL, Søyseth V, Hetland SM, Saltyte-Benth J, Kongerud J (2008) *Production of silicon alloys is associated with respiratory symptoms among employees in Norwegian smelters*. International Archives of Occupational and Environmental Health 81(4) p.451-459

[5] Johnsen H. L. (2009) *Lung function, respiratory symptoms and occupational exposure* PhD-thesis, Faculty of Medicine, University of Oslo, 2009

[6] Hobbesland Å, Kjuus H, Thelle DS (1997) *Mortality from cardiovascular diseases and sudden death in ferroalloy plants*. Scandinavian Journal of Work, Environment and Health 23(5) p. 334-341

[7] Søyseth V, Johnsen HL, Bugge MD, Hetland SM, Kongerud J (2011) *Incidence of airflow limitation among employees in Norwegian smelters*. American Journal of Industrial Medicine 54 9 p. 707-713 https://doi.org/10.1002/ajim.20946

[8] Gibbs GW, Labrèche F, Busque, M-A, Duguay PL (2014) *Mortality and Cancer Incidence in Aluminum Smelter Workers: A 5-Year Update*. Journal of Occupational and Environmental Medicine 56(7) p. 739-764

[9] Milham S Jr. (1979) *Mortality in aluminum reduction plant workers*. Journal of Occupational Medicine. 21(7):475-80

[10] Eduard W, Lie A (1981) *Influence of fluoride recovery alumina on the work environment and the health of aluminum potroom workers*. Scandinavian Journal of Work, Environment & Health. 7(3):214-22

[11] Bast-Pettersen R, Ellingsen DG, Hetland SM, Thomassen Y (2004) *Neuropsychological function in manganese alloy plant workers*. International Archives of Occupational and Environmental Health 77 p.277-287

[12] Luccini RG, Martin CJ, Doney BC (2009) *From manganism to manganese-induced parkinsonism: a conceptual model based on the evolution of exposure*. Neuromolecular Medicine 11 p.311-321

[13] Racette BA, Aschner M, Guilarte TR, Dydak U, Criswell SR, Zheng W (2012) *Pathophysiology of Manganese-Associated Neurotoxicity*. Neurotoxicology 33 4 p. 881-886 doi: 10.1016/j.neuro.2011.12.010

[14] Wong DS (2013) *Sources of potroom dust emissions from aluminium smelters*. Ph.D. thesis. The University of Auckland

[15] Arnoldussen YJ, Ervik TK, Eriksen MB, Kero I, Skaug V, Zienolddiny S (2019) *Cellular Responses of Industrially Relevant Silica Dust on Human Glial Cells In Vitro* Int. J. Mol. Sci. 2019, 20, 358; doi:10.3390/ijms20020358

[16] Monteiller C, Tran L, MacNee W, Faux S, Jones A, Miller B, Donaldson K (2007) *The pro-inflammatory effects of low-toxicity low-solubility particles, nanoparticles and fine particles, on epithelial cells in vitro: the role of surface area*. Occupational and Environmental Medicine 64 p. 609-615

[17] Obersdörster G (2001) *Pulmonary effects of inhaled ultrafine particles*. International Archives of Occupational and Environmental Health 74 p. 1-8

[18] Schmid O, Möller W, Behnke-Semmler MA, Ferron GA, Lipka J, Schulz H, Kreyling WG, Stöger T (2009) *Dosimetry and toxicology of inhaled ultrafine particles*. Biomarkers, 14 S1 p. 67-73 DOI: 10.1080/13547500902965617

[19] Dockery DW, Stone PH (2007) *Cardiovascular risks from fine particulate air pollution*. N. Engl. J. Med. 2007, 356, 511–513.

[20] Pérez L, Medina-Ramón M, Künzli N, Alastuey A, Pey J, Pérez N, García R, Tobías A, Querol X, Sunyer J (2009) *Size fractionate particulate matter, vehicle traffic, and case-specific daily mortality in Barcelona (Spain).*. Environ. Sci. Technol. 2009, 43, 4707–4714.

[21] Liu H-Y, Schneider P, Haugen R, Vogt M (2019) *Performance Assessment of a Low-Cost PM2.5 Sensor for a near Four-Month Period in Oslo, Norway*. Atmosphere 2019, 10, 41, DOI: 10.3390/atmos10020041

[22] Olsen SE, Tangstad M, Lindstad T (2007) *Production of Manganese Ferroalloys*. 1st ed.; SINTEF and Tapir Academic Press: Trondheim, Norway, 2007; pp. 11–69.

[23] You B-D, Lee B-W, Pak J-J (1999) *Manganese Loss During the Oxygen Refining of High-Carbon Ferromanganese Melts*. Metals and Materials, 1999, 5, p497-502.

[24] Ma Y, Kero I, Tranell G (2017) *Fume Formation from Oxidation of Liquid SiMn Alloy*. Oxid Met, 89, p. 211–231, 2017 DOI 10.1007/s11085-017-9780-y

[25] Turkdogan ET, Grieveson P, Darken LS (1963) *Enhancement of Diffusion-Limited Rates of Vaporization*. Journal of Physical Chemistry 1963, 67, 8, p. 1647-1654

[26] Rosner DE (1972) *Effects of Product Condensation on Reaction Enhanced Vaporization Rates and on the Transition from Homogeneous to Heterogeneous Reaction in High-Temperature Metal Oxidation*. Oxidation of Metals, vol 4, no. 1. p. 1–25

[27] European Comission (2019) *Air Quality Standards*. Website providing european standards, visited september 2020, Link: https://ec.europa.eu/environment/air/quality/standards.htm

[28] European Comission (2017) *Measuring air pollution with low-cost sensors*. Ares(2017) 5883418 - 01/12/2017. Accessed 8. Sept 2019. https://ec.europa.eu/jrc/sites/jrcsh/files/innovative_methods_such_as_sensors_are_being_evaluated_for_their_suitability.pdf.

[29] Whalley J, Zandi S (2016) *Particulate Matter Sampling Techniques and Data Modelling Methods, Air Quality - Measurement and Modeling* Philip Sallis, IntechOpen, DOI: 10.5772/65054. Available

from: https://www.intechopen.com/books/air-quality-measurement-and-modeling/particulate-matter-sampling-techniques-and-data-modelling-methods

[30] Gonser M, Hogan T (2011) *Arc Welding Health Effects, Fume Formation Mechanisms, and Characterization Methods* intechopen, chapter on arc welding, July 2011 DOI: 10.5772/29131

[31] Kero I, Grådahl S, Tranell G (2017) *Airborne Emissions from Si/FeSi Production JOM volume 69, pages365–380(2017)*

[32] Ravary B, Grådahl S (2010) *Improving Environment in the Tapping Area of a Ferromanganese Furnace* Conference: INFACON XII, Helsinki, Finland Volume: Proceedings of the twelfth international ferroalloys congress 2010

[33] Panjwani B, Olsen JE (2019) *Design and Modelling of Dust Capturing System in Thermally Stratified Flowing Conditions* Building and Environment 171:106607 DOI: 10.1016/j.buildenv.2019.106607

[34] United States Environmental Protection Agency (1998) *Background report: primary aluminium* AP-42 SECTION 12.1, November 1998 https://www.epa.gov/sites/production/files/2020-11/documents/b12s01.pdf Visited on 17.02.21

[35] Aarhaug TA, Ratvik AP (2019) *Aluminium primary production off-gas composition and emissions: An overview*. JOM, 71(9), p.2966-2977

[36] Gaertner H, Ratvik AP, Aarhaug TA (2012) *Impurity Elements in Raw Gas Ultra-Fines from Aluminium Electrolysis Cells* Light Metals. 2012, p. 839-844

[37] Wong DS, Tjahyono NI, Hyland MM (2014) *The Nature of Particles and Fines in Potroom Dust*. Grandfield J. (eds) Light Metals 2014. Springer, Cham. https://doi.org/10.1007/978-3-319-48144-9_94

[38] Boullemant A, (2011) *PM2.5 Emissions from Aluminum Smelters: Coefficients and Environmental Impact* Journal of the Air & Waste Management Association, 61(3) (2011), p.311-318

[39] Hoflich BLW, Weinbruch S, Theissmann R, Gorzawski H, Ebert M, Ortner HM, Skogstad A, Ellingsen DG, Drabløs PA, Thomassen Y (2005) *Characterization of Individual Aerosol Particles in Workroom Air of Aluminium Smelter Potrooms* JEM, 7(5) (2005), p.419-424

[40] United States Environmental Protection Agency (1984) *Locating and estimating air emissions from sources of manganese* EPA-450/4-84-007h, March 1984 https://www3.epa.gov/ttnchie1/le/manganes.pdf Visited on 16.02.21

[41] Kamfjord NE (2012) *Mass and energy balances of the silicon process—Improved emission standards* PhD-thesis, Department of Materials Science and Engineering, Norwegian University of Science and Technology, Trondheim, 2012

[42] Næss MK, Olsen JE, Andersson S, Tranell G (2014) *Parameters Affecting the Rate and Product of Liquid Silicon Oxidation*. Oxid Met, 82, p.395–413, 2014

[43] Næss MK (2013) *Mechanisms and kinetics of liquid silicon oxidation*. Doctoral thesis at NTNU

[44] Næss MK, Tranell G, Olsen JE, Kamfjord NE, Tang K (2012) *Mechanisms and Kinetics of Liquid Silicon Oxidation During Industrial Refinig*. Oxid Met (2012) 78:239-251

[45] Wagner C (1958) *Passivity during the oxidation of silicon at elevated temperatures*. Journal of Applied Physics 29, p1295-1297.

[46] Kero I, Eidem PA, Ma Y, Indresand H, Aarhaug TA, Grådahl S (2019) *Airborne Emissions from Mn Ferroalloy Production JOM volume 71, pages349–365(2019)*

[47] M Gasik (2013) *Handbook of Ferroalloys, Theory and Technology*. 2013 Elsevier Ltd., ISBN 978-0-08-097753-9

[48] Ma Y, Kero I, Tranell G (2017) *Fume Formation from Oxidation of Liquid SiMn Alloy*. Oxid Met, 89, p.211–231 DOI 10.1007/s11085-017-9780-y

[49] Factsage, *Factsage 7.3* 2019, http://www.Factsage.com/

[50] Kero I, Slizovskiy D, Wittgens B, Tranell G *Fume Formation From Liquid Ferromanganese*. FLOGEN, Volume 3 (2015)

[51] Kero I, Naess MK, Tranell G (2014) *Particle Size Distributions of Particulate Emissions from the Ferroalloy Industry Evaluated by Electrical Low Pressure Impactor (ELPI)*. Journal of Occupational and Environmental Hygiene, 12:1, 37-44, DOI:10.1080/15459624.2014.935783

[52] Gates SJ, Kero I, Hunsbedt L, Tranell GM. *How water mist alters the fuming rate and particle agglomeration during ferromanganese casting* Infacon XV, Southern African Institute of Mining and Metallurgy (SAIMM) 2018.

[53] Safarian J, Engh TA (2013) *Vacuum Evaporation of Pure Metals* Metall and Mat Trans A (2013) Volume 44, Number 2, p. 747-753 DOI:10.1007/s11661-012-1464-2

[54] Bakken JA, Lobo S, Kolbeinsen L (2009) *Compendium Fluid Flow and Heat Transfer Advanced Course*. Norwegian University of Science and Technology

[55] Lee YE, Kolbeinsen L *Kinetics of Oxygen Refining Process for Ferromanganese Alloys*. ISIJ International Vol. 45 (2005), No. 9, pp. 1282–1290

[56] Gates SJ, Kornelius G, Kero I, Tranell GM. *The Influence of Water Vapour on the Fuming Rate in a Ferromanganese System* Energy Materials 2017, The Minerals, Metals & Materials Series, p73-83.

[57] Aliexpress, HS Electronics LTD (2020) *Product Description Nova PM SDS011*. Website delivering the Nova sensor, visited Sept 2020, Link: https://www.aliexpress.com/item/32617788139.html

[58] Tzarouchis D, Sihvola A (2018) *Light Scattering by a Dielectric Sphere: Perspectives on the Mie Resonances*. Appl. Sci. 2018, 8, 184; doi:10.3390/app8020184

[59] Yong Z *Digital Universal Particle Concentration Sensor* http://www.aqmd.gov/docs/default-source/aq-spec/resources-page/plantower-pms1003-manual_v2-5.pdf. Accessed on 17 Feb 2021.

[60] Palas (2020) *EN 16450 approved fine dust measurement device for simultaneous measurement of PM2.5 and PM10*. Instrument specifications provided by Palas, Version: June 30, 2020.

[61] Hagan DH, Kroll JH (2020) *Assessing the accuracy of low-cost optical particle sensors using a physics-based approach* Atmospheric Measurement Techniques 2020, Preprint https://doi.org/10.5194/amt-2020.188

[62] Alphasense *Alphasense Air Sensors for Air Quality Networks—Particulates* http://www.alphasense.com/index.php/products/optical-particle-counter/. Accessed on 17 Feb 2021.

[63] NeoMonitors *LaserDust*™ LaserDust website, visited 20.05.2021 https://neomonitors.com/product/laserdust/

[64] Dekati *ELPI®+ Brochure* ELPI brochure accessible online, downloaded 20.05.2021 https://www.dekati.com/wp-content/uploads/dekati_elpi_brochure.pdf

[65] TSI *MOUDI II ROTATING IMPACTORS* MOUDI product information accessible online, visited 02.06.21 https://tsi.com/products/cascade-impactors/moudi-ii-rotating-impactors/

[66] Roberts DL, Mitchell JP (2019) *Measurement of Aerodynamic Particle Size Distribution of Orally Inhaled Products by Cascade Impactor: How to Let the Product Specification Drive the Quality Requirements of the Cascade Impactor* AAPS PharmSciTech 20, 57 (2019). https://doi.org/10.1208/s12249-018-1276-9

[67] Burtscher H, Majewski A W, Khalek I A (2016) *PM Measurement: Collecting Methods* https://dieselnet.com/tech/measure_pm_col.php. Accessed 21. Feb 2021

[68] Sven Leckel Ingenieurbüro GmbH *SEQ47/50-RV* Sven Leckel website, product information, visited 23.05.21 https://www.leckel.de/devices/seq4750-rv/

[69] Abu-Rahmah A, Arnott WP, Moosmüller H *Integrating nephelometer with a low truncation angle and an extended calibration scheme* Measurement Science and Technology 17(7):1723 DOI: 10.1088/0957-0233/17/7/010

[70] Pinnick RG, Rosen JM, Hofmann DJ (1973) *Measured Light-Scattering Properties of Individual Aerosol Particles Compared to Mie Scattering Theory* Applied Optics 1973, Vol. 12, No. 1, p.37-41

[71] Kroslid D (2010) *Pimex for effektivt arbeidsmiljøarbeid i aluminiumindustrien*. Project report

[72] Jørgensen RB, Kero IT, Blom A, Grove EE, Svendsen KvH (2020) *Exposure to Ultrafine Particles in the Ferroalloy Industry Using a Logbook Method* Nanomaterials 2020, 10, 2546; doi:10.3390/nano10122546

[73] Myklebust HAHO, Aarhaug TA, Tranell G (2018) *Measurement system for diffuse emissions in primary aluminum produc-tion*. The Minerals, Metals & Materials Series 2020; p. 735-743

[74] SparkFun *GP2Y1010AU0F: Compact Optical Dust Sensor* https://www.sparkfun.com/datasheets/Sensors/gp2y1010au_e.pdf. Accessed on 17 Feb 2021.

[75] Shinyei *Shinyei PPD42 Particle Sensor*. Accessed on 17 Feb 2021. https://github.com/mozilla-sensorweb/sensorwebwiki/wiki/Shinyei-PPD42-Particle-Sensor.

[76] PurpleAir *PA-II Dual Laser Air Quality Sensor* https://www.purpleair.com/sensors. Accessed on 17 Feb 2021.

[77] AirBeam *AirBeam Technical Specifications, Operation & Performance* http://www.takingspace.org/airbeam-technical-specifications-operation-. performance/ Accessed on 17 Feb 2021.

[78] Cubic Sensor and Instrument Co.,Ltd *Laser dust sensor PM3006T* https://www.directindustry.com/prod/cubic-sensor-instrument-co-ltd/ product-54752-2240291.html. Accessed on 17 Feb 2021.

[79] Kuula J, Mäkelä T, Aurela M, Teinilä K, Varjonen S, Gonzáles O, Timonen H (2020) *Laboratory evaluation of particle-size selectivity of optical low-cost particulate matter sensors* Atmospheric Measurement Techniques 2020, 13, p.2413-2423 https://doi.org/10.5194/amt-13-2413-2020

[80] Badura M, Batog P, Drzeniecka-Osiadacz A, Modze P (2018) *Evaluation of Low-Cost Sensors for Ambient PM2.5 Monitoring*. Hindawi, Journal of Sensors, Volume 2018

[81] Palas (2021) *Fine dust measurement device Fidas® 200 S*. Palas official product description, visited 08.02.21 https://www.palas.de/en/product/fidas200s

[82] Standards (2013) *Air quality - Certification of automated measuring systems - Part 1: General principles* Website compiling stardards, visited 14.05.21 Link: https://standards.iteh.ai/catalog/standards/cen/e7c26010-6168-4efe-abf1-44d146ed82d1/en-15267-1-2009

[83] Genikomsakis KN, Galatoulas FK, Dallas PI, Ibarra LMC, Margaritis D, Ioakimidis C *Development and On-Field Testing of Low-Cost Portable System for Monitoring PM2.5 Concentrations*. Sensors (Basel). 2018 Apr; 18(4): 1056.

[84] Jayaratne R, Liu X, Ahn KH, Asumadu-Sakyi A, Fisher G, Gao J, Mabon A, Mazaheri M, Mullins B, Nyaku M, Ristovski Z, Scorgie Y, Thai P, Dunbabin

M, Morawska L (2020). *Low-cost PM2.5 Sensors: An Assessment of their Suitability for Various Applications*. Aerosol Air Qual. Res. 20: p 520-532. https://doi.org/10.4209/aaqr.2018.10.0390

[85] Zervaki O, Zheng L, Dionysiou D, Kulkarni P, Zarus GM (2017) *Calibration of Low-cost Dust Sensors*. 110th Annual Conference and Exhibition of the Air and Waste Management, June 2017

[86] Jayaratne R, Liu X, Thai P, Dunbabin M, Morawska L (2018) *The influence of humidity on the performance of a low-cost air particle mass sensor and the effect of atmospheric fog*. Atmos. Meas. Tech., vol 11, p 4883–4890, 2018

[87] G Tranell, *Conversation with Prof. Gabriella Tranell* Aug. 2021

[88] Chapman S, Cowling TG (1970) *The Mathematical Theory of Non-Uniform Gases.* 3rd ed; Cambridge University Press, 1970.

[89] Bird RB, Stewart WE, Lightfoot, EN (2007) *Transport Phenomena.* 2nd ed; Wiley, 2007.

[90] Kendall, RA, Dunning Jr. TH, Harrison, RJ (1992) *Electron affinities of the first-row atoms revisited. Systematic basis sets and wave functions.* The Journal of Chemical Physics, 1992, vol 96, pp 6796-6806.

[91] Balabanov NB, Peterson, KA (2005) *Systematically convergent basis sets for transition metals. I. All-electron correlation constistent basis sets for the 3d elements Sc-Zn.* The Journal of Chemical Physics, 2005, vol 123, 064107.

[92] CFOUR, a quantum chemical program package written by J.F. Stanton, J. Gauss, L. Cheng, M.E. Harding, D.A. Matthews, P.G. Szalay with contributions from A.A. Auer, R.J. Bartlett, U. Benedikt, C. Berger, D.E. Bernholdt, Y.J. Bomble, O. Christiansen, F. Engel, R. Faber, M. Heckert, O. Heun, M. Hilgenberg, C. Huber, T.-C. Jagau, D. Jonsson, J. Jusélius, T. Kirsch, K. Klein, W.J. Lauderdale, F. Lipparini, T. Metzroth, L.A. Mück, D.P. O'Neill, D.R. Price, E. Prochnow, C. Puzzarini, K. Ruud, F. Schiffmann, W. Schwalbach, C. Simmons, S. Stopkowicz, A. Tajti, J. Vázquez, F. Wang, J.D. Watts and the integral packages MOLECULE (J. Almlöf and P.R. Taylor), PROPS (P.R. Taylor), ABACUS (T. Helgaker, H.J. Aa. Jensen, P. Jørgensen, and J. Olsen), and ECP routines by A. V. Mitin and C. van Wüllen. For the current version, see `http://www.cfour.de`.

[93] Matthews DA, Cheng L, Harding ME, Lipparini F, Stopkowicz S, Jagau TC, Szalay PG, Gauss J, Stanton JF (2020) *Coupled-Cluster Techniques for Com-*

putational Chemistry: the CFOUR Program Package. The Journal of Chemical Physics, 2020, vol 152, 214108.

[94] Smith FJ, Munn RJ (1964) *Automatic Calculation of the Transport Collision Integrals with Tables for the Morse Potential.* The Journal of Chemical Physics, 1964, vol 41, pp 3560-3568.

[95] Chase MW, Jr. (1998) *NIST-JANAF Themochemical Tables, Fourth Edition*. J. Phys. Chem. Ref. Data, Monograph 9, 1998, 1-1951.

[96] Joo S-W, Hong S-H, Lee G-H, You B-D *Evaporation Behavior of Low Carbon Ferromanganese Alloy Melt at Reduced Pressure*. Metals and Materials, 2013, vol 19, nr 3, p 585-590.

[97] Landolt-Börnstein *Thermodynamic Properties of Elements, H to Ni*
Landolt-Börnstein - Group IV Physical Chemistry 19A1
https://materials.springer.com/lb/docs/sm_lbs_978-3-540-69077-1
10.1007/10652891_6 (Springer-Verlag Berlin Heidelberg © 1999)
Accessed: 05-10-2021

[98] Black DL, McQuay MQ, Bonin MP (1996) *Laser-based techniques for particle-size measurement, a review of sizing methods and their industrial applications*. Progress in Energy and Combustion Science, 22:267-306

[99] Matlab *Matlab R2019b* 2019, lisenced through NTNU https://se.mathworks.com/products/matlab.html

[100] Comsol *Comsol Multiphysics*. 2021, lisenced through NTNU http://www.comsol.com, Accessed: 2017-09-06.

[101] LibreTexts Chemistry *Physical and Theoretical Chemistry Textbook Maps ch 2.5 Reaction Rates*
https://chem.libretexts.org/Bookshelves/Physical_and_Theoretical_Chemistry_Textbook_Maps/Supplemental_Modules_(Physical_and_Theoretical_Chemistry)/Kinetics/02%3A_Reaction_Rates/2.05%3A_Reaction_Rate accessed 17.09.2021

[102] Lee YE (1998) *Thermodynamic Assessment of Liquid Fe-Mn-C System*. Metallurgical and Materials Transactions, 1998, vol 29B, p397-403.

[103] Tanaka A (1980) *Activities of Manganese in Mn-Fe-C, Mn-Si-C and Mn-Fe-Si-C Melts at 1673 K**. Trans. JIM, 1980, vol 21, p27-33.

[104] Silveira JL (2017) *Sustainable Hydrogen Prodution Processes, Appendix A: Tables Showing Gibbs Free Energy as a Function of Temperature of Formation Reactions* Springer, edition 1, 2017 DOI: 10.1007/978-3-319-41616-8

[105] Scholtz MT, Trass O (1970) *Mass Transfer in an Impinging Jet. Part 2: Boundary Layer Flow Mass Transfer* American Institute of Chemical Engineers Journal, vol 16, 1970, p90-96

[106] Ma Y. (2018) *Element Distribution in the Silicomanganese Production Process* Metallurgical and Materials Transactions B 2018, vol 49, p2444–2457
.

Appendix A

Experimental data

A.1 HCFeMn fuming experiments

Table A.1: Experimental Flux values for fuming of HCFeMn. Summarized

Gas flow rate	O_2 conc.	Experimental Flux values (g/m^2s)				
0 l/min	21 %	0.05				
1 l/min	0 %	0.10	0.04	0.05		
1 l/min	10.5 %	0.06	0.08	0.12	0.08	
1 l/min	21 %	0.54	0.48	0.46		
1 l/min	35 %	0.14	0.67	0.48		
1 l/min	50 %	0.74	0.69			
3 l/min	0 %	0.11	0.09	0.05		
3 l/min	5 %	0.57	0.68	0.74	0.47	0.64
3 l/min	10.5 %	1.07	0.94	0.92		
3 l/min	21 %	1.82	1.97	1.85		
3 l/min	35 %	1.46	2.92	2.33	2.37	
3 l/min	50 %	2.87	2.54	2.43		

Table A.2: Experimental values for fuming of HCFeMn. Measured through pre- and post experimental weighing of the individual parts of the outflow system. The distribution between the filter box, transition tube, and cooler is also listed.

Experimental		Measurement before and after experiement								
Parameters		Difference (g)						Part of total		
Gas comp.	Gas vel.							Filter		
(% O2)	(l/min)	Lid	Box	Filter	Tube	Cooler	Total	total	Tube	Cooler
21	3	16.9	0.2	0.04	3.55	1.6	22.29	0.77	0.16	0.07
21	3	17.9	0.4	-0.46	3.83	2.4	24.07	0.74	0.16	0.10
21	1	3.3	0.3	2.09	0.86	0.1	6.65	0.86	0.13	0.02
21	1	4.4	0.1	0.76	1.03	-0.4	5.89	0.89	0.17	-0.07
21	0	0.1	0.1	0.08	0.4	-0.1	0.58	0.48	0.69	-0.17
21	1	2.1	0	2.45	0.74	0.3	5.59	0.81	0.13	0.05
10.5	3	0.2	0.1	7.52	2.03	3.2	13.05	0.60	0.16	0.25
10.5	3	0.3	0.1	6.85	2.12	2.2	11.57	0.63	0.18	0.19
10.5	3	0.1	0.2	6.53	2.54	1.9	11.27	0.61	0.23	0.17
21	3	0.1	0	10.29	1.83	1.4	13.62	0.76	0.13	0.10
0	3	0.1	0	0.57	0.38	0.3	1.35	0.50	0.28	0.22
0	3	0.1	0	0.58	0.32	0.1	1.1	0.62	0.29	0.09
0	3	-0.9	0	0.76	0.48	0.3	0.64	-0.22	0.75	0.47
5	3	1	0	3.21	1.12	1.6	6.93	0.61	0.16	0.23
5	3	0.3	0	4.77	1.11	2.1	8.28	0.61	0.13	0.25
5	3	0.5	0	4.68	1.46	2.4	9.04	0.57	0.16	0.27
5	3	0.2	0	2.98	1.03	1.6	5.81	0.55	0.18	0.28
5	3	0.2	0.1	4.5	1	2	7.8	0.62	0.13	0.26
50	3	0.5	0	8.38	2.07	6.6	17.55	0.51	0.12	0.38
50	3	0.4	0	8.65	1.62	4.9	15.57	0.58	0.10	0.31
50	3	0.3	0	6.99	2.58	5	14.87	0.49	0.17	0.34
35	3	1.3	0	3.23	1.61	1	7.14	0.63	0.23	0.14
35	3	0.5	0.2	2.61	0.94	4.7	8.95	0.37	0.11	0.53
35	3	1.6	0.4	2.34	1.12	3.1	8.56	0.51	0.13	0.36
35	3	2.9	0.3	2.97	1.43	1.1	8.7	0.71	0.16	0.13
35	3	3.1	0.4	1.75	1.11	1.7	8.06	0.65	0.14	0.21
35	3	1	0.1	6.18	1.59	2.7	11.57	0.63	0.14	0.23
10.5	1	0	0	0.5	0	0.2	0.7	0.71	0.00	0.29
10.5	1	0	0.2	0.29	0.25	0.3	1.04	0.47	0.24	0.29
10.5	1	0.2	0	0.6	0.31	0.3	1.41	0.57	0.22	0.21
10.5	1	0	0	0.23	0.1	0.6	0.93	0.25	0.11	0.65
35	1	0.1	0	0.72	0.15	0.7	1.67	0.49	0.09	0.42
35	1	3.3	0.1	0.52	1.14	3.1	8.16	0.48	0.14	0.38
35	1	1.16	0	3.01	0.41	1.3	5.88	0.71	0.07	0.22
0	1	0.01	0	1.05	0.05	0.16	1.27	0.83	0.04	0.13
0	1	0.09	0	0.07	0.11	0.17	0.44	0.36	0.25	0.39
0	1	0.1	0	0.16	0.14	0.23	0.63	0.41	0.22	0.37

Table A.3: Calculated averages, standard deviations, and 95% confidence interval for the fume distribution between the filter box, transition tube, and cooler.

	Filter	Tube	Cooler
Avg	0.62	0.27	0.11
Stdev	0.19	0.14	0.16
95% CA	0.04	0.03	0.03

A.2 Size analysis

Table A.4: Experimental laser diffraction (LD) and particle counting (PD) results from filter fumes showing the mean particle/cluster diameter and their corresponding 95% confidence intervals.

Gas flow rate	**O_2 conc.**	**LD size (μm)**	**LD 95% CI (μm)**	**PC size (μm)**	**PC 95% CI (μm)**
1 l/min	10.5 %	2.33	0.613		
1 l/min	21 %	5.262	1.094		
1 l/min	35 %	6.037	1.106	1.008	0.147
3 l/min	0 %	1.736	0.248		
3 l/min	5 %	1.263	0.119		
3 l/min	10.5 %	1.133	0.284		
3 l/min	21 %	1.433	0.41	0.174	0.016
3 l/min	35 %	1.327	0.573		
3 l/min	50 %	1.021	0.402		
5 l/min	10.5 %	0.591	0.0949	0.116	0.010
5 l/min	21 %	1.003	0.279		
5 l/min	35 %	0.79	0.172	0.113	0.011

A.3 Elemental analysis

Table A.5: ICP-MS results (mass %) of filter fumes from the 3 l/min flow rate experiments at varying oxygen concentration as well as a sample of the HCFeMn metal used in the experiments.

	0% O_2	**5% O_2**	**10.5% O_2**	**21% O_2**	**35% O_2**	**50% O_2**	**Metal**
Mn	34.40 %	62.30 %	67.60 %	66.50 %	72.70 %	71.30 %	72.10 %
Zn	26.20 %	5.46 %	1.900 %	2.060 %	0.032 %	2.140 %	0.001 %
Si	0.040 %	0.074 %	0.366 %	1.090 %	0.070 %	0.064 %	0.020 %
Mg	2.280 %	2.600 %	0.615 %	0.406 %	0.568 %	0.161 %	0.004 %
Pb	2.110 %	1.070 %	0.191 %	0.204 %	0.037 %	0.283 %	0.003 %
Na	0.629 %	0.161 %	0.148 %	0.197 %	0.170 %	0.186 %	0.060 %
K	0.950 %	0.329 %	0.201 %	0.115 %	0.237 %	0.529 %	0.003 %
Fe	0.054 %	0.045 %	0.087 %	0.032 %	0.073 %	0.538 %	12.30 %
S	0.024 %	0.013 %	0.021 %	0.023 %	0.015 %	0.016 %	0.009 %
Al	0.019 %	0.006 %	0.004 %	0.010 %	0.005 %	0.004 %	0.001 %
P	0.001 %	0.001 %	0.001 %	0.001 %	0.001 %	0.014 %	0.137 %

Appendix B

Model comparison

Table B.1: Flux values (g/m^{2}s) for Mn evaporation calculated with the original model, with the original model after correcting for numerical errors, with the new model using Comsol, and the experimental averages. The changes done in the corrected model include changing the crucible radius from 0.012m to the correct 0.0135m, reformatting a math expression which applied the Temperature in Celsius instead of Kelvin, and generating values in a larger range of flow rates which allowed for a more accurate exponential interpolation model compared to the original linear interpolation based on 3 modelled values.

Flow rate (l/min)	0	0.01	0.1	0.25	0.5	1
1400°C Old model	0.020	0.020	0.023	0.029	0.038	0.056
1550°C Old model	0.122	0.124	0.145	0.179	0.235	0.349
1700°C Old model	0.533	0.543	0.632	0.780	1.027	1.520
1400°C Corrected model	0.000	0.018	0.057	0.090	0.128	0.181
1550°C Corrected model	0.000	0.079	0.250	0.396	0.560	0.792
1700°C Corrected model	0.000	0.271	0.855	1.353	1.913	2.707
1400°C New model	0.000	0.004	0.020	0.068	0.191	0.386
1550°C New model	0.000	0.019	0.087	0.281	0.803	1.633
1700°C New model	0.000	0.063	0.295	0.878	2.629	5.402
1400°C exp.	0.000				0.194	0.485
1550°C exp.	0.034			0.378	0.798	1.543
1700°C exp.	0.141				3.760	4.997

Appendix C

Published papers

C.1 Paper I

Evaporation and Diffusion of Mn in Inert Systems

Håkon Aleksander Hartvedt Olsen, Stefan Andersson, and Gabriella Tranell

Abstract

This research is aimed to improve our knowledge on the dust formation and clustering in the ferroalloy industry. Specifically, this paper focuses on the evaporation of manganese metal, and how different parameters influence the evaporation rate. Experiments were done with pure manganese metal heated to between 1400 and 1700°C in a pure argon atmosphere, where the change in weight was measured to calculate the loss of manganese over time. A mathematical model was constructed to link theoretical values to the results from the experiments. The high control over the system parameters allowed for the validation, rejection or creation of values and theories used in the model.

Keywords

Manganese, Evaporation, Diffusion, CFD

1 Introduction

Airborne particulate matters, originating from various sources in the metallurgical industry are not only a concern in terms of workers health, but the fumes from industrial plants also contribute to the so-called fugitive emissions which may be harmful to the local, urban communities as well as the environment at large.

Håkon Aleksander Hartvedt Olsen, PhD Candidate
Department of Materials Science and Engineering, Norwegian University of Science and Technology, Alfred Getz vei 2, NO-7491, Trondheim, Norway, e-mail: hakon.a.h.olsen@ntnu.no

Stefan Andersson, Research scientist
SINTEF Materials and Chemistry, P.O. Box 4760 Torgarden, NO-7465 Trondheim, Norwaye-mail: Stefan.Andersson@sintef.no

Gabriella Tranell, Professor
Department of Materials Science and Engineering, Norwegian University of Science and Technology, Alfred Getz vei 2, NO-7491, Trondheim, Norway, e-mail: Gabriella.tranell@ntnu.no

The aerosols produced in most metallurgical processes may be harmful if inhaled and exposure to high levels of particles has been linked to cancer, pneumonia, chronic obstructive pulmonary disease (COPD) and other respiratory and cardiovascular syndromes [1][2][3][4][5]. Inhalation of certain manganese (Mn) compounds has also been linked to inflammation and neuropsychological disturbances [6][7][8].

Characteristic properties of the particles, especially particle size and chemical composition, may influence their impact on human health. It is now well known that ultrafine particles (nanoparticles, particles <100 nm) have a much greater surface area and different physic-chemical characteristics [9][10] compared to their larger counterparts. They may therefore be more reactive, behave differently in the respiratory system, and give rise to increased biological responses [11].

As the chemical composition and morphology (particle shape) of particles originating from different ferroalloy industries and processes vary greatly, it is important to understand the mechanisms of which dusts are generated and how the characteristic properties of the particles depend on process parameters. With such knowledge, primary dust generation may be partially controlled.

An important and not yet thoroughly studied part of the dust formation from liquid manganese alloys such as ferromanganese (FeMn) and silicomanganese (SiMn) is the evaporation and gas-phase diffusion of manganese. In contrast to silicon, which has a very low vapor pressure and will mostly react with oxygen to form dust, manganese evaporates noticeably at temperatures close to the melting point. With silicomanganese, this leads to possible reactions between silicon oxides and manganese fumes, but can also cause a competition for oxygen close to the surface where if no oxygen reaches the surface, one might get no silicon in the dust at all. [12] Because of these reasons, the experimental study and subsequent modelling of evaporation rates of Mn is important.

2 Model development

In the production process for ferroalloys such as ferromanganese and silicomanganese, the produced melt is in contact with air during several steps of the process. Most notably during tapping, refining and casting, the melt is exposed to air without a protective slag layer over an extended duration. During this time, there are two possible reactions for each metal in the

alloy, Evaporation and oxidation, which may be summed as shown in equation 1 and 2.

$$Me(l) \Rightarrow Me(g) \quad (1)$$

$$Me(l) + xO_2(g) \Rightarrow MeO_{2x}(s,l) \quad (2)$$

Both reactions are thermodynamically driven towards equilibrium, and the distance from equilibrium is the driving force of the mass flux. This work purely studies reaction 1. for pure manganese, and the equilibrium partial pressure for this reaction is defined as shown in equation 3.

$$p_{eq} = \frac{1}{exp(^{-\Delta G}/_{R*T})} \quad (3)$$

Where R is the gas constant, T is the temperature in Kelvin, and ΔG is the change in Gibbs free energy. The Gibbs free energy for each side of the equation is calculated as shown in equation 4.

$$G = H - TS \quad (4)$$

Where S is the entropy and H is the enthalpy of formation. The flux from evaporation at the surface can then be defined as shown in equation 5,

$$Flux_{evaporation} = (p_{eq} - p) * \sqrt{\frac{Mm}{N_A*2*\pi*k_B*T}} \quad (5)$$

Here, N_A is Avogadro's number, k_B is Boltzmann's constant, and Mm is the molar mass of Mn. For diffusion, the flux can be defined by equation 6,

$$Flux_{diffusion} = D * \frac{(n_{eq} - n_{bulk})}{DiffZ} * \frac{Mm}{N_A} \quad (6)$$

Where DiffZ is the diffusion layer thickness defined by equation 7 [13], D is the diffusion coefficient, and n is the molar concentration of Mn(g) for equilibrium and bulk gas respectively.

$$DiffZ = \frac{L*4.52}{Re^{1/2}*Sc^{1/3}} \quad (7)$$

Reynold's number and Schmidt's number are defined by equation 8 and 9 respectively. L is here defined as the radius of the crucible, ν is the viscosity, v is the bulk flow velocity, D is the diffusion coefficient and ρ is the density of the gas.

$$Re \quad \frac{v*L*\rho}{\nu} \quad (8)$$

$$Sc = \frac{\nu}{D*\rho} \quad (9)$$

In order to model the evaporation and diffusion kinetically, diffusion coefficients for Mn and Ar gas as well as a Mn-Ar gas mixture were derived from Chapman-Enskog kinetic theory [14] based on Lennard-Jones parameters for Ar-Ar and a Morse potential used to describe the Mn-Mn and Mn-Ar interactions. The Ar-Ar parameters were taken from the literature [14] whereas the Mn-Ar and Mn-Mn interaction potentials were evaluated by high-level quantum chemical calculations. Coupled cluster with single and double excitations with a perturbative treatment of triple excitations [CCSD(T)][15] calculations were applied to Mn-Mn and Mn-Ar pair interactions at a range of separation distances (3-7 Å) using the CFOUR program package [16]. These results were subsequently fitted to Morse potentials, respectively, since the Lennard-Jones potential was found not to reproduce the calculated interaction energy curves well enough. Expressions and values of collision integrals for calculating diffusion coefficients for the two types of potential were taken from literature [14,17].

The model for the evaporation was created in two parts: One that calculated the flux of vaporization using thermodynamic and kinetic data, and one that calculated the diffusion flux from flow conditions and kinetic theory. For each temperature and flow rate investigated experimentally (see section 3), the gas velocity over the metal surface was calculated using a Comsol model. The model uses finite element analysis, assuming steady state and incompressible flow, and using laminar flow conditions as the calculated Reynold's number for the relevant area is less than 100. The mesh used is shown in Figure 1, it can be noted that a finer mesh is used near the metal surface. For the surfaces, no slip is the assumed boundary condition, and for each element, a form of the Navier-Stokes equation and the continuity equation are solved. The exact equations solved are shown in equation (10) and (11) [18].

$$\rho(\boldsymbol{u} \cdot \nabla)\boldsymbol{u} = \nabla[-p\mathbf{I} + \mu(\nabla\mathbf{u} + (\nabla\mathbf{u})^T)] + \boldsymbol{F} \quad (10)$$

$$\rho\nabla \cdot (\mathbf{u}) = 0 \quad (11)$$

Where **u** is the velocity field, ρ is the density, μ is the dynamic viscosity, p is the pressure, **F** is the external force, and **I** is the identity matrix. The flow pattern for one experiment is shown in Figure 2, with Figure 3 showing a more detailed image of the flow pattern close to the metal surface.

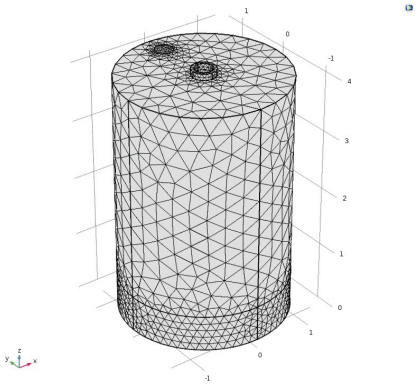

Figure 1: The mesh used in the comsol model. It has a total of 36587 domain elements, 4286 boundary elements, and 395 edge elements.

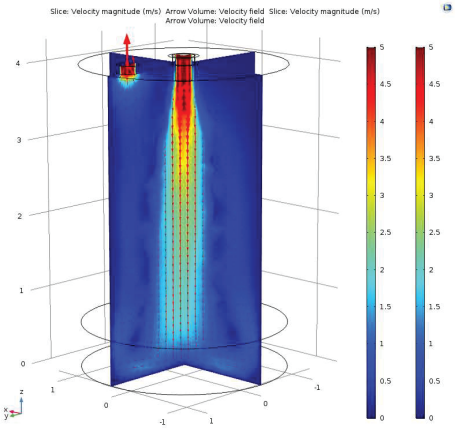

Figure 2: Flow conditions inside crucible, model made using Comsol software. Conditions assumed: laminar flow, no slip boundaries, incompressible flow, steady state. This image was from an experiment with T = 1550 °C and 0.5 l/min flow rate.

The thermodynamic data used in the model was taken from NIST-JANAF Thermochemical Tables [19], where values for gases below boiling temperature were extrapolated from the data given. The extrapolated data was found not to deviate much at 1400 °C. Other parameters used in the model are listed in table 1.

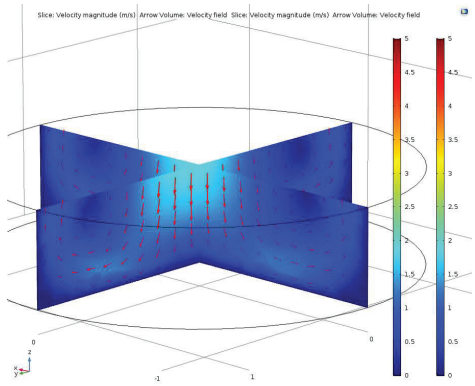

Figure 3: Flow conditions near the metal surface, model made using Comsol software. Conditions assumed: laminar flow, no slip boundaries, incompressible flow, steady state. This image was from an experiment with T = 1550 °C and 0.5 l/min flow rate.

Table 1: Parameters used in the model.

Parameter	**Value**
L	0.0135 m
Mm_{Mn}	0.054938 kg/mol
ν	8.42-7.87 * 10^{-5} Pa*s
D	2.93-3.97 *10^{-4} m^2/s
ρ	0.246-0.290 kg/m^3

These two parts are both dependent on the partial pressure of Mn(g) just above the surface of the metal. We know however, that under stable conditions, there is a constant flux of vapour from the surface to the bulk phase, which means the flux from metal to diffusion layer and through the layer to the bulk must be equal. Using the solver function in Excel, the partial pressure at which these two fluxes are equal can then be found, which gives the total flux through the system.

3 Experiments

The apparatus used for the experiments was a graphite tube furnace, the design which is sketched in Figure 2. The inside of the furnace was kept in an 6N argon atmosphere of around 1.3 bar to avoid oxidation. Inside the graphite tube, an alumina crucible with height 40mm and diameter 27mm was used as the container for the experiments. The crucible was fitted with a lid to further limit contamination from the

surrounding atmosphere, and an alumina paste was used to seal the lid. An alumina tube with inner diameter of 3mm was inserted into a hole in the center of the lid, through which argon was blown into the crucible. Another hole in the lid with diameter 3mm was the only outlet in the system. Figure 3 shows a crucible after a finished experiment, without the alumina tube.

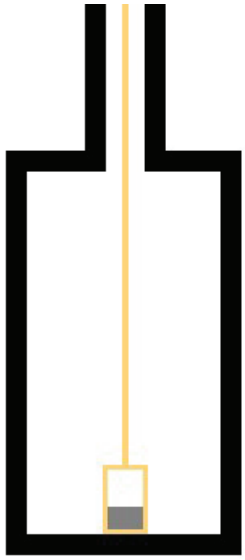

Figure 4: Sketch of the experimental setup. An outer tube of graphite with an inner alumina crucible and tube connected to an argon source. The atmosphere inside the tube was purged with argon before and during the experiments, and argon was blown at different rates through the tube in each experiment.

Figure 5: Alumina crucible after finished experiment. The middle hole was used for the alumina tube, while the smaller hole was used as the outlet for the gas and vapor.

The crucible was filled with 15 (+/- 0.5) grams of 99.9% Mn chips. The chips had a slightly tarnished, oxidized surface before the experiments and as such, there was a small amount of oxide present in the experiments. However, as a first approach, this was assumed not to affect the evaporation rate. Each sample was pre-treated at 150 °C for 30 minutes to remove any humidity from the sample and the sealing paste, and the crucible set-up was weighted before and after pre-treatment as well as after the experiment. Longer pre-treatment time or higher temperatures were found not to produce any further weight loss in the sample.

The sample was inserted into the furnace, which was then vacuumed to between 80 and 200 mTorr before it was purged with argon and kept at around 1.3 bar. After purging, the chamber was heated to the desired temperature over 30 minutes and held at that temperature for further 60 minutes before being cooled. During the entire heating, holding and cooling period, argon was inserted through the alumina tube at a constant flowrate. The different temperatures and flowrates for each experiment are shown in Table 2.

Table 2: Flow rates, temperatures, holding times, and Sample contents for the experiments

Exp #	Ar flow rate (l/min)	Temp (°C)	Holding time (min)	Sample content
10	0.0	1400	60	100% Mn
5	0.5	1400	60	100% Mn
7	1.0	1400	60	100% Mn
2	0.0	1550	60	100% Mn
12	0.25	1550	60	100% Mn
3	0.5	1550	60	100% Mn
6	0.5	1550	60	100% Mn
1	1.0	1550	60	100% Mn
4	1.0	1550	60	100% Mn
8	0.0	1700	60	100% Mn
11	0.5	1700	60	100% Mn
9	1.0	1700	60	100% Mn
13	1.0	1700	60	100% Mn

After cooling, the crucible weight was again measured and the mass loss calculated. As the only reaction happening was evaporation of Mn, the flux of Mn out of the system could be calculated for each experiment.

4 Results

The measured weight losses for each experiment are shown in Table 3 together with the calculated mass flux and the parameters. Figure 4 show the mass loss as a function of the flow rate with linear trend lines for each temperature.

Table 3: Experimental results: Total mass loss and flux for each set of parameters.

Exp #	Ar flow rate (l/min)	Temp (°C)	Loss (g)	Flux (g/m^2s)
10	0.0	1400	-0.11	-0.07
5	0.5	1400	0.40	0.25
7	1.0	1400	1.00	0.61
2	0.0	1550	0.07	0.04
12	0.25	1550	0.78	0.48
3	0.5	1550	1.66	1.02
6	0.5	1550	1.63	1.00
1	1.0	1550	3.67	2.25
4	1.0	1550	3.18	1.95
8	0.0	1700	0.29	0.18
11	0.5	1700	7.75	4.76
9	1.0	1700	11.24	6.90
13	1.0	1700	10.3	6.32

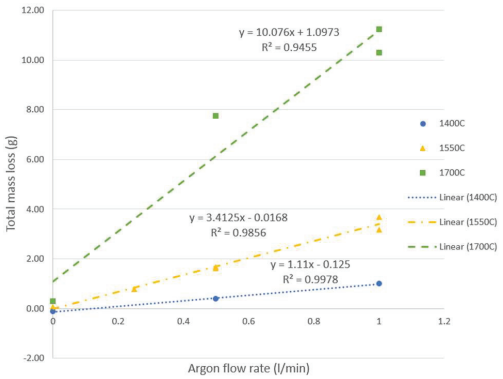

Figure 6: Total mass loss in grams over the flow rate of argon in l/min. Linear trend lines are given for each temperature.

5. Discussion

The crucible from experiment 10 (1400°, no Ar flow) has increased in weight by a very small amount. A potential reason for this might be a small amount of oxygen, supplied either from the ppm concentration in the Ar, the alumina crucible or from the tarnished starting Mn-chip surface reacting with the metal to form heavier oxides. The amount would not be very high however, and it is assumed that there has been practically no evaporation of manganese in this experiment.

The two experiments at 1700 °C and with 1 l/min flow rate were found to have very little metal left at the end of the experiment. This would likely cause a lower rate of evaporation during the later stages of the experiment as the surface area would be smaller. This would also explain why there is not the same linearity for the 1700 °C experiments as for the lower temperatures. Figure 5 shows the inside of crucible #13, where the metal content has been reduced to the point where it no longer covers the full area of the crucible.

Figure 7: Crucible from experiment #13, 1700 °C and 1 l/min flow rate. The surface area of the metal is clearly reduced due to excessive evaporation.

The model does show the same tendency to taper off at higher flow rates, but not to the same degree as in the experiments.

Data from the experiments can be compared with the model, which was used to generate data points for the same parameters as the experiments. These values are shown in Table 3, and plotted in Figure 6.

Table 3: Modelling results: Total mass loss for a choice set of parameters.

Ar flow rate (l/min)	Temp (°C)	Loss (g)
0.25	1400	0.06
0.5	1400	0.08
1.0	1400	0.12
0.25	1550	0.36
0.5	1550	0.50
1.0	1550	0.71
0.25	1700	1.55
0.5	1700	2.20
1.0	1700	3.11

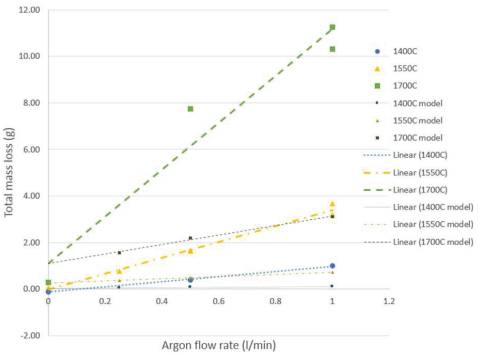

Figure 8: Mass loss in grams over the flow rate in l/min. Experimental and modelled values.

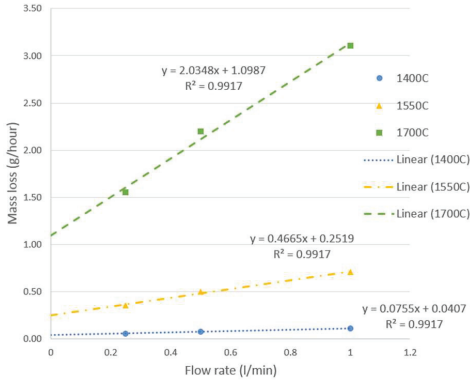

Figure 9: Modelled mass loss in grams/hour over the flow rate in l/minfrom the model.

The mass loss calculated with the model are around one fourth of the experimental values for all parameters. For comparison, Figure 7 shows both data sets together.

The curves are similar, but the model has evaporation rates that are about a fourth of the experimental values. Figure 8 shows both data sets together, but with the values from the model multiplied by 4 to show the similarities in the curves.

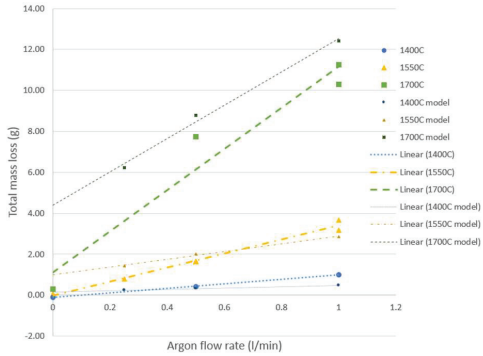

Figure 10: Mass loss in grams over the flow rate in l/min. Experimental and modelled values. Values from model are multiplied by 4.

6. Conclusions

In order to better understand the kinetics of fume/dust formation in the Mn-ferroalloys production industries, experiments investigating the evaporation rate and diffusion of Mn in an argon atmosphere at different temperatures and flow conditions, have been carried out. The results were compared to values calculated using a mathematical model of the same system. There was a mismatch in the results between model and experiments on the scale of factor 4, but the trends shown were very similar. Possible uncertainties in the model include the diffusion coefficient, enthalpy and entropy at lower temperatures, approximation of Reynolds number, and the gas velocities from the Comsol model.

There are also uncertainties in the experimental work, which could have influenced the experimentally obtained results. The evaporation during heating and cooling might have been measurably large, as there is up to fifteen minutes of time where the temperature is above the melting point during heating and cooling. The flux would in that time probably lie between the values for our experiments. The thin layer of oxide

might have slowed the evaporation process, and the temperature profile might be inaccurate as there is a delay between the outside of the tube where the furnace measures temperature, and the inside of the crucible.

The data from the experiments can be further used when modelling the dust formation in more complex systems where Mn evaporation is just a part of the whole. If improved, the model can also be expanded to take further reactions into account.

7. Further work

This work is the beginning of a larger study, and there is much work still to be done. Following is a list of planned work in the continuation of the project:

- Perform experiments where the temperature is measured inside the crucible to find temperature delay.
- Perform experiment without holding time to measure mass loss during heating and cooling.
- Etch the Mn before the experiment to remove any oxides.
- Use a crucible that doesn't contain oxides.
- Perform experiments with 0.25 l/min flow rate for 1400 and 1700°C.
- Review assumptions and uncertainties in the model, and then improve on it.
- Continue the experiments and model work with manganese and iron alloys, as well as including oxygen in the gas.

References

[1] Johnsen et al. (2008) International Archives of Occupational and Environmental Health 81 p.451-459

[2] Johnsen H L (2009) Ph.D. -thesis. University of Oslo, Fakultetsdivisjon Akershus universitetssykehus

[3] Hobbesland et al. (1997) Scandinavian Journal of Work, Environment and Health 23 5 p. 334-341

[4] Søyseth et al. (2011) American Journal of Industrial Medicine 54 9 p. 707-713

[5] Gibbs et al. (2014) Journal of Occupational and Environmental Medicine 56 7 p. 739-764

[6] Bast-Pettersen et al. (2004) International Archives of Occupational and Environmental Health 77p.277-287

[7] Luccini et al. (2009) Neuromolecular Medicine 11 p.311-321

[8] Racette et al. (2012) Neurotoxicology 33 4 p. 881-886

[9] Monteiller et al. (2007) Occupational and Environmental Medicine 64 p. 609-615

[10] Obersdörster. (2001) International Archives of Occupational and Environmental Health 74 p. 1-8

[11] Schmid et al. (2009) Biomarkers, 14 S1 p. 67-73

[12] Ma Y, Kero I, Tranell G. (2017) Fume Formation from Oxidation of Liquid SiMn Alloy. Oxidation of Metals.

[13] Bakken J A, Lobo S, Kolbeinsen L (2009) Compendium Fluid Flow and Heat Transfer Advanced Course, NTNU.

[14] Bird R B, Stewart W E, Lightfoot E N (2007) Transport Phenomena, Wiley, New York, NY.

[15] Stanton J F, Gauss J, Harding M E, Szalay P G, Auer A A, Bartlett R J, Benedikt U, Berger C, Bernholdt D E, Bomble Y J, et al. (2015) CFOUR, Coupled-Cluster techniques for Computational Chemistry, 2015. For the current version, see http://www.cfour.de.

[16] Bartlett R J, Musial M (2007) Rev. Mod. Phys. 79 p. 291-352

[17] Smith F J, Munn R J (1964) J. Chem. Phys. 41, 3560 – 3568.

[18] Comsol Multiphysics http://www.comsol.com/ comsol-multiphysics. Accessed: 2017-09-06.

[19] Chase M W, Jr. (1998) NIST-JANAF Themochemical Tables, Fourth Edition, J. Phys. Chem. Ref. Data, Monograph 9, 1998, 1-1951.

C.2 Paper II

Measurement System for Fugitive Emissions in Primary Aluminium Electrolysis

Håkon Aleksander Hartvedt Olsen Myklebust, Thor A. Aarhaug, and Gabriella Tranell

Abstract

Fugitive emissions from primary aluminium production is a concern both for occupational health and the environment. Current measuring equipment for in-situ measurements of such emissions is generally large and expensive or lacks the required time and spatial resolution to provide accurate information on the source of the emissions. This research is aimed at testing and evaluating distributed micro sensors for in-situ monitoring of dust intensity in the electrolysis hall. Multiple sensors are tested simultaneously in clusters at each location to study variation between individual sensors, giving a statistical average. These clusters are spread out in the relevant areas to map how the emission varies over both time and location based on operational activities such as anode changes. The sensor system yielded results that could be correlated to the process activities, and also showed clear variation in the fractions of PM10 and PM2.5 measured for different process operations.

Keywords

Microsensors • Fugitive emissions • Workers health

H. A. H. Olsen Myklebust ( ) · G. Tranell
NTNU, Trondheim, Norway
e-mail: hakon.a.h.olsen@ntnu.no

G. Tranell
e-mail: gabriella.tranell@ntnu.no

T. A. Aarhaug
SINTEF Industry, Trondheim, Norway
e-mail: thor.a.aarhaug@sintef.no

Introduction

Dust in the Electrolysis Process

The air-suspended particles produced in the aluminium production processes may be harmful if inhaled and exposure to high levels of particles has been linked to occupational asthma, with indications of increased mortality from cancer and pulmonary emphysema [1,2]. The dust produced in aluminium electrolysis often contain high levels of Flourine which may generate hydrofluoric acid if it comes into contact with water. These fumes are not only a concern in terms of workers health, but also contribute to the so-called fugitive emissions which may be harmful to the local, urban communities as well as the environment at large [3].

A schematic of the electrolysis process is shown in Fig. 1, and while most of the fumes are contained within the cells where the off-gas is filtered before its release, it is necessary to open the cells for several operations over the course of the production cycle. Examples of such operations are the anode change and cell tapping. To effectively gauge the particulate emissions from each different operation, a constant measurement system in necessary. Several previous studies provide an incomplete picture as the time-resolution is limited [3].

In the EU, regulations for fugitive emissions are tightening, and as such, measuring these categories of fumes are important [5]. Particularly fluoride emissions is considered important, and this is known to be a large component of the dust which is measured in this work [6]. Particulate emission by size fraction is also considered highly significant by the European commission, particularly in secondary aluminium production [6]. It is important to measure these emissions not just for the purpose of reporting to the authorities, but also to monitor the effects of implementations made towards reduction of fugitive emissions and improvement of working conditions.

A. Tomsett (ed.), *Light Metals 2020*, The Minerals, Metals & Materials Series,
https://doi.org/10.1007/978-3-030-36408-3_99

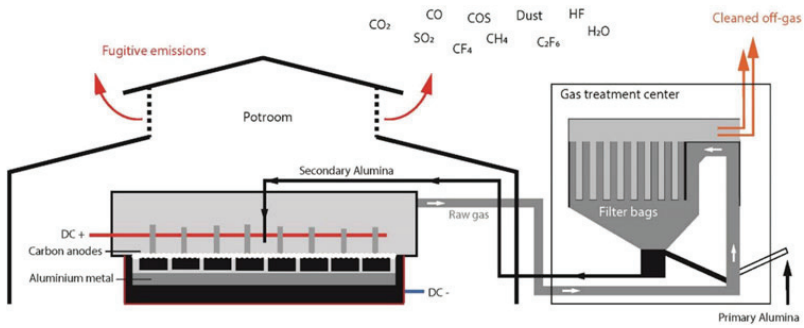

Fig. 1 Schematic of the material flow among the smelting process, gas treatment centre and emissions [4]

Current Monitoring Systems

The traditional system for monitoring fugitive emissions is capturing of dust through filter systems. The simple setup consists of tubes and pumps that allow the air from the potroom to be iso-kinetically lead through a filter which collects the dust. After a set period the dust is measured and can be analysed, which can provide accurate monitoring of its content. It does however give a low time-resolution and it would be very expensive to map an entire facility to account for spatial variance.

Technology for measuring dust levels through visual telemetry is also under development, with plans for constant measurement of hydrogen fluoride gas, SO_2, and CO, but is still not widely used [7].

The Use of Micro-sensors

Low-cost microsensors are not widely in use neither in the aluminium industry, nor yet for air-pollution monitoring in general and industry in particular. It is however being considered by the European Commission for air pollution monitoring and personal exposure, and with the technological improvements could become a "game changer" [8]. The technology is rapidly evolving, and both the sensors themselves and the framework (such as microchips and power supplies) needed to facilitate their use, is growing smaller and cheaper. Small sensor systems, while less accurate and with higher uncertainty than reference systems, can already provide reliable coarse information after calibration and quality data assurance [9].

Project Goals

The primary goal of the current study is to investigate the reliability and usefulness of a system based on microsensors in monitoring fugitive emissions from primary aluminium production. The secondary objective is to use the data generated through the study to improve our knowledge of the dynamics in the generation and emission of pot room dust, especially with regards to which operations produce the most dust, and which size fractions these dusts fall into. The system used in this work was set up to measure PM10 and PM2.5 along with temperature and relative humidity, and each sensor system delivers a value for each of these parameters every 5 s.

Sensor Setup

Figure 2 shows the sensor system used in this work. The system consists of two sensors and a microchip which collects and forwards the data to a central server, all contained in a 3D-printed PVC box which measures around 13 * 10 * 4 cm. The Nova PM SDS011 sensor reports the concentration of PM10 and PM2.5 in $\mu g/Nm^3$, while the HTU21D reports temperature in °C and relative humidity. Air from outside the box is sucked into the dust sensor through a short 2 mm diameter tube, while the temperature and humidity sensor is placed on

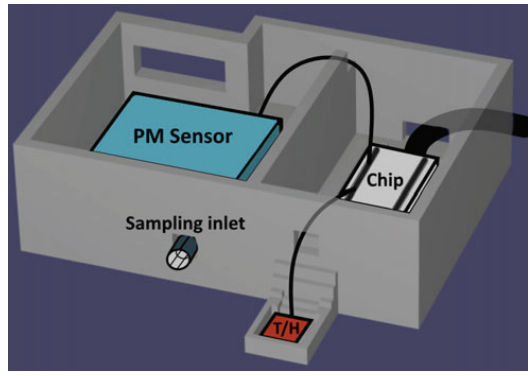

Fig. 2 Schematic of the setup prototype. Shows the dust sensor (PM sensor), temperature and humidity sensor (T/H), the the microchip (Chip), and the sampling inlet for dust (Sampling inlet)

the outside of the box where it measured the ambient air. The complete setup runs on standard 5 V 1 A current which can be supplied through power cables or batteries depending on preference. Weather data were taken from a weather station on the aluminium plant and used as background data for the measurements.

The dust sensor uses the laser scattering principle to measure the concentration of fine particles [10], while the humidity is measured through change of capacitance and temperature though changing resistance. The system measures continuously and provides a snapshot of these values approximately every five seconds.

The data is transferred through local WiFi, and the sensors can as such be spread across as large an area as a single network can cover. In this work, the sensors were placed in groups of four at three different positions inside a Robertson roof monitor (A natural draft roof ventilator which funnels the air out while stopping rain, marked in Fig. 3), one in the center, and one halfway to each side along the same axis as the production cells are placed. This roof monitor room is 9.75 m long and is located 12 m above the hall floor. Fumes from the processes of several cells pass through here as shown in Fig. 3. Sensor 1–4 are placed in the middle, sensor 5–8 to the left and sensor 9–12 to the right, relative to a person standing in the middle and looking towards the sensors, with a distance of 2.4 m between each group as well as the end walls as shown in Fig. 4. The end result is a file with data points for time, PM10, PM2.5, humidity, and temperature, for each sensor over the course of each day. Afterwards, the data is aggregated to an average value over each minute, allowing for standard deviations across the sensors in each group to be calculated.

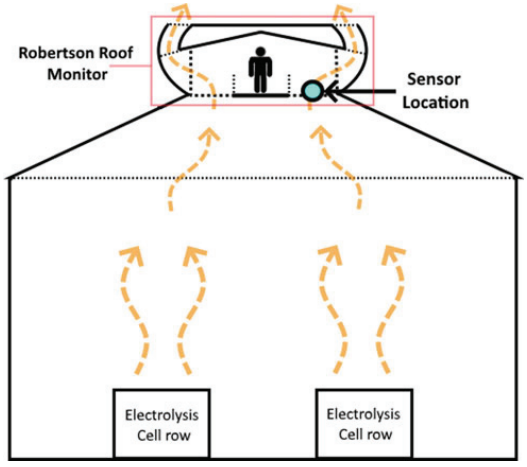

Fig. 3 Locations of the sensors marked with an arrow above the electrolysis cell rows, inside the Robertson roof monitor

Results

Basis for the Data

For the purpose of this work, data from two dates were chosen. On the first day, the weather was hot with temperatures reaching almost 30 °C after noon, while on the second day the temperature never exceeded 20 °C. Both days had periods of rain, which is shown alongside the temperatures in Fig. 5.

Figure 6 shows the mean temperature and humidity values for sensor 1–4 for both days. The connection between rain, and humidity is very notable, especially around 18:00 on the first day and 11:00 on the second day. The same can be said for the temperature indoor and outdoor. No statistically significant correlation between temperature and dust nor humidity and dust was found.

Dust Load Variation, Size Fraction and Process Events

Figures 7 and 8 show how the dust concentrations vary over the course of the two days as measured by the middle group of sensors. 3 periods are highlighted in Figs. 8, and 9 shows the difference in size fractions between these highlighted peaks. 18 lines labeled (a)–(r) refer to the actions listed in Table 1.

From this example alone, it is clear that different distinct operations within the plant produces different size fraction of fumes. Subtracting PM2.5 from PM10 gives the concentration of the larger particles, and that is the value used in Fig. 9. For the two smaller peaks the fraction of larger particles is around than 80%, while the larger peak from before noon has more than 60% of small particles for the most part.

Table 1 shows the recorded actions that were performed during these two days on the two cells just below the sensors, and each actions has a label referring to the lines shown in Figs. 7 and 8. The three peaks highlighted in Fig. 8 corresponds clearly with three events performed on cell 148: The anode changed started 10:39, the covering after the exchange at 14:54, and the covering of the measurement hole at 20:29. This tells us that the anode exchange produces far more of the finer particles compared to the two covering processes.

Deviation from Sensor Location

Figure 10 shows the mean values of PM10 for each of the three groups for one hour on the second day. The values for the rightmost group (sensor 9–12) is clearly higher in the beginning of the 3 o'clock peak with the leftmost group (sensor 5–8) shows the lowest values. After 3 o'clock it is the opposite however, with the leftmost group (sensor 5–8) having the largest values. In both these peaks, the middle group

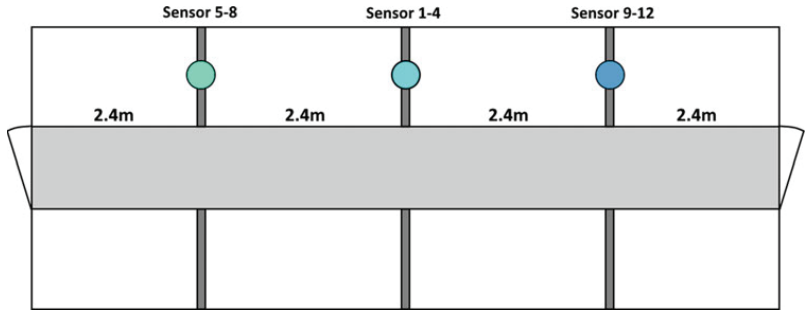

Fig. 4 Locations of the three sensor groups inside the Robertson roof monitor

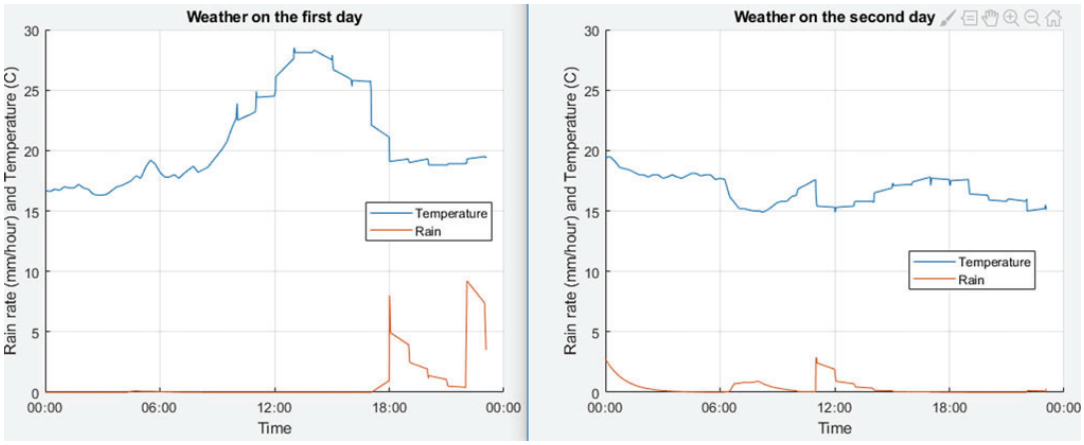

Fig. 5 The temperature and rain rates over the course of the two days. Data taken from a weather station on site

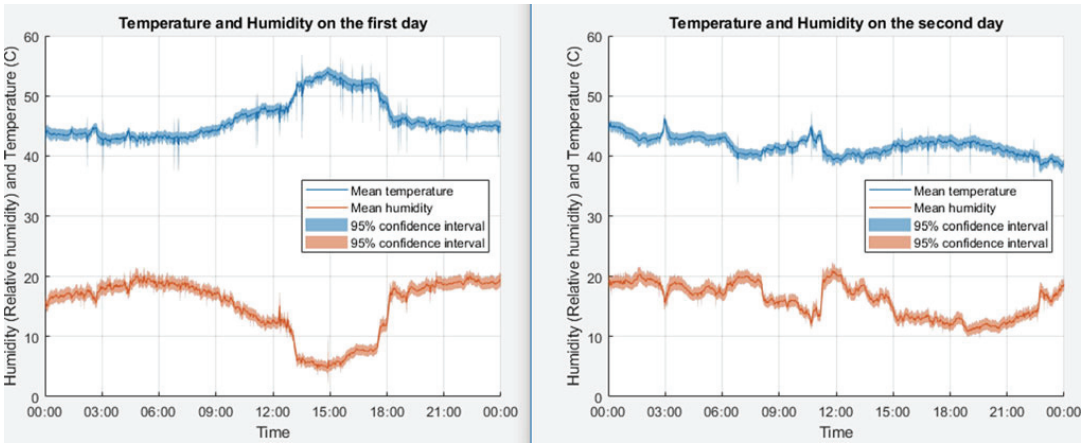

Fig. 6 Mean values of temperature and humidity for sensors 1–4 with 95% confidence intervals for both days

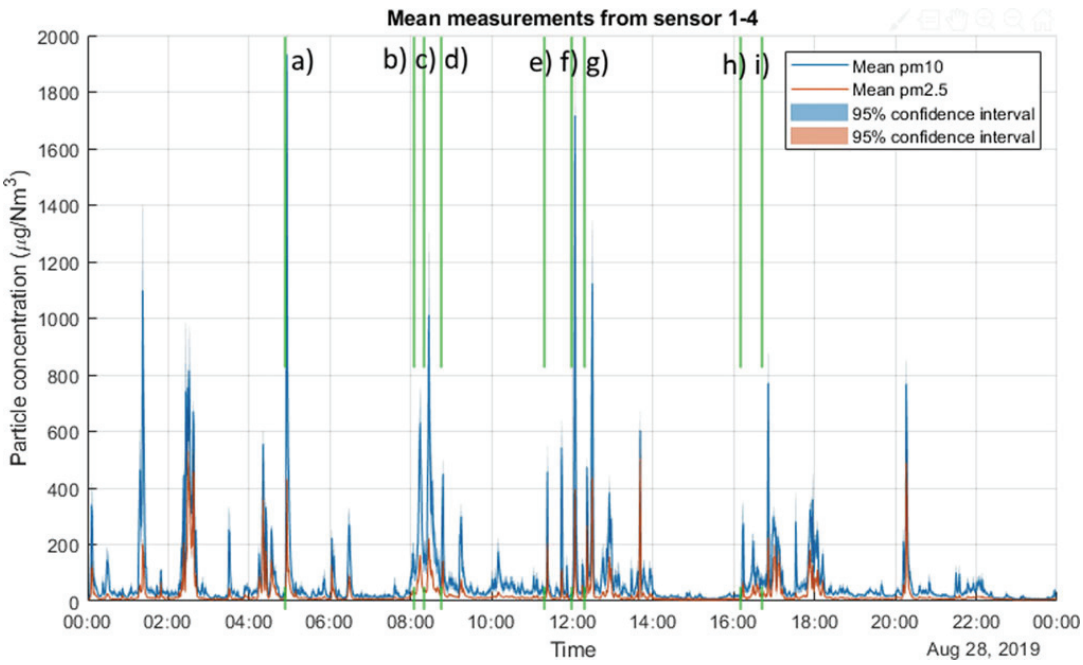

Fig. 7 Mean values of PM10 and PM2.5 for sensors 1–4 over the course of the first day. 95% confidence intervals are shown as a shaded area above and below the mean values. The lines labeled **a**–**i** refer to the actions listed in Table 1

(sensor 1–4) measures values between the two outer groups. Just after 03:30 there is another peak where the middle group is clearly higher than the two on the side. The 95% confidence intervals between the group measuring the lowest and the highest at each peak do not overlap at all. This lets us conclude that there is a statistically significant difference in the measurements based on the location of the sensors with the groups being only meters apart.

Statistical Reliability

Figure 11 shows the dust measurements for sensor 1–4 over a couple of peaks together with their mean value. There is some variance between the sensors, but by having 4 sensors together we achieve a generally small 95% confidence interval. The confidence interval ranges from close to zero to $\pm 130\,\mu g/Nm^3$, with a mean for the period being $\pm 18.5\,\mu g/Nm^3$. The mean 95% confidence interval for the entire day is only $\pm 6.5\,\mu g/Nm^3$, and it is clear from the figure that the variance increases mostly where the values and the change of value over time is large. It can also be seen that it is the same sensors that measure below and above average respectively, which points to inherent variations between the sensors. Unlike random variations, this is possible to compensate for through calibration and benchmark testing.

Discussion

The results indicate the reliability of the data gathered, and the importance of having multiple sensors in each group as well as several points to measure the variance across an area, but more importantly they show how much the fugitive emissions change over the course of a day in the electrolysis hall. They also show a large difference in dust particle size fractions across different peaks, clearly displayed in Fig. 9. The different peaks can be correlated to events in the production, which allows for comparisons of the dust formation from the different operations. For example, the anode change was shown to produce a much larger fraction of fine dust compared to the covering operations afterwards.

This information can be readily accessible from the affordable sensor system (<$200 for a group of 4) allowing for a large spread of sensors if needed. As such, it can allow for live monitoring of emissions across an entire aluminium production

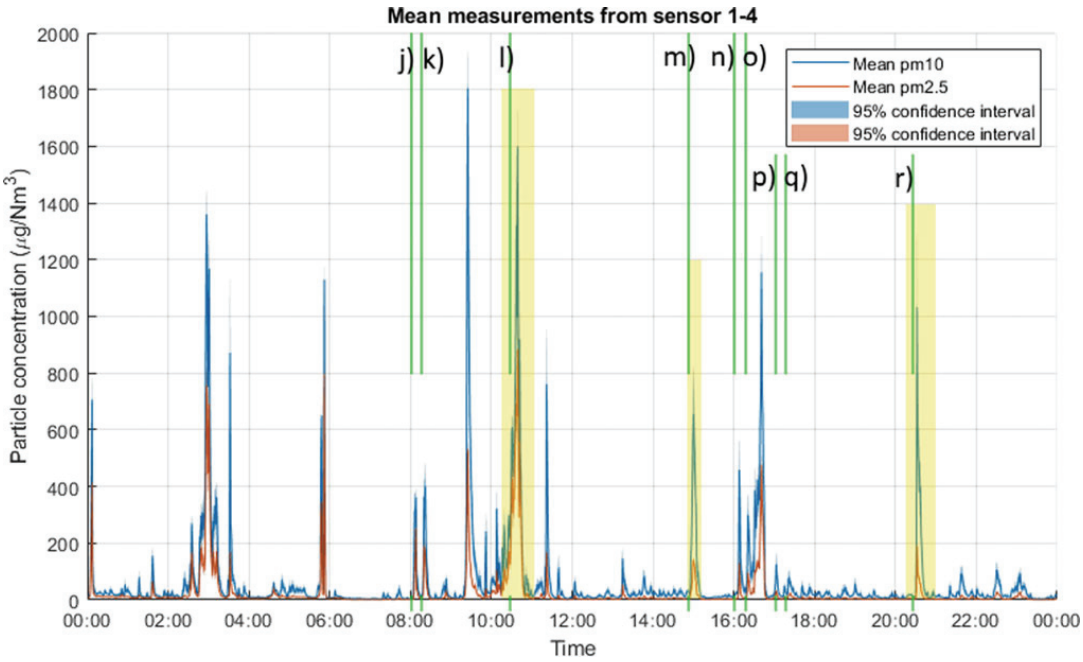

Fig. 8 Mean values of PM10 and PM2.5 for sensors 1–4 over the course of the second day. 95% confidence intervals are shown as a shaded area above and below the mean values. Three peaks are highlighted, with Fig. 9 showing the difference in size fractions between these highlighted peaks. The lines labeled **j**–**r** refer to the actions listed in Table 1

Table 1 The recorded processes performed on the two cells (148 and 149) below the sensors. The labels match the lines marked in Figs. 7 and 8

Day	Time	Event	Cell	Label
1	04:50	Covering of measurement hole	149	(a)
1	08:04	Drilling measurement hole	148	(b)
1	08:24	Covering after anode exchange	148	(c)
1	08:39	Measuring	148	(d)
1	11:17	Drilling of tapping hole	149	(e)
1	12:00	Covering of measurement hole	148	(f)
1	12:22	Tapping	149	(g)
1	16:09	Drilling of tapping hole	148	(h)
1	16:29	Tapping	148	(i)
2	08:02	Covering after anode exchange	149	(j)
2	08:14	Cutting for anode exchange	148	(k)
2	10:39	Anode exchange	148	(l)
2	14:54	Covering after anode exchange	148	m)
2	16:02	Drilling of tapping hole	149	(n)
2	16:14	Drilling of measurement hole	148	(o)
2	17:04	Measuring	148	(p)
2	17:17	Tapping	149	(q)
2	20:29	Covering of measurement hole	148	(r)

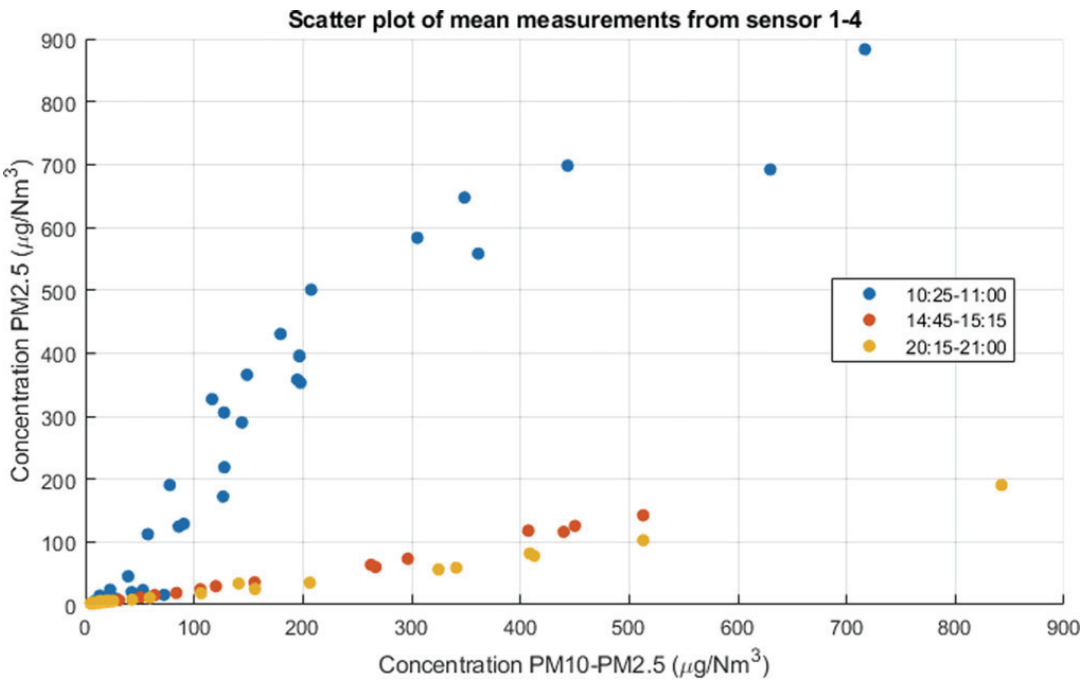

Fig. 9 Mean values of PM10 and PM2.5 for sensors 1–4 for certain periods on the second day. The values for PM10 minus the value for PM2.5 is shown on the x-axis and the values for PM2.5 are shown on the y-axis. Each color corresponds to measurements from a specific time period, which relates to a specific process as shown in Table 1

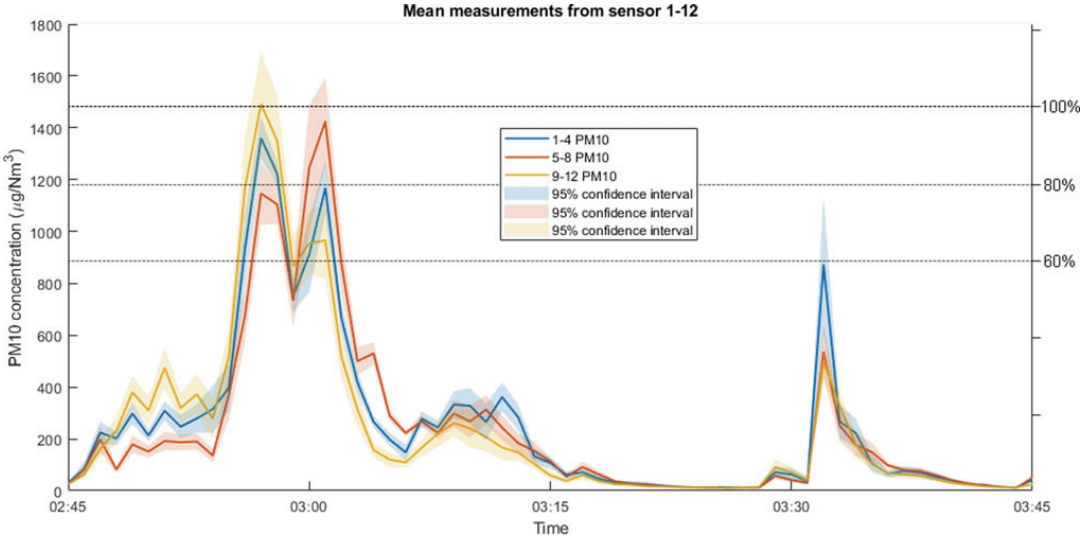

Fig. 10 Mean values and 95% confidence interval for each sensor group for one hour on the second day. The right hand y-axis is normalized with respect to the highest value measured in this period for easier comparison

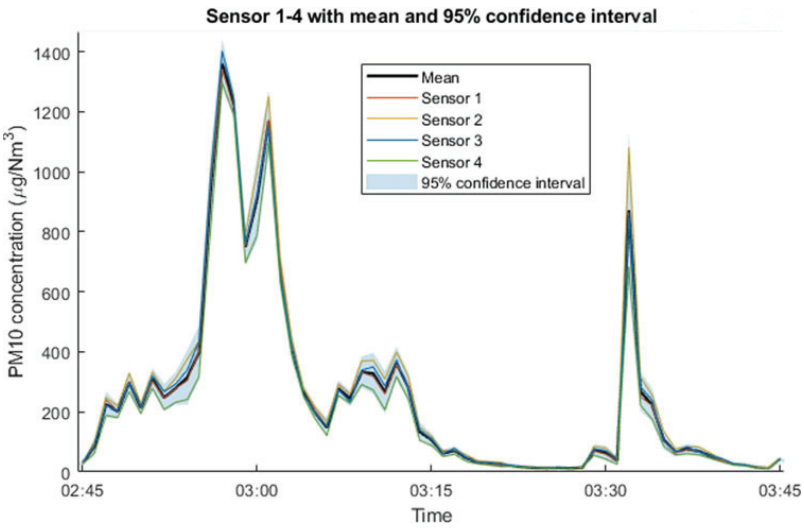

Fig. 11 PM10 values for sensors 1–4 together with the mean value and 95% confidence interval

facility, where it can be used to monitor the effect of changed procedures and other implemented efforts to reduce emissions.

While the reported PM2.5 and PM10 dust intensity values in the current study are given by the sensor factory settings, verification of the absolute values for the specific dust type is necessary for accurate reporting. Such verification and benchmark testing is currently in progress. The study does however, show accurately when and where the dust emissions are generated, which is important for implementation of reduction efforts. The sensors greatly compliment filter measurements, which can show composition and accurately measure average dust emissions over longer time periods. Analysis of dust particles can reveal which size fractions are the most dangerous, at which point the measurements from the sensors used here can reveal which processes yield the most of these fractions. This can be especially relevant for the working environment, for example to regulate when dust masks are necessary and which grade the filters need to be.

Conclusions

In this study, a micro-sensor system for dust monitoring was tested at a primary aluminium production site in Norway. Three groups of four sensors each were placed 2.4 m apart in the Robertson roof monitor above the electrolysis cells, where data for PM10, PM2.5, temperature, and humidity was gathered. Results from the study may be summarized as:

- The micro-sensors gave data that could be clearly correlated to the process operations.
- The variance within a sensor group of four in the same location typically gave an average 95% confidence interval of $\pm 6.5 \mu g/Nm^3$ over the course of a day.
- Temperature and humidity was not found to influence the dust measurements to a noticeable amount.
- A correlation between dust size fraction, amount and process activities was found, and hence it is plausible to use sensors for tracking dust from specific operations over time.
- The mean values over a reported concentration peak could vary based on sensor group location, which speaks to the spatial differences in dust concentrations and thus the importance of sensor coverage.
- Microsensors for monitoring of emissions and mitigation efforts has been found to be of potential great use. The sensors provide spatial reliability at a reasonable cost, which is harder to achieve when using more expensive and larger systems.
- Future work will include calibrating data against certified instruments for increased reliability in measurements.

Acknowledgements The authors would like to thank Hydro Aluminium with support from Morten Isaksen and the people working on the production site. The authors would also like to thank the Centre for Research-Based Innovation (SFI Metal Production), (NFR Project number 237738) for funding the project.

References

1. Milham S Jr. (1979) *Mortality in aluminum reduction plant workers*. Journal of Occupational Medicine. 21(7):475–80
2. Eduard W, Lie A (1981) *Influence of fluoride recovery alumina on the work environment and the health of aluminum potroom workers*. Scandinavian Journal of Work, Environment & Health. 7(3):214–22
3. Wong DS (2013) *Sources of potroom dust emissions from aluminium smelters*. Ph.D. thesis. The University of Auckland
4. Aarhaug TA, Ratvik AP (2019) *Aluminium primary production off-gas composition and emissions: An overview*. JOM, 71(9):2966–2977
5. Vinck N. (2018) *An update of the EU regulatory developments in industrial emissions, their implementation and impact on ferro-alloys production in Europe*. Infacon XV
6. Cusano G, Gonzalo MR, Farell F, Remus R, Roudier S, Sancho LD (2010) *Best available techniques (BAT) reference document for the non-ferrous metals industries*. Industrial Emissions Directive. 2010/75/EU
7. Kroslid D (2010) *Pimex for effektivt arbeidsmiljøarbeid i aluminiumindustrien*. Project report
8. European Comission (2017) *Measuring air pollution with low-cost sensors*. Ares(2017)5883418 - 01/12/2017. https://ec.europa.eu/jrc/sites/jrcsh/files/innovative_methods_such_as_sensors_are_being_evaluated_for_their_suitability.pdf. Accessed 8 Sept 2019
9. Norwegian Institute for Air Research (2018) *Annual report 2018 from NILU*. https://www.nilu.no/wp-content/uploads/2019/07/Aarsrapport_2018_Engelsk.pdf. Accessed 10 Sept 2019
10. Black DL, McQuay MQ, Bonin MP (1996) *Laser-based techniques for particle-size measurement, a review of sizing methods and their industrial applications*. Progress in Energy and Combustion Science, 22:267–306

C.3 Paper III

Oxidation of Metals (2021) 95:269–290
https://doi.org/10.1007/s11085-021-10023-0

ORIGINAL PAPER

Oxidation-Enhanced Evaporation in High-Carbon Ferromanganese

Håkon Aleksander Hartvedt Olsen Myklebust[1] · **Stefan Andersson**[2] · **Gabriella Tranell**[1]

Received: 15 September 2020 / Revised: 1 February 2021 / Accepted: 9 February 2021 /
Published online: 20 March 2021

Abstract

Thermal fume formation is a problem in manganese ferroalloy production and the metal production industry at large. A better understanding of the mechanisms of fume formation and the operational parameters affecting the fume formation rate may help in reducing and managing fuming. This paper aims to investigate the effects of oxygen content and gas flow rate on the fuming rate and fume particulate properties for liquid high-carbon ferromanganese. The fuming rates were attained experimentally by measuring the fume flux with respect to oxygen content and gas velocity above the metal melt. The generated fumes were also characterized in terms of particle size and element distribution between fume and melt. The fuming rates were found to steadily increase with increasing oxygen content and flow rate of the gas up to a point where the curve flattens, following theoretical predictions. However, the highest flux values measured were above the theoretical limitations of the evaporation flux in vacuo given the alloy bulk composition. It is hypothesized that the high rate of fuming is caused by an increased manganese activity at the alloy surface due to local decarburization of the alloy in contact with the oxidizing gas.

✉ Håkon Aleksander Hartvedt Olsen Myklebust
hakon.a.h.olsen@ntnu.no

Stefan Andersson
stefan.andersson@sintef.no

Gabriella Tranell
gabriella.tranell@ntnu.no

[1] Norwegian Institute of Science and Technology, Alfred Getz Vei 2, 7034 Trondheim, Norway

[2] Sintef Energy, Alfred Getz Vei 2, 7034 Trondheim, Norway

Graphical Abstract

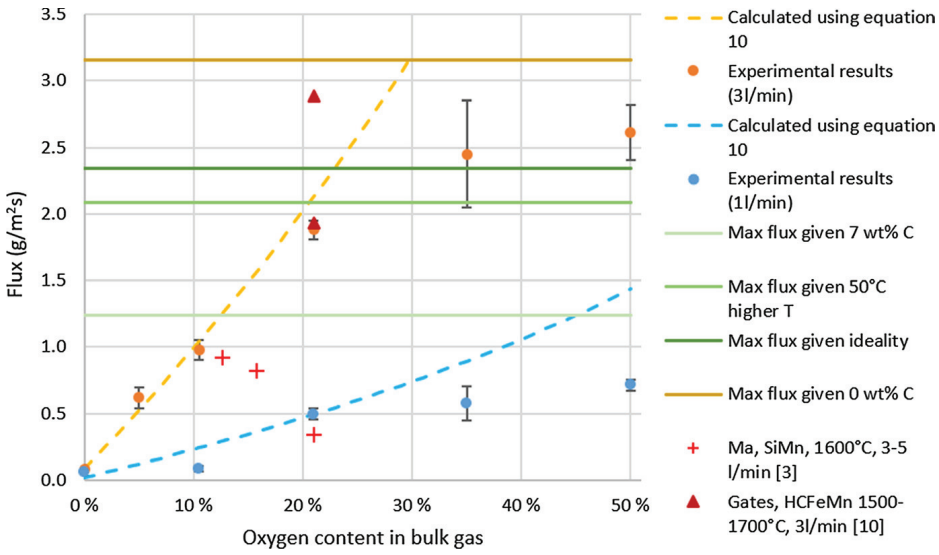

Keywords Modelling · Fume formation · Oxidation · Ferromanganese

Introduction

Manganese is extensively used as an alloying element for the iron- and steelmaking industry in the form of ferromanganese and silicomanganese [1]. The production of ferromanganese commonly takes place in an electric submerged arc furnace through carbothermic reduction of manganese ores. Ferromanganese alloys can be classified into high-carbon ([C]-7.0wt%), medium-carbon ([C]<2.5wt%), and low-carbon ([C]<0.5wt%) grades [2]. The liquid ferromanganese metal is cast at temperatures above 1500 °C in air, where the vapor pressure of manganese is high, typically > 0.01 atm.

Reactions between the Mn vapor and oxygen in the atmosphere leads to the formation of oxide fumes, and these fumes contribute not only to product losses, but are also detrimental to the working environment [3]. Early studies focusing on modelling of the generic metal-oxidizer system by Wagner [4], Turkdogan et al. [5] and Rosner [6] have laid the theoretical foundation for modelling evaporation and oxidation rates. However, development and validation of kinetic models for more specific applications such as high-carbon ferromanganese (HCFeMn) have not yet been performed.

The main goal of the current study is to experimentally investigate the effects of increased oxygen content and gas flow rate over liquid high-carbon ferromanganese (HCFeMn) on the fuming/oxidation rate, and to evaluate these results using the methodology for oxidation-enhanced evaporation developed by Rosner

[6] and Turkdogan et al. [5]. Furthermore, an additional goal is to increase our knowledge of fume-oxide particle growth and clustering in ferromanganese fumes under these conditions, as well as studying minor element distribution between liquid metal and condensed fumes as a function of gas flow rate and composition.

Theory and Literature

Turkdogan et al. [5] established the theory of direct metal oxidation based on metal evaporation, where the formation of oxide mists enhances the fume flux. Theory states that the metal evaporation rate is rate-limiting at ambient oxygen levels above a certain "critical" value, and that below this value, for a given gas flow-rate and temperature, the flux is directly proportional to the ambient oxygen partial pressure following Eq. 1.

$$J_i = \frac{\alpha h}{RT} p_{O_2} \tag{1}$$

where J_i is the fume flux in g/m^{2}s, R is the ideal gas constant, T is the temperature in Kelvin, p_{O_2} is the ambient partial pressure of oxygen in pascal, h is the average film mass-transfer coefficient for the transport of oxygen through the aerodynamic diffusion boundary layer which is calculable for known flow conditions, and α is the

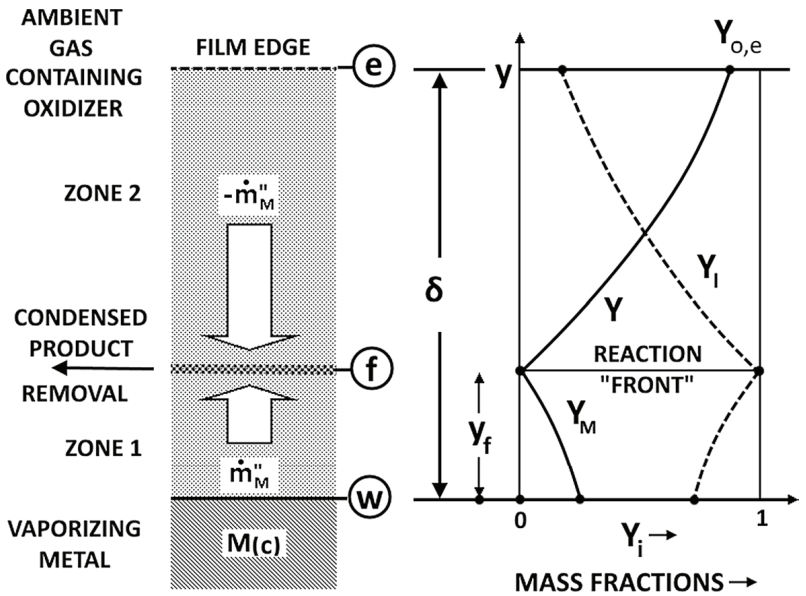

Fig. 1 Reaction and condensation-enhanced metal vaporization; two-film model and notation. Redrawn from Rosner [6]. Here, e denotes the film edge, f the reaction front, w the liquid surface, $\dot{m}''_M$ the metal flux, Y the mass fraction, I the inert gas, M the metal, and O oxygen. y is the distance from the surface and δ the film thickness, often referred to as the diffusion layer thickness

number of moles of metal vapor required to combine with one mole of oxygen, and is valid for any metal.

Ma et al. used Factsage to generate a stability diagram for manganese and its oxides for different oxygen partial pressures and temperatures, where it can be seen that at 1500 °C, oxygen pressures above 10^{-15} atm will lead to the formation of manganese monoxide (solid), and as the temperature decreases, higher oxides become stable. The oxide formation happens through several reactions which includes a number of phases: Mn(g), MnO(s), $Mn_3O_4(s_1)$, $Mn_2O_3(s_2)$, and MnO_2(s) where $Mn_3O_4(s_1)$ and $Mn_2O_3(s_2)$ represent tetragonal (low-temperature) Mn_3O_4 and cubic (high-temperature) Mn_2O_3, respectively [7, 8]. At the surface temperature used in this work (1550 °C), the relevant phases for the diffusion layer are Mn(g) and MnO(s) which further oxidizes and agglomerates in the bulk gas.

Rosner's work on this "oxidation-enhanced" evaporation [6] confirmed the results of Turkdogan et al. in highly dilute isothermal systems, and also found additional effects based on the condensation process as a limit for fuming in oxidizer-rich ambient gasses. He described the system graphically as shown in Fig. 1, and while both Rosner and Turkdogan's work was generic, their calculations are applicable for the Fe–Mn-system and both Fe and Mn are mentioned alongside Ni, Co and Cu in their work, and as such the metal "M" in the following equations relates to Mn in the system studied in this work. The figure describes how the concentration of metal and oxygen goes down toward the reaction "front" inside the diffusion layer where the concentration of both is 0 as the oxidation reaction is very fast and the condensed product no longer affects the diffusion and reaction. The higher concentration of oxygen, the steeper the concentration curve in zone 2 will be, and the closer to the surface the reaction "front" will be. Similarly a higher fraction of metal vapor at the surface increases the diffusion rate in zone 1 which pushes the reaction "front" away from the surface until it again is in equilibrium with the diffusion rate of oxygen. Both cases would increase the flux of metal from the surface, and as such would increase the fuming rate.

Rosner's model is explained in further under the modelling section, and is an integral part of this work.

You et al. [2] studied evaporation of manganese during the oxygen refining process experimentally, and confirmed that due to the high vapor pressure of manganese in ferromanganese melts there is a significant loss due to evaporation. An empirical equation for the evaporation loss was derived based on a sampling system, and is shown in Eq. 2:

$$\frac{(W_{\mathrm{Mn}})_{\mathrm{evap}}}{W_{\mathrm{metal}}} = \beta \cdot \sum_{i=1}^{n} \left(\frac{(P_{\mathrm{Mn}})_i}{\sqrt{T_i}} \cdot (t_{i+1} - t_i) \right) \tag{2}$$

where $(W_{\mathrm{Mn}})_{\mathrm{evap}}$ is the evaporation loss of manganese in kilograms, W_{metal} is the amount of hot metal charged(iron), "i" is the order of sampling, and $(t_{i+1}\text{-}t_i)$ is the time interval between sampling in minutes. The apparent vaporization coefficient, β, was found to be significantly affected by the fraction of top blown oxygen, which concurs with the previously discussed theories.

Lee and Kolbeinsen [9] studied the kinetics of the oxygen refining process for high-carbon ferromanganese, where they found that when the vapor pressure of manganese vapor becomes high, the rate of manganese loss is controlled by the mass transfer of manganese vapor through the diffusion boundary layer adjacent to the interface of melt and gas, and that the formation of MnO mist increases the melt temperature. As the temperature is an important factor in the evaporation rate of manganese, this can potentially have an impact on the fuming rates.

Gates et al. [10, 11] also studied fuming rates in ferromanganese, with a focus on the effect of water vapor in the bulk gas. The rate of fuming was found to decrease with increased water content in the atmosphere and that fume particles were found in larger clusters rather than fine dust with moist atmospheres. While this effect was not fully explained, a decrease in temperature with the addition of water to the atmosphere may partly explain the results. They also found notable amounts of ZnO in the dust from their experiments with higher water vapor content.

Experimental Procedures

The experimental setup is shown in Fig. 2, and has been used in previous studies by Kero et al. [12], Næss et al. [13], Gates et al. [10], and Ma et al. [7]. A standard grade HCFeMn was used with a composition as shown in Table 1. The gas flow rate was controlled with a mass flow controller in each gas tube allowing for controlled mixing of oxygen and nitrogen, with the total flow varying from 1 to 5 l/min, which

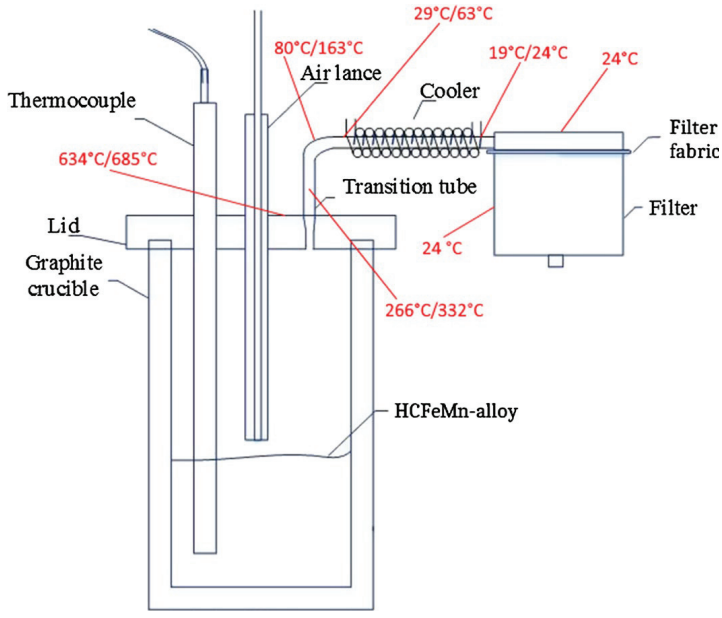

Fig. 2 The experimental setup with average temperatures (with/without gas flow) as measured during the 16 first experiments. The experiments were carried out with a temperature of 1550 °C in the alloy

Table 1 Chemical composition of the HCFeMn used in the experiments as measured by ICP and given in WT%

Mn	Fe	C	P	Na	Si
72.1%	12.3%	6.5–7.5%	0.137%	0.06%	0.02%
S	Mg	K	Pb	Al	Zn
0.009%	0.004%	0.003%	0.003%	0.001%	0.001%

The range in the carbon content is specified by the supplier

corresponds to a gas velocity of approximately 5.28 to 26.39 m/s at the lance tip. Each experiment was subjected to a gas flow for at most 20 minutes at 1550 °C, and temperature measurements were conducted at several points between the crucible and filter before and after the gas flow was initiated. Experiments exhibiting a high fume formation had their gas flow duration cut short to avoid clogging of the gas outlet system, and in the experiments with the highest flow rate the fume formation was too high for the system to handle leading to constant fume leakage through the safety valve. The latter lead to the flux data from experiments with 5 l/min flow rate being removed from the flux data pool as the fluxes measured were very inaccurate.

After each experiment, the dust from the fume was collected at three sites: the tube connecting the cooler to the lid, named the "transition tube", the cooler, and the filter. An average of more than 70% of the dust was collected in the filter, 10% in the cooler and the rest in the transition tube. Figure 2 shows the average deposition temperatures, with the first number showing the temperature just before the gas flow was turned on, and the second showing the temperature in the middle of the experiment. The deposition temperatures measured was considered sufficiently established after measuring across 16 experiments, and further measurements were not deemed necessary for the remainder of the experiments.

Table 1 shows the chemical composition of the metal used in the experiments as measured by inductively coupled plasma-mass spectroscopy (ICP-MS). The range in the carbon content is specified by the supplier, but since the experiment occurs in a graphite crucible, the bulk carbon concentration is expected to approach saturation during the experiment.

After each experiment, the amount of dust in each part of the outflow system was measured by comparing the weight of each individual component before and after the experiment. The components were thoroughly cleaned and dried in between each experiment. As soon as the measurements were completed, the dust from each site was gathered for further studies. The resulting mass flux (J_m) from each experiment was calculated from the total mass increase in the filter system, following Eq. 3:

$$J_{\mathrm{m}} = \mathrm{m}/\mathrm{A}t \tag{3}$$

where m is the measured dust mass, A is the alloy-to-air surface area as measured by the crucible cross-section, and t is the holding time. There was no observable slag formation during the experiments.

To investigate the importance of oxygen access to the reactions, experiments were conducted with different gas mixtures between oxygen and air. Table 2 shows the list of all experiments performed for this study. Synthetic air, with a composition

of 21% O_2 and 79% N_2, was used together with pure N_2 and O_2 to reach the required concentrations. All gasses were at 5.0 quality, with maximum amount of H_2O equal to 5ppmX.

Dust generated during fuming was analyzed using ICP-MS, laser diffraction (LD), and imaged by scanning electron microscopy (SEM), to see how both elemental and size distributions are affected by the varying flow rates and oxygen concentrations. LD is a method of measuring the particle size distribution by measuring the angular variation in intensity of light scattered as a laser beam passes through a dispersed particulate sample [14], and in this work the equipment used for LD was a Coulter LS230 [15].

Modelling

Rosner derived a formula for the critical transition pressure of oxidizing agents valid even when approaching pure gaseous oxidizers, shown in Eq. 4. Assuming oxygen contents below this value, he introduced the formula shown in Eq. 6, which defines the flux ratio between a system with no oxygen in the ambient gas and one with a given oxygen partial pressure;

$$Y^*_{O,e} = 1 - \left(\frac{1}{1 - Y_{M,w}}\right)^{-(r/D)(F^*_{RXN}-1)} \tag{4}$$

where $Y^*_{O,e}$ is the critical mass fraction of oxygen in the ambient gas, $Y_{M,w}$ is the mass fraction of metal vapor at the gas-metal interface, r is the mass of oxidizer that

Table 2 Experimental matrix, all experiments performed at 1550 °C, with a holding time of 20minutes

O_2-content (%)	Gas flow rate (l/min)	No of parallels
0	1	3
10.5	1	4
21	1	3
35	1	2
50	1	2
0	3	3
5	3	5
10.5	3	3
21	3	3
35	3	6
50	3	3
10.5	5	2*
21	5	3*
35	5	4*

*5 l/min flow rate experiments were not viable for flux analysis as the high flow lead to substantial fume leakage, but dust was still analyzed. Between 2 and 6 experiments were successfully performed with each set of parameters

reacts with a unit mass of metal vapor, F^{*}_{RXN} is the critical reaction factor defined in Eq. 5, and D is an oxidizer-to-metal diffusion density ratio defined by Eq. 8.

$$F^{*}_{RXN} = \dot{m}''_{\mathrm{vac}} / \dot{m}''^{0} \tag{5}$$

$$F_{RXN} = 1 + \frac{(\overline{D_{O-I}\rho})_2}{(\overline{D_{M-I}})_1} \cdot \frac{1}{r} \cdot \frac{ln[1/(1 - Y_{O,e})]}{ln[1/(1 - Y_{M,w})]} \tag{6}$$

$\dot{m}''^{0}$ is here the flux given no homogeneous chemical reaction, which in our case relates to an ambient oxygen partial pressure at effectively zero, and $\dot{m}''_{\mathrm{vac}}$ is the maximum evaporation flux which can be given by the Hertz–Langmuir expression shown in Eq. 7 according to kinetic theory:

$$\dot{m}''_{\mathrm{vac}} = \frac{\alpha_s}{4} \cdot \frac{p_{\mathrm{Mn,eq}}}{kT_w} \cdot \left(\frac{8kT_w}{\pi m_{\mathrm{Mn}}} \right)^{1/2} \cdot_{\mathrm{Mn}} \tag{7}$$

where α_s is the sticking factor, which describes the ratio between the number of molecules that desorb and adsorb from the same surface during a time interval, and is considered to be 1 in the case of a liquid metal. $p_{\mathrm{Mn,eq}}$ is the equilibrium partial pressure of manganese vapor at the metal surface, k is Boltzmann's constant, T_w is the temperature at the metal surface, and M_{Mn} is the molecular mass of manganese.

$$D = (\overline{D_{\mathrm{O\text{-}I}}\rho})_2 / (\overline{D_{\mathrm{M\text{-}I}}})_1 \tag{8}$$

Here $(\overline{D_{i-j}\rho})x$ is the mean Fickian binary diffusion coefficient for species i and j multiplied by the total mass density of the gas mixture in zone x relating to the zones in Fig. 1. O relates to the oxidizer, I the inert gas, and M the metal vapor. $Y_{i,j}$ is the mass fraction of species i at surface j relating to Fig. 1.

With this, the critical oxygen fraction where evaporation becomes the rate limiting factor can be calculated if the flux with no oxidizer present can be calculated or found through experiments. The theoretical fluxes given an ambient oxygen partial pressure below this critical fraction can also be calculated.

This model based on Rosner's reaction factor F_{RXN} [6] was used alongside the experimental data to predict the experimental yield. The model was based on Eq. 6, where the experimental value for 0% O_2 is multiplied with the calculated reaction factor F_{RXN} at each point. The values for diffusion coefficients and mass fractions at the different boundaries were calculated for each 1% O_2 starting at 0%, and used to generate the F_{RXN} for each point using Eq. 6. The flux was then estimated at each point according to Eq. 9.

$$J_i = J_{0\%} \cdot F_{RXN,i} \tag{9}$$

where i denotes the O_2 percentage for each individual flux value and reaction factor. When utilizing this model it is important to note that if any assumptions concerning either the diffusion density ratio, mass fraction of the metal in the vapor, or oxygen in the bulk gas are compromised, then the model values from Eq. 6 must be

recalculated. This is due to the flux calculation being very sensitive with respect to these parameters.

The theoretical value for the manganese evaporation flux in vacuo was also calculated using the Hertz–Langmuir expression as shown in Eq. 7. In theory this value should constitute an "upper bound" which the flux values would converge toward as the oxygen content is increased [6]. The partial pressure of manganese can be calculated from the formula for Gibbs free energy, which rearranged for partial pressure is shown in Eq. 10 [16]:

$$p_{\mathrm{Mn,eq}} = 101325 \cdot a_{\mathrm{Mn}} \cdot exp\left(\frac{241780 - 104.46 \cdot T}{-8.314 \cdot T}\right)(Pa) \tag{10}$$

where a_{Mn} is the activity of manganese in the melt and T is the temperature in Kelvin. The activity of manganese was calculated using Factsage 7.3 [8] with chemical compositions given in Table 1, and an initial carbon content of 7wt%, which represents the system's carbon saturation. The software performs Gibbs energy minimization to calculate the distribution of elements in the different phases, using among others the Gibbs-Duhem equation. This equation does not take surface effects into consideration.

Diffusion coefficients of Mn–N_2 were calculated using Chapman–Enskog kinetic theory [17, 18] for an intermolecular interaction potential in the form of a Morse potential in a similar manner as performed previously for the Mn–Ar system [19]. The interaction potential was calculated using quantum chemistry. More specifically, the CCSD(T) (coupled cluster with single and double excitations and a perturbative treatment of triple excitations) method was used with the aug-cc-pVQZ basis set [20, 21]. The CFOUR code [22, 23] was used for all CCSD(T) calculations.

Diffusion coefficients of a gas mixture of A and B were calculated by [18]

$$D_{\mathrm{AB}} = \frac{3}{16}\sqrt{\frac{2(RT)^3}{\pi}\left(\frac{1}{M_{\mathrm{A}}} + \frac{1}{M_{\mathrm{B}}}\right)}\frac{1}{N_A p \sigma_{\mathrm{AB}}^2 \Omega_{D,\mathrm{AB}}} \tag{11}$$

where σ_{AB} is the average of the individual hard-sphere radii

$$\sigma_{\mathrm{AB}} = \frac{1}{2}(\sigma_{\mathrm{A}} + \sigma_{\mathrm{B}}) \tag{12}$$

and $\Omega_{D,AB}$ is the temperature-dependent *collision integral*, which describes the deviation of a real gas from the ideal hard-sphere gas behavior. In the case of Mn and N_2 the interaction potential has been fitted to a Morse potential expression, for several angles of approach, θ, of the Mn atom toward the N_2 molecule:

$$V(R,\theta) = D_{e,\theta}\left(e^{-2a(R-R_{e,\theta})} - 2e^{-a(R-R_{e,\theta})}\right) \tag{13}$$

where R is the center-of-mass distance between Mn and N_2. By placing the N_2 bond vector along the z–axis and the N_2 center of mass at the origin, one can express the system in spherical coordinates R, θ, ϕ. R then lies along the vector between the Mn atom and the N_2 center of mass and the θ angle is the angle between this vector and

the N_2 bond vector. The ϕ angle describes rotation of Mn around the N_2 bond. Subsequently, the *effective* interaction potential was calculated by averaging the angle-dependent potential over all Mn–N_2 angles:

$$V_{\text{eff}}(R) = \frac{\int_0^{\pi}\int_0^{2\pi} V(R,\theta)\sin\theta \mathrm{d}\theta\mathrm{d}\phi}{\int_0^{\pi}\int_0^{2\pi}\sin\theta\mathrm{d}\theta d\phi} = \int_0^{\frac{\pi}{2}} V(R,\theta)\sin\theta\mathrm{d}\theta \tag{14}$$

with the second equality being due to the potential being cylindrically symmetric around the N_2 bond and also symmetric with respect to approach of Mn toward either end of N_2. $V_{\text{eff}}(R)$ was thereafter fitted to a new set of Morse parameters:

$$V_{\text{eff,fit}}(R) = D_{\text{e,eff}}\left(e^{-2a_{\text{eff}}(R-R_{\text{e,eff}})} - 2e^{-a_{\text{eff}}(R-R_{\text{e,eff}})}\right) \tag{15}$$

with $D_{\text{e,eff}} = 88.2$ K, $R_{\text{e,eff}} = 4.93$ Å and $a_{\text{eff}} = 1.04$ Å^{-1}. Using these parameters, values of $\Omega_{D,\text{AB}}$ were interpolated from tabulated values for Morse potentials for relevant temperatures [24].

Diffusion coefficients of the N_2-O_2 gas mixture were also calculated using Eq. (11) but with literature Lennard-Jones parameters [18] and the corresponding expressions for the collision integral. This resulted in diffusion coefficients of 3.66 cm^2/s for Mn–N_2 and 4.37 cm^2/s for O_2–N_2 at 1550 °C and a pressure of 1 atm.

Results

Flux

Table 3 shows the average fluxes along with the calculated 95% confidence interval for each set of experimental parameters. It should be noted that experiments with a flow rate of 5 l/min were not analyzed for flux due to the previously

Table 3 Flux results, mean values and 95% confidence intervals, for the experiments performed in this study

O_2-content (%)	Gas flow rate	Mean flux (g/m^{2}s)	95% CI (g/m^{2}s)
0	1	0.0637	0.0328
10.5	1	0.0833	0.0205
21	1	0.4934	0.0412
35	1	0.5731	0.129
50	1	0.7151	0.0407
0	3	0.0841	0.0272
5	3	0.6182	0.0798
10.5	3	0.9767	0.0719
21	3	1.8794	0.0703
30	3	2.4501	0.4024
50	3	2.6120	0.2097

mentioned loss of fumes, but the dust was analyzed for size distribution in Sect. 4.3.

Figure 3 shows the measured dust fluxes from the experiments, with their respective 95% confidence intervals. The flux values for both 1l/min and 3l/min gas flow increase steadily at lower oxygen contents, before the curve flattens at higher oxygen contents.

Elemental Distribution

The distribution of major elements in the dust for varying bulk oxygen concentrations as well as for the HCFeMn alloy used is shown in Fig. 4 together with SiMn pilot scale results from Ma et al. [30] and shows clear relations between the concentration of most of the elements and the oxygen content in the bulk gas, i.e. for all the trace elements except phosphorous, the concentration is higher in the dust than in the metal. The elements Zn, Mg, Pb, Na, S, and Al show a general trend of lowered concentration with increasing oxygen in the bulk gas, with Zn having an especially high concentration at low O_2 levels. Si has a distinct peak at and around the regular oxygen level of 21%, whereas the K concentration is at its lowest in the dust at the same level. P and Fe both increase significantly at the 35 and 50% level, while staying relatively flat at lower O_2 concentrations.

Figure 5 shows a SEM image of typical dust particles from an experiments with 3l/min flow rate of synthetic air, showing the structure of the particles. These are primarily cF8 MnO-crystals, given that more than 90wt% of the dust, excluding oxygen, is manganese. The green color of the dust from the filters matches the characteristic green color of MnO-crystals.

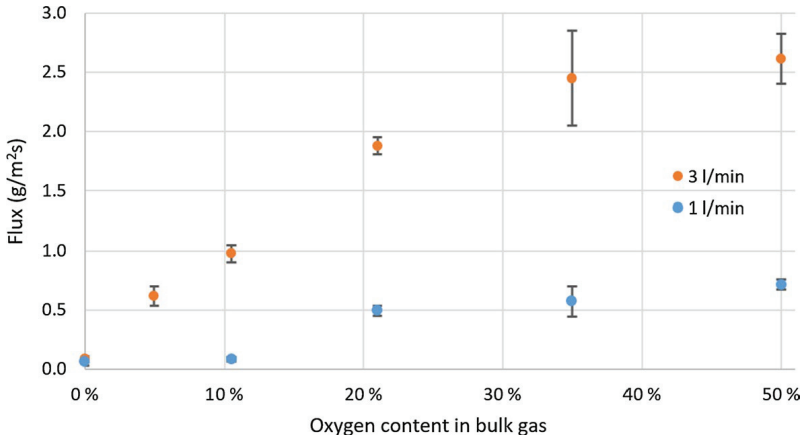

Fig. 3 Experimental data shown with 95% confidence interval bars

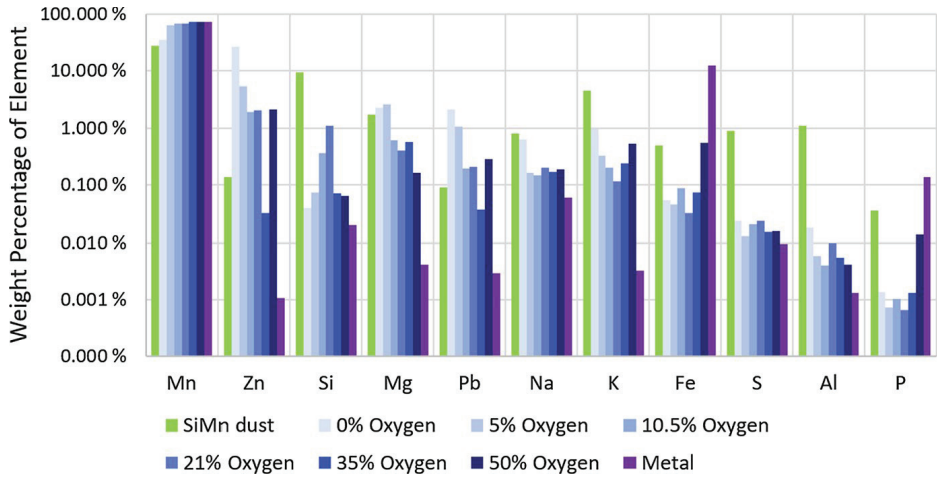

Fig. 4 Element distribution for the most relevant elements (except oxygen) as measured by ICP-MS. The purple bars refer to samples taken from the metal chips used in the experiments, while the remaining blue bars are from dust samples taken from the filter in each experiment. The green bars show SiMn pilot scale results from Ma et al. [30]. Note the logarithmic scale on the Y-axis

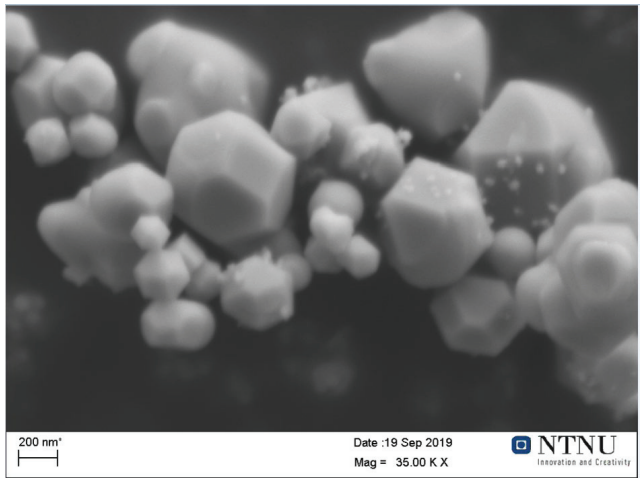

Fig. 5 SEM picture of filter dust particles from an experiment with 3l/min flow rate of synthetic air

Size Distribution

Manual particle counting (PC) was performed on SEM-images of the dust from the filters. This size distribution is shown in Fig. 6a, with the mean(median) values being 113(98)nm, 116(111)nm and 1008(719)nm for 5l/min 35% O_2, 5l/min 10% O_2, and 1l/min 35% O_2, respectively. Varying oxygen content in the gas did not result in significantly different particle size distribution.

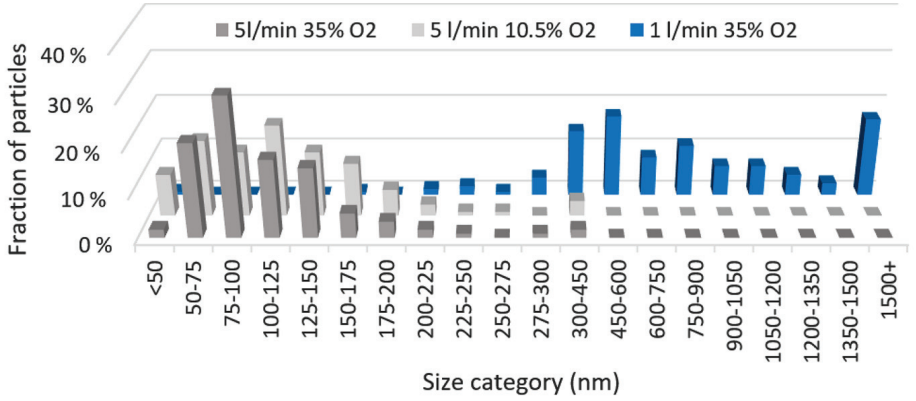

(a) Size distribution of particles from the filter dust of three experiments, measured manually from SEM-images. Note the change in box width from 300nm.

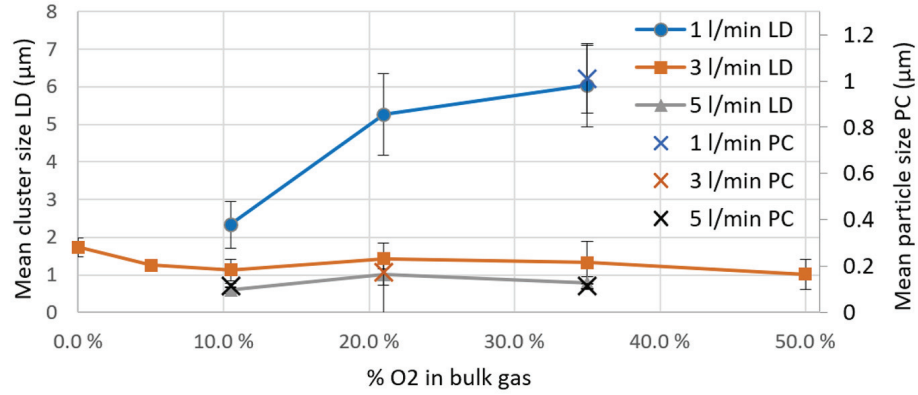

(b) LD and PC results, showing average cluster and particle sizes for each flow rate with respect to the oxygen partial pressure. Error bars show the 95% confidence interval given the data.

Fig. 6 Size distribution measured with laser diffraction and particle counting

LD was also performed on the filter samples from each category of bulk gas oxygen content and flow rate, and the resulting average particle sizes for each flow rate are shown in Fig. 6b with respect to the partial pressure, together with the average particle size from the PC. The results show a clear correlation between the mean cluster size measured with LD and the mean particle size measured through PC, with the mean cluster size being around six times larger than the mean primary particle size. The bulk oxygen concentration only had a significant impact on the dust from the 1l/min experiments, and it overall had a lesser impact on the particle and cluster size compared to the flow rate.

Discussions

Flux

Figure 7 shows the relation between the measured experimental flux values and the ones calculated with the formula from Rosner, together with the maximum evaporation flux calculated with Eq. 7 given the experimental conditions. It also includes data from Ma et al. [7] and Gates et al. [10] for comparison, and several maximum evaporation fluxes calculated given different assumptions. There is a good correlation between the calculated values and the experimental values up to a certain point, but there is a clear disparity between the highest experimental flux values and the theoretical maximum flux limited by Mn evaporation in vacuo.

Possible explanations for these results are:

1. The activity and subsequent vapor partial pressure of manganese on the surface is higher than calculated
2. The temperature at the surface is higher than assumed
3. The parameters or assumptions used in this paper are incorrect

To evaluate the activity of manganese it is useful to look at the oxygen utilization in the system, which gives insight into reactions at the metal surface:

Figure 8 shows the average oxygen utilization in the dust measured for the varying gas flow rates and oxygen concentrations. The oxygen utilization was typically between 15 and 50%, decreasing with increasing bulk oxygen concentration in bulk gas, and was somewhat higher for 3 l/min than for 1 l/min. The increase when comparing different flow rates is presumably because of the shorter diffusion distance for oxygen at higher flow rates across the melt, which in turn allows more of the oxygen to diffuse toward the surface. The decreasing utilization with increasing bulk oxygen concentration is assumed to be due to the evaporation flux limitations, which has been shown to lower the fume formation flux more with increasing bulk oxygen concentration compared to the theoretical flux given no such limit.

When the oxygen content in the gas is increased and a high flow makes the diffusion layer thin, the distance between the reaction front and the metal surface grows very short. Given such circumstances, the assumption that the reaction front is essentially a surface and has no volume might not hold true, and the chance that some oxygen molecules pass the front and reach the surface before reacting to evaporated manganese is no longer zero.

If such conditions leads to oxygen molecules reaching the surface, this has two potential interesting interactions with the fuming rate:

1. Oxygen reacts directly with liquid manganese, forming oxides on the surface.
2. Oxygen reacts with the carbon at the surface to form CO-gas. This reduces the carbon content at the surface, increasing the Mn activity as previously mentioned.

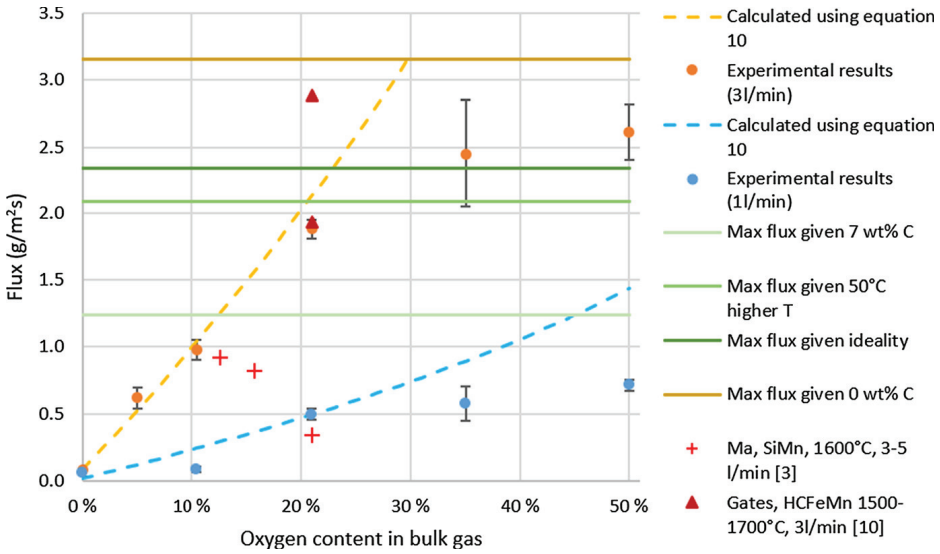

Fig. 7 Relation between the measured experimental flux values and the ones calculated with the formula from Rosner [6]. Includes the maximum evaporation flux, calculated using Eqs. 10 and 16 given four different assumptions affecting the Mn(g) partial pressure. The calculated line for 1 l/min uses 21% oxygen as the baseline due to instability in the fume generation at the lowest levels of oxygen and flow. Data from Ma et al. [7] and Gates et al. [10] are shown for comparison, but the difference in temperature, flow rate, and/or metal composition must be considered. The higher fluxes correspond to the higher flow rate and temperature for Ma and Gates, respectively

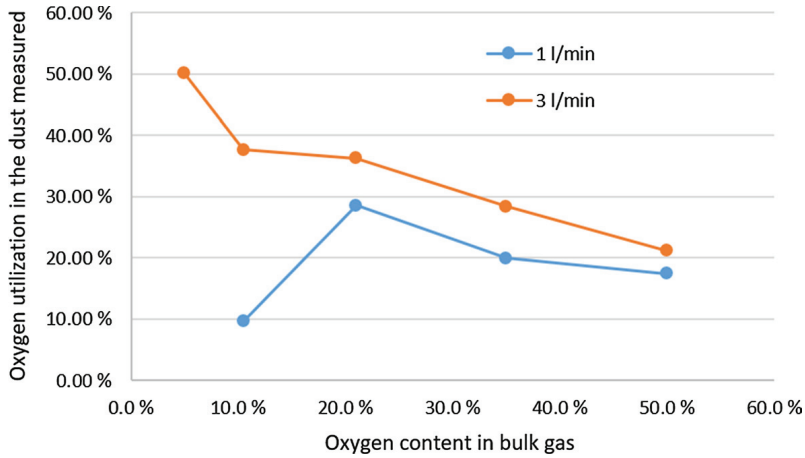

Fig. 8 Oxygen utilization over the bulk gas oxygen concentration calculated from the dust weight and oxygen flow in the experiments. The value for 10% O_2 at 1 l/min appears to be an outlier

Little to no slag was observed during the experiments however, which should have been the case given interaction number one. This makes direct oxidation of carbon the most likely case if oxygen has reached the surface during these experiments. If that is the case, the surface could become decarburized, as the diffusion rate generally is much lower in liquids compared to gas, and as such the rate of carbon diffusing to the surface would realistically be much lower than the rate it reacts with oxygen diffusing to the surface. At temperatures between 1550 and 1650 °C, oxygen is more reactive with carbon than with manganese [2], which further supports the theory of decarburization at the conditions used in this study. Furthermore, above 1650 °C the limiting factor for decarburization is carbon transfer to the gas/liquid interface, and carbon contents in the bulk as low as 0.5-1% can be achieved at temperatures approaching 1800 °C and CO-pressures approaching 1 atm [25].

This is of particular interest, as the most important element affecting the activity coefficient of manganese in the melt, and subsequently the Mn vapor pressure above the liquid melt, is carbon. Lee [26] presented a formula for the activity coefficient of manganese based on the assumption that manganese and iron behave ideally, which is shown in Eq. 16:

$$\begin{aligned} ln(\gamma_{\mathrm{Mn}}(\mathrm{Fe–Mn–C})) =& (-0.4822 + 576.7/T)x_C + (5.1498 - 10842/T)x_C^2 + \\ & (-25.821 + 8289.7/T)x_C^3 - 4943.8x_C^4x_{Fe}^5 \end{aligned} \tag{16}$$

where n_i is the atom fraction of species i for both equations and T is the temperature in Kelvin.

Given that the melt in our system is in contact with solid carbon, the graphite crucible, we can assume carbon saturation in the bulk melt. Using the approximation for carbon saturation levels done by Lee [26], we get a C atom fraction of 0.271, which when entered into Eq. 16 gives a Mn activity coefficient of 0.59 for a total Mn activity of 0.375. The value calculated with the Factsage software as previously mentioned was slightly lower at 0.345.

If we assume that the air blown on the alloy to a significant extent reaches the melt surface and decarburizes the melt surface, the result is a higher Mn concentration at the surface than in the bulk, which coupled with a higher activity coefficient results in an associated higher Mn activity and Mn vapor pressure. As the Fe-Mn system behaves close to ideally [27], the activity coefficient is close to 1, and the activity in our system approaches 0.856. Table 4 shows the maximum evaporation flux given different assumptions calculated with Eq. 7, 10 and 16 together with the Mn(l) activity for the same assumptions. The experimental flux values compared to the four maximum evaporation fluxes from Table 4 are shown in Fig. 7, and in reality the maximum evaporation flux should be in somewhere between these values:

Assuming no other changes, there is a 1:1 correlation between the Mn(l) activity and the evaporation flux. Changing the carbon content from 7 to 0 wt% more than doubles the activity, which then more than doubles the evaporation flux. This shows how sensitive the system is to changes in the carbon content, as higher carbon content both lowers the concentration of manganese and leads to a negative deviation in the manganese activity.

Table 4 Maximum evaporation fluxes calculated with Eqs. 7, 10 and 16 based of various assumptions, with the intermediary Mn(l) activity

Assumption	Mn(l) activity	Flux (g/m^2s)
7wt% carbon, Factsage Mn(g) partial pressure	0.345	1.239
7wt% carbon, theoretical Mn(l) activity	0.375	1.381
7wt% carbon, theoretical Mn(l) activity, +50 °C	0.375	2.085
7wt% carbon, ideal Mn(l) activity	0.636	2.342
no carbon, ideal Mn(l) activity	0.856	3.152

Theoretical values are calculated with Eq. 16 taking into account negative deviation from ideality between Mn, Fe, and C. Ideal values are simply the molar concentration of Mn given the different carbon contents

Ma [28] studied the fuming rates from silicomanganese where 0-2 l/min of Argon was added to a static 3 l/min flow rate of synthetic air. The result was an average flux increase of around 142 and 167% for additional 1 and 2 l/min Argon compared to just the synthetic air. This aligns with the results of the current study, albeit the increase was lower here, which implied that the rate of oxygen toward the surface and the boundary layer thickness is of greater importance than the partial pressure of oxygen in the bulk gas. The much lower flux with SiMn when comparing the data for experiments with 3 l/min total flow rate likely stem from the difference in materials, that there is a lower fuming rate from SiMn compared to HCFeMn.

By studying the results shown in Fig. 7 it can be seen that just assuming ideality or an increased surface temperature is not enough to bring the evaporation flux above the experimental values. Assuming a carbon concentration on the surface close to 0 would be enough however, and any combination of lower carbon content, lower activity coefficient, and higher temperature could explain the high fluxes measured.

As the crucible is heated through induction, which usually implies good stirring, the melt should be reasonably isothermal, but exothermic reactions might increase local temperatures [9]. From reaction equations and Gibbs energy calculations [7, 8], one mole of liquid manganese evaporating and then reacting with half a mole of oxygen gas to form MnO(s)-particles yields a net positive of 223.43 kJ. A mean of 0.00757 g/s oxygen reacts to form MnO_x during the 3 l/min 50% O_2 experiments. the O:Mn stoichiometry X in MnOx dust is presumably close to 2 in the final dust, and it would as such be a reasonable assumption that half of that amount reacts inside the diffusion layer, which leads to a reaction heating effect of around 52.85W. Reactions between carbon and oxygen at the surface would yield additional heating effect, but the amount is not quantifiable given the accessible data.

Another note on activities can be made when comparing the fluxes measured here with the experiments done on silicomanganese by Ma et al. [7]. The average flux at 1550 °C with 3l/min synthetic air was measured to be around 0.12 g/m^2s, with a majority of the dust being from manganese and less from silicon, far below the 1.88 g/m^2s measured with ferromanganese. The negative deviation from ideality from mixing Mn and Si is particularly strong, with the activity of Mn being in the area

of 0.1-0.2 given the 68wt% Mn, 17.6wt% Si in the aforementioned silicomanganese [29].

The fluxes measured by Gates et al. [10, 11] were comparable to the ones measured in this study for dry air at the same flow rate and similar temperature, with a downward trend as the water vapor partial pressure was increased and a larger flux when the temperature was increased. The ZnO found in the dust from high vapor experiments is also similar to the increased ZnO fraction in the dust from experiments with lower O_2 content in this study.

A note must be made on $Y_{M,w}$, as the value is calculated based on the assumption that N_2 constitutes the remainder of the gas at the gas-metal interface, but given the content of the metal used Na-vapor could be a large component as well, which could change the value of $Y_{M,w}$ slightly as Na(g) is somewhat lighter than N_2(g). This change however, has a small effect compared to the other relevant factors.

The flux results are relevant for reducing dust in the metal production industry by virtue of increasing our understanding of the influence the different factors have on the amount of fumes produced, in addition to improving our knowledge on how these factors influence elemental and size distribution as discussed in the following sections. Comparing the theoretical maximum evaporation fluxes with the experimental data give insight to which conditions are likely to have been the case at the metal surface, where decarburization of the surface and increased temperatures have been identifies as likely causes for the high fuming rates, in addition to high flow rates and high oxygen content in the gas. The results in this work imply that any implementation that reduces the temperature of the metal surface, lowers the flow of air across it, lowers the amount of oxygen that reaches the surface, or increases the amount of carbon at the surface will contribute to reducing the fuming rate. An example would be addition of water vapor which reduced the temperature and also lowers the oxygen concentration, and which already has been tested at melting plants [11].

Elemental Distribution

The trend of decreasing element concentration for the majority of the trace elements is theorized to be due to the excess of manganese compared to these elements. As the amount of oxygen is increased, the flux also increases, which would deplete the metal surface of the trace elements more quickly than at lower oxygen concentrations and fluxes. This is not the case for iron, and the similarities between the curves for iron and phosphorous may be due to strong negative interactions between the two elements.

Ma et al. [30] studied the elemental distribution in the silicomanganese production, where they found that base and transition metal elemental distribution mostly behave in good accordance with Gibbs energy of oxidation, while alkali metals fuming is controlled by their low boiling point. The most prevalent elements in the dust from pilot scale experiments were in order: Mn, Si, K, Ca, Mg, Al, S, Na, Fe, Ba, B, Zn, Pb, Sr, P. This matches fairly well with the distribution found in this study,

given that Mn, Fe and Si concentrations in the metal are different, and that Ca, Ba, B, and Sr were not screened for in this study. The most notable differences are the high amount of Zn and the low amount of Al, S and P in the FeMn dust, compared to the SiMn dust.

Size Distribution

The most notable information from the size distribution results is the clear increase in particle and cluster size when the flow rate is lowered, especially when going from 3 to 1 l/min. This is assumed to be because the time that particles and clusters have to grow is inversely proportional to the gas flow rate, and the relative change in growth time is as such much larger when going from 3 to 1 l/min than from 5 to 3 l/min. The flow rate has a much larger effect on particle size compared to the oxygen content, which only yields a large difference in average size for the lowest flow rate.

The average size for both methods match well when comparing different flow rates and oxygen content, with the LD results being around six times larger than the PC measurements for each set of parameters. This indicates that the difference between the cluster size measured with LD and the individual particle size measured directly in SEM-images is similar regardless of the experimental parameters. A parallel can be made to the work of Gates et al. [11] where the size distribution measured showed a clear increase in mean particle size when adding water vapor. Their work also showed a significant decrease in size when comparing fumes that had traveled a shorter distance to those that had travelled further, which aligns well with the results from the current study.

Conclusions

A model based on the work of Rosner [6] was compared to experimental results for the fuming rates of high-carbon ferromanganese at 1550 °C blown with air at varying oxygen concentrations and flow rates. Dust from the experiments were also analyzed with ICP-MS, LD, and SEM, to study the elemental and size distributions. From this work, the following conclusions may be drawn:

On the fuming rates comparing with Rosner's theories [6]:

- The fuming flux seems to follow the theoretical rate up to a certain O_2 concentration as described by Rosner, and then tapers off concurring with Rosner's theory, but toward a higher flux than the theoretical evaporation rate limit given bulk alloy composition at the metal surface. Some factor is believed to increase the flux beyond the value limited by evaporation in vacuo.
- A theory for the high flux rates is that the activity of manganese is higher at the surface than in the bulk phase, possibly due to the carbon-manganese interaction being weakened through either a lower carbon content at the surface, or that manganese and carbon behaves closer to ideality at the surface due to the different conditions compared to the bulk phase. Lowered surface carbon content

could be because oxygen reaches the surface and decarburizes it. The temperature could also be higher at the surface, which would increase evaporation, possibly due to exothermic reactions happening at or above the surface of the melt.

On the elemental distribution:

- The concentration of most trace elements was found to decrease as the oxygen content increased, which is believed to be due to depletion at the metal surface being a factor at higher total fluxes.
- Iron and phosphorous both increased sharply at the highest oxygen concentrations at a very similar rate, and there is reason to believe there is a connection between the two elements that is the cause. In the metal, there is a strong affinity between iron and phosphorous which leads to iron affecting the phosphorous vapor pressure [30], and this property may carry over to the dust.

On the size distribution:

- The size of both individual fume particles and clusters increases when the flow rate is reduced.
- The average size for both clusters and particles increases at a similar rate, with the clusters having an average radii of around six times the individual particle average.
- The flow rate was found to have a much larger effect on the size distribution compared to the oxygen content, especially at low flow rates.

Acknowledgements The authors would like to thank the Centre for Research-Based Innovation (SFI Metal Production, NFR Project Number 237738) for funding the project. UNINETT Sigma2 - the National Infrastructure for High Performance Computing and Data Storage in Norway is acknowledged for a generous grant of computer time (project NN9353K). The authors would also like to thank Erlend Lunnan Bjørnstad for contributing with comments and discussions throughout the work.

Funding Open access funding provided by NTNU Norwegian University of Science and Technology (incl St. Olavs Hospital - Trondheim University Hospital). Funding is provided by the Centre for Research-Based Innovation (SFI Metal Production, NFR Project Number 237738).

Availability of data and material Not applicable

Declarations

Conflicts of interest The authors are aware of no conflicts of interest.

Code availability Not applicable

References

1. S.E Olsen, M. Tangstad and T. Lindstad, *Production of Manganese Ferroalloys*. 1st ed.; (SINTEF and Tapir Academic Press: Trondheim, Norway, 2007); pp. 11–69.
2. B.-D. You, B.-W. Lee and J.-J. Pak, *Metals and Materials*, **5**, 497 (1999).
3. S. Gunst, S. Weinbruch, M. Wentzel, H. M. Ortner, A. Skogstad, S. Hetland and Y. Thomassen, *Journal of Environmental Monitoring*, **2**, 65 (2000).
4. C. Wagner, *Journal of Applied Physics* **29**, 1295 (1958).
5. E. T. Turkdogan, P. Grieveson and L. S. Darken, *Journal of Physical Chemistry* **67**(8), 1647 (1963).
6. D. E. Rosner, *Oxidation of Metals* **4**(1), 1 (1972).
7. Y. Ma, I. Kero and G. Tranell, *Oxid Met*, https://doi.org/10.1007/s11085-017-9780-y.
8. Factsage, *Factsage 7.3* 2019, http://www.Factsage.com/.
9. Y. E. Lee and L. Kolbeinsen, *ISIJ International* **45**(9), 1282 (2005).
10. S. J. Gates, G. Kornelius, I. Kero and G. M. Tranell, *The Influence of Water Vapour on the Fuming Rate in a Ferromanganese System, Energy Materials* 73 (2017).
11. S. J. Gates , I. Kero, L. Hunsbedt and G. M. Tranell, *How water mist alters the fuming rate and particle agglomeration during ferromanganese casting* Conference article: Infacon XV, Southern African Institute of Mining and Metallurgy (SAIMM) (2018).
12. I. Kero, D. Slizovskiy, B. Wittgens and G. Tranell, *Fume Formation From Liquid Ferromanganese*. Conference article: Sustainable Industrial Processing Summit 2015, volume 3, FLOGEN.
13. M. K. Næss, J. E. Olsen, S. Andersson and G. Tranell, *Oxid Met* **82**, 395 (2014).
14. Malvern Panalytical *Laser Diffraction (LD), Particle size distributions from nanometers to millimeters*. https://www.malvernpanalytical.com/en/products/technology/light-scattering/laser-diffraction, Visited 22.01.2021.
15. Coulter International Corporation *COULTER LS Series*. http://www.cyto.purdue.edu/cdroms/cyto2/6/coulter/ss000096.htm, Visited 27.01.2021.
16. S.-W. Joo, S.-H. Hong, G.-H. Lee and B.-D. You, *Metals and Materials* **19**(3) 585 (2013).
17. S. Chapman and T. G. Cowling, *The Mathematical Theory of Non-Uniform Gases*. 3rd ed; (Cambridge University Press, 1970).
18. R.B. Bird, W. E. Stewart and E. N. Lightfoot, *Transport Phenomena*. 2nd ed. (Wiley, 2007).
19. H. A. H. Olsen, S. Andersson and G. Tranell, *Evaporation and Diffusion of Mn in Inert Systems. CFD Modeling and Simulation in Materials Processing 2018, The Minerals, Metals & Materials Series* (Springer, 2018).
20. R. A. Kendall, T. H. Dunning Jr. and R. J. Harrison, *The Journal of Chemical Physics* **96** 6796 (1992).
21. N. B. Balabanov and K. A. Peterson, *The Journal of Chemical Physics* **123** 064107 (2005).
22. CFOUR, a quantum chemical program package written by J.F. Stanton, J. Gauss, L. Cheng, M.E. Harding, D.A. Matthews, P.G. Szalay with contributions from A.A. Auer, R.J. Bartlett, U. Benedikt, C. Berger, D.E. Bernholdt, Y.J. Bomble, O. Christiansen, F. Engel, R. Faber, M. Heckert, O. Heun, M. Hilgenberg, C. Huber, T.-C. Jagau, D. Jonsson, J. Jusélius, T. Kirsch, K. Klein, W.J. Lauderdale, F. Lipparini, T. Metzroth, L.A. Mück, D.P. O'Neill, D.R. Price, E. Prochnow, C. Puzzarini, K. Ruud, F. Schiffmann, W. Schwalbach, C. Simmons, S. Stopkowicz, A. Tajti, J. Vázquez, F. Wang, J.D. Watts and the integral packages MOLECULE (J. Almlöf and P.R. Taylor), PROPS (P.R. Taylor), ABACUS (T. Helgaker, H.J. Aa. Jensen, P. Jørgensen, and J. Olsen), and ECP routines by A. V. Mitin and C. van Wüllen. For the current version, see `http://www.cfour.de`.
23. D.A. Matthews, L. Cheng, M. E. Harding, F. Lipparini, S. Stopkowicz, T. C. Jagau, P. G. Szalay, J. Gauss and J. F. Stanton, *The Journal of Chemical Physics* **152** 214108 (2020).
24. F. J. Smith and R.J. Munn, *The Journal of Chemical Physics* **41** 3560 (1964).
25. M. Gasik *Handbook of Ferroalloys, Theory and Technology* (Elsevier Ltd., ISBN 978-0-08-097753-9, 2013).

26. Y. E. Lee, *Metallurgical and Materials Transactions* **29B** 397 (1998).
27. A. Tanaka, *Trans. JIM* **21** 27 (1980).
28. Y. Ma, *Oxidation and Fume Formation During Production of Si and Mn-based alloys* Doctoral-thesis, Norwegian University of Science and Technology. Trondheim, October 2018.
29. J. Safarian, L. Kolbeinsen and M. Tangstad. *Journal of Materials Science* **47**, 5561 (2012).
30. Y. Ma, *Metallurgical and Materials Transactions B* **49**, 2444 (2018).

C.4 Paper IV

MDPI

Article

USE OF A DISTRIBUTED MICRO-SENSOR SYSTEM FOR MONITORING THE INDOOR PARTICULATE MATTER CONCENTRATION IN THE ATMOSPHERE OF FERROALLOY PRODUCTION PLANTS

Håkon Myklebust [1,*], Thor Anders Aarhaug [2] and Gabriella Tranell [3]

[1] Norwegian University of Science and Technology; hakon.a.h.olsen@ntnu.com
[2] SINTEF Industry; thor.a.aarhaug@sintef.no
[3] Norwegian University of Science and Technology;gabriella.tranell@ntnu.no
* Correspondence: hakon.a.h.olsen@ntnu.com; +47 90606459

Abstract: Airborne Particulate Matter (PM) is a concern for both occupational health and the environment, and in the ferroalloy industry, the level of such particles in the air can be considerable. Small, low cost sensors for measuring PM have generated interest in recent years, providing widespread monitoring of PM-levels in the environment. However, such sensors have not yet been sufficiently tested under conditions relevant for the indoor environment of the metallurgical industry. This study aims to bridge this gap by benchmarking the commercial, low-cost Nova PM SDS011 particle sensor in two different ferroalloy plants towards the Fidas 200S which has been suitability-tested and certified according to the latest EU requirements (EN 15267, EN 16450) [1]. 12 Nova sensors were tested over three months at a silicomanganese alloy (SiMn) plant, and 35 sensors were tested during one month at a silicon (Si) plant. The results showed that the low-cost Nova sensors exhibited all the same trends and peaks in terms of PM concentration, but consequently measured lower dust concentrations than the Fidas 200S. The difference was larger at the silicon plant, which is in line with expectations due to the size- and mass fractions of particles in Si-dust compared to SiMn dust and the larger measurement range of the Fidas, measuring down to 180nm compared to the Nova which measures down to 300nm. Despite the difference in absolute values, the Nova sensors were found to provide data for comparing dust levels over time for different processes, at different locations, and under different operational conditions.

Keywords: fume formation; metal production; sensors

Citation: Myklebust, H.; Aarhaug, T. A.; Tranell, G. Title. *Atmosphere* **2021**, *1*, 0. https://doi.org/

Received:
Accepted:
Published:

1. Introduction

Airborne Particulate Matter (PM) is considered a concern for both occupational health and the environment. Effects of PM on human health have been found to include asthma, lung cancer, and cardiovascular diseases [2] [3], the level of which relate to the size, composition and properties of the particles. The smaller the particles, the further into the human system they can penetrate, including the bronchi for PM up to 10 µm(PM10), the lungs for PM up to 2.5 µm(PM2.5), and even through the lungs and into the circulatory system for ultrafine particles below 0.1 µm(PM0.1) [4] [5] [6].

In metallurgical plants producing silicon and silicomanganese alloys, the level of PM can be considerable. This PM is formed both mechanically through fines generation during raw materials handling and thermally through reduction and oxidation of raw materials and products. Thermally generated SiMn fumes formed by oxidation of liquid (Si) and evaporated (Mn) metals consists mainly of Si, Mn, and O, forming various complex oxides. Secondary elements include Mg, Ca, Al and K, and trace elements include Na, Fe,

Zn, Cu and Cl [7]. The industrial average aerodynamic diameter of these fume particles, as recorded by Electrical Low Pressure Impactor (ELPI), is on average approximately 100nm [7], while SEM analysis of fumes generated experimentally in laboratory scale by Ma et al. [8] show that the majority of protoparticles (the singular particles, in this case mostly spheres, defined before agglomeration and clustering) have a diameter between 50 and 200nm, although fume particles generated at higher temperatures are notable smaller. For agglomerate size fractions measured through laser diffraction (LD) on the same dust however, the majority of particulates have a diameter in the range of 500-2000nm, and are also less influenced by temperature. Thermally generated Si-fumes formed by oxidation of liquid Si consists mainly of Si and O, forming silica dust [9]. Average protoparticle sizes range from 66-91nm [9]. These particles also agglomerate after formation, leading to the size fractions measured through laser diffraction being much higher. Figure 1 a and b show SEM imagery of the fume particles from SiMn and Si production respectively [8] [9].

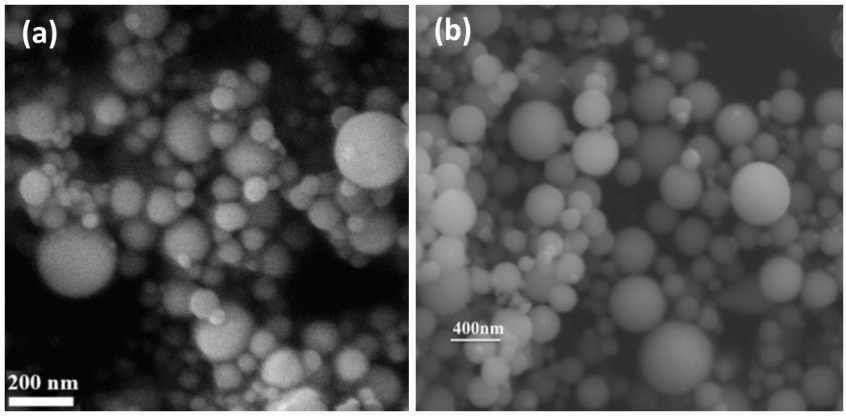

Figure 1. SEM images showing fume particles from a) Si filter fume generated experimentally at 1550 °C [9] and b) typical SiMn filter fume generated experimentally at 1500–1700 °C [8]. Note the difference in scale.

According to current EU-regulations, exposure to PM10 in ambient air should be limited to a maximum of 50 µg/m^3 averaged over a 24-hour period with a maximum of 35 permitted exceedences per year. The yearly average is limited to 40 µg/m^3 for PM10 and 25 µg/m^3 for PM2.5 [10]. Workplace PM exposure is often monitored by personal portable devices while monitoring of ambient plant PM levels are often measured using one or more fixed measurement stations that measure for long periods at a time. These stations are expensive to set up, which limits the number of spatial measurement points that can be realistically achieved. The use of less expensive, portable setups would circumvent this issue and allow for a much higher resolution spatial resolution, which can be of particular use in the extremely varied environment that is the case for metal production plants. A better spatial resolution allows for tracking the flow of particles in the plant and can work as a tool for evaluating measures taken to reduce and capture PM emissions.

There are several categories of low-cost micro-sensors available, but in the current study, the aim was to investigate and benchmark the performance in terms of precision and reliability of a specific low-cost sensor - the Nova PM SDS11 ("Nova") - in two different metallurgical plant environments. The Nova sensor which has been developed for low-cost fume monitoring, was benchmarked towards the Fidas 200S ("Fidas"). The Nova measures particulate matter in the ranges of 0.3-2.5 µm(PM2.5) and 0.3-10 µm(PM10),

while the Fidas 200S measures from 0.18 µm to 100 µm, separated into four values capped at maximum 1, 2.5, 4 and 10 µm (PM1, PM2.5, PM4, and PM10). Both sensors use optical light scattering to register particles in the air, where coherent pulses of infrared light is aimed through the flow of particles where the particles scatters the light according to laser diffraction theory [13]. This allows the number of particles to be inferred from the number of scattered light pulses, and the size of the particles from the intensity of the scattered light pulse. The most important differences in the equipment is the range of particle sizes measured, particularly the lower limit. For Fidas 200S, precise optics, high light output from the poly-chromatic LED used, and powerful signal processing electronics using logarithmic A/D conversion allowing detection of particles down to 180 nm diameter, where the Nova is limited to a lower boundary of 300nm at which point the detection rate is only at 70% [11] [12]. As the Fidas dries the sample fumes before it reaches the sensor it is better suited for measurements in high relative humidity, whereas the Nova has no such feature. The quality of the components used in general is also a potentially important factor in regards to stability of measurements and lifetime for the sensor. The central technical parameters of the two sensors are described in table 1.

Table 1: Technical parameters for the Nova SDS011 and Fidas 200S as given by the manufacturers [12] [11].

Parameter	Nova	Fidas
Measuring output(PM)	PM2.5,PM10	PM1,PM2.5,PM4,PM10
Concentration range	0-999.9 µg/m^3	0-10000 µg/m^3
Measuring range	0.3-10 µm	0.18-100 µm
Response time	1s	<2s
Sample treatment	none	Drying and heating
Dimensions	71 · 70 · 23 mm	450 · 320 · 180.5 mm
Power consumption	max. 0.5W	approx. 200W

The Nova sensor has been the subject of several studies in varied settings. Genikomsakis et al. performed mobile field testing comparing the Nova with a AP-370 by HORIBA suitable for constant air pollution measurements on an electric bike in the city of Mons, Belgium. PM values ranged from 0 to 5 µg/m^3 with the resulting R^2 values ranging from 0.93-0.95 after taking temperature and relative humidity into account [13]. Badura et al. compared a group of three copies of the Nova sensor together with groups of three other similarly low-cost systems in a common box under the same measurement conditions over half a year near a park and a residential area in Wroclaw, Poland. The Nova was found to be one of the most precise in terms of reproducability between units, and also when compared to the control unit with an R^2 value of 0.82 using 15 minute averages, but it was found to be sensitive to high relative humidities (RH > 80%) [14]. Liu et al. tested the Nova sensors by co-locating three of the sensors at an official, air quality monitoring station equipped with reference-equivalent instrumentation in Oslo, Norway over a four month period and found inter-sensor correlations R values higher than 0.97, and confirmed the sensor's susceptibility to high relative humidity. They concluded that when used correctly, the sensor could have significant potential for implementing dense monitor networks in areas with relative humidities below 80% [6]. In industrial settings there has been less work done to test these sensors, but the Nova sensors were found by the current authors to provide useful data in the Aluminum industry where the value of having multiple groups spaced out was shown [15]. When compared to similar low-cost sensors, the Nova sensor has been shown to be amongst the best in several studies [16] [17], but as mentioned it is less reliable at higher humidities, which was further investigated by Jayaratne et.al along with other sensors where several showed an increase in PM-level above a relative Humidity of 75% [18].

This work aims to compare how well the Nova sensors compare to the Fidas when measuring the PM concentration in two different metallurgical plants. The first measurement campaign was performed at a silicomanganese (SiMn) plant, and the second at a plant producing metallurgical grade Silicon(MG-Si). The thermally and mechanically produced fumes formed during the metallurgical processes at these plants as outlined above, vary greatly, particularly in regards to size fractions, which is believed to affect the measurements. An additional objective is to study the long term performance of the Nova sensors in high dust level environments.

2. Industrial Measurements

The complete setup for the Nova sensor system included the Nova PM SDS011 sensor connected to a microchip together with a temperature and humidity sensor [19] placed in a closed box as shown in Figure 2. The system was powered with 5V 1A of electricity provided from an external power source, and while the system protects the components to a degree, the model was not airtight.

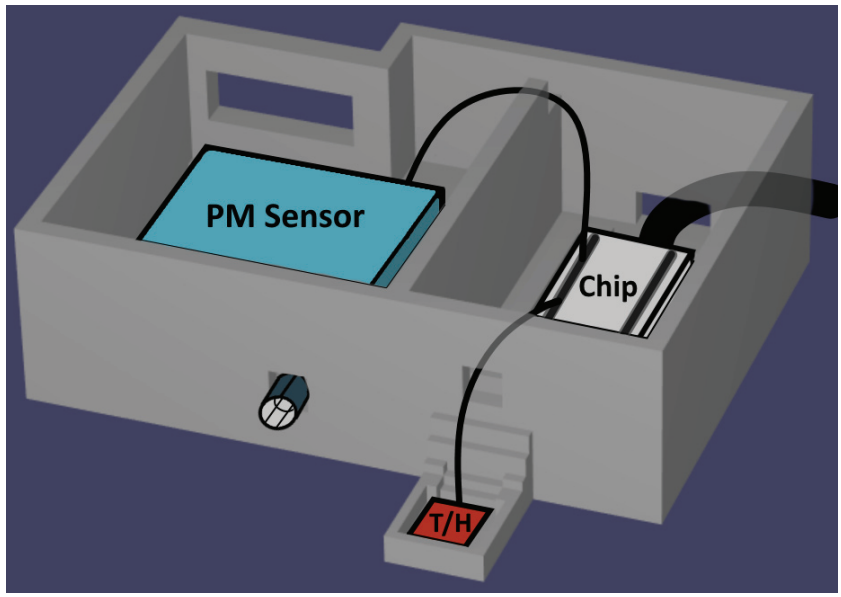

Figure 2. Schematic of the sensor system for the Nova PM SDS011. Each box was closed with a matching lid to limit exposure.

2.1. Silicomanganese plant

At the silicomanganese plant, the measurement period was divided into two parts. The first, extended period lasted for more than two months with only the Nova sensors, while the subsequent calibration period lasted for almost 24h where the Nova sensors were placed close to the Fidas. For both periods, twelve Nova sensors were divided into three groups of four sensors stacked on top of each other. In both periods, the sensors were placed in a hallway adjacent to the metal tapping hall, with one wall-section being an opening towards the furnace hall, and another being the outer walls of the furnace itself. Figure 3 shows the approximate sensor locations for the measurement periods, here the ceiling height is 6.45 m, and the entire section leading out to the smelting hall is open allowing for free flow of fumes into the measurement area. During the middle period, four Nova sensors were each placed at point 1, 2 and 3, roughly 1.5 m above the floor along the wall section. During the last period, all 12 Nova sensors were placed together at point 3, with the Fidas sensor placed with the fume intake approximately 30

cm away from the Nova sensors.

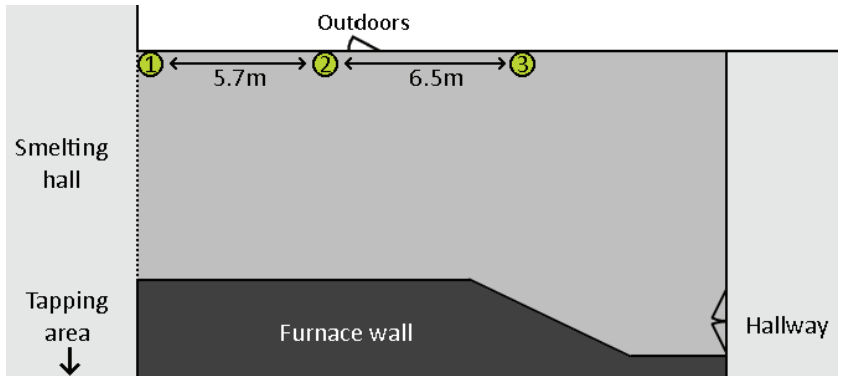

Figure 3. Approximate sensor locations during the middle and last measurement period for the measurement campaign at the SiMn-plant.

2.2. Silicon plant

At the Silicon plant, there was one measurement period of close to one month, with 35 Nova sensors placed in vertical groups of 5 near the inlet for a Fidas sensor for the full duration. The sensors were placed on a mezzanine floor above the furnace body where the electrode feeding takes place, inside the hall in which tapping is performed. Figure 4 shows the approximate location of the sensor group along with the relevant process locations. All 35 Nova sensors were placed with their fume inlets within 20cm of the Fidas' fume inlet. There is a fuming hood designed to capture most of the tapping fumes, and there is also several layers of partial flooring between both the tapping and stoking areas, and the sensors. Fumes and smoke not captured by the fuming hood will eventually flow up along the sides of the furnace and reach the sensors however, and fumes that gathers below the roof will also be picked up by the sensors which are only a couple meters below.

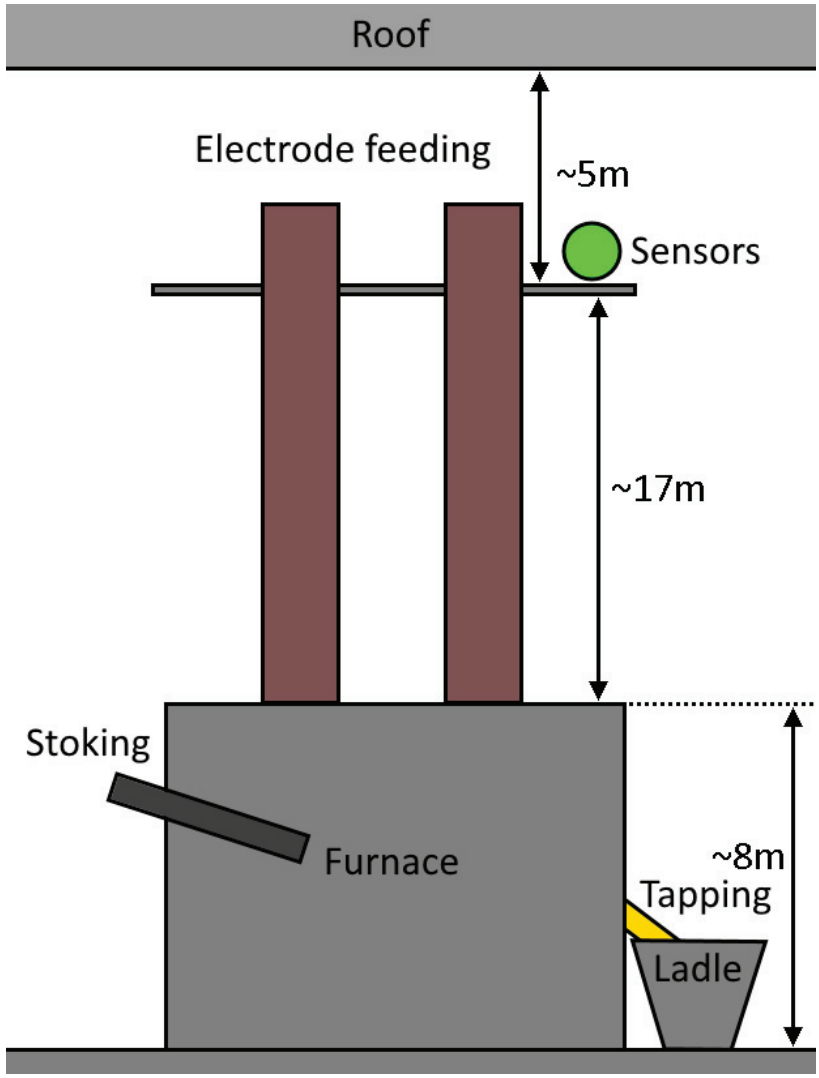

Figure 4. Approximate sensor location (Green circle near the top) during the measurement campaign at the Si-plant. Redrawn from sketch provided by the smelting plant.

The fumes measured at the silicon plant is assumed to be mostly thermally generated oxides originating from the Si-melt during the tapping process and other periods in which molten Si is in contact with open air.

3. Results and Discussions

3.1. PM intensity variations over time

Figure 5 to 10b shows the PM10-PM2.5 and PM2.5 values measured by the Nova sensors during the extended periods of the two measurement campaigns, as well as during a shorter period together with the Fidas data, in addition to the diurnal patterns for PM10.

164 3.1.1. SiMn-plant

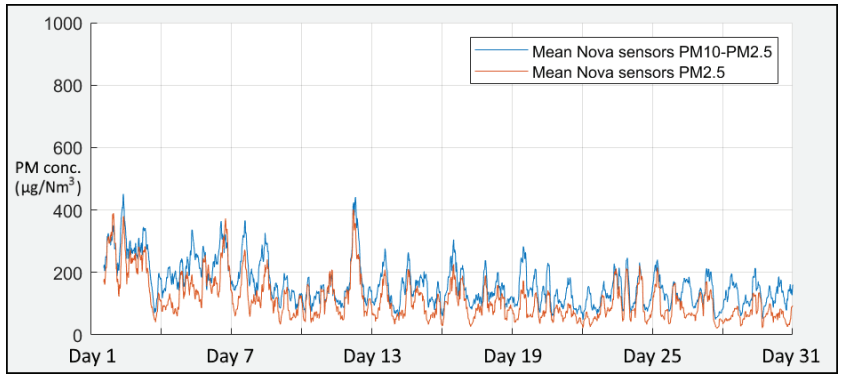

Figure 5. PM10-PM2.5 and PM2.5 as measured by 4 Nova sensors over a period of around one month in the SiMn-plant. The data was gathered in 15-minute averages which were in turn smoothed with a sliding average spanning 6 hours total.

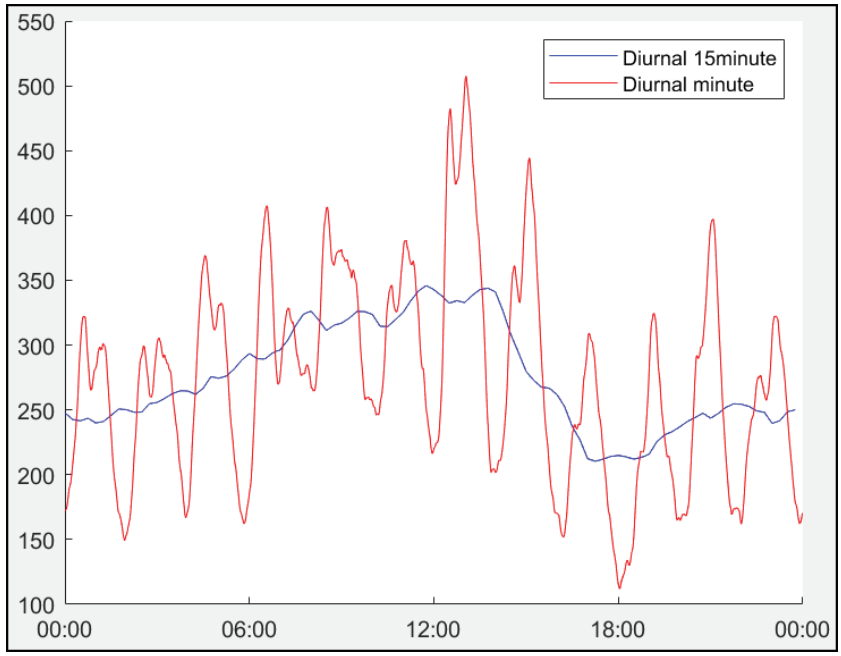

Figure 6. Diurnal pattern of the PM10 as measured by 4 Nova sensors over a period of around one month in the Si-plant. The data was gathered in 15- and 1-minute averages which were in turn smoothed with a sliding average spanning 6 hours and 30 minutes total respectively.

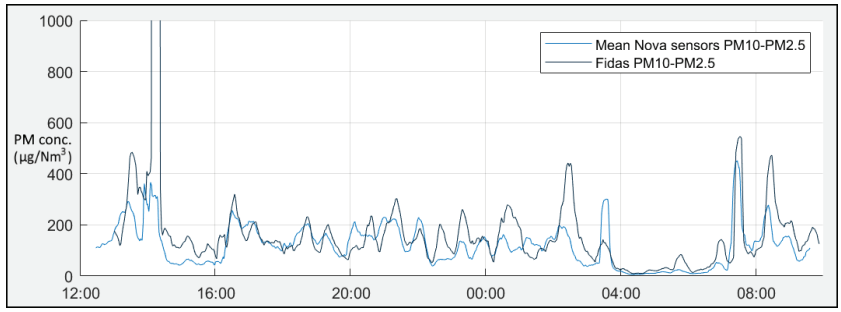

(a)

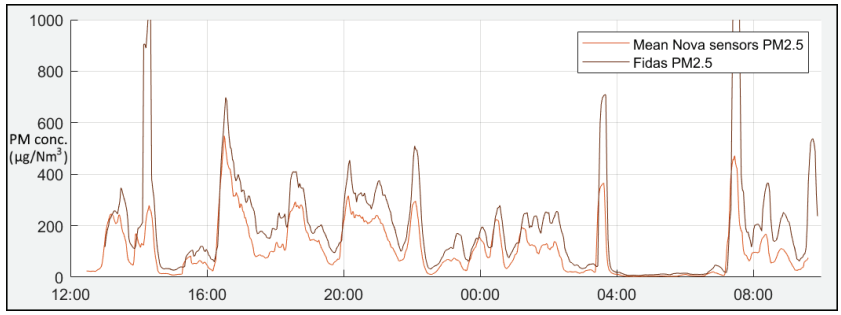

(b)

Figure 7. PM10-PM2.5 (a) and PM2.5 (b) as measured by 12 Nova sensors and the Fidas 200S over a period of 21 hours during the final calibration period at the SiMn-plant. The data was gathered in 1-minute averages which were in turn smoothed with a sliding average spanning 15 minutes total. Mean values for the Nova sensors are shown together with the 95% confidence interval and the Fidas values.

The long-term measurements at the SiMn-plant show the erratic day-to-day changes in fume levels, but from the diurnal pattern it can be seen that the PM levels are generally at a lower value in the evening and night, and at a maximum around noon. It is also easy to detect differences between days and periods which could be correlated to changes in the weather, internal processes, routines, or events. For instance, the first week, as well as daytime on day 12, show a clearly higher PM-level compared to the latter half of the period shown in figure 5.

When comparing the Nova and Fidas measurements, it can be noted that the two sensors pick up on most of the same peaks and changes in dust levels, both for PM2.5 and PM10-PM2.5. While there are some peaks where the difference is large, the trends are similar for most of the period. The difference seems to be higher for PM2.5, which is natural due to the lower minimum measurement boundary on the Fidas compared to the Nova. The level of the larger fumes (PM10-PM2.5) are generally slightly higher than the level of the smaller fumes (PM2.5) on average, but there are notable spikes with a higher level of fine dust which could relate to specific process or workplace events producing and/or dispersing more fine particles.

3.1.2. Si-plant

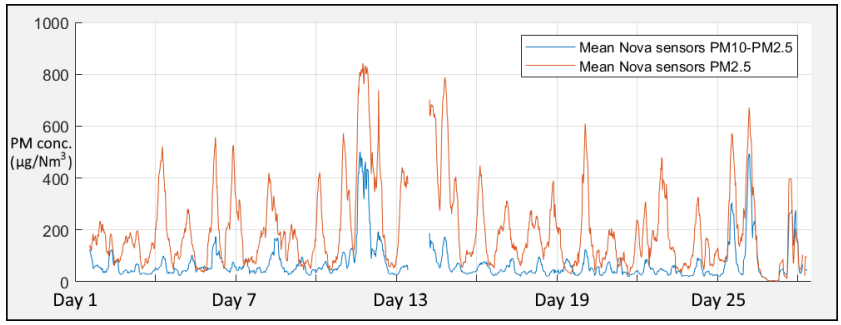

Figure 8. PM10-PM2.5 and PM2.5 as measured by 35 Nova sensors over a period of around one month in the Si-plant. The data was gathered in 15-minute averages which were in turn smoothed with a sliding average spanning 6 hours total.

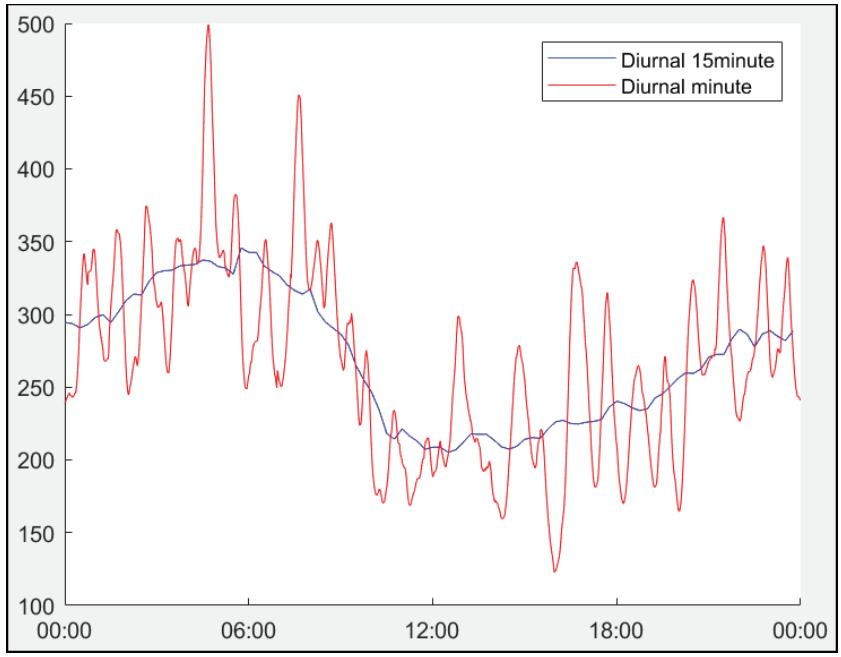

Figure 9. Diurnal pattern of the PM10 as measured by 35 Nova sensors over a period of around one month in the Si-plant. The data was gathered in 15- and 1-minute averages which were in turn smoothed with a sliding average spanning 6 hours and 30 minutes total respectively.

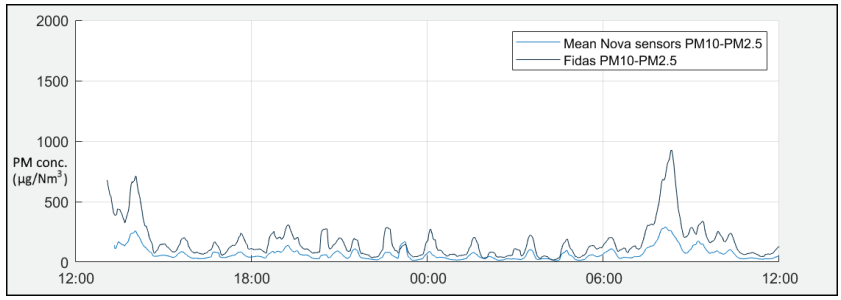

(a)

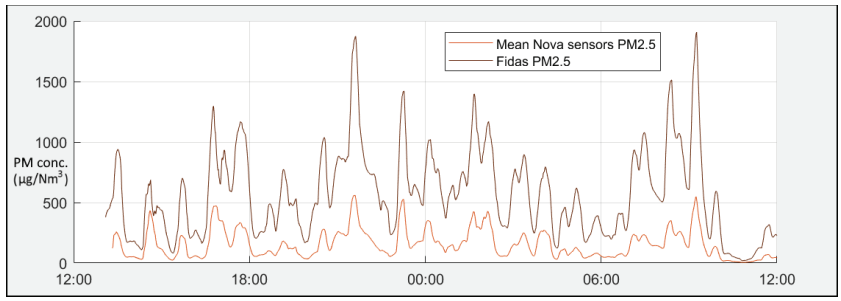

(b)

Figure 10. PM10-PM2.5 (a) and PM2.5 (b) as measured by 35 Nova sensors and the Fidas sensor over a period of 24 hours in the Si-plant. The data was gathered in 1-minute averages which were in turn smoothed with a sliding average spanning 15 minutes total. Mean values for the Nova sensors are shown together with the 95% confidence interval and the Fidas values.

For the long term Nova measurements at the Si-plant shown in figure 8, one can see that the fumes have a much larger fraction of PM2.5 compared to PM10-PM2.5, while the change in PM-levels are slightly less varied compared to at the SiMn-plant with the average number of peaks per day is larger than 1 for this period. The diurnal pattern shows an opposite trend compared to at the SiMn-plant, with higher values in the morning and the lowest values around noon. The difference between the peak values and the baseline fume level is higher at the Si-plant, which might stem from the higher proximity to the fume source at this location.

Also at the Si-plant it can be noted that the two sensor types pick up on most of the same peaks and changes in dust levels, both for PM2.5 and PM10-PM2.5. Here a notable difference in fume levels is apparent however, with the difference being largest for PM2.5, which was also the dust fraction with the most variation over time. With the difference in the lower boundary of fume size measured by the two sensors, it stands to reason that the Fidas would measure larger values for PM2.5 when the fume to be measured has a significant fraction of fumes in the 180-300nm range, which seems likely in this case. This is further supported by the fact that the largest fraction measured by the Fidas for most of the period is PM1, as can be seen in Figure 12. The fraction of PM10-PM2.5 is quite low for Si, with the exception of a few clear spikes. These probably represent particular events in the furnace area, but data for processes relating to those times were not available for study.

When considering the dust level differences between Si and SiMn fumes, an important thing to note is the difference in density between different fumes. This is due to the measuring equipment having to calculate the mass of the detected fumes to provide the

standard units for PM ($\mu g/m^3$). For Si-fumes, a typical density used is that of amorphous silica (2.2 g/cm^3) [7]. For SiMn-fumes a typical density model would be to assume pure MnO (5.37 g/cm^3) which is most prominent in SiMn-fumes, almost to exclusion of other elements when generated from SiMn-melts at below 1500°C [8]. With sensors not being calibrated for the specific dusts and their densities, it can be assumed that there will be a similar discrepancy in the measured fume mass per volume as there is a difference in fume density. In this case the density of the lighter fumes (Si) are less than half the density of the heavier fumes (SiMn), which speaks to the necessity in calibrating for the correct fumes when using PM sensors to avoid getting inaccurate data. When the sensor systems convert particle counting data to PM concentrations it is dependent on the particle shape and density, and a difference in choice of calibration density can also to a degree explain the difference in dust levels measured by the Nova compared to the Fidas. A list of tapping events was studied along with the sensor data for a period, but the frequency of peaks was too high to be correlated with the lower frequency of tapping events, and the attempt at correlation is deemed inconclusive given the limit of available data for other process events.

3.2. Size fractions

Figure 11 and 12 shows the different size fractions measured by the Fidas sensor at the SiMn and Si-plant respectively over a period of around 24 hours. The fractions are split into 0.180-1.0µm (PM1) 1.0-2.5µm (PM2.5-PM1) 2.5-4µm (PM4-PM2.5) and 4-10µm (PM10-PM2.5).

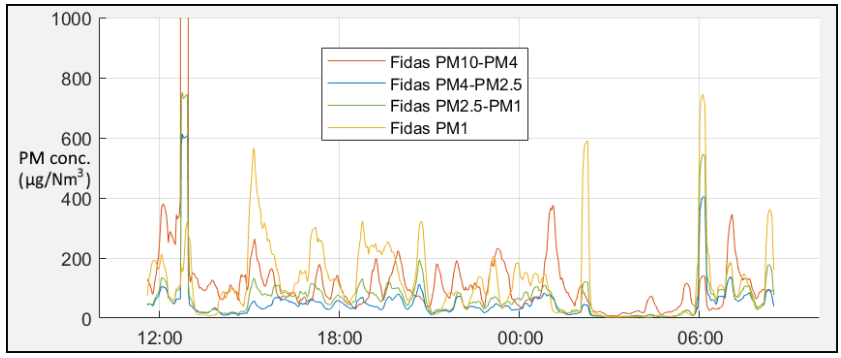

Figure 11. Size fractions as measured by the Fidas sensor at the SiMn-plant.

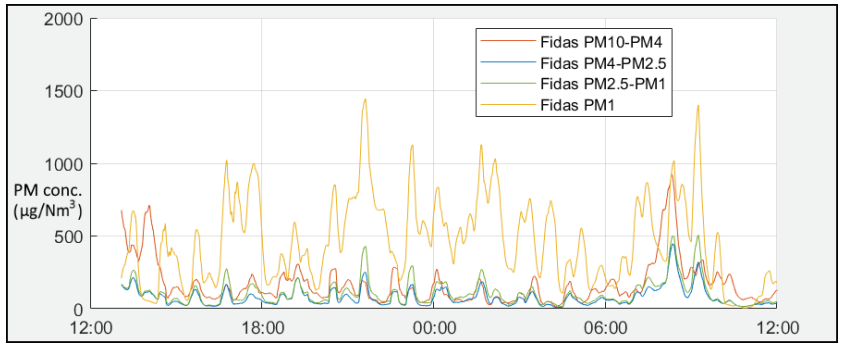

Figure 12. Size fractions as measured by the Fidas sensor at the Si-plant.

As can be seen in Figure 11 and 12, the largest fraction of PM measured by the Fidas is almost always PM1 for Si fumes, and usually by a large margin. For SiMn, the largest fraction varies between PM10-PM4, and PM1. This seems in line with the deviation found between Nova and Fidas and how it differs from SiMn to Si fumes, as the Fidas measures particles in the 180-300nm range, which the Nova do not. It seems evident that the Si fumes have more of the smaller agglomerates, which in turn leads to a larger deviation between the Nova and the Fidas for Si fumes. The variations in size fractions over time can be related to events and activities in the vicinity of the sensors, as different fume sources are likely to produce different fumes.

3.3. Quantitative measurement differences between the Nova and Fidas sensors

Figure 13 to 14 shows the mean PM10-PM2.5 divided by PM2.5 and the PM2.5 values as measured by the Nova sensors as a function of the same values as measured by the Fidas sensor for both plants over a period of around 24 hours.

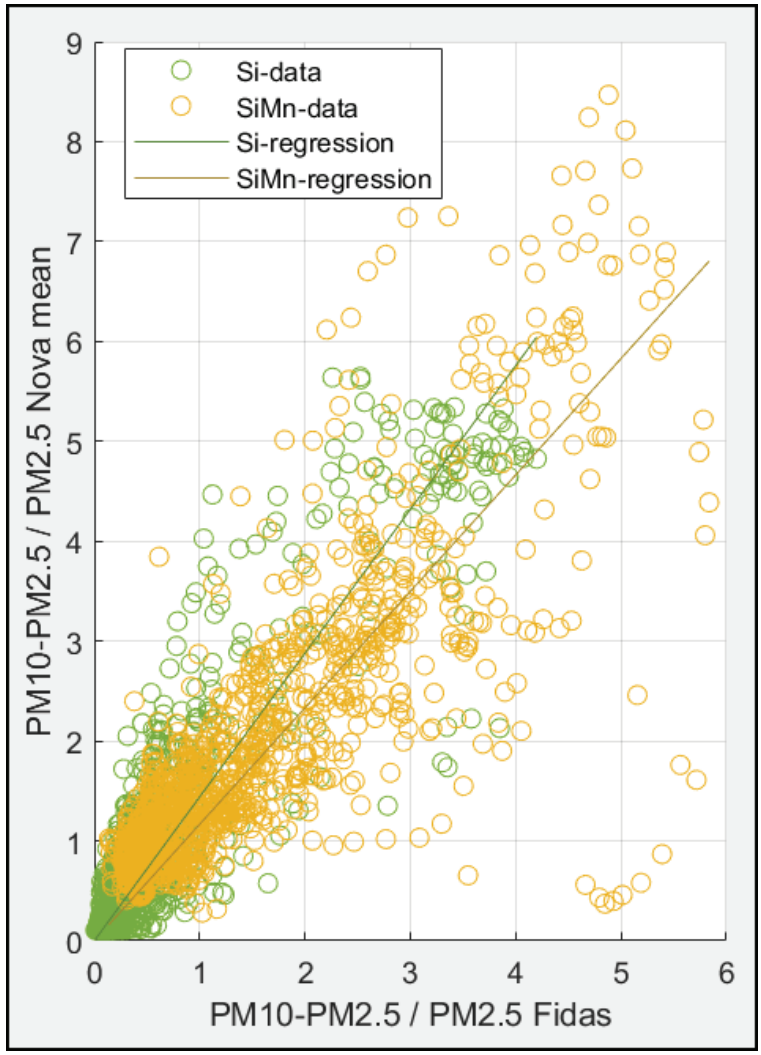

Figure 13. PM10-PM2.5 divided by PM2.5 mean values as measured by the Nova sensors as a function of the same values as measured by the Fidas sensor at both plants. Linear regression through origo was performed yielding an R^2-value of 0.7989 and 0.5891 for the Si and SiMn dataset respectively. The linear formulas were y = 1.4396x and Y = 1.1659x respectively.

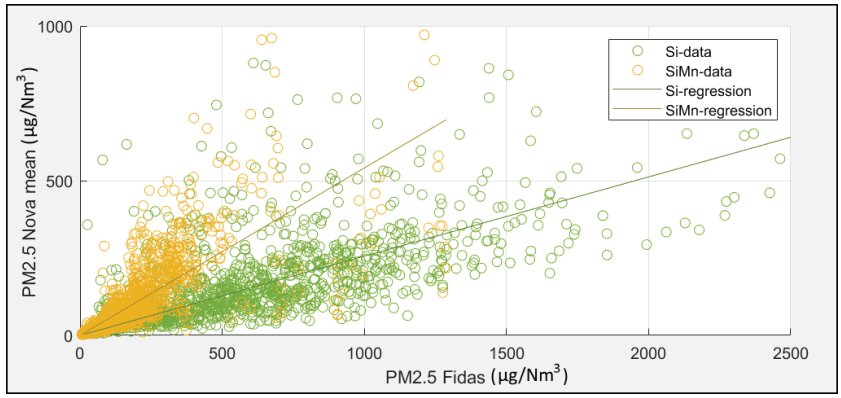

Figure 14. PM2.5 mean values as measured by the Nova sensors as a function of the same values as measured by the Fidas sensor at both plants. Linear regression through origo was performed yielding an R^2-value of 0.1082 and 0.3021 for the Si and SiMn dataset respectively. The linear formulas were y = 0.2561x and y = 0.5412x respectively.

From the comparisons between Nova and Fidas shown in Figure 13, the difference between SiMn and Si fumes in regards to the fraction of larger particles measured by the Nova compared to the Fidas becomes apparent. For the Si fumes, the relations between the two sensors measured PM10-PM2.5/PM2.5 is clustered around the line y = 1.14x with an R^2-value of 0.80. The trend is strong, but the spread is still quite large and it is skewed towards a greater fraction of the larger particles measured by the Nova sensors. It can also be noted that the actual curve given by the Si-data does not follow linearity. For the SiMn fumes, the spread is somewhat larger with an R^2-value of 0.59 around the line of y = 1.17x, showing a trend with less difference between the Fidas and Nova measurements, albeit with a larger spread. In both cases, the Nova tends to measure a greater fraction of larger particles compared to the Fidas. For Si fumes, this points to the need for better calibration of the Nova sensor, and the non-linearity of the trend. More points are gathered below the (1,1) point for Si compared to SiMn, which shows the tendency of larger fractions of the smaller particles measured in the Si-plant regardless of sensor used.

The PM2.5 comparisons between Nova and Fidas shown in Figure 14 shows that the Fidas measures notably higher values for PM2.5, although the difference is several times higher for the Si-fumes. This aligns with the increased lower measurement range on the Fidas, but the linearity in the comparisons for both fumes imply that it is possible to infer the realistic values as measured by the Fidas by multiplying the Nova measurements with a factor established through calibration with the relevant fumes. Here the factor would be 1/0.2561=3.905 and 1/0.5412=1.849 for Si and SiMn respectively, but the R^2-values of 0.1082 and 0.3021 for the linear regression of the Si and SiMn data respectively speak to the notable spread present in the data still. However, if the size distribution of the fumes are mostly stable over time, the fraction of fumes that are compensated for due to particles being below the measurement range of the Nova should also stay comparatively constant, and applying such a correction factor should eliminate a large portion of the error.

3.4. Calibration and Particle Densities

The main component of the fumes in the two different plants, SiO_2 in the Si-plant and MnO_2 in the SiMn-plant, have molar masses of 60.08 and 86.94g/mol, and densities of 2.096 and 5.026g/cm^3 respectively. The heavier nature of manganese fumes is likely to make the concentration measured higher in the SiMn-plant compared to the Si-plant

when no density calibration or post-processing has been performed, and this should be taken into account when reading the data in this work. It is not known to which density the Nova were calibrated to when delivered, but the Fidas was calibrated for SiO_2, and a difference in calibration could explain some of the differences between the measurements made with the sensors.

3.5. Deviations between individual and groups of Nova sensors

Figure 15 shows the relative deviation to mean for each of the 7 groups of up to 5 Nova sensors over the first 20 hours of the measurement period at the Si-plant together with the 95% confidence interval. Figure 16 and 17 shows the relative deviation to mean for the Nova sensors within one of the groups at the Si- and SiMn-plant respectively together with their 95% confidence intervals. The limited time period used for the deviation graphs is due to the failure of several sensors at the Si-plant as discussed further in section 3.5, and the data from the SiMn-plant was shortened to allow for easier comparison. Due to the spacing in placement of the three groups used at the SiMn-plant, relative deviation between groups is not relevant here. The data in Figure 15 to 17 are presented to show how the deviation in measurements for the sensors in each group or between the different groups change over time. Stable deviation curves relate to a systematic difference between sensors that can be compensated for or be mostly eliminated through calibration.

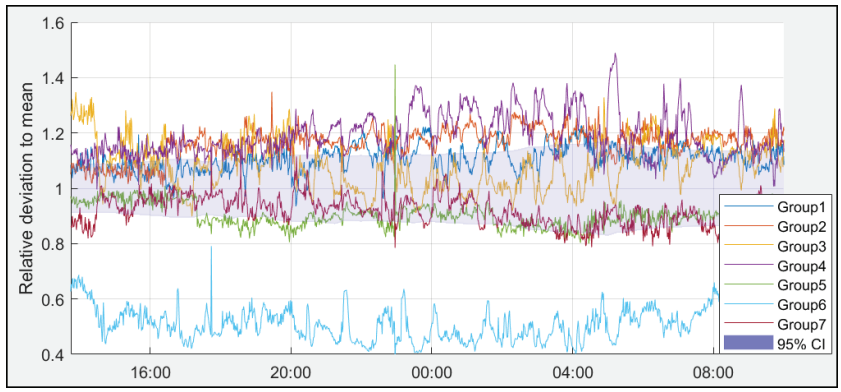

Figure 15. Relative deviation to the mean PM10 values for each of the 7 groups of up to 5 Nova sensors over the first 20 hours of the measurement period at the Si-plant together with the 95% confidence interval for the dataset including all active sensors.

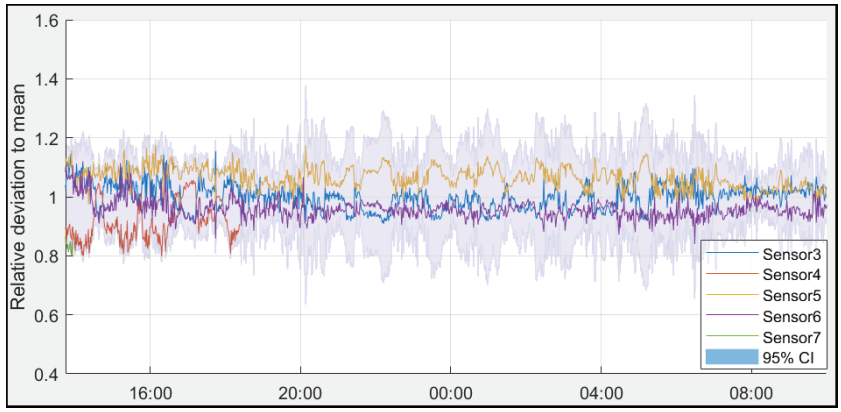

Figure 16. Relative deviation to the mean PM10 values for the first group of Nova sensors over the first 20 hours of the measurement period at the Si-plant together with the 95% confidence interval for the dataset.

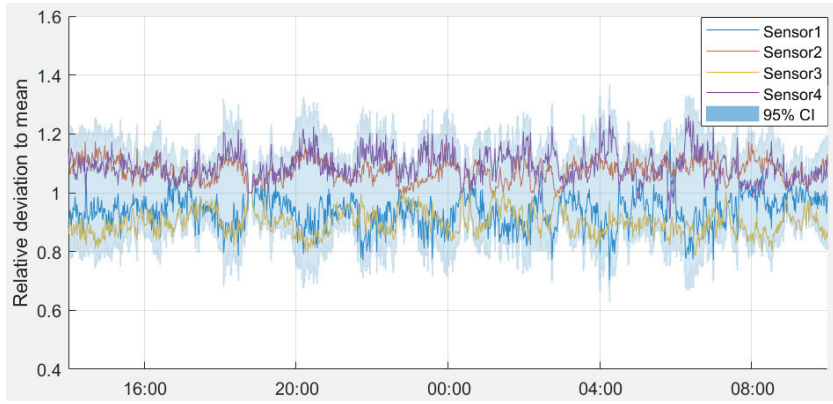

Figure 17. Relative deviation to the mean PM10 values for the first group of Nova sensors over the first 20 hours of the measurement period at the SiMn-plant together with the 95% confidence interval for the dataset.

Only one group from each plant was used to show the trend here, but the remaining groups showed similar trends over time, thus from Figure 17 to 16 showing the relative deviation in and between the sensor groups, one can infer that over time the individual sensors within each group tend to have a relatively stable deviation from the mean value, barring changes caused by the loss of sensors. Full two month comparisons of relative deviations at the SiMn-plant showed a similar pattern over time as the 20-hour period. The individual variation on the sensors deviation is for most of the sensors within the 15% relative deviation level provided by the manufacturer [12]. It is slightly larger than the internal deviation between 3 Nova sensors of maximum 5% found by Liu et.al [2], however the PM concentration during these measurements were around ten times lower than in this study. That the internal deviation is to a degree stable over time is very useful information, as it would imply that a large part of the deviation between sensors could be corrected through simple calibration where each sensors measurements are multiplied with a correction factor or equation, which is in line with conclusions from similar work testing the viability of low-cost sensors [20]. It can be noted that the deviation is lower for the SiMn measurements, both in total relative deviation, and the variations of that value for each sensor. This could be due to the larger fraction of

smaller particles in the Si fume, as the fraction of particles in the size range where there is uncertainty on if they would be detected by the Nova sensor would be much larger.

3.6. Sensor Reliability

Most of the sensors had already been used for several months at different campaigns before the campaign at the Si-plant, and as there was a consistent high concentrations of dust in the areas where the sensors were placed in both plants, sensor failures were expected to some degree during both campaigns, particularly at the Si-plant. 6 sensors were removed from the pool of 35 after the measurement period at the Si-plant, as the data they provided became erroneous instead of stopping completely, leading to a pool of maximum 29 sensors. During the measurement period, more of the sensors cut out at some points, but restarting the sensors worked in getting some of them back up. 3 out of the 12 sensors in the SiMn-campaign did not give measurements during the entire measurement period, while almost all of the sensors cut out at some point during the measurement period at the Si-plant. Over the entire measurements period, the mean up-time of the sensors was 21.7% at the Si-plant and almost 100% at the Mn-plant. This limited the accessible data for the Si-campaign, but due to the many sensors placed during the campaign, the amount of data available is still considered sufficient for analysis, particularly using the periods and groups where a larger fraction of sensors were active. The highest measured relative humidities where below 40% at the SiMn-plant and below 45% at the Si-plant, which is significantly lower than the boundary of around 80% RH where condensation causes inflation in the PM readings for the Nova and is as such not considered to have influenced the PM readings in this work.

While the higher degree of failure during the Si-campaign could be just due to wear over time, it is also possible that the Si-fumes affected the electronics to a higher degree than the dust from SiMn, leading to a faster decay in functionality. This is also supported by the fact that the campaign at the SiMn-plant lasted for more than 3 months, and at the end of the campaign all 12 sensors were functional after being reset and having their system blown clear of excess dust. The sensors yielding erroneous data instead of stopping completely at the Si-plant also supports this theory as previous campaigns did not show similar signs of malfunctioning besides a complete stop in the flow of measurements. In such a case, this problem should be solvable by using an airtight case for the sensor system. In some of the cases, blowing through the system to clear it out is enough for the sensor to start working again, and in some cases just restarting the system worked, but for other sensors did not and in such cases replacement of malfunctioning parts or wires would most likely be necessary to get the sensor up and running again.

4. Conclusions

A low-cost PM sensor for PM2.5 and PM10, Nova PM SDS011, was tested and benchmarked towards the Fidas 200S during two measurements campaigns at a SiMn- and a MG-Si production plant where 12 and 35 Nova sensors in groups of 4 and 5 were used respectively. The long term data (around 1 month) for the Nova sensors were studied in regards to deviation within each group and to investigate the differences between the two plants. Short term data (around 24h) with both sensor types were studied to compare the deviation between the sensors both for PM10-PM2.5 and PM2.5. More detailed size fraction comparisons were compiled from the Fidas data, highlighting the difference in size fraction between SiMn and Si fumes.

Following are the main conclusions inferred within each category previously discussed:

- For measurements in both SiMn and MG-Si production plants, the Nova sensors picked up on almost all the same peaks as the Fidas sensor, and the increases and decreases in fume levels are similarly captured by both sensor systems.
- For the SiMn-fumes, the measured fume levels are mostly quite comparable between the Nova and the Fidas. The relation between Nova and Fidas for larger particles (PM10 - PM2.5) divided by smaller particles (PM2.5) is strongly clustered and show linearity close to 1:1.
- For the Si-fumes, the Fidas measured on average close to three times as high as the Nova sensors, and the difference was largest for PM2.5. This is believed to be largely due to the finer fumes coupled to lower measurement boundary of the Fidas being 180nm compared to the 300nm of the Nova.
- Deviation within each group of Nova sensors and between groups for both the SiMn and Si-campaign showed a relatively stable deviation from the mean value. Given a stable deviation over time, it would be possible to compensate for the internal deviation of the Nova sensors through a calibration period to get a much lower spread of measurements. For most groups the spread was within +/- 20% relative deviation, close to the 15% relative deviation level provided by the manufacturer.
- For future industrial measurements campaigns, an improved and preferably airtight casing for the Nova system is considered important to improve length of life, and it is believed that using 4-5 sensors in each group to have room for 1-2 failures before service and potential replacements are needed would provide sufficient lifetime for the system as a whole to not cause unnecessary expenses in this regard.

Funding: This research was funded by Centre for Research-Based Innovation grant number 237738.

Acknowledgments: The authors would like to thank Eramet and Elkem for collaboration with setting up the sensors in their smelting plans, and Norce (through Hege Indresand) for supplying the calibration equipment and their expertise for one of the campaigns.

Conflicts of Interest: The authors declare no conflict of interest. The funders had no role in the design of the study; in the collection, analyses, or interpretation of data; in the writing of the manuscript, or in the decision to publish the results.

References

1. Contrec (2020) *Fine dust measuring instrument model Fidas® 200 S*. Contrec, Technology in Science and Health. https://www.contrec.ch/en/fir dust-measurement-devices/feinstaubmessgeraet-modell-fidas-200s-3, accessed 24.11.2020
2. Liu H-Y, Dunea D, Iordache S, Pohoata A (2018) *Review of Airborne Particulate Matter Effects on Young Children's Respiratory Symptoms and Diseases.*. Atmosphere 2018, 9, 150.
3. Liu H-Y, Bartonova A, Schindler M, Sharma M, Behera SN, Katiyar K, Dikshit O. (2013) *Respiratory Disease in Relation to Outdoor Air Pollution in Kanpur, India.*. Arch. Environ. Occup. Health 2013, 68, 204–217.
4. Dockery DW, Stone PH (2007) *Cardiovascular risks from fine particulate air pollution*. N. Engl. J. Med. 2007, 356, 511–513.
5. Pérez L, Medina-Ramón M, Künzli N, Alastuey A, Pey J, Pérez N, García R, Tobías A, Querol X, Sunyer J (2009) *Size fractionate particulate matter, vehicle traffic, and case-specific daily mortality in Barcelona (Spain)*.. Environ. Sci. Technol. 2009, 43, 4707–4714.
6. Liu H-Y, Schneider P, Haugen R, Vogt M (2019) *Performance Assessment of a Low-Cost PM2.5 Sensor for a near Four-Month Period in Oslo, Norway*. Atmosphere 2019, 10, 41, DOI: 10.3390/atmos10020041
7. Kero I, Naess MK, Tranell G (2014) *Particle Size Distributions of Particulate Emissions from the Ferroalloy Industry Evaluated by Electrical Low Pressure Impactor (ELPI)*. Journal of Occupational and Environmental Hygiene, 12:1, 37-44, DOI:10.1080/15459624.2014.935783
8. Ma Y, Kero I, Tranell G (2017) *Fume Formation from Oxidation of Liquid SiMn Alloy*. Oxidation of Metals, DOI 10.1007/s11085-017-9780-y
9. Næss MK, Olsen JE, Andersson S, Tranell G *Parameters Affecting the Rate and Product of Liquid Silicon Oxidation*. Oxid Met (2014) 82:395–413
10. European Comission (2019) *Air Quality Standards*. Website providing european standards, visited september 2020, Link: https://ec.europa.eu/environment/air/quality/standards.htm
11. Palas (2020) *EN 16450 approved fine dust measurement device for simultaneous measurement of PM2.5 and PM10*. Instrument specifications provided by Palas, Version: June 30, 2020.
12. Aliexpress, HS Electronics LTD (2020) *Product Description Nova PM SDS011*. Website delivering the Nova sensor, visited Sept 2020, Link: https://www.aliexpress.com/item/32617788139.html

13. Genikomsakis KN, Galatoulas FK, Dallas PI, Ibarra LMC, Margaritis D, Ioakimidis C (2018) *Development and On-Field Testing of Low-Cost Portable System for Monitoring PM2.5 Concentrations*. Sensors (Basel). 2018 Apr; 18(4): 1056.
14. Badura M, Batog P, Drzeniecka-Osiadacz A, Modze P (2018) *Evaluation of Low-Cost Sensors for Ambient PM2.5 Monitoring*. Hindawi, Journal of Sensors, Volume 2018.
15. Myklebust H, Aarhaug T, Tranell G (2020) *Measurement system for fugitive emissions in primary aluminium electrolysis*. The Minerals, Metals and Materials Series 2020 p 735-743.
16. Jayaratne R, Liu X, Ahn KH, Asumadu-Sakyi A, Fisher G, Gao J, Mabon A, Mazaheri M, Mullins B, Nyaku M, Ristovski Z, Scorgie Y, Thai P, Dunbabin M, Morawska L (2020). *Low-cost PM2.5 Sensors: An Assessment of their Suitability for Various Applications*. Aerosol Air Qual. Res. 20: p 520-532. https://doi.org/10.4209/aaqr.2018.10.0390
17. Zervaki O, Zheng L, Dionysiou D, Kulkarni P, Zarus GM (2017) *Calibration of Low-cost Dust Sensors*. 110th Annual Conference and Exhibition of the Air and Waste Management, June 2017
18. Jayaratne R, Liu X, Thai P, Dunbabin M, Morawska L (2018) *The influence of humidity on the performance of a low-cost air particle mass sensor and the effect of atmospheric fog*. Atmos. Meas. Tech., vol 11, p 4883–4890, 2018
19. Aliexpress, HS Electronics LTD (2021) *Product Description HTU21d*. Website delivering the temperature and humidity sensor, visited April 2021, Link: https://www.aliexpress.com/item/32694783990.html
20. Alvarado M, Gonzalez F, Fletcher A, Doshi A (2016) *Towards the Development of a Low Cost Airborne Sensing System to Monitor Dust Particles after Blasting at Open-Pit Mine Sites*. Sensors 2015, 15(8), 19667-19687; https://doi.org/10.3390/s150819667ors

ISBN 978-82-326-5959-3 (printed ver.)
ISBN 978-82-326-5234-1 (electronic ver.)
ISSN 1503-8181 (printed ver.)
ISSN 2703-8084 (online ver.)

NTNU

Norwegian University of
Science and Technology